# HIGHLY TRANSIENT AXI-SYMMETRIC SQUEEZE FLOWS

A thesis submitted to the Faculty of Engineering and the Built Environment, University of the Witwatersrand, Johannesburg, in fulfilment of the requirements for the degree of Doctor of Philosophy in Engineering.

Alexei E. Krass de Krassnokutski

Supervisor Prof. E. A. Moss

Co-supervisor: Prof. B.W. Skews

February 2010

# DECLARATION

I hereby declare that this thesis is my own unaided work. It is submitted for the Degree of Doctor of Philosophy to the University of the Witwatersrand, Johannesburg. It has not been submitted before for any degree or examination to any other University.

.....

..... day of ..... year.....

# ABSTRACT

The aim of this work was to use experimental, analytical and computational (Computational Fluid Dynamic - CFD) methodologies to investigate so-called *highly transient axi-symmetric squeeze flows*. These flows occur between two co-axial and parallel discs which are subjected to an impact, arising from a falling mass, which induces a *constant energy* squeezing system, as distinct from the traditionally investigated constant force or constant velocity squeezing systems.

Experiments were conducted using a test cell comprising two parallel discs of diameter 120 mm with a flexible bladder used to contain fluid. This test cell was bolted onto the base of a drop-weight tester used to induce constant energy squeeze flows. Glycerine was used as the working fluid, the temperature of which was appropriately monitored. Disc separation, together with pressures (at three radial positions), were measured throughout the experimental stroke (typically less than 10 ms duration). Two additional pressure transducers (at the same radial position as the outermost transducer) were also used to monitor (and subsequently correct for) minor non-axi-symmetries that arose in the system. Approximately 150 tests were conducted, embracing combinations of drop height from 0.1 to 1 m, drop mass from 10 to 55 kg and initial disc separation from 3 to 10 mm.

Three elementary features were typically observed: a distinct preliminary pressure spike (1) immediately after impact corresponding to very large accelerations (exceeding over 6 km/s$^2$ in some experiments), a secondary major pressure spike (2) towards the termination of the stroke corresponding to diminishing disc separations and a bridging region (3) joining the two spikes corresponding to somewhat reduced pressures. While pressure distributions were observed to be closely parabolic during the major pressure spike, some uncertainty was present during the preliminary pressure spike, ascribed to sensitivities to deviations from axi-symmetry, and the likelihood of inertially generated pressures at the edge of the disc.

By applying newly defined parameters of inertial composition $\Re$ (which characterizes the ratio of temporal to spatial inertia effects) and dynamic Reynolds number $Re_{dyn}$ (which represents the instantaneous ratio of inertial to viscous effects), it was established that the preliminary pressure spike is dominated by temporal inertia whereas the major pressure spike is viscous dominant. The former feature appears not to have been reported on in the formal literature.

Four analytical models were considered, invoking the parallel flow assumption in conjunction with the Navier Stokes equations: an inviscid/inertial model, a viscous model (the lubrication approximation), a quasi-steady linear (*QSL*) model and a quasi-steady corrected linear (*QSCL*) model. The first two of these models, on incorporation of measured disc separations, and the derived velocities and accelerations, achieved acceptable correlations with pressure measurements (largely within uncertainty bounds) during the initial impact and towards the end of the stroke, respectively. The *QSL* model agreed satisfactorily with measurements throughout the entire duration of the experiment, while the *QSCL* model, by incorporating non-linear effects in an approximate linear way, yielded somewhat better correlations. By invoking the parallel flow assumption, all four models predict a parabolic radial pressure distribution.

Utilizing a hypothetical case in which variations of disc separation, velocity and acceleration were considered (employing similar magnitudes and timescales to those that were measured), outputs of the *QSL* model yielded results that correlated closely with CFD predictions, while the *QSCL* data were somewhat better. On the basis of the CFD data it was also inferred that, within practical uncertainty bounds, the parallel flow assumption was valid for the range of disc separation to radius ratios embraced in the current investigation.

*To Nona*

*Pia Wesemann*

# ACKNOWLEDGEMENTS

I am indebted to the following people without whom I would not have been able to complete this thesis:

- Prof. E A Moss and Prof. B W Skews for motivating for me to convert my MSc to a PhD and for their in depth knowledge and passion for their respective fields of study which has greatly contributed to this thesis. Moreover, I am grateful for the financial support received from both supervisors.
- An extra word of thanks goes to Prof. E A Moss for the countless hours of supervisor meetings and for his personal time spent proof reading this thesis and for preparing papers on this topic.
- Mr. R Paton for assisting me with software packages FLUENT™ and MATLAB™.
- Prof. B Watson, for his help in solving differential equations.
- My parents, Ling and Leo, for their love, support and for tolerating my grossly prolonged university career.
- My partner, Joanna, for her love, support and for affording me the space needed to complete this thesis.

# CONTENTS

# LIST OF FIGURES

# LIST OF TABLES

# NOMENCLATURE

| Symbol | Meaning | Units |
|---|---|---|
| $h$ | Disc separation | m |
| $z$ | Axial coordinate | m |
| $z^*$ | Dimensionless axial separation | - |
| $U$ | Disc velocity ($U = -\dot{h}$) | m/s |
| $a$ | Disc acceleration ($a = \ddot{h}$) | $m/s^2$ |
| $r$ | Radial coordinate (of discs) | m |
| $R$ | Disc radius | m |
| $r^*$ | Dimensionless disc radius | - |
| $p$ | Pressure | Pa |
| $v$ | Velocity | m/s |
| $\rho$ | Density | $kg/m^3$ |
| $\mu$ | Absolute viscosity | $Ns/m^2$ |
| $\nu$ | Kinematic viscosity | $m^2/s$ |
| $F$ | Squeeze force | N |
| $g$ | Dimensionless axial fluid velocity | - |
| $f$ | Dimensionless radial fluid velocity | - |
| $\Re$ | Inertial composition | - |
| $\alpha, \beta$ and $\gamma$ | Shape parameter variables | |
| $\lambda$ | Shape parameter | - |
| $\lambda_{cor}$ | Corrected shape parameter | - |
| $\kappa$ | Linearization variable | - |
| $X$ | Evolution ratio | - |
| $Re$ | Reynolds number | - |
| $Re_{dyn}$ | Dynamic Reynolds number | - |
| $p_{cir}$ | Circumferential pressure offset (analytically determined) | Pa |

| | | |
|---|---|---|
| $p_R$ | Circumferential pressure offset (experimentally inferred) | Pa |
| $b$ | Radial coordinate (of bladder) | m |
| $m$ | Source strength | $m^2/s$ |
| $\varphi$ | Effective annular jet angle | rad |
| $\theta$ | Skewness angle | rad |
| $\psi$ | Sinusoidal displacement | rad |
| $\phi$ | Symmetry angle | rad |
| $\sigma$ | Skewness magnitude | - |
| $\chi$ | Eccentricity magnitude | Pa |
| $\xi$ | Peak offset | m |
| $\varepsilon$ | Parabolic deviation variable | - |

| **Operator** | **Meaning** |
|---|---|
| $(\dot{\ })$ | Denotes a time derivative |
| $()'$ | Denotes a dimensionless axial separation derivative (see above) |
| $O()$ | Denotes an order of magnitude |
| $\overline{()}$ | Denotes a mean or average measurement |
| $()^*$ | Denotes a dimensionless variable |

| **Subscript** | **Meaning** |
|---|---|
| $()_r, ()_z$ and $()_\theta$ | Respectfully denotes radial, axial and tangential coordinates |
| $()_b$ | Denotes a radial direction within the fluid bladder |
| $()_\mu$ | Denotes only viscous forces have been considered |
| $()_\rho$ | Denotes only inertial forces have been considered |

## Acronyms

- CFD: Computational Fluid Dynamics.
- CAD: Computer Aided Design.
- QS: Quasi-Steady.
- QSL: Quasi-Steady Approximately Linear.
- QSCL: Quasi-Steady Corrected Linear.

# 1 INTRODUCTION

Squeeze flows are flows in which a material is compressed between two parallel plates and is thus squeezed out. Axi-symmetric squeeze flow geometries are regularly investigated, i.e. the squeeze flow between two circular, parallel and co-axial discs as shown in Figure 1-1 (other investigated squeeze flow geometries are briefly discussed in Section 2.1.1, p. 3).

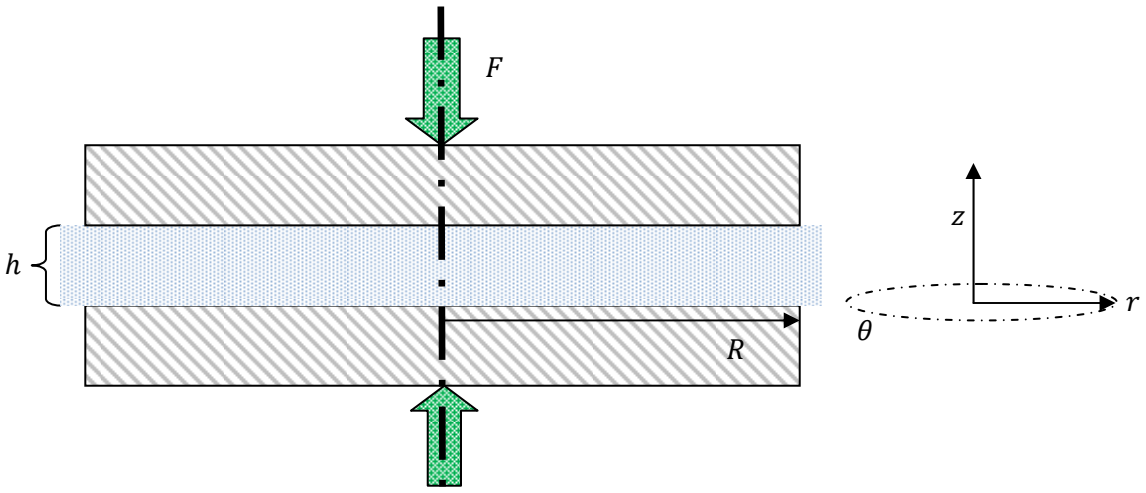


Figure 1-1: Axi-symmetric squeeze flow schematic

Squeeze flows have long been recognised as one of the most basic problems in lubrication theory (Hamza, et al., 1981), with the earliest attempts to solve the problem dating back to Stefan (1874) and Reynolds (1886). Due to the interesting combination of shear and extension in various parts of the flow field, it also has attractions from a basic continuum mechanics viewpoint (Brindley, et al., 1976).

Squeeze flows are inherently transient and inhomogeneous flows due to the changing geometry, and are one of a few deformation systems that have applications for a wide range of materials including purely viscous liquids, viscoelastic solids and liquids, and purely elastic solids. Hence squeeze flows are studied in various scientific disciplines ranging from soil mechanics and metal deformation research to fluid mechanics (Engmann, et al., 2005).

In order for squeeze flows to be considered highly transient, the discs must be squeezed together rapidly (in the order of milliseconds), in such a way that the pressure development varies from temporal inertial dominance through to viscous dominance. A logical way to induce large forces (rapid squeezing motions)

is to drop a mass from a predetermined height onto the upper disc which is initially separated from its stationary lower counterpart (Figure 1-2). These tests are hereafter referred to as ‘drop-hammer’ tests.

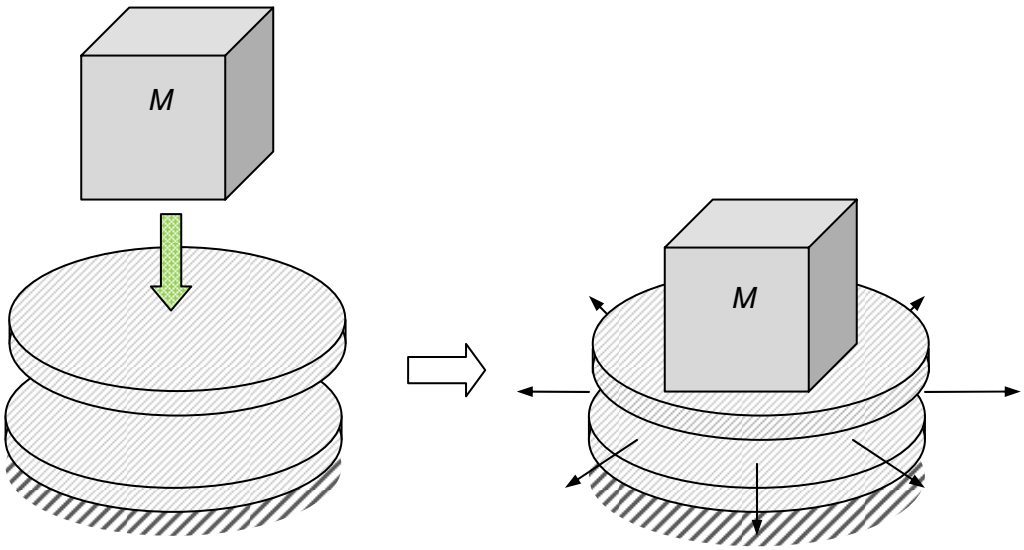


Figure 1-2: ‘Drop-hammer’ tests used to induce highly transient squeeze flows

Traditionally, however, experimental squeeze flows have primarily been concerned with slow or ‘creeping’ flows corresponding to low Reynolds numbers ($Re \ll 1$) (Engmann, et al., 2005). In general, these flows are experimentally induced by releasing a mass (or hammer) already in contact with the upper disc that is initially separated from its stationary lower counterpart (Figure 1-3). These tests are hereafter referred to as ‘contact-hammer’ tests.

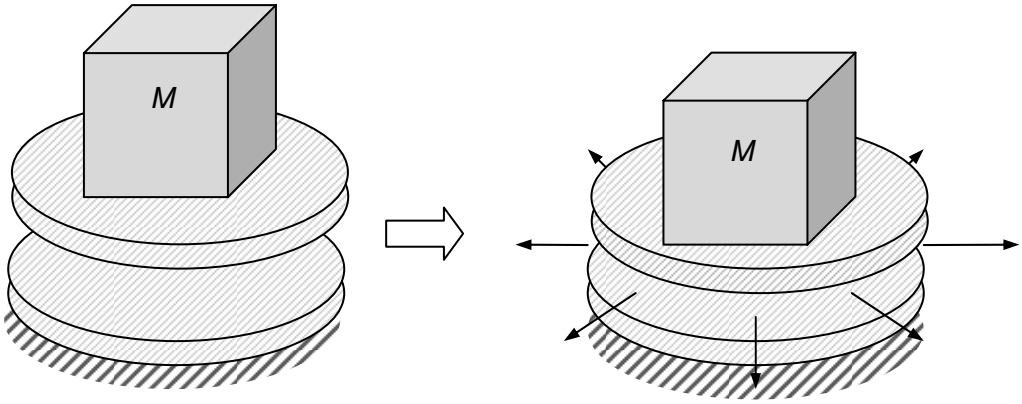


Figure 1-3: ‘Contact-hammer’ tests used to induce creeping squeeze flows

# 2 REVIEW MATERIAL

## 2.1 Squeeze Flow Systems

Squeeze flows can occur between plates of any plan-form; however the flow dynamics may vary depending on the surface geometry, squeezing motion and the initial geometry of the squeeze sample, as defined and concisely discussed in the subsequent sections.

### 2.1.1 Surface geometries

Commonly investigated surface geometries (Engmann, et al., 2005) include:

i. Circular parallel discs (Figure 1-1), resulting in axi-symmetric squeeze flows.
ii. Long rectangular plates, resulting in two-dimensional squeeze flows.

### 2.1.2 Squeezing motions

Generally, analyses of squeeze flows are concerned with either one of two squeezing motions:

i. Constant velocity squeezing motion: This motion assumes a velocity step-change from zero to a prescribed disc velocity. Consequently, analysis is only performed to a time before the discs would theoretically contact and the resultant pressure tends to infinity.
ii. Constant force squeezing motion or the motion resulting for a constant squeezing force. The disc separation forms an asymptotic relationship with time for this squeezing motion.

Both of these hypothetical disc motions prove difficult to reproduce experimentally. A true velocity step-change would require an instantaneous infinite squeezing force which is physically impossible. It is however possible to induce a velocity ramp that may be approximated as a step-change if the time duration of the velocity ramp is negligible in comparison to other associated experimental timescales, for example viscous diffusion. On the other hand, a constant force is hard to realize because of the inertia associated with the driving masses (Figure 1-3). For this reason various authors have included disc and

driving mass inertia within their calculations; nevertheless, these tests are still generally classified as constant force squeezing motions.

### Symmetrical and asymmetrical squeezing motions

Symmetrical and asymmetrical squeezing motions respectively refer to whether:

a. Both discs are squeezed together with mirrored velocities.
b. A single disc is dynamic while the other remains static.

Experimentally inducing asymmetrical squeezing motions is mechanically simpler than inducing symmetrical squeezing motions (Figure 1-2). On the other hand, theoretically modeling symmetrical squeezing motions is simpler than modeling asymmetrical ones due to the symmetry of the radial fluid velocities and resultant pressure distributions (about the radial plane bisecting the disc separation). However, if spatial inertia (which is responsible for the skewing of the radial velocity and resultant pressure distribution) is considered to be negligible, asymmetrical squeezing motion experimentation may be compared directly against a symmetrical squeezing motion analysis. Spatial inertia in creeping flows ($Re \ll 1$) is generally considered negligible; however, it is unknown if this assumption is valid for highly transient squeeze flows. This issue is later investigated in Section 6.5, p. 63.

## 2.1.3 Squeeze sample geometries

The initial geometry of the squeeze sample (Engmann, et al., 2005) may also be split into the two following categories:

i. Constant contact area squeeze material: The entire area of the both plates initially makes contact with the squeeze sample before squeezing, for example submerging two separated discs in a liquid before squeezing.
ii. Constant mass squeeze material: A cylindrical squeeze sample (mass), of radius less than that of the discs, for the case of an axi-symmetric squeeze, is concentrically placed between the discs before squeezing. Generally this squeeze sample geometry only applies to non-liquid material squeeze flows because radially unrestrained liquids are unable to maintain the initial geometry existing before the squeezing motion.

This thesis is only concerned with axi-symmetric squeeze flows (circular discs) with a constant contact area squeeze sample. Furthermore, since highly transient disc dynamics are investigated, neither of the above squeezing motions is exclusively considered.

## 2.2 Research Trends

Squeeze flows are an attractive technique for measuring rheological properties of materials that create difficulties in conventional rheometers; for example very viscous materials, fluids with an apparent yield stress, fluids that tend to slip at instrument interfaces or materials with large particles (often, these characteristics appear together) (Engmann, et al., 2005). Hence constant squeeze force, axi-symmetric squeeze flows form the basic configuration for parallel plate viscometers or plastometers as they are known today (Phan-Thien, et al., 1983). Plastometers use either constant contact area or constant volume squeeze material and generally only measure creeping flows ($Re \ll 1$). As a consequence of these commercial applications, the following research trends of squeeze flow rheometry are observed in the comprehensive review compiled by Engmann et al (2005):

i. In general, work on Newtonian squeeze flows took place before the 1980s. During and post the 1980's there was a shift in research from Newtonian to non-Newtonian fluids. This trend is apparent in table 8 of Engmann's review, which gives the peak period during which most publications have appeared for a particular material class.

ii. As a consequence of the multitude of the non-Newtonian models, and owing to the increase in theoretical (mathematical) complexity of non-Newtonian fluids, the number of papers concerning non-Newtonian fluids outnumbers those exclusively concerning Newtonian fluids. This trend is apparent by reviewing the referenced titles in Engmann's review.

iii. Although inertia for non-Newtonian squeeze flows has been considered by a handful of authors, most notably Phan-Thien (1983), in general research of non-Newtonian squeeze flows pertains only to creeping flows (negligible inertia). More specifically, in table 3 of Engmann's review, 52 references of various models approximating solutions to non-slip squeeze flows with varying boundary conditions (varying fluid models in particular) are made. Of these 52 referenced models, only 16 take inertia into account. It is noted that Newtonian fluids can be considered as a limiting case of non-Newtonian fluids; however, it is generally found that these studies have made limiting assumptions regarding inertia and concentrated rather on the mathematical complexities arising from the specific fluid under investigation.

## 2.3 Governing Equations

For the sake of convenient referencing, governing equations are introduced preceding the literature review.

The following squeeze flow assumptions are made:

i. The flow is incompressible and isothermal.
ii. Gravitational body forces are negligible.
iii. The disc separation $h$ is small in comparison to the disc radius $R$.
$\Rightarrow \partial(\text{all velocities})/\partial z \gg \partial(\text{all velocities})/\partial r$ .
iv. Axial flows are negligible, i.e. the flow is two-dimensional ($\Rightarrow v_z \approx 0$).
v. The flows are axi-symmetric ($\Rightarrow \partial/\partial\theta's = 0;\ v_\theta = 0$).

Applying the above squeeze flow assumptions to the Navier-Stokes[a] equations yields

$$\underset{(A)}{\frac{dp}{dr}} = \underset{(B)}{\mu\frac{\partial^2 v_r}{\partial z^2}} - \underset{(C)\quad(D_1)\quad(D_2)}{\rho\left(\frac{\partial v_r}{\partial t} + v_r\frac{\partial v_r}{\partial r} + v_z\frac{\partial v_r}{\partial z}\right)} \tag{2-1}$$

and

$$\frac{\partial p}{\partial z} \approx 0 \tag{2-2}$$

where $p$ is pressure, $\mu$ is absolute viscosity, $v$ is velocity, $\rho$ is density and $t$ is time. The suffices $r$ and $z$ respectively denote radial and axial components as shown in Figure 1-1, p. 1.

The terms of equation (2-1) are labelled and are physically interpreted as follows:

- *A* represents the radial pressure gradient.
- *B* represents viscous forces.
- *C* represents temporal inertia.
- $D_1$ and $D_2$ represent spatial inertia.

[a] Refer to Appendix A to review the reduction of the Navier-Stokes equation yielding equation (2-1).

Continuity of the flow system (Brindley, et al., 1976) is be given as

$$\frac{\partial v_r}{\partial r} + \frac{v_r}{r} + \frac{\partial v_z}{\partial z} = 0. \tag{2-3}$$

In addition, from the condition of continuity (Ishizawa, 1966), the mean velocity through any radial strip is given as

$$\overline{v_r} = -\frac{r}{2}\frac{\dot{h}}{h} \tag{2-4}$$

where the dot operator denotes a time derivative.

Within the reviewed literature, unless otherwise specified, the Reynolds number (Tichy, 1981) is given as

$$Re \equiv -\frac{h\dot{h}}{\nu} \tag{2-5}$$

in which ν is the kinematic viscosity where

$$\nu \equiv \frac{\mu}{\rho}. \tag{2-6}$$

## 2.4 Literature Review

Stefan (1874) first considered two separating discs, or "reverse squeeze flows" and the apparent adhesion (negative pressures) observed. Later Reynolds (1886) rediscovered many of Stefan's results for conventional squeeze flows. Both authors considered squeeze flows for incompressible Newtonian fluids with negligible inertia effects, i.e. only terms *C* and *D* of equation (2-1). This assumption of negligible inertia effects later became known as the *lubrication approximation* (Tichy, 1981). Under the lubrication approximation, these authors discovered that both the radial fluid velocity profiles and resultant pressure distribution are invariably parabolic (Phan-Thien, et al., 1987), with radial and axial fluid velocities, and pressure respectively given by

$$v_{r\mu} = \frac{3r\dot{h}}{h^3}(z^2 - hz), \qquad v_{z\mu} = -\frac{\dot{h}}{h^3}(2z^3 - 3hz^3), \tag{2-7a, b}$$

and

$$p_\mu = -3\mu\frac{\dot{h}}{h^3}(R^2 - r^2) \equiv -3\mu R^2\frac{\dot{h}}{h^3}\left(1 - r^{*2}\right), \tag{2-8}$$

where the $\mu$ subscript indicates the solution considers only viscosity (neglects inertia) and where $r^*$ is defined as the dimensionless radius where

$$r^* \equiv \frac{r}{R}. \tag{2-9}$$

Finally both authors derived an expression, equating the squeezing force with the disc separation and velocity given by

$$F_\mu = \frac{3}{2}\pi\mu\frac{\dot{h}}{h^3}R^4 \tag{2-10}$$

where $F$ is the squeezing force applied to the discs.

Scott (1931) proceeded to show that the radial pressure distribution for an incompressible power law (non-Newtonian) fluid with negligible inertia effects remains invariably parabolic and then derived an expression for the squeezing force

$$F_{\mu,pl} = -2\frac{\left(-\dot{h}\right)^n}{h^{2n+1}}\pi\mu\left(\frac{2n+1}{n}\right)^n\frac{\pi m R^{n+3}}{n+3} \tag{2-11}$$

where $m$ and $n$ represent the fluid consistency and power law index respectively and the $pl$ subscript indicates power-law fluids. Although the investigation of non-Newtonian fluids is beyond the scope of this thesis, it is noted that for the limiting case of a Newtonian fluid, where $m = n = 1$, equation (2-11) reduces to equation (2-10), as expected.

Axi-symmetric squeeze flows experimentation with power-law fluids was carried out by Leider (1974) who showed that $t_{1/2}$ (the so-called 'separation half-time' or the time required to squeeze half the fluid out from between the discs) is a useful measurement and is a relatively constant experimental variable for constant force squeezing motions. Leider's analysis was extended by McClelland et al (1983), who considered both viscometric functions and compressibility effects of squeeze flows. However, both authors neglected inertia effects, and consequently results obtained from their models, like those obtained from of Scott's model [equation (2-11)] differed increasingly from experimental results as squeeze velocities increased.

In order to derive an analytically determinable squeeze flow model that incorporates both viscous and inertial forces, further simplification of the governing equations is required. This simplification is given in the form of the exact kinematics of the Newtonian fluid (including all inertia terms) in which the radial and axial fluid velocities are given by

$$v_r = -\frac{r}{2}\frac{\dot{h}}{h}g'(z^*,t) \quad \text{and} \quad v_z = \dot{h}g(z^*,t), \tag{2-12a, b}$$

where $t$ is time, $g$[a] is the dimensionless axial velocity and the prime denotes a derivative with respect to the dimensionless axial derivative $z^*$ which is defined as

[a] Authors generally use $f$ as opposed to $g$. However in this thesis $f$ is defined as $f = g'$.

$$z^* \equiv \frac{z}{h}. \tag{2-13}$$

Equations (2-12a, b) later became known as the *parallel flow assumption* because fluid planes initially parallel to the plates remain parallel throughout (Engmann, et al., 2005). Since the axial flow is independent of radius, this leads to a partial differential governing equation with two independent variables ( $z^*$ and $t$) as opposed to three ($r$ , $z^*$ and $t$) when applied to equation (2-1). This was explicitly demonstrated by Phan-Thien et al (1987) who showed that for an incompressible Newtonian fluid under the parallel flow assumption, $g$ satisfies the following relationship

$$g'^{v} - \frac{\dot{h}h}{\nu}\left\{\left[\frac{\ddot{h}h}{\dot{h}^2} - 2\right]g'' + \frac{h}{\dot{h}}\dot{g}'' + (g - z^*)g'''\right\} = 0 \tag{2-14}$$

with boundary conditions of

$$z^* = 0; g = g' = 0$$
$$z^* = 1; g = 1, g' = 0$$

for an asymmetrical squeezing motion. Appendix A contains the derivation of equation (2-14).

Although it is noted that the parallel flow assumptions is embedded in even the simplest models of Stefan and Reynolds [equations (2-7a, b)], it appears that its first deliberate application was made by Ishizawa (1966). Ishizawa presented an elegant model for axi-symmetric squeeze flows at arbitrary varying disc separations, including disc acceleration. Ishizawa first derived a governing equation under the parallel flow assumption, similar to equation (2-14) but which neglected disc acceleration. He then used a standard series perturbation technique to obtain an infinite set of time dependent parameters (which included disc acceleration) given by the series

$$\frac{h}{\nu}\dot{h}, \qquad \frac{h^3}{\nu^2}\ddot{h}, \qquad \frac{h^5}{\nu^3}\dddot{h}, \qquad \ldots \tag{2-15}$$

These parameters were used to define a multifold power series of parameters to accurately obtain the dimensionless axial velocity $g$ when applied to the governing equation; in turn, $g$ was used to solve for the radial pressure gradient. This expansion technique assumes that the arbitrary disc separation is infinitely differentiable with time [series (2-15)] and applies only to Reynolds numbers of less than unity

[equation (2-5)]. Hence, when applied to systems with large Reynolds numbers, Ishizawa's model produces erroneous results; this was later demonstrated by Grimm (1976) (discussed below).

Jones and Wilson (1975), Tichy and Modest (1980), and Gupta and Gupta (1977) also took cognisance of inertia effects under the parallel flow assumption and solved the resultant equations using perturbation methods. A peculiarity was noted by Jones and Wilson in that while most perturbation solutions are theoretically valid for $Re < 1$, accurate results were obtained up to $Re \approx 10$.

Brindley et al (1976) showed that the parallel flow assumption is only valid for power-law fluid (of which Newtonian fluids are a limiting case). Brindley then showed that the parallel flow assumption needs to be 'relaxed' for a fluid with an arbitrary viscosity/shear rate relationship which may result in a non-parabolic pressure distribution.

Equation (2-14) is a partial differential equation that represents a non-linear system and is best solved by numerical means. This was done by Hamza and MacDonald (1981), who solved equation (2-14) numerically, using a finite difference scheme for a theoretical investigation of a Newtonian fluid under a constant velocity squeezing motion. Hamza and MacDonald's equation is similar to equation (2-14), albeit in a more elaborate non-dimensional form, which was derived from the non-dimensional momentum equations. However, due to the assumed velocity step-change, Hamza and MacDonald's equation neglects the term encompassing the disc acceleration (Section 2.1.2, p. 3). Non-dimensional terms defined by Hamza and MacDonald include

$$Re \equiv -\frac{h_0 \dot{h}}{\nu}, \qquad t^* \equiv -\frac{\dot{h} t}{h_0} \qquad \text{and} \qquad \tau \equiv \frac{t^*}{Re} = \frac{\nu t}{h_0^2}$$

where $h_0$ is the initial disc separation (hence, it is noted that the authors consider $Re$ as constant throughout the experimental stroke) and $t^*$ is defined as the dimensionless time where $t^* \in (0,1)$.

Essentially, Hamza and MacDonald proceeded to perform an order of magnitude analysis on equation (2-14), where for $Re\tau^{1/2} \sim O(1)$, their equation approximates to

$$\frac{h^2}{\nu} \dot{g}'' = g'^{v}. \tag{2-16}$$

After being analytically solved for a given $Re$ and $t^*$, the solution of equation (2-16) was then used to solve the radial pressure gradient of the hypothetical system. This result, in turn, was compared against radial pressure gradient obtained by the numerical solution of equation (2-14) in its entirety at the same $Re$ and $t^*$values. Hence a parametric testing range of $Re$ ($0.5 \leq Re \leq 96$) and $t^*$ ($0.0175 \leq t^* \leq 0.960$) was then set up in which the numerical and analytical solutions for the radial pressure gradient are tabulated and compared. Deviations of less than 5% between numerical and analytical results were achieved for low $Re$ ($Re < 20$) throughout the experimental stroke (all ranges of $t^*$). However, as $Re$ increased to $Re = 96$, a discrepancy of approximately 15% was observed.

Closer investigation of the restriction $Re\tau^{1/2} \sim O(1)$ reveals that

$$\sqrt{Re}\sqrt{t^*} \sim O(1). \tag{2-17}$$

Hence values of the Reynolds number were limited to $0.5 \leq Re \leq 96$ as not to violate equation (2-17). Similarly $t^*$ was also truncated at $t^* \geq 0.0175$ and also limited to $t^* \geq 0.96$ because of the infinite pressure gradient experienced at zero disc separation corresponding to $t^* = 1$. At the above selected parametric space limits, $Re\tau^{1/2}$ falls between the liberal range of $0.935 \leq Re\tau^{1/2} \leq 9.6$.

Kuzma (1967) used the first term of a successive approximation method to solve for the radial velocity profiles of incompressible, axi-symmetric squeeze flows. Kuzma's approach was similar to that of Jackson (1962) in that the *inertia components* of *purely viscous velocity profiles* are used to calculate an approximate radial fluid velocity profile. However, unlike Jackson's work, Kuzma considered the inertia contributions of both of the *dominant* spatial inertia terms entirety while Jackson neglected, amongst others, the $v_{r\mu}\,\partial v_{r\mu}/\partial r$ term in the expression

$$\mu\frac{\partial^2 v_r}{\partial z^2} = -\frac{1}{\mu}\frac{\partial p}{\partial r} + \frac{1}{\nu}\left(\frac{\partial v_{r\mu}}{\partial t} + v_{r\mu}\frac{\partial v_{r\mu}}{\partial r} + v_{z\mu}\frac{\partial v_{r\mu}}{\partial z}\right) - \left(\frac{\partial^2 v_{r\mu}}{\partial r^2} + \frac{1}{r}\frac{\partial v_{r\mu}}{\partial r} - \frac{v_{r\mu}}{\partial r^2}\right) \tag{2-18}$$

where $v_{r\mu}$ and $v_{z\mu}$ are recalled from equations (2-7a, b). Even though the last bracket of equation (2-18) is considered extraneous for squeeze flow systems in accord with standard practice (Van Dyke, 1964), Kuzma solved for the velocity profile as

$$v_r = \frac{1}{\mu}\left[\frac{6\mu r\dot{h}}{h^3} + \left(\frac{3\rho r\ddot{h}}{5h} - \frac{15\rho r\dot{h}^2}{14h^2}\right)\right]\left(\frac{y^2}{2} - \frac{hy}{2}\right) + \frac{1}{\nu}\left[\frac{3r\ddot{h}}{h^3}\left(\frac{y^4}{12} - \frac{hy^3}{6} + \frac{h^3y}{12}\right) + \frac{3r\dot{h}^2}{h^6} - \frac{y^6}{10} + \frac{3hy^5}{10} - \frac{3h^2y^4}{4} + h^3y^3 + \frac{9h^4y^2}{20}\right] \quad (2\text{-}19)$$

and the pressure between the discs is given by

$$p - p_0 = \frac{r^2 - R^2}{2}\left(\frac{6\mu\dot{h}}{h^3} + \frac{3\rho\ddot{h}}{5h} - \frac{15\rho\dot{h}^2}{14h^2}\right) \quad (2\text{-}20)$$

which may to integrated across the disc area to give a squeeze force of

$$F = \frac{\pi R^4}{4}\left(\frac{6\mu\dot{h}}{h^3} + \frac{3\rho\ddot{h}}{5h} - \frac{15\rho\dot{h}^2}{14h^2}\right). \quad (2\text{-}21)$$

Kuzma also conducted constant force squeeze flow experiments in which he used mercury as a working fluid as to minimize the kinematic viscosity and hence maximize the contribution of inertia to the pressure generation. Kuzma experimentally measured the disc separation traces of squeeze flow systems, which he compared against the theoretical disc separation traces resulting from both the lubrication approximation [equations (2-10)] and his approximate solution [equation (2-21)]. In conclusion, Kuzma showed that there was a large discrepancy between the lubrication approximation and experimental results, whereas his approximate analytical solution showed good agreement with experimental results for systems for Reynolds numbers up to approximately 60 (as suggested by Kuzma's results).

It is subsequently shown in Figure 6-13 (Section 6.4.1, p. 62) that Kuzma's approximate pressure trace solution corresponds very accurately with the Computational Fluid Dynamics (CFD) solution for the hypothetical highly transient squeeze flow given in Section 6.1, p. 47. It is also shown that this correlation is most accurate where fluid velocity profiles are similar to that of the lubrication approximation, i.e. where $v_r \approx v_{r\mu}$ and $v_z \approx v_{z\mu}$. Correspondingly, Kuzma's radial velocity shapes (Figure 6-14) appear erroneous at the stroke initiation (associated with a squarer radial velocity profile).

A simpler way of including inertia in squeeze flow flows was used by Lin and Hung (2007) and Batra and Kanasamy (1989), who assumed that the fluid inertial forces are constant across thin film thickness and are thus relatively simple to include in conjunction with viscous forces. Lin and Hung investigated non-

Newtonian (Bingham) squeeze flows and hence were primarily concerned with non-Newtonian effects; however for the limiting case where non-Newtonian fluids tend to Newtonian fluids, their expression for pressure simply becomes

$$p = \frac{r^2 - R^2}{2}\left(\frac{6\mu\dot{h}}{h^3} + \frac{\rho\ddot{h}}{2h} - \frac{18\rho\dot{h}^2}{20h^2}\right). \tag{2-22}$$

It can be seen that equation (2-22) is similar to equation (2-20), with only coefficients of the last two terms varying slightly due to different assumptions.

Kramer (1974) considered both viscous and inertial effects in squeeze flows and derived a partial differential equation defining the complete numerical solution of the disc separation given in a convected coordinate system given by

$$-\frac{\rho}{q}\ddot{q} + \mu q^4 \frac{\pi R^4}{h^4}\left[\frac{\dot{q}''}{\dot{q}}\right] = \frac{F(t)}{4R^4} \qquad \text{where} \qquad h = \int_0^{h_0} q^{-2} dz^*. \tag{2-23a, b}$$

Kramer did not solve equation (2-23a) as it stands, but rather went on to consider non-Newtonian flows ignoring inertial effects. Grimm (1976) however, proceeded to solve Kramer's equation numerically to obtain an accurate solution of the disc separation. Grimm also expressed the squeezing force in terms of Ishizawa's expansion series (2-15) as

$$\frac{F}{\rho\nu^2} = -\frac{\pi R^4}{h^4}\left[\frac{4h}{\nu}\dot{h} - \frac{5}{7}\left(\frac{h}{\nu}\dot{h}\right)^2 + \frac{2}{5}\frac{h^3}{\nu^2}\ddot{h} - \frac{1}{2100}\frac{h^5}{\nu^3}\dddot{h} + \frac{2}{315}\left(\frac{h}{\nu}\dot{h}\right)\left(\frac{h^2}{\nu^2}\ddot{h}\right) - \frac{554}{40425}\left(\frac{h}{\nu}\dot{h}\right)^3 + \cdots\right] \tag{2-24}$$

where he used the first three terms in the right-hand bracket as the first-order perturbation solution and the entire equation as the second-order perturbation solution. Ultimately Grimm compared the disc separation trace obtained from equation (2-23a) (the complete numerical solution) against the first and second order perturbation solution and that of the lubrication approximation [equation (2-10)], for a variety of hypothetical test results with varying absolute viscosities. The results showed that inertia effects are significant and the first order perturbation solution is in relatively good agreement with the complete numerical solution. Conversely, the second order perturbation solution deviates radically from the

complete numerical solution; hence, Grimm concluded that Ishizawa's perturbation solution is divergent and it is therefore preferable to use numerical techniques for solving squeeze flow problems when possible. However, closer analysis of Grimm's data suggests that his experiments were conducted at Reynolds numbers of order 50 to 500 and his initial gap to radius ratio was, in some experiments, close unity. Both of the above factors may explain the deviation of Ishizawa's perturbation solution at higher orders.

Equation (2-14) and (2-23a) are partial differential equations with two partial derivatives, namely a dimensionless axial coordinate and time $t$. Hence many authors have sought similarity solutions in order to analytically solve either equation. Ishizawa (1966) first discovered a similarity solution in which a disc velocity, given by $\dot{h} = k\sqrt{1-\alpha t^*}$ reduces the problem to an ordinary differential equation. This approach was subsequently adopted by Wang (1976), in the context of a perturbation approach and more recently by Rashidi et al (1998) who adopted a homotopy analysis solution for the same equation.

On the other hand, Tichy (1981) developed a similarity solution in which the only constraint is small disc accelerations. Tichy shows that through an *Oseen* or *slug-flow linearization* approximation, where $v_r\,\partial v_r/\partial r + v_z \partial\, v_r/\partial z \approx \bar{v_r}\,\partial v_r/\partial r - (2\,z/r)\bar{v_r}\,\partial v_r/\partial z$ [where $\bar{v_r}$ is recalled from equation (2-4)] allows equation (2-1) to be linearized, for plate accelerations satisfying $\left|\ddot{h}h/\dot{h}^2\right| \ll 3/2$, as follows

$$g'^v - \frac{(Re)}{|Re|}m^2 g'' = 0 \qquad \text{where} \qquad m = \sqrt{\left|\frac{3}{2}Re\right|}. \qquad \text{(2-25a, b)}$$

Hence Tichy analytically solved equation (2-25a) to give a radial velocity shape of

$$g'(z^*) = \frac{m}{2\cosh(m-z^*) - m\sin m} \times [\sin m(1-z^*) + \sin mz^* + \sin m] \qquad \text{(2-26)}$$

for $Re < 0$ [equation (2-5)], and

$$g'(z^*) = \frac{m}{2(1-\cos m) - m\sinh m} \times [\sinh m(1-z^*) + \sinh mz^* + \sinh m] \qquad \text{(2-27)}$$

for $Re > 0$ [equation (2-5)].

Weinbaum et al (1985) studied the drainage between two axi-symmetric discs under a constant normal force applied to a mass that is in contact with the upper disc. They formulated the problem by coupling the inertia of the driving mass with that of the fluid. The solutions obtained showed that two dimensionless groups characterise the system; the Reynolds number based on the initial disc separation (as for Hamza and MacDonald) and a characteristic inertial settling velocity, and the ratio of the squares of the gravitational and the fluid inertia settling times, given by

$$\beta \equiv \frac{t_g^2}{t_i^2} = \frac{4h_0 m}{\pi \rho R^4}. \tag{2-28}$$

The authors then proceeded to solve the resultant equations for various $\beta$ and $Re$ combinations at different asymptotic limits, under the parallel flow assumption. The authors showed that their analytically determinable solutions agreed accurately with complete numerical solutions at the asymptotic limits and relatively well throughout the various hypothetical numerical experiments.

They obtained closed form solutions in the infinite $Re$ limit for $\beta \to \infty$ and $\beta \to 0$ respectively, representing motion through a vacuum and a system in which hydrodynamically generated pressures instantaneously support the mass. For example, Kuzma's experiment in which mercury is squeezed between two discs corresponds to $\beta \ll 0$, whereas for a sheet of paper dropped onto a desk from 1 cm, $\beta \sim 1$ and for a book dropped from the same height, $\beta \sim 10^2$. The authors also obtained solutions corresponding to:- (i) early times ($h \sim h_0$) for all values of $\beta$, (ii) small $\beta$ values for the limiting cases $Re \gg 1, h \sim h_0$ and (iii) $Re \ll 1$.

Lawrence continued his work with Weinbaum and Kuang (1985) and developed an approximate high $Re$ solution to the above problem using an integral approach and assuming negligible inertia of the driving mass. The results showed an interesting combination of a time dependent invicid core adjacent to an unsteady boundary layer. This solution compared favourably with numerical predictions.

The work of Weinbaum et al is interesting in that its holistic formulation (coupling of inertia forces) allows it to be applied to a myriad of constant force squeeze flow problems, as described above. However, it is because of this inertia coupling in the $\beta$ parameter that this work cannot readily be applied to highly transient squeeze flows in which a large impulsive force is applied to the driving mass.

Rukmani and Usha (1994) conducted an investigation into axi-symmetric squeeze flows in which the solution is obtained in a power series of a single non-dimensional parameter called the squeeze number $S$ where

$$S = \frac{h^2}{8\nu T}, \tag{2-29}$$

in which $T$ is the experimental stroke period. The squeeze motions considered are constant disc velocities, constant squeeze force motions and constant squeeze power motions, all for small squeeze numbers $S \ll 1$.

In general, Phan-Thien's work [(1983), (1985), (1987)] was primarily concerned with non-Newtonian squeeze flows. Hence, due to the mathematical complexities arising from the modeling of non-Newtonian fluids, Phan-Thien often omitted or drastically simplified inertial effects. However, Phan-Thien (1986) has shown that a 'transmission loss' occurs for an asymmetrical squeezing motion (Section 2.1.2, p. 3) with the force and pressure difference between the top (dynamic) and the bottom (stationary) disc respectfully given by

$$\Delta F = -\frac{1}{2}\rho\pi R^2 h\ddot{h} \quad \text{and} \quad \Delta p_{cent} = -\rho h\ddot{h}. \tag{2-30a, b}$$

# 3 MOTIVATION

The reviewed literature indicates that constant velocity squeeze flows have been analysed in detail by various authors, most notably by Hamza and MacDonald (1981). However, no physical experimentation regarding the constant velocity squeeze motion has been found, due to complexity of experimentally replicating such a highly idealised squeezing motion. On the other hand, constant force squeeze flows have been both experimentally and analytically investigated by various authors, most successfully by Kuzma (1967). Kuzma's first term successive approximation method yields a theoretical disc separation trace which agrees closely with experimentally obtained disc separation traces.

Other authors have endeavoured to derive squeeze flow models that can be applied to squeeze flows with arbitrary disc motions. The most noteworthy work of which is presented by Ishizawa (1966), however, Ishizawa's work is only applicable for Reynolds numbers of order unity or less. Likewise Tichy's (1981) similarity solution is only valid for small disc accelerations; it is later shown in Figure 6-2, p. 49, that Tichy's restriction $\left|\ddot{h}h/\dot{h}^2\right| \ll 3/2$ (similar to so-called *inertial composition* [defined in Section 5.2, p. 21]), is not appropriate for highly transient squeeze flows. Moreover, Rukmani and Usha's (1998) model is only valid for small squeeze numbers $S \ll 1$ [equation (2-29), p. 17] and applicable to only specific squeezing motions.

With the exception of Kuzma's model, due to the above limitations, none of the reviewed models have applicability extending to highly transient squeeze flows, i.e. flows with large Reynolds numbers and/or large disc accelerations (p. 2).

It follows that the broad motivation of this thesis is to analytically establish the mechanics of highly transient axi-symmetric squeeze flows for Newtonian fluids, and proceed to experimentally examine these squeeze flows induced by a drop-hammer system (Figure 1-2, p. 2). Drop-hammer tests require a given amount of energy to be dissipated over a small distance through the generation of fluid forces (i.e. the pressures); hence *constant energy* squeeze flows are introduced as a new squeeze flow system, as distinct from the traditionally investigated constant force or constant velocity squeezing systems.

# 4 OBJECTIVES

The broad aim of this work was to use experimental, analytical and computational (CFD) methodologies to investigate the pressure variations with time in fluid between two parallel discs that have been subjected to a constant energy squeezing system, as distinct from the traditionally investigated constant force or constant velocity squeezing systems. Primary questions to be answered were as follows:

1. the relative magnitudes of viscous versus inertia effects, and temporal inertia versus spatial inertia effects – and the manner in which these affect pressures - throughout the event;
2. the validity of using simple analyses in the limits where viscous and inertia effects are likely to be dominant – for example, towards the end and beginning of each event respectively;
3. the possibility of developing an analytical model that is capable of incorporating both viscous and inertial affects throughout the event;
4. the legitimacy of the parallel flow assumption and
5. the extent to which measured pressure distributions are radially parabolic.

The means by which the above issues were considered are contained in the following specific objectives addressed during the investigation:

1. Develop a test cell that induces highly transient axi-symmetric squeeze flows when used in conjunction with a drop-hammer test facility, and incorporates the capability of monitoring (i) pressure variations with time and radial position, (ii) the effects of non-axi-symmetric testing conditions, and (iii) disc separations with time.
2. Conduct a systematically planned series of tests during which pressures and disc separation are measured with time, under appropriate variations of the independent parameters initial disc separation, drop mass, and drop height.
3. Develop a solution for inviscid squeeze flows, i.e. a solution that only considers fluid inertia. In addition, using equation (2-14), p. 10, which encompasses the reduced Navier Stokes equations and parallel flow assumption derive a more comprehensive model that embraces both viscous and inertial effects. Reconcile these models with the measurements, thereby establishing their limitations.
4. Employ hypothetical variations of disc separation, velocity and acceleration (using similar magnitudes and time scales to those that are measured) in a CFD model and in so doing evaluate the validity of:- (i) the analytical models developed in 3. and (ii) the parallel flow assumption.

# 5 THEORETICAL ANALYSIS

The reviewed models (Section 2.4, p. 8) fail to deliver accurate results for squeeze flow systems with large Reynolds numbers and/or large disc accelerations, with the exception of Kuzma's model (as later discussed in Section 6.4.1, p. 61). Hence highly transient axi-symmetric squeeze flows (squeeze flows with large Reynolds numbers and large disc accelerations) are analyzed within this chapter.

## 5.1 Inviscid/Inertial Model

If a fluid is assumed inviscid, only inertia contributes to the pressure development between the discs, i.e. terms *A*, *C*, $D_1$ and $D_2$ of equation (2-1) are considered. By definition the no-slip boundary condition is violated and so the radial fluid velocity simply becomes the average flow rate [equation (2-4), p.7]. Hence the radial and axial velocities are given by

$$v_{r\rho} = \bar{v_r} = -\frac{r}{2}\frac{\dot{h}}{h} \qquad \text{and} \qquad v_{z\rho} = -\frac{\dot{h}}{h}z \qquad (5\text{-}1a, b)$$

where the $\rho$ subscript indicate that the solution considers only fluid density, i.e. inertial effects. It is easy to substitute equations (5-1a, b) into equation (2-1) to obtain an expression for pressure of

$$p_\rho = -\frac{\rho}{8}\left[2\frac{\ddot{h}}{h} - 3\left(\frac{\dot{h}}{h}\right)^2\right](R^2 - r^2) \equiv -\frac{\rho R^2}{8}\left[2\frac{\ddot{h}}{h} - 3\left(\frac{\dot{h}}{h}\right)^2\right]\left(1 - r^{*2}\right), \qquad (5\text{-}2)$$

which when integrated across the disc area gives a squeeze force of

$$F_\rho = -\frac{\rho R^4}{16}\left[2\frac{\ddot{h}}{h} - 3\left(\frac{\dot{h}}{h}\right)^2\right]. \qquad (5\text{-}3)$$

## 5.2 Inertial Composition

Through the derivation of equation (5-2) it can be shown that both the temporal and spatial inertia contribute to the term containing $\dot{h}$, whereas only the temporal inertia contributes the term containing $\ddot{h}$. Since the Reynolds number for squeeze flows [equation (2-5)] only considers disc velocity (and not acceleration), it is useful to establish the ratio of temporal to spatial inertia. For the inviscid/inertial model, the corresponding constituents of equation (5-2) are used to yield a ratio of

$$\frac{\text{Temporal inertia}}{\text{Spatial inertia}} \equiv O\left(\frac{\ddot{h}h}{\dot{h}^2} - 1\right), \tag{5-4}$$

and so it is appropriate to define this dimensionless grouping as a parameter

$$\Re \equiv \left|\frac{\ddot{h}h}{\dot{h}^2} - 1\right|, \tag{5-5}$$

where $\Re$ is introduced as the *inertial composition*.

If the experimental data of Kuzma (1967) is examined in this light, their $\Re \sim O(1)$. It is therefore of interest to examine a dynamic situation in which $\Re \gg 1$.

## 5.3 Parallel Flow Assumption

It is uncertain to whether or not effects initially assumed negligible would sufficiently violate the parallel flow assumption in the context of *highly transient* squeeze flows as to render it an inappropriate assumption for use in further analysis. Hence, a CFD evaluation of the system was setup as described in Section 6, p. 47 in order to test this assumption for highly transient squeeze flows. The CFD results (all the figures in Section 6.3.1, p. 50) strongly support a parallel flow assumption for an incompressible fluid, therefore it is assumed that the parallel flow assumption is a good approximation and is utilised in further analysis.

For the sake of convenient referencing, the parallel flow assumption, equations (2-12a, b), p. 9, are recalled as

$$v_r = -\frac{r}{2}\frac{\dot{h}}{h}g' = \overline{v_r}f(z^*,t) \quad \text{and} \quad v_z = \dot{h}g(z^*,t), \qquad \text{(2-12a, b)}$$

where $g$ is the dimensionless axial velocity variable and $f$ is conveniently introduced as the dimensionless radial velocity with $g' = f$. The radial fluid velocity for a symmetrical squeeze is visually represented in
Figure 5-1.

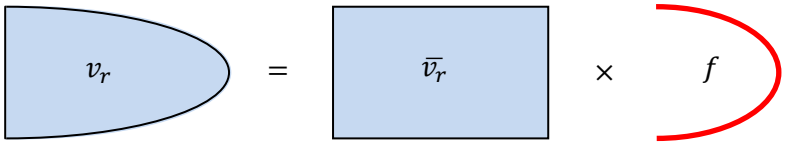


Figure 5-1: Visual interpretation of dimensionless radial velocity for symmetrical squeeze flows

The dimensionless axial and radial fluid velocity profiles for a symmetrical squeezing motion have the following boundary conditions:

i. Symmetry of the dimensionless radial velocity dictates that

$$f'\left(\frac{1}{2}\right) = g''\left(\frac{1}{2}\right) = 0. \qquad \text{(5-6)}$$

ii. Flow conservation is embodied in

$$\int_0^{\frac{1}{2}} f\,dz^* = \int_{\frac{1}{2}}^{1} f\,dz^* = -g(0) = g(1) = \frac{1}{2}. \qquad \text{(5-7)}$$

iii. The no-slip condition on the discs is given by

$$f(0) = g'(0) = 0. \qquad \text{(5-8)}$$

## 5.4 Exact Kinematic Model

After substituting equations (2-12a, b) into equation (2-1), it can be shown that the radial pressure gradient is given by[a]

$$\frac{dp}{dr} = -r\frac{\rho}{2}\left\{\nu\frac{\dot{h}}{h^3}g''' - \left(\frac{\dot{h}}{h}\right)^2(g-z^*)g'' - \left(\frac{\dot{h}}{h}\right)\dot{g}' + \frac{1}{2}\left(\frac{\dot{h}}{h}\right)^2 g'^2 - \left[\frac{\ddot{h}}{h} - \left(\frac{\dot{h}}{h}\right)^2\right]g'\right\} \qquad (5\text{-}9)$$

whence it can be seen that $dp/dr \propto r$ and therefore, once the assumed boundary condition of zero circumferential pressure offset $p(R) = 0$ is used to solve for the constant of integration, the radial pressure profile is shown to be parabolic given by $p = p_{cent}(1 - r^{*2})$, where $p_{cent}$ is the central pressure. Hence this confirms the CFD observation of an invariantly parabolic pressure distribution for an incompressible axi-symmetric squeeze flow under the parallel flow assumption (Figure 6-5, p. 52).

In order to eliminate the radial pressure distribution term from the dimensionless velocity terms in equation (5-9), with the intension of ultimately solving for the dimensionless velocities, equation (5-9) is differentiated with respect to $z^*$ [since $dp/dz \approx 0$ in equation (2-2)] to give[b]

$$\underset{(B_1')}{\nu\left(\frac{\dot{h}}{h^4}\right)g'^{v}} - \underset{(D_2')}{\left(\frac{\dot{h}^2}{h^3}\right)(g-z^*)g'''} - \underset{(C_2')}{\left(\frac{\dot{h}}{h^2}\right)\dot{g}''} - \underset{(C_1')\ (C'D')}{\left[\frac{\ddot{h}}{h^2} - 2\left(\frac{\dot{h}^2}{h^3}\right)\right]g''} = 0. \qquad (5\text{-}10)$$

Equation (5-10) is equivalent to equation (2-14), p. 10, as derived by Phan-Thien. In this context of this thesis, equation (5-10) is referred to as the *Exact Kinematic* model, as it is assumed to solve for the exact fluid kinematics for an axi-symmetric squeeze flow under the parallel flow assumption. In equation (5-10) each remaining term is labelled with dashed letters. These letters correspond to the previously defined labelled terms of equation (2-1), while the dash indicates the derivative with respect to $z^*$. To reiterate, terms *B'*, *C'* and *D'* are physically interpreted as viscous, temporal inertial and spatial inertial forces respectively. More specifically, the interpretations of the inertia force terms are classified as follows:

i. $C_1'$- represents the temporal inertia developed by the disc acceleration.

[a] The full derivations are given in Appendix A.

[b] The full derivations are given in Appendix A.

ii. $C_2$'- represents the newly introduced so-called *shape evolution* term (as it contains the only partial time derivative).

iii. *C'D'*- is a combined term arising from temporal and spatial inertia of equal proportions.

iv. $D_2$'- represents the spatial inertia derived from a fraction of the $D_2$ term. Term $D_1$' has been cancelled by a component of the $D_2$' term.

The exact kinematic model [equation (5-10)] is a fourth order partial differential equation which is difficult to solve analytically and is hence best solved by numerical means. However, in order to establish an approximate analytical solution, equation (5-10) is reduced yielding the limiting models as discussed in the subsequent chapters.

## 5.5 Quasi-Steady (QS) Model

Recalling equation (5-10), term $C_2$' contains the only partial time derivative, hence its elimination reduces equation (5-10) to an ordinary semi-linear[a] differential equation

$$\gamma g'^{v} - \beta[g - z^*]g''' - [\alpha - 2\beta]g'' = 0, \tag{5-11}$$

where the prime now denotes an ordinary derivative and the coefficient variables are introduced as

$$\alpha = \frac{\ddot{h}}{h^2} \qquad \beta = \frac{\dot{h}^2}{h^3} \qquad \gamma = \nu\frac{\dot{h}}{h^4}. \tag{5-12a, b, c}$$

These variables are subsequently used to determine the so-called *shape parameter* (Section 5.6, p. 26) and hence are introduced as the *shape parameter variables*. Equation (5-11) is a *quasi-steady approximation* of equation (5-10) in that *all partial time derivatives* have been *omitted*; hence, equation (5-10) is introduced as the so-called *Quasi-Steady* (QS) model.

Although quasi-steady approximation is common practice in analysis, the error magnitude associated with the quasi-steady approximation is currently undetermined. It is however known that quasi-steady

[a] Differential equation (5-11) is semi-linear because in isolation the left and right terms compose a linear differential equation, however, when introduced into this linear system, the middle term represents a non-linear term.

approximations will be experiment-specific and also time specific within each experiment. Therefore, in order to quantify whether the quasi-steady approximation is sufficiently accurate during an experiment, and more specifically at any time instant within the experiment, the Quasi-Steady Applicability Analysis (Section 5.9, pp 36) is subsequently employed.

If a fluid is considered massless, or purely viscous, by equation (2-6) $\nu \to \infty$; therefore from equation (5-12c) it can be seen that equation (5-11) reduces to $\gamma g'^{v} = 0$ or $f''' = 0$ which in combination with the boundary conditions (Section 5.3) leads to

$$f = -6\left(z^{*2} - z^{*}\right), \tag{5-13}$$

which is a parabolic dimensionless radial velocity distribution as previously determined by the lubrication approximation [equation (2-7a)]. It logically follows that when this $f$ value [equation (5-13)] is inserted into equation (5-9), the resultant pressure is the same as that given by the lubrication approximation [equation (2-8)].

For the case of a transient squeeze flow (where $\alpha$, $\beta$ and $\gamma$ are dynamic variables), the semi-linear differential eqation (5-11) may be solved numerically (by say MATLAB's Simulink toolbox) by introducing two trial variables, namely $m$ and $n$, as the initial conditions for the second and third derivatives respectively, i.e.

$$g''(0) = m \qquad \text{and} \qquad g'''(0) = n.$$

Then through a double iterative process, varying both $m$ and $n$, equation (5-11) may be solved ensuring that the boundary conditions are met (Section 5.3, p. 21). This iterative process involves manual feedback and therefore is arduous when applied to a large number of discrete data points. The initial condition of $g(0) = -1/2$ is used for a symmetrical squeeze motion and $g(0) = 0$ for an asymmetrical squeeze motion at the stationary disc (Section 2.1.2, p.3).

The block diagrams for the QS model is shown in Appendix B and the 'QS model' MATLAB Simulink program are given in CD-Appendix A. In both instances, the QS model is accompanied by the QSL model which is discussed in Section 5.6.

## 5.6 Quasi-Steady Linear (QSL) Model

In order to determine the starting values for $g''(0) = m$ and $g'''(0) = n$ for equation (5-11) [Section 5.6, p. 25], equation (5-11) is approximated as a linear differential equation by neglecting the non-linear term $[\beta g - z^*]g'''$.This is equivalent to further reducing equation (5-10) by eliminating term $D_2$', so that both terms $C_2$' and $D_2$' have been eliminated from equation (5-10) reducing it to

$$\gamma g'^v - [\alpha - 2\beta]g'' = 0. \tag{5-14}$$

This may alternatively be given as

$$(D^2 - \lambda)k = 0 \tag{5-15}$$

where $D = d/dz^*$, $\lambda$ is the *dimensionless shape parameter* defined as

$$\lambda \equiv \frac{\alpha - 2\beta}{\gamma} \equiv \frac{1}{\nu}\left(\frac{\ddot{h}h^2 - 2\dot{h}^2 h}{\dot{h}}\right) \tag{5-16}$$

and

$$k(z^*) = \frac{df}{dz^*} = \frac{d^2 g}{dz^{*2}} \tag{5-17}$$

Equation (5-14)/(5-15) is an analytically determinable ordinary linear differential equation which has three potential solution categories given as follows:

- $\lambda > 0$ results in an exponential solution.
- $\lambda < 0$ results in an oscillatory solution.
- $\lambda = 0$ results in a border-case solution.

It is noted that if term $D_2$' is determined to be small in magnitude as compared to term $C_1$' in equation (5-11), then it may be unnecessary to solve for $g$ numerically via the semi-linear differential equation (5-11) altogether because the approximated ordinary differential equation (5-14), may yield sufficiently

accurate results. Hence the approximated dimensionless axial velocity profiles may be obtained analytically without the utilization of iterative methods; equation (5-14) thus represents the appropriately named *Quasi Steady Linear* (QSL) model[a].

### 5.6.1 Dimensionless fluid velocity determination

The general solution[b] of the dimensionless axial velocity $g(z^*)$, the dimensionless radial velocity $f(z^*)$ and its first and second dimensionless axial derivatives for exponential solutions ($\lambda > 0$) are respectively given by

$$g(\lambda, z^*) = \frac{\left(\cosh\sqrt{\lambda}z^* - 1\right) - \left(\sinh\sqrt{\lambda}z^* - \sqrt{\lambda}z^*\right)\coth\frac{\sqrt{\lambda}}{2}}{\sqrt{\lambda}\coth\frac{\sqrt{\lambda}}{2} - 2} \tag{5-18}$$

$$f(\lambda, z^*) = \frac{\sinh\sqrt{\lambda}z^* - \left(\cosh\sqrt{\lambda}z^* - 1\right)\coth\frac{\sqrt{\lambda}}{2}}{\coth\frac{\sqrt{\lambda}}{2} - \frac{2}{\sqrt{\lambda}}} \tag{5-19}$$

$$f'(\lambda, z^*) = \frac{\sqrt{\lambda}\left(\cosh\sqrt{\lambda}z^* - \sinh\sqrt{\lambda}z^*\coth\frac{\sqrt{\lambda}}{2}\right)}{\coth\frac{\sqrt{\lambda}}{2} - \frac{2}{\sqrt{\lambda}}} \tag{5-20}$$

$$f''(\lambda, z^*) = \frac{\lambda\left(\sinh\sqrt{\lambda}z^* - \cosh\sqrt{\lambda}z^*\coth\frac{\sqrt{\lambda}}{2}\right)}{\coth\frac{\sqrt{\lambda}}{2} - \frac{2}{\sqrt{\lambda}}}. \tag{5-21}$$

For the case of oscillatory solutions, a complex value of $\lambda$ is substituted into the above exponential solutions, in which

[a] It is later be shown in Section 5.7, pp 13, that a correction can be made to the QSL model in order to include an approximate *linear* value of the non-linear term, i.e. the Quasi Steady Corrected Linear (QSCL) model.

[b] The derivations are given in Appendix A.

$$-\lambda = \left(i\sqrt{|\lambda|}\right)^2 \tag{5-22}$$

where $i = \sqrt{-1}$ .

Hence for oscillatory solutions ($\lambda < 0$), dimensionless axial velocity $g(z^*)$, the dimensionless radial velocity $f(z^*)$ and its first and second dimensionless axial derivatives are respectively given by

$$g(\lambda, z^*) = \frac{\left(\cos\sqrt{|\lambda|}z^* - 1\right) - \left(\sin\sqrt{|\lambda|}z^* - \sqrt{|\lambda|}z^*\right)\cot\frac{\sqrt{|\lambda|}}{2}}{\sqrt{|\lambda|}\cot\frac{\sqrt{|\lambda|}}{2} - 2} \tag{5-23}$$

$$f(\lambda, z^*) = -\frac{\sin\sqrt{|\lambda|}z^* + \left(\cos\sqrt{|\lambda|}z^* - 1\right)\cot\frac{\sqrt{|\lambda|}}{2}}{\cot\frac{\sqrt{|\lambda|}}{2} - \frac{2}{\sqrt{|\lambda|}}} \tag{5-24}$$

$$f'(\lambda, z^*) = -\frac{\sqrt{|\lambda|}\left(\cos\sqrt{|\lambda|}z^* - \sin\sqrt{|\lambda|}z^*\cot\frac{\sqrt{|\lambda|}}{2}\right)}{\cot\frac{\sqrt{|\lambda|}}{2} - \frac{2}{\sqrt{|\lambda|}}} \tag{5-25}$$

$$f''(\lambda, z^*) = \frac{|\lambda|\left(\sin\sqrt{|\lambda|}z^* + \cos\sqrt{|\lambda|}z^*\cot\frac{\sqrt{|\lambda|}}{2}\right)}{\cot\frac{\sqrt{|\lambda|}}{2} - \frac{2}{\sqrt{|\lambda|}}}. \tag{5-26}$$

It can be shown by L'Hospital's rule that, as expected, the solutions of both equations (5-19) and (5-24) reduce to a parabolic velocity distribution as $\lambda \to 0$ (derivatives taken with respect to $\lambda$). This limiting solution is given by the lubrication approximation in equation (5-13).

It is later shown in Figure 5-3 that $\lambda$ has the lower limit of $\lambda \geq -4\pi^2$, which restricts the flow adjacent to the discs from reversing direction.

Dimensionless axial velocities are calculated with equations (5-19) and (5-24) at discrete values of $\lambda$ and are plotted against dimensionless disc separation in Figure 5-2.

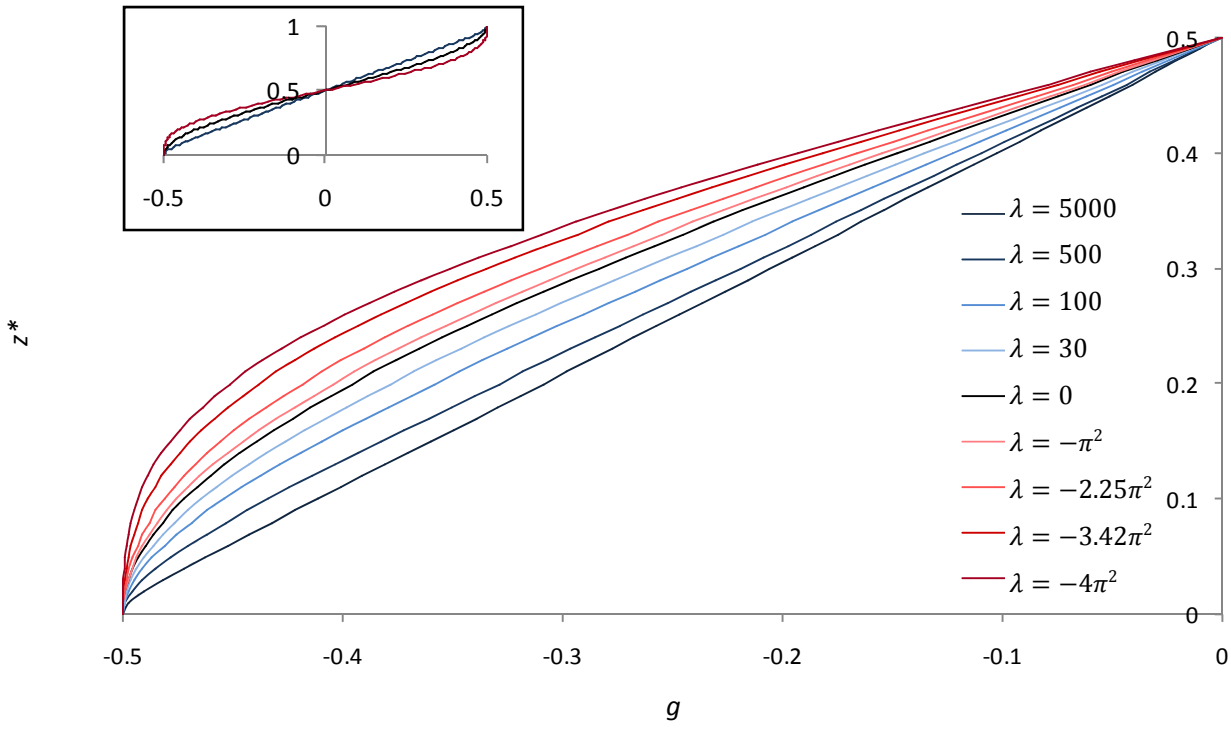


Figure 5-2: Dimensionless axial velocity profiles at discrete shape parameter values

It can be seen from Figure 5-2 that for large possitive $\lambda$ values, $g$ changes almost proportionally with $z^*$. However, for large negative values of $\lambda$ there is only a negligible axial fluid velocity change in the fluid layer adjacent to the disc surface.

Similarly using equations (5-19) and (5-24), dimensionless radial fluid velocities at discrete values of $\lambda$ are plotted against dimensionless disc separation in Figure 5-3.

Finally using equations (5-21) and (5-26), second axial derivative curves of the dimensionless radial fluid velocities at discrete values of $\lambda$ are plotted against dimensionless disc separation in Figure 5-4.

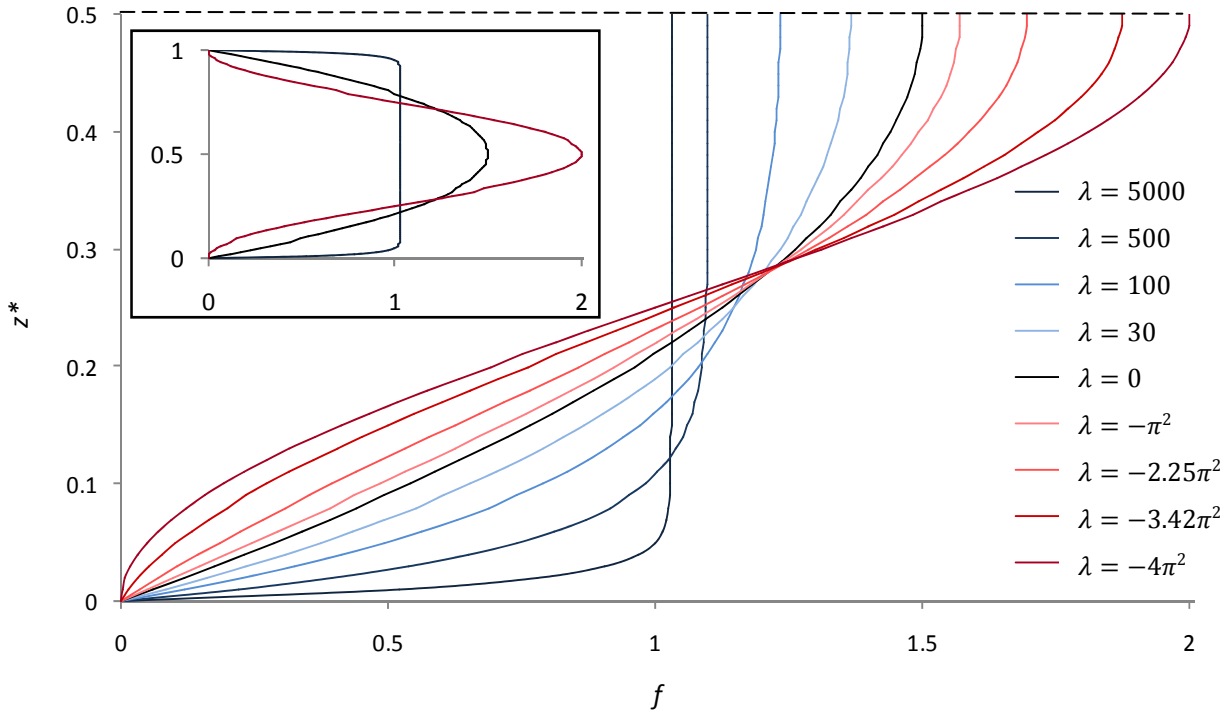


Figure 5-3: Dimensionless radial velocity profiles at discrete shape parameter values

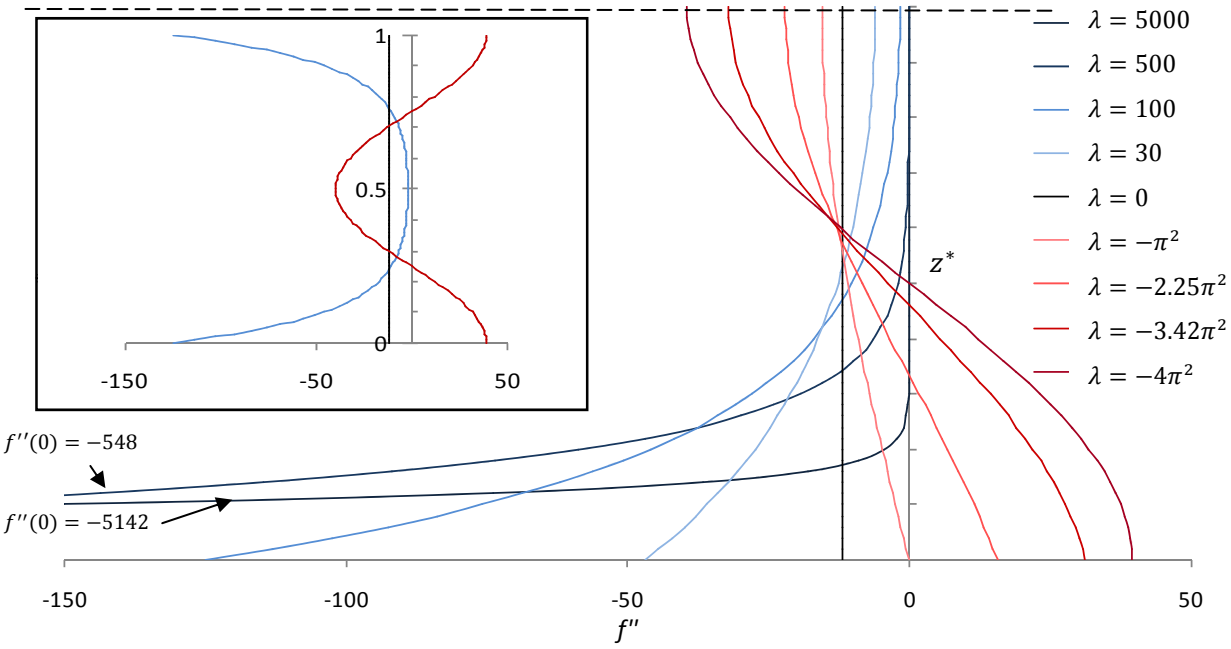


Figure 5-4: Second derivative profiles of dimensionless radial velocity at discrete shape parameter values

The dimensionless radial fluid velocity shapes in Figure 5-3 are intuitively satisfactory in which the following features are observed:

- High values of $\lambda$ ($\lambda \geq 500$) yield radial fluid velocity shapes that correspond to impulsive flow patterns with a well defined boundary layer, such as the Rayleigh problem (Schlichting, 1960).
- $\lambda = 0$ yields the abovementioned parabolic radial fluid velocity as determined by the lubrication approximation ($Re = 0$), equation (5-13).
- Low values of $\lambda$ ($\lambda < -\pi^2$) yield inflexional radial fluid velocity shapes (Schlichting, 1960), hence negative pressures are generated. The shape parameter is limited to $\lambda \geq -4\pi^2$ so the flow adjacent to the disc interfaces which presumably would initiate the onset of turbulence (Schlichting, 1960).

Hence from one relatively simplistic equation set [equations (5-19) and (5-24)], the QSL model produces radial fluid velocity shapes that form an elegant set of solutions for a myriad of flow patterns.

Before Figure 5-4 is discussed, it is noted that at the disc interface, there is no radial fluid motion and therefore no radial inertial force. Hence the pressure development at the disc interface is purely due to viscous forces; therefore by equation (5-9), $dp/dr|_{z^*=0} \propto f''|_{z^*=0}$. In addition, since the axial pressure gradient is assumed negligible [equation (2-2)] it follows that $dp/dr \propto f''|_{z^*=0}$. Therefore, the shapes of $f''$ versus $z^*$ represent the ratio of viscous to inertial fluid forces across the disc separation. This becomes pertinent later in determining the so-called *dynamic Reynolds number* (Section 5.10, p. 38).

Figure 5-4 shows that dimensionless radial fluid velocity shapes with high values of $\lambda$ ($\lambda \geq 500$) are associated with high viscous forces (high shear stresses) at the disc interfaces and no viscous forces midway between the discs (only inertial forces act on the fluid in this region). As expected, there is a uniform viscous force $\propto f'' = -12$ independent of $z^*$ for a parabolic fluid velocity profile $f(\lambda = 0)$, i.e. the lubrication approximation. Hence it can be seen that a purely viscous flow does not have the lowest average viscous force across the disc separation, because for $\lambda < -\pi^2$ negative viscous forces are developed at disc interfaces, even though the radial fluid velocity shapes for $\lambda \to -\pi^2$ are visually similar to a parabolic velocity distribution (Figure 5-3).

The ‘Dimensionless Velocities’ Excel spreadsheet used to develop Figures 5-2, 5-3 and 5-4 is given in CD-Appendix B.

## 5.7 Quasi-Steady Corrected Linear (QSCL) Model

From equation (5-11) it is noted that the $\beta$ coefficient is common to both $g''$ and $[g - z^*]g'''$ terms. Therefore, a correction can be made to the existing QSL model in which an approximate linear value for the neglected non-linear $D_2$' term [equation (5-10)] can be included into equation (5-14). This correction follows a similar method to a first term approximation of a successive approximation technique, and is made using the following steps:

i. The QSL model's dimensionless fluid velocities [equations (5-18) to (5-26)] are used to determine $[g - z^*]g'''$ ('Dimensionless velocities' Excel spreadsheet, CD-Appendix B).

ii. Since the coefficients of these terms are the same, the average magnitude (integral with respect to $z^*$) of $[g - z^*]g'''$ is equated with the average magnitude $g''$ across the disc separation by $\kappa$, i.e.

$$\int_0^{1/2} [g - z^*]g'''dz^* = \kappa \int_0^{1/2} g''dz^* \qquad \text{or} \qquad \kappa(\lambda) = \frac{\int_0^{1/2} [g - z^*]g'''dz^*}{g'|_{z^*=1/2}} \qquad (5\text{-}27)$$

where $\kappa$ is introduced as the *linearization term*. The linearization term is determined at various values of $\lambda$ as shown in Figure 5-5 where a fourth order polynomial fit gives an approximate value $\kappa$ for $\lambda \leq 100$ and $\kappa \approx 0.4$ for $\lambda > 100$ (Figure 5-5 insert).

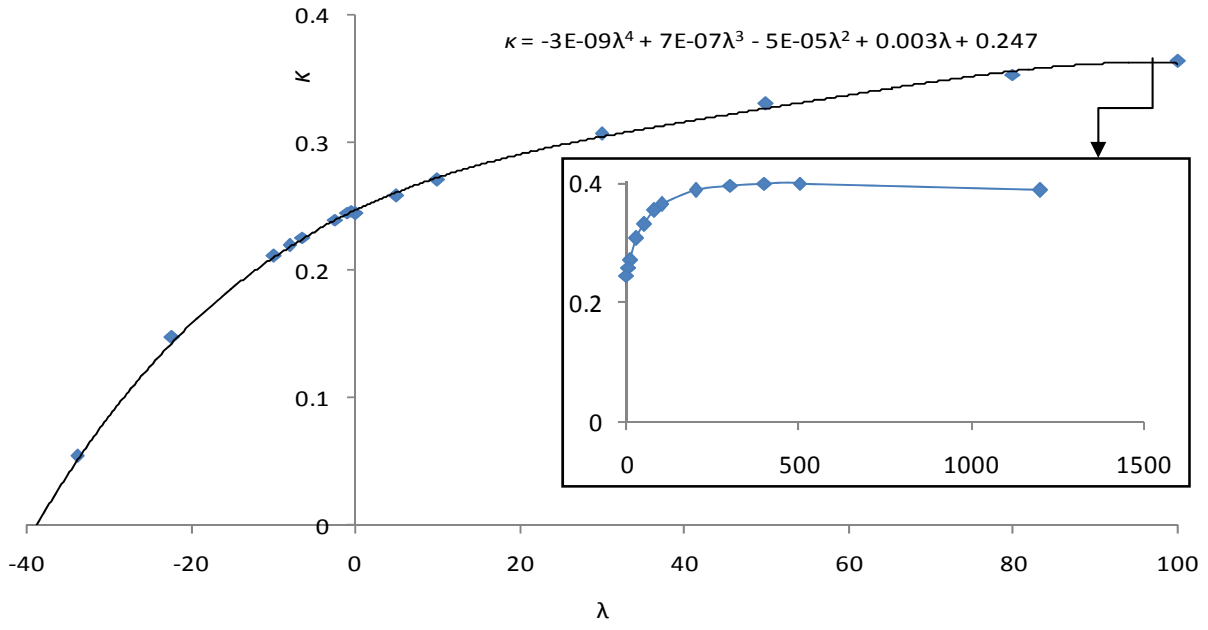


Figure 5-5: Linearization term change with shape parameter variation

Hence $\kappa g''$ may be used as an approximate substitution for the non-linear term $[g - z^*]g'''$ in equation (5-11) to account for the spatial inertia term previously neglected by the QSL model, i.e.

$$[\alpha - 2\beta]g'' + \beta[g - z^*]g''' - \gamma g'^{v} \cong [\alpha + (\kappa - 2)\beta]g'' - \gamma g'^{v},$$

so that

$$[\alpha + (\kappa - 2)\beta]g'' - \gamma g'^{v} = 0 \tag{5-28}$$

which is identical to the equation (5-14) of the QSL model apart from the coefficients of $\beta$. Hence the solution of the QSCL model [equation (5-28)] is determined in an identical fashion to that by which the QSL model [equation (5-14)] is determined, with the exception that a *corrected shape parameter* $\lambda_{cor}$ replaces $\lambda$, in which $\lambda_{cor}$ calculated as

$$\lambda_{cor} \equiv \frac{\alpha + (\kappa - 2)\beta}{\gamma} \equiv \frac{1}{\nu}\left[\frac{\ddot{h}h^2 + (\kappa - 2)\dot{h}^2 h}{\dot{h}}\right]. \tag{5-29}$$

It is noted that $\lambda$ must first be established so that $\kappa(\lambda)$ can be obtained (Figure 5-5) in order to establish a value of $\lambda_{cor}$. Thereafter $\lambda_{cor}$ may be substituted into equations (5-18) or (5-24) to obtain more accurate instantaneous dimensionless radial velocities. Hence the so-called *Quasi-Steady Corrected Linear* (QSCL) model is calculated identically to the QSL model after $\lambda_{cor}$ is determined by equation (5-29).

It can be seen in the Excel 'Dimensionless velocities' spreadsheet (CD-Appendix B), that the *shapes* ($z^*$ variations) of $g''$ are *not very similar* to $[g - z^*]g'''$. Nevertheless, it is later shown that when the resultant pressure traces of the QSCL model are compared with those of the QSL model in Figure 6-12, p. 59, the increase in accuracy of the QSCL model is substantial as the QSCL model's trace intersects every marker of the QS model, i.e. less than a maximum of 2% error throughout the pressure trace. Furthermore, it is noted that this percentage-wise accuracy is not experiment specific as the $\beta$ coefficients of equation (5-11) are grouped in equation (5-28). Hence the QSCL model is considered to *accurately approximate* the *inclusion* of the *non-linear term* and hence warrants no error analysis.

From Figure 5-5 it can be seen that the value of $\kappa$ never exceeds 0.4 for any value of $\lambda$. It follows that since the coefficient of $\beta$ in the QSL model is 2 [equation (5-16)], in excess of 80% of the magnitude of the spatial inertia is always included within the QSL model (by the above analysis).

## 5.8 Pressure Determination

From Figure 5-4 and associated text, the radial pressure gradient can be determined at the disc interface by recalling equation (5-9) with neglected inertial forces

$$\frac{dp}{dr} = \frac{dp}{dr}\Big|_{z^*=0} = -\frac{r\mu}{2}\frac{\dot{h}}{h^3} f''|_{z^*=0}. \tag{5-30}$$

Depanding on the sign of $\lambda$, either equation (5-21) or (5-26) is substituted into equation (5-30) at $z^* = 0$.

When equation (5-30) is integrated with respect to $r$, the pressure in dimensionless radial form is given by

$$p = \frac{R^2\mu}{4}\frac{\dot{h}}{h^3} f''|_{z^*=0}\left(1 - r^{*2}\right) + p_{cir} \tag{5-31}$$

where $p_{cir}$ is the (analytically determined) circumferential offset pressure. Generally a zero circumferential offset pressure is assumed ($p_{cir} = 0$). It is noted that the quasi-steady model pressures are determined by three dynamic variables, namely $f''(h, \dot{h},\ddot{h})$, $h(t)$ and $\dot{h}(t)$, hence as expected $p(h, \dot{h}, \ddot{h})$.

The pressure determined in equation (5-32) may be integrated with respect to disc area to give a squeeze force of

$$F = \frac{R^4\mu\pi}{8}\frac{\dot{h}}{h^3} f''|_{z^*=0} + p_{cir}\pi R^2. \tag{5-32}$$

Solving equations (5-21) and/or (5-26) can become analytically and even numerically intensive for a large set of discrete data points. However, since only $f''|_{z^*=0}$ is required to determine the resultant pressure or radial pressure gradient; $f''|_{z^*=0}$ is plotted against $\lambda$ for small values of $\lambda$ ($4\pi^2 \leq \lambda \leq 100$) in Figure 5-6.

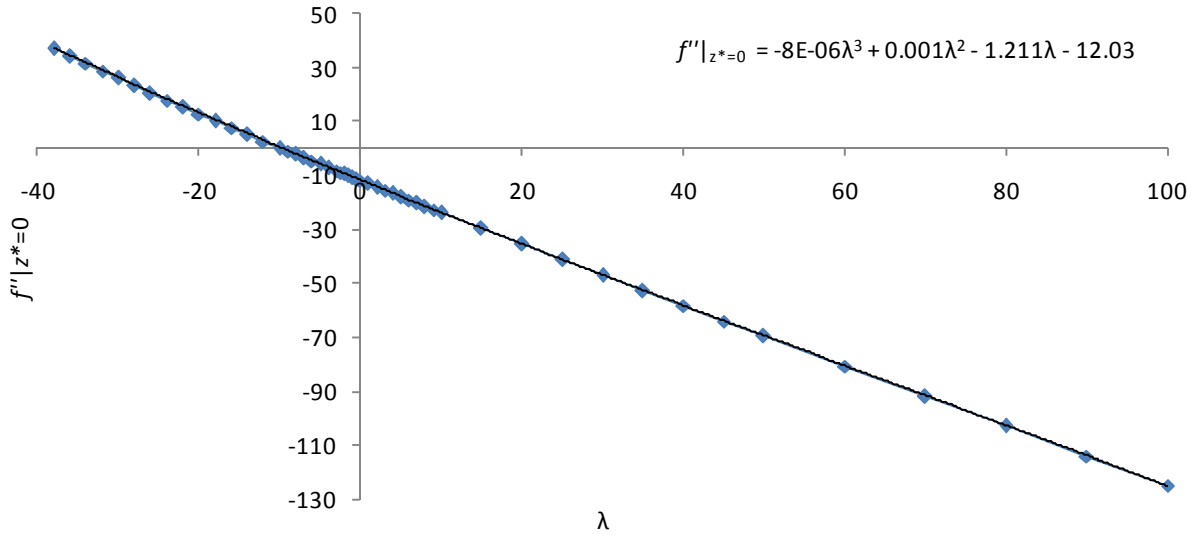


Figure 5-6: Variation of second axial derivative of radial velocity at disc interface with shape parameter $(4\pi^2 \leq \lambda \leq 100)$

The variation of $f''|_{z^*=0}$ with large values of $\lambda$ ($\lambda > 100$) are plotted in Figure 5-7.

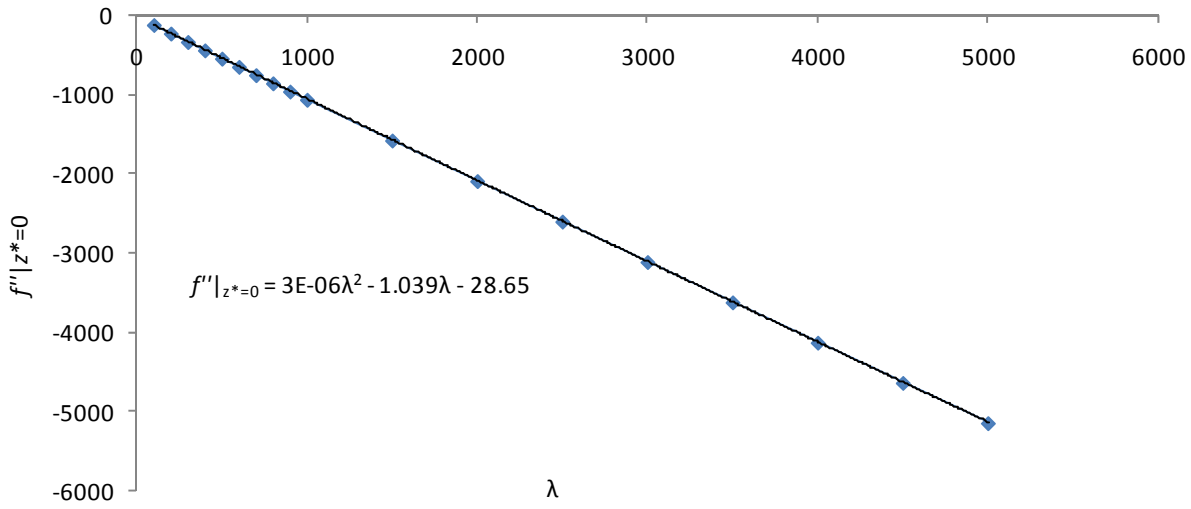


Figure 5-7: Variation of second axial derivative of radial velocity at disc interface with shape parameter $(\lambda > 100)$

A third and second order polynomial curve fit are respectively fitted to the data points of Figure 5-6 and Figure 5-7. It is found that using these polynomial as opposed to equations (5-21) and/or (5-26) is a more efficient numerical means to process a large set of discrete data points.

Holistic modeling of the system would necessitate the coupling of the resultant pressure force with the impulsive impact force. However, the impact dynamics comprises a complex combination of restitution and dissipation dynamics (Section 8.1.5 p. 107), and is thus an inappropriate analysis for this thesis.

## 5.9 Quasi-Steady Applicability Analysis

In order to quantify an approximate error associated with the quasi-steady approximation, i.e. the elimination of the evolution term *C₂'* of equation (5-10) (Sections 5.5, pp 24), the following quasi-steady applicability analysis is used. The average magnitude of term $C_2'$ across the disc separation (or integral with respect to $z^*$) is divided through by the average inertial forces developed by terms $C_1' + C'D'$ yielding

$$X \equiv \left| \frac{\int_0^{1/2} C_2' \, dz^*}{\int_0^{1/2} C_1' + C'D' \, dz^*} \right| = \left| \frac{\int_0^{1/2} \left( \frac{\dot{h}}{h^2} \right) \dot{g}'' \, dz^*}{\int_0^{1/2} \left[ \frac{\ddot{h}}{h^2} - 2\left( \frac{\dot{h}^2}{h^3} \right) \right] g'' \, dz^*} \right| = \left| \frac{1}{\left[ \frac{\ddot{h}}{\dot{h}} - \frac{2\dot{h}}{h} \right]} \frac{\dot{g}'|_{z^*=1/2}}{g'|_{z^*=1/2}} \right| \tag{5-33}$$

where *X* is the so-called *evolution ratio*. This technique makes use of the approximate values of $g$ and its derivatives that have been determined by the QSL model, i.e. equations (5-16) and (5-18) though (5-26)[a]. The value of $g'|_{z^*=1/2} = f|_{z^*=1/2}$ can be determined from Figure 5-3 in which $f|_{z^*=1/2}$ lies within the narrow range of $1 \leq f|_{z^*=1/2} \leq 2$ throughout the applicable range of $\lambda$ ($4\pi^2 \leq \lambda < \infty$); hence it is approximated that $f|_{z^*=1/2} \approx f(\lambda = 0)|_{z^*=1/2} = 3/2$. Furthermore the partial derivatives are replaced with ordinary derivatives (since the already established values of $g$ and its derivatives are used) and hence $\dot{f}\big|_{z^*=1/2} = \dot{g}'|_{z^*=1/2}$ (the order of differentiation is unimportant) and therefore equation (5-33) becomes

[a] It is noted that the values of $g, g', g'', \ldots$ should be derived from the complete numerical solution of equation (5-10). However since the complete numerical solution is unavailable, this *approximate* technique is utilised. Owing to the transient nature of the system under investigation, neither an order of magnitude technique nor a perturbation technique is found suitable as an applicability analysis for this system.

$$X \equiv \left| \frac{2}{3\left[\frac{\ddot{h}}{\dot{h}} - \frac{2\dot{h}}{h}\right]} \dot{f}\Big|_{z^*=1/2} \right|. \tag{5-34}$$

In order to determine the value of $\dot{f}\big|_{z^*=1/2}$, the following derivative product is introduced

$$\frac{df}{dt}\Big|_{z^*=1/2} = \frac{df}{d\lambda}\Big|_{z^*=1/2} \frac{d\lambda}{dt} \tag{5-35}$$

in which $d\lambda/dt$ is determinable for a discrete series of $\lambda(h, \dot{h}, \ddot{h})$ values. The term $df/d\lambda|_{z^*=1/2}$ in equation (5-35) is determined by differentiating equations (5-19) and (5-24) at $z^* = 1/2$ with respect to $\lambda$, as is numerically done in the Excel spreadsheet 'Dimensionless Velocities' (CD-Appendix B), the evaluation of which is given in Table 5-1 and shown in Figure 5-8 with varying shape parameter.

Table 5-1: Variation of the evolution ratio component with shape parameter

| $\lambda$ | -37.7 | -30.9 | -25.1 | -18.6 | -12.4 | -7.43 | -2.5 | 15 | 75 | 200 | 750 | 3000 |
|---|---|---|---|---|---|---|---|---|---|---|---|---|
| $df/d\lambda\big\|_{z^*=\frac{1}{2}}$ | 2.30 E-02 | 1.72 E-02 | 1.37 E-02 | 1.09 E-02 | 8.90 E-03 | 7.67 E-03 | 6.69 E-03 | 4.54 E-03 | 1.58 E-03 | 5.15 E-04 | 6.14 E-05 | 9.60 E-06 |

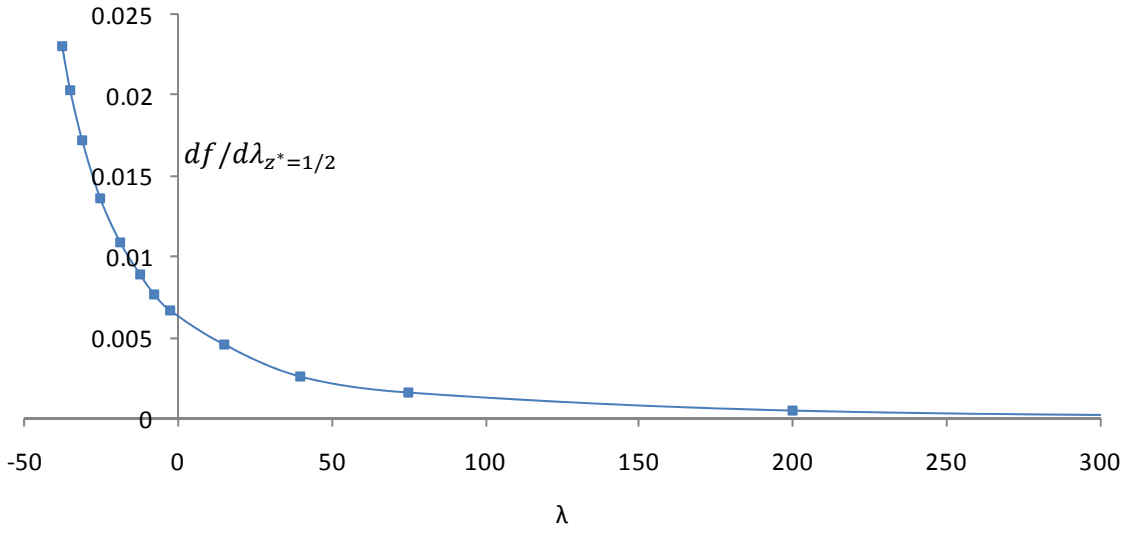


Figure 5-8: Variation of the evolution ratio component with shape parameter

From Table 5-1 the instantaneous average value of $df/d\lambda$ can be interpolated at any value of $\lambda$. Hence an evolution ratio trace for a given experiment is obtainable if a discrete series of data points of $h$, $\dot{h}$ and $\ddot{h}$ are known.

During the very early stages of a constant energy squeeze flow experiment, directly following the drop-hammer impact, the disc acceleration will be relatively large and the velocity relatively small. Consequently $\lambda$ will be large (say $\lambda > 1000$) [equation (5-16)] and therefore $df/d\lambda_{z^*=1/2}$ will be relatively small (Figure 5-8). As a consequence of the above relationships it can be seen from equation (5-34) that $X$ will be relatively small during this initial 'impact' stage and therefore a quasi-steady approximation is appropriate (according to this simplistic qualitative analysis).

It must, however, be noted that instantaneously small values of $X$ following large $X$ values potentially may not indicate an accurate quasi-steady assumption. This is because of the partial time derivative omission and therefore the history dependence. Instead, $X$ must *not exceed* a certain limiting *magnitude* for a predetermined *period* to before the quasi-steady approximation may be considered accurate. This *magnitude/lag combination* is presently undetermined.

## 5.10 Dynamic Reynolds Number Determination

Traditionally Reynolds numbers are applied to steady-state system such as pipe flows(Schlichting, 1960). However, due to squeeze flows being inherently transient and inhomogeneous flows, the application of a fixed Reynolds number to a squeeze flow system is somewhat ambiguous.

Nevertheless the Reynolds number for squeeze flows has traditionally been defined as either

$$Re \equiv -\frac{h_0\dot{h}}{\nu} \qquad \text{or} \qquad Re_{trad} \equiv -\frac{h\dot{h}}{\nu}, \qquad (5\text{-}36a, b)$$

for a constant velocity squeeze flow(Hamza, et al., 1981) or a constant force squeeze flow (Tichy, 1981) respectively. Due to the changing disc kinematics in equation (5-36b), the Reynolds number itself has become a dynamic variable through the experimental stroke. It is also noted, as pointed out by Tichy, that since the discs may be squeezing or separating, the Reynolds number may be defined as either positive or negative.

A so-called *dynamic Reynolds number*, which adheres to the traditional Reynolds number definition as the ratio of inertial forces to viscous forces, is introduced as

$$Re_{dyn} \equiv \frac{\text{inertial forces}}{\text{viscous fores}}. \tag{5-37}$$

Referring to Figure 5-4 and the accompanying text, if the axial pressure gradient is assumed negligible then the ratio of viscous to inertial forces at any specific value of $z^*$ is given by

$$Re_{dyn}\big|_{z^*} \equiv \frac{[f''|_{z^*=0} - f'']}{f''}. \tag{5-38}$$

However, in order to establish a mean dynamic Reynolds number across the disc separation, the numerator and denominator of equation (5-38) are integrated across half the disc separation to yield

$$Re_{dyn} \equiv Re_{dyn}\big|_0^{1/2} \equiv \frac{\int_0^{1/2}[f''|_{z^*=0} - f'']dz^*}{\int_0^{1/2} f''dz^*} = \frac{\frac{1}{2}f''|_{z^*=0} - f'|_{z^*=0}}{f'|_{z^*=0}}. \tag{5-39}$$

Equations (5-20) and (5-21) are substituted into equation (5-39) for an exponential solution ($\lambda > 0$) to yield

$$Re_{dyn} = \frac{1}{2}\sqrt{\lambda}\coth\frac{\sqrt{\lambda}}{2} - 1. \tag{5-40}$$

Equation (5-22) is substituted into equation (5-40) to solve for an oscillatory solution ($\lambda < 0$) to give

$$Re_{dyn} = \frac{1}{2}\sqrt{|\lambda|}\cot\frac{\sqrt{|\lambda|}}{2} - 1, \tag{5-41}$$

which yield only negative values of $Re_{dyn}$.

The interpretation of a positive $Re_{dyn}$ is that both the average values of viscous and inertial forces act in the same direction whereas a negative $Re_{dyn}$ indicates that the averaged viscous and inertial forces are acting in opposing directions.

Using equation (5-41) and (5-42), the variation of $Re_{dyn}$ with $\lambda$ and the 'traditional' Reynolds number $Re_{trad}$ (5-36b) are plotted in Figure 5-9.

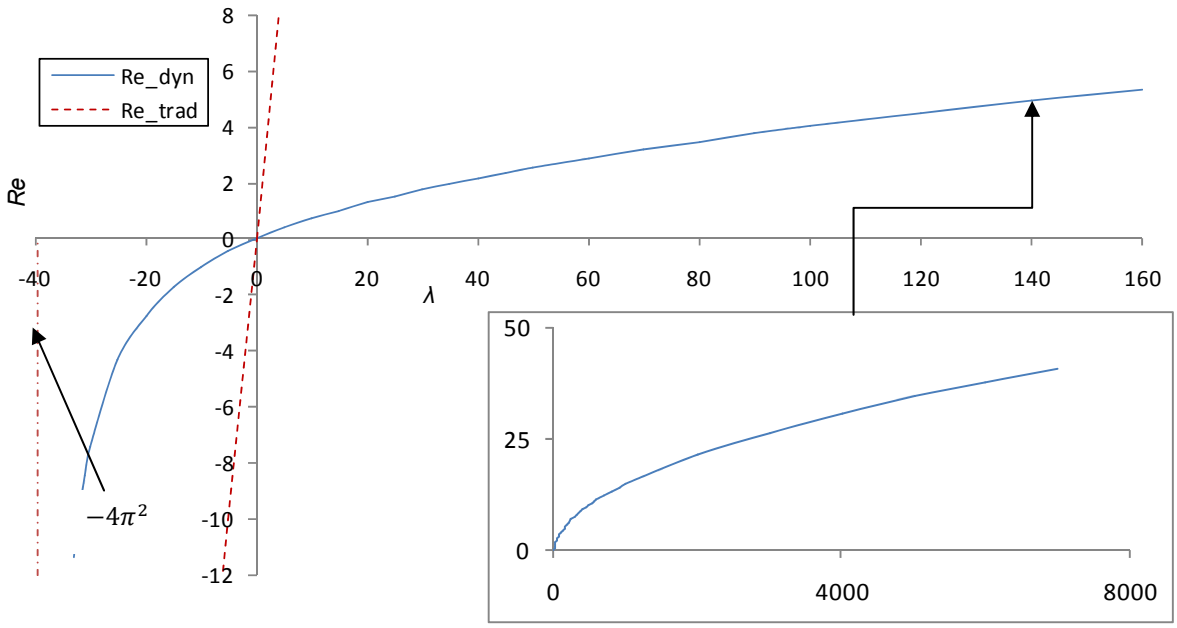


Figure 5-9: Variation of dynamic Reynolds number with shape parameter

The zero intersection of $Re_{dyn}$ occurs at $\lambda = 0$ (Figure 5-9), this corresponds to the parabolic fluid velocity profile of the lubrication approximation. It is also noted how the curve forms an asymptote at $\lambda = -4\pi^2$, which corresponds to incipient separation as defined in the text associated with Figure 5-3.

The traditional Reynolds number is invariant with disc acceleration and hence by equation (5-16), it can be shown that $Re_{trad} = 1/2\,\lambda$. Figure 5-9 shows very poor correlation between $Re_{trad}$ and $Re_{dyn}$, hence the traditional Reynolds number is a poor representation of the ratio of viscous to inertial forces [equation (5-37)].

## 5.11 Circumferential Pressure Approximation

Within the reviewed literature, a zero circumferential gauge pressure is generally assumed. However, the constant of integration arising from the integral of the radial pressure gradient allows the inclusion of instantaneous circumferential pressures [equation (5-31)].

In the context of highly transient squeeze flows it is speculated that circumferential pressures may be generated due to fluid inertia effects which extend beyond circumferences of the discs. Initially it was thought that containing the fluid precisely between the discs before the experimental stroke (by say a burst diaphragm) would eliminate such this effect. However, in this configuration, shortly into the experimental stoke, the fluid would extend past the disc circumference due to the radial outflow, and thus again promote this effect. Hence if this speculated pressure generation mechanism is correct, circumferential offset pressures are unavoidable for a constant contact area squeeze flow (Section 2.1.3, p.4).

It is pre-emptively shown that the experimental test cell contains fluid within a flexible fluid bladder attached to both disc circumferences as shown in Figure 7-3, pp 70, and the assembly drawing on p. 72. Viewing a radial section of the squeeze flow system and the fluid bladder, it can be seen that the fluid bladder may be approximated as a constricted source flow system (Figure 5-10).

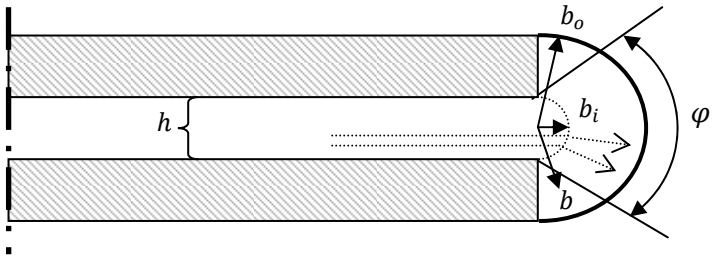


Figure 5-10: Fluid bladder boundary system modelled as souse flow

In Figure 5-10, $b$ is the bladder radius and $\varphi$ is the effective annular jet angle:\. If an unimpeded source flow is assumed then $\varphi = \pi$, which has the unphysical interpretation that fluid adjacent to the disc would flow unimpeded through a right angle. Instead the effective annular jet angle is assumed to satisfy

$\pi/2 < \varphi < \pi$; this is an purely speculative range because no research material investigating this specific submerged annular jet flow has been found.

A constricted source flow is given as

$$v_b = \frac{m}{\varphi b} \tag{5-42}$$

where $v_b$ is the radial fluid velocity (within the bladder) and $m$ is the source strength. The source strength may be approximated to

$$m = \bar{v_r} h = -\frac{R}{2}\dot{h} \tag{5-43}$$

where $\bar{v_r}$ is recalled from equation (2-4), p. 7. Equation (5-43) is substituted into equation (5-42) which in turn is differentiated with respect to time to give

$$\frac{dv_b}{dt} = -\frac{R}{2\varphi b}\ddot{h}. \tag{5-44}$$

The pressure development for a temporal inertia dominant cylindrical flow system (refer to the Navier-Stokes equation in Appendix A) is given by

$$\frac{dp_{cir}}{db} = \rho\frac{dv_b}{dt} \tag{5-45}$$

where $p_{cir}$ is the pressure at the disc circumference, so that when equation (5-44) is substituted into equation (5-45) and integrated with respect to radius, the circumferential pressure is obtained as

$$p_{cir} = \rho\int_{b_i}^{b_o} -\frac{R}{2\varphi b}\ddot{h}\, db = -\frac{\rho R}{2\varphi}\ddot{h}\,\ln\frac{b_o}{b_i} \tag{5-46}$$

where $b_i$ denotes the approximated radial start of the source flow and $b_o$ denotes the approximate bladder radius (Figure 5-10).

Experimental system constants are substituted into equation (5-46) in Section 7.5.1, p. 84, in order to solve for the experimental circumferential pressure. The resultant circumferential pressure offsets and corrections made to the experimentally measured radial pressure distributions are shown in Section 8.1.3, Figure 8-6, p. 103.

## 5.12 Eccentric Pressure Distributions

Under the parallel flow assumption, by equation (5-9) the resultant pressure distribution is invariably parabolic $p^* = \left(1 - r^{*2}\right)$. When this parabolic pressure distribution is rotated through $2\pi$, the result is an elliptical paraboloid. It is speculated that through experimental errors such as disc misalignment or non-uniform circumferential pressures, this paraboloid may become skewed or eccentric, i.e. $dp/d\theta \neq 0$ and $p_{max} \neq p_{cent}$, where $p_{max}$ and $p_{cent}$ are the maximum and central pressures respectively.

An eccentric pressure distribution is empirically modelled as being sinusoidally eccentric, i.e. an empirical sinusoidal skewness term $(1 + \sigma r^* \cos\theta)$ is introduced and multiplied by the paraboloid pressure distribution term to yield

$$p^* = (1 + \sigma r^* \cos\theta)\left(1 - r^{*2}\right) = -\sigma \cos\theta \, r^{*3} - r^{*2} + \sigma \cos\theta \, r^* + 1 \qquad (5\text{-}47)$$

where $\theta$ and $\sigma$ are defined as the skewness angle and the skewness magnitude respectively and $p^*$ is the dimensionless pressure given by $p^* \equiv p/p_{max}$. This empirical model is assumed to correspond accurately with experimental results for small values of $\sigma$ ($\sigma \leq 0.3$).

For illustrative purposes, Figure 5-11 shows an oblique and top (contour) view of a sectioned eccentric paraboloid with a skewness magnitude of $\sigma = 0.3$ (upper limit of applicability) and with a skewness angle of $0 \leq \theta \leq 3\pi/2$.

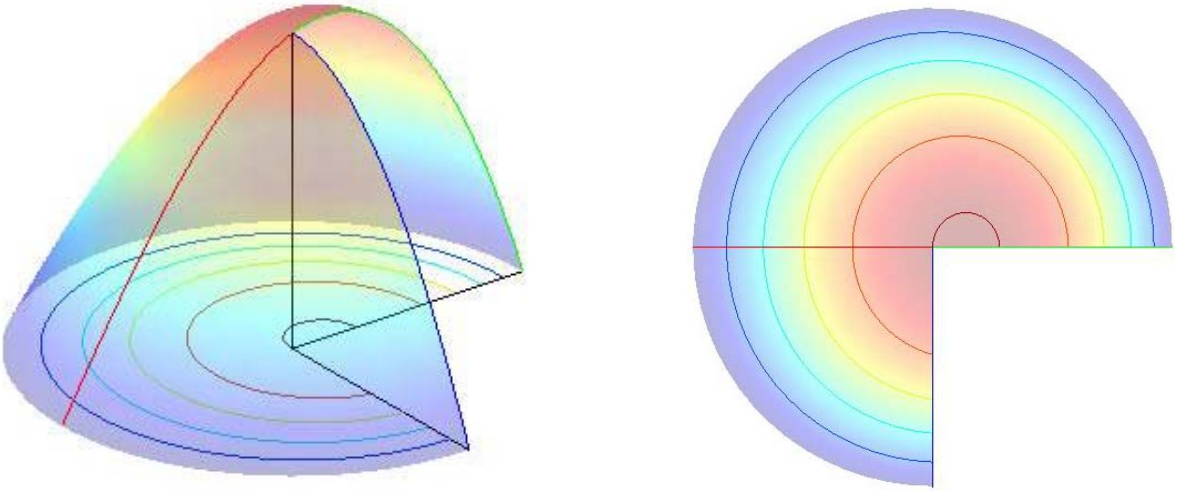

Figure 5-11: Eccentric paraboloid radial pressure distributions (three-dimensional)

The plane of symmetry of the eccentric paraboloid lies along the $0{:}\,\pi$ plane (Figure 5-11). Pressure distribution lines at specific angles have been highlighted with various colours; these pressure distribution lines are re-plotted against $r^*$ in Figure 5-12.

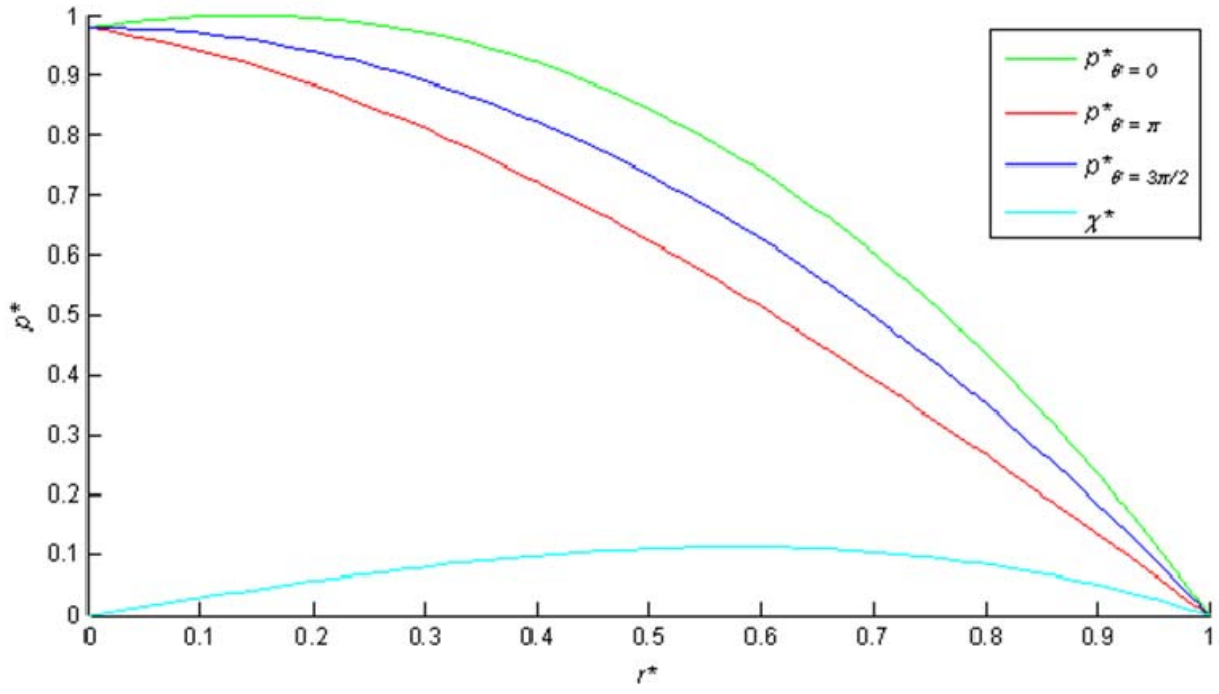


Figure 5-12: Eccentric paraboloid radial pressure distributions (two-dimensional)

The 'Eccentric Paraboloid' MATLAB program used to derive Figures 5-11 and 5-12 is given in CD-Appendix A.

The dimensionless eccentricity magnitude $\chi^*$ is defined as the maximum dimensionless pressure difference between an eccentric and a concentric paraboloid at equal radii with equal maximum pressures. This is equivalent to the pressure difference between two points at equal radii on either edge of the sectioned base in Figure 5-11). Hence $\chi^*$is determined as $\chi^* = p^*(0) - p^*(\pi/2)$ from equation (5-47) this yields

$$\chi^* = -\sigma r^* \left(r^{*2} - 1\right) \tag{5-48}$$

which is also plotted in Figure 5-12. In order to determine the radius of at which the maximum pressure difference occurs, equation (5-48) is differentiated with respect to $r^*$and equated to zero, giving

$$\frac{d\chi^*}{dr^*} = -\sigma\left(3r^{*2} - 1\right) = 0$$
$$\therefore r^* = \frac{1}{\sqrt{3}} \approx 0.577. \tag{5-49}$$

Hence, for the eccentric pressure distribution model investigated, equation (5-49) gives the optimum radial position at which a set of pressure transducers used to measure pressure paraboloid skewness (or the so-called axi-symmetric pressure transducers) should be positioned[a].

The peak offset $\xi$ is defined as the radial distance from the disc/s center to the apex of the skewed paraboloid. Similar to the non-dimensional radius, the non-dimensional peak offset is defined as $\xi^* \equiv \xi/R$. The peak offset may be obtained as the radius at which the gradient of $p^*$ along the plane of symmetry of the eccentric paraboloid is zero. Hence differentiating equation (5-47) at $\theta = 0$ with respect to $r^*$ and equating it to zero gives

[a] The reason the axi-symmetric pressure transducers of the test rig are not placed at approximately $R/\sqrt{3}$ (Figure 7-7, p. 89) is due to this non-axi-symmetric model being developed after the fabrication of the test rig. Non-axi-symmetry was only realized as a significant effect after the experimentation was conducted utilizing the already fabricated test rig.

$$\frac{dp^*}{dr^*} = -3\sigma {r^*}^2 - 2r^* + \sigma = 0$$

which may be solved using the quadratic formula in which the plus/minum operator will always be positive since the peak offset is positive, then after simplification

$$\xi^* = \frac{\sqrt{1+3\sigma^2}-1}{3\sigma} = \frac{3\sigma^2}{3\sigma\left(\sqrt{1+3\sigma^2}+1\right)} = \frac{\sigma}{\sqrt{1+3\sigma^2}+1} \approx \frac{\sigma}{2} \tag{5-50}$$

for small values of $\sigma$. (if $0 \leq \sigma \leq 0.3$, then $2 \leq \sqrt{1+3\sigma^2}+1 < 2.13$).

Hence when equating the central and maximum pressures, by equations (5-47) and (5-50)

$$p_{cent} = \frac{p_{max}}{(1+\sigma\xi^*)\left(1-{\xi^*}^2\right)} \approx \frac{p_{max}}{\left(1+\frac{\sigma^2}{2}\right)\left(1-\frac{\sigma^2}{4}\right)} \approx \frac{p_{max}}{1+\frac{\sigma^2}{4}}. \tag{5-51}$$

The above theoretical model is adapted for the experimental results in Section 7.5.2, p. 90, in order to correct for any errors associated with the eccentricity of the experimentally measured radial pressure distributions, the results of which are shown in Section 8.1.3, Figure 8-6.

# 6 CFD MODELING

This CFD evaluation is developed in parallel with the theoretical analysis (Section 0, p.19) to serve as a numerical model against which various analytical assumptions and approximations are tested. More specifically, the derived theoretical models are directly compared against a hypothetical CFD model in order to quantify errors associated with various assumptions and approximations made.

## 6.1 Hypothetical Disc Motion

Since experimental values of $h$, $\dot{h}$ and $\ddot{h}$ are currently unknown, a hypothetical velocity curve is created. This hypothetical velocity is of sinusoidal form given by

$$U(t) = \frac{U_{max}}{2}\left[1 - \cos\left(\frac{2a_{max}}{U_{max}}\right)t\right] \tag{6-1}$$

where $U = -\dot{h}$ and $U_{max}$ is the maximum disc velocity which is set to $U_{max} = 4$ m/s and $a_{max}$ is the maximum acceleration which is set to $a = \ddot{h} = 8000$ m/s$^2$. The initial disc separation is $h_0 = 4$ mm and the experimental stroke time is set to $0 \leq t < 1.6$ ms. The resulting sinusoidal disc velocity curve and corresponding acceleration and separation curves are shown in Figure 6-1.

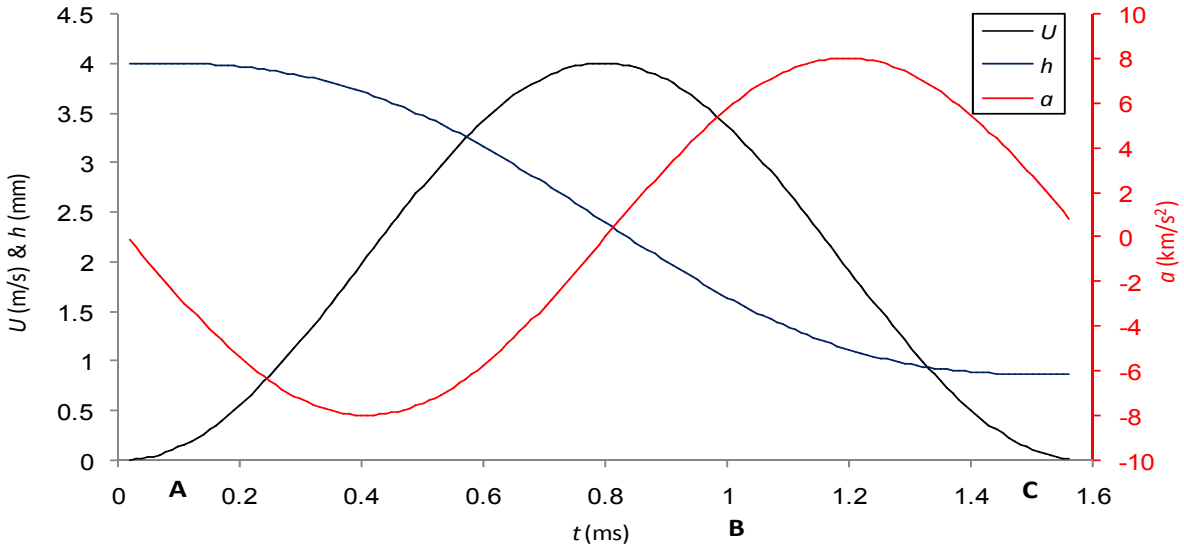


Figure 6-1: Hypothetical CFD disc separation, velocity and acceleration vs time

A symmetrical squeezing motion is modelled (Section 2.1.2, p. 3), so that each disc moves towards its counterpart with half the velocity specified by equation (6-1) and shown in Figure 6-1.

Dimensionless radial fluid velocity profiles are analyzed at the three discrete time instants highlighted with letters **A**, **B** and **C** in Figure 6-1 corresponding to time $t = 0.1,\ 1.0$ and 1.5 ms[a] respectively.

### 6.1.1 Forecast Reynolds Numbers

The traditional Reynolds number [equation (2-5), p. 7] and dynamic Reynolds number [equations (5-40) and (5-41), p. 39] for the hypothetical CFD simulation are derived and plotted on the left-hand scale of Figure 6-2. In addition the inertial composition [equation (5-7), p. 22] is also plotted in Figure 6-2 on a secondary right-hand log scale.

Figure 6-2 shows that the traditional Reynolds number follows a similar form to the disc velocity (Figure 6-1). However, $Re_{trad}$ holds no correlation with the $Re_{dyn}$ and hence it be inferred that the traditional Reynolds number for squeeze flows is not a good reflection of the ratio of inertial to viscous forces when applied to highly transient squeeze flows.

The dynamic Reynolds number is greater than ten during the stroke initiation ($t < 0.1$ ms) indicating inertial force dominance during this phase which is expected. It is also noted that $|Re_{dyn}| < 1$ for the narrow time range of $0.9 < t < 1.35$ ms, during which it is inferred that viscous forces are dominant. Viewing the inertial composition, it can be seen that temporal inertia is the dominant inertial force contributor throughout the experimental stroke (on a time average basis) with spatial inertia only becoming dominant through a narrow time region surrounding $t = 1$ ms.

From the dynamic Reynolds number and inertial composition in Figure 6-2, it may be inferred that the pressure generation mechanism at time **A** (0.1 ms) is dominated by temporal inertia whereas at time **B** (1 ms) the pressure generation mechanism is viscous dominant. Finally, at time instant **C** (1.5 ms) the pressure generation mechanism is once again dominated by temporal inertia.

[a] These three discrete time points were selected with hindsight to best illustrate the dimensionless radial fluid velocity evolution.

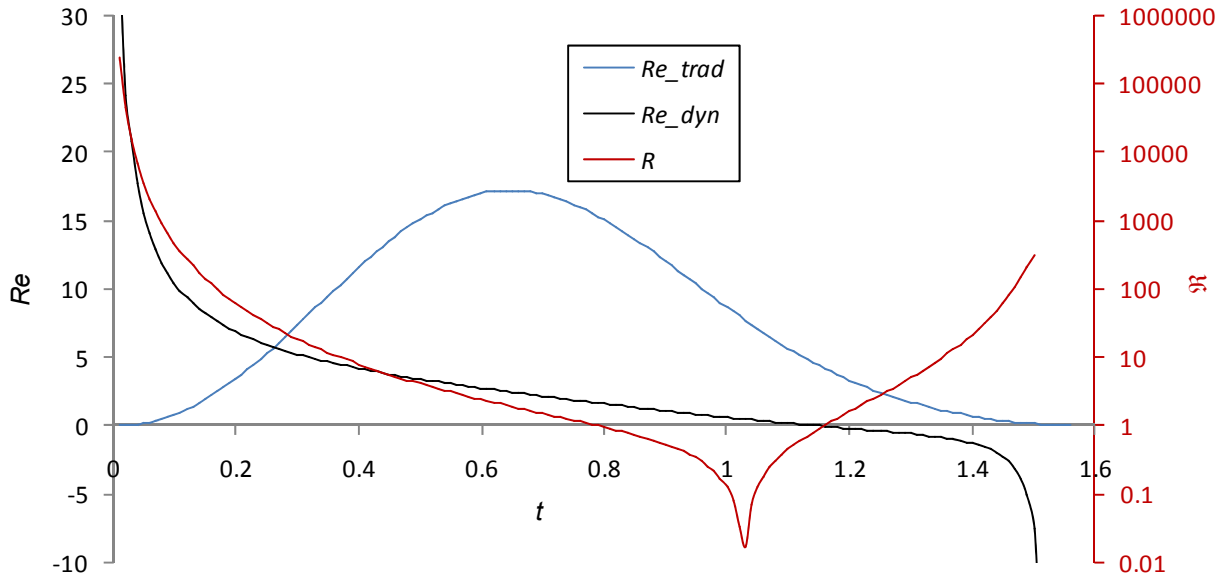


Figure 6-2: Traditional and dynamic Reynolds numbers and inertial force composition vs time

## 6.2 Computational Setup

The disc is set to a 60 mm radius with a 4 mm initial disc separation. Gambit™ (the meshing program) is set up as a rectangular grid representing a radial slice through the disc separation. This rectangle is 30 (radial) cells by 51 cells (axial). This 'Preliminary_4mm' mesh file is available in CD-Appendix D.

Fluent™ (2ddp) is set up with an axi-symmetric pressure based solver with a laminar viscous flow regime. The working fluid is set as incompressible glycerine with $\rho = 1259$ kg/m$^3$ and $\mu = 0.799$ Ns/m$^2$. The Fluent case and data files are given in CD-Appendix D by the 'Preliminary_4mm' program.

The step times are set to $1\times10^{-5}$ s, i.e. a total of 150 steps are needed to complete the experimental stroke of 1.5 ms. At time instants **B** and **C** the case and data files are saved and are available in Appendix D as '4mm_1ms' and '4mm_1.5ms' respectively along with other time instants which are similarly, appropriately named.

## 6.3 Results

### 6.3.1 Evaluation of parallel flow assumption

Figures 6-3 and 6-4 respectively show the CFD dimensionless axial velocities and pressure distribution contours between the two discs at time instant **A** ($t = 0.1$ ms)[a], where these dimensionless variables are defined as

$$v_a{}^* = \frac{v_a}{U} \quad \text{and} \quad p^* = \frac{p}{p_{max}}. \qquad \text{(6-2a, b)}$$

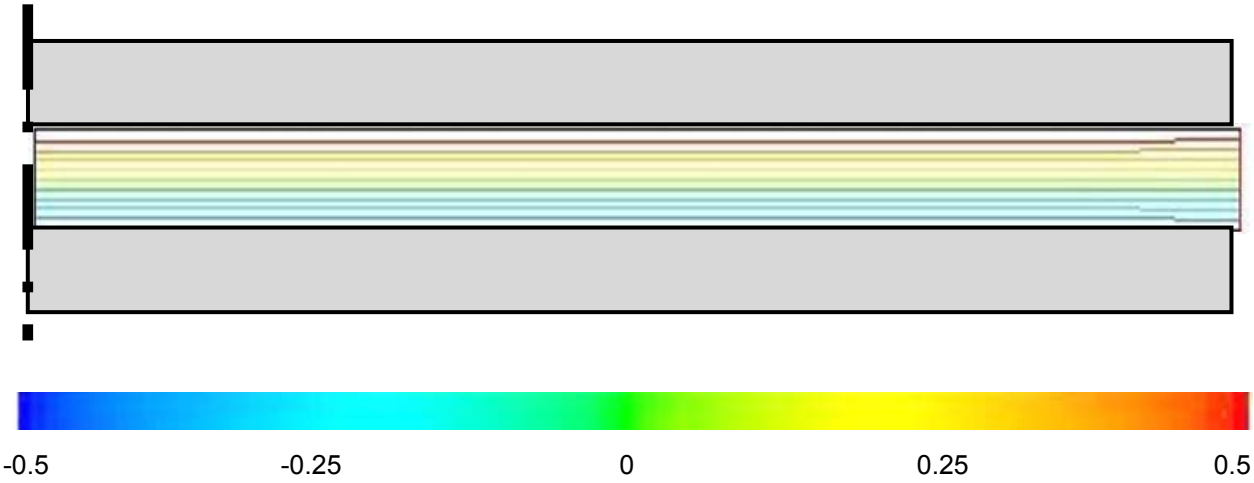


Figure 6-3: Dimensionless axial velocity contours at time instant A

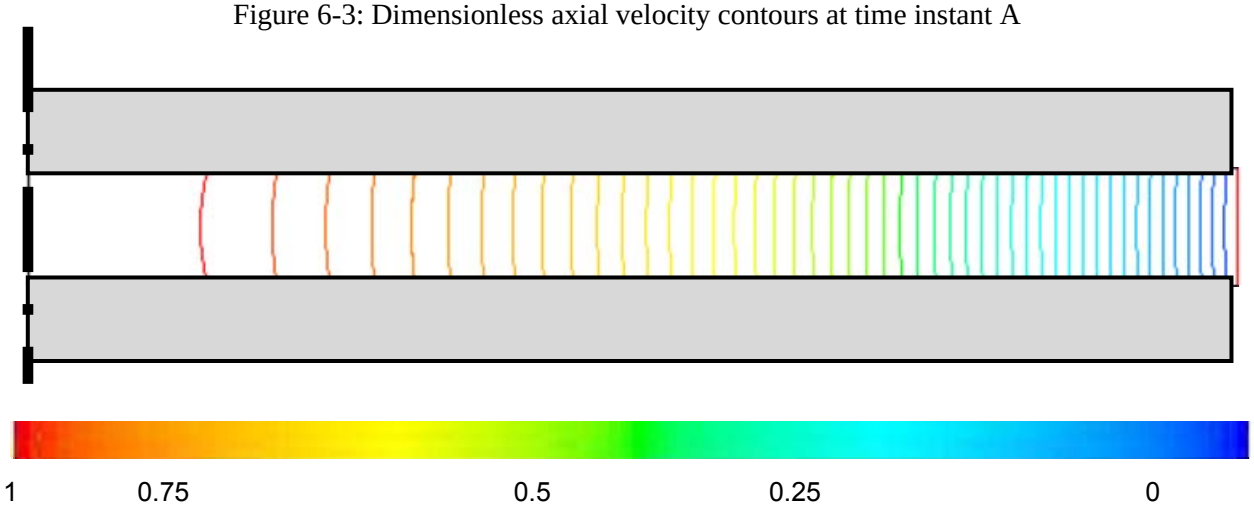


Figure 6-4: Dimensionless pressure distribution contours at time instant A

[a] The ratio of separation to radius is not to scale in the above figures.

Figure 6-3 shows that the dimensionless axial velocity contours are accurately parallel across the disc separation with only a marginal distortion towards the disc circumference (right-hand side). It is speculated that these distortions are due to edge effects; nevertheless for the purpose of analysis it can be assumed that these distortions are negligible and therefore the axial velocities contours are parallel and thus the parallel flow assumption is supported [refer to equation (2-12a, b), p. 9, and associated text].

Figure 6-4 shows a slight axial pressure gradient as seen by the cambering of the vertical pressure contour lines (most apparent closest to the centre of the discs). This transverse pressure gradient is very slight and can be considered negligible, however it must be noted that $dp/dz^* \approx 0$ is an approximate constraint. As expected, the pressure distribution is symmetrical about $z^* = 1/2$ due to the symmetrical squeezing motion.

Figure 6-5 shows the dimensionless radial pressure distributions at the disc interface (either disc) versus dimensionless radius at time instant **A**, **B** and **C**. In addition, an exact parabolic pressure distribution is superimposed upon these axes; these four traces are visually so similar that they appear as a single curve[a]. Parabolic pressure distributions are theoretically expected under the parallel flow assumption (Section 5.4, p. 23). Therefore, in order to quantify the errors of the radial pressure distributions against that of a parabolic pressure distribution at time instant **A**, **B** and **C**, a *parabolic deviation* or error is introduced as

$$\varepsilon = |p^*| - p^*_{parabolic}. \tag{6-3}$$

Parabolic deviations for time instant **A**, **B** and **C** are plotted on the right-hand scale in Figure 6-4. It can be seen that for each measured time instance $\varepsilon < \pm 1\%$. This small error is speculated to be due to the abovementioned edge affects and other second order affects (terms of the Navier–Stokes equations which are considered negligible for analytical derivations, refer to Appendix A). With a maximum measured deviation of $\varepsilon < \pm 1\%$, the radial pressure distribution may be approximated as invariably parabolic.

[a] It is noted that the pressure distribution at time instant **C** is plotted as a negative pressure because at this time instant a negative pressure is developed between the discs. This is elaborated upon in Section 6.4, pp26.

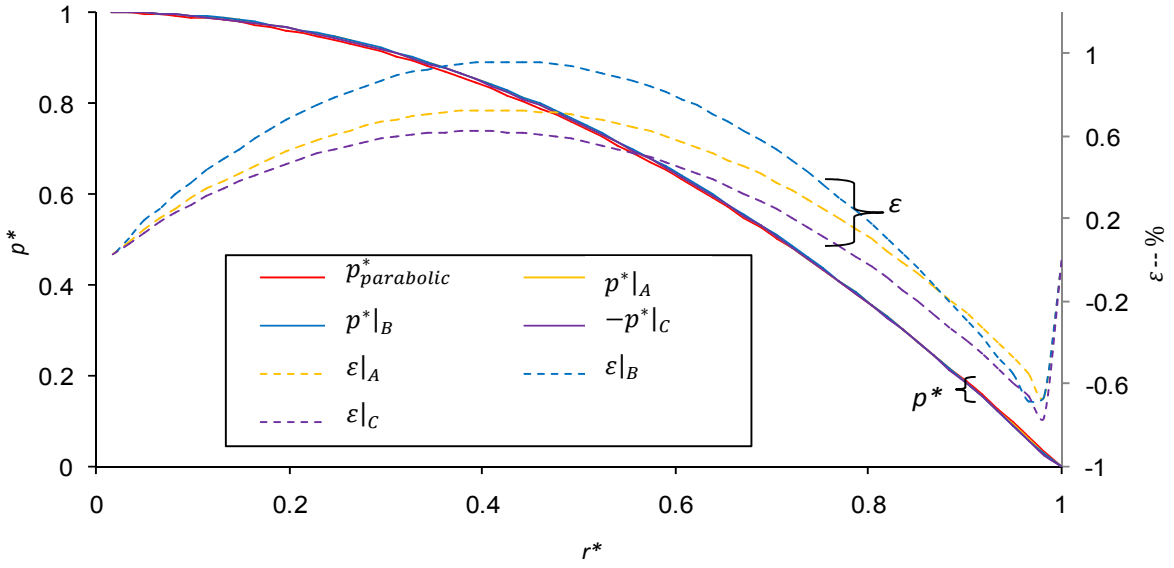


Figure 6-5: CFD dimensionless radial pressure distributions and associated parabolic deviations vs dimensionless radius

The dimensionless radial fluid velocities at four predetermined circumferential strips along the disc radius [at $r^* = 0.25,\ 0.5,\ 0.75$ and 1 (disc circumference)] are shown at time instant **A**, **B** and **C** in Figure 6-6.

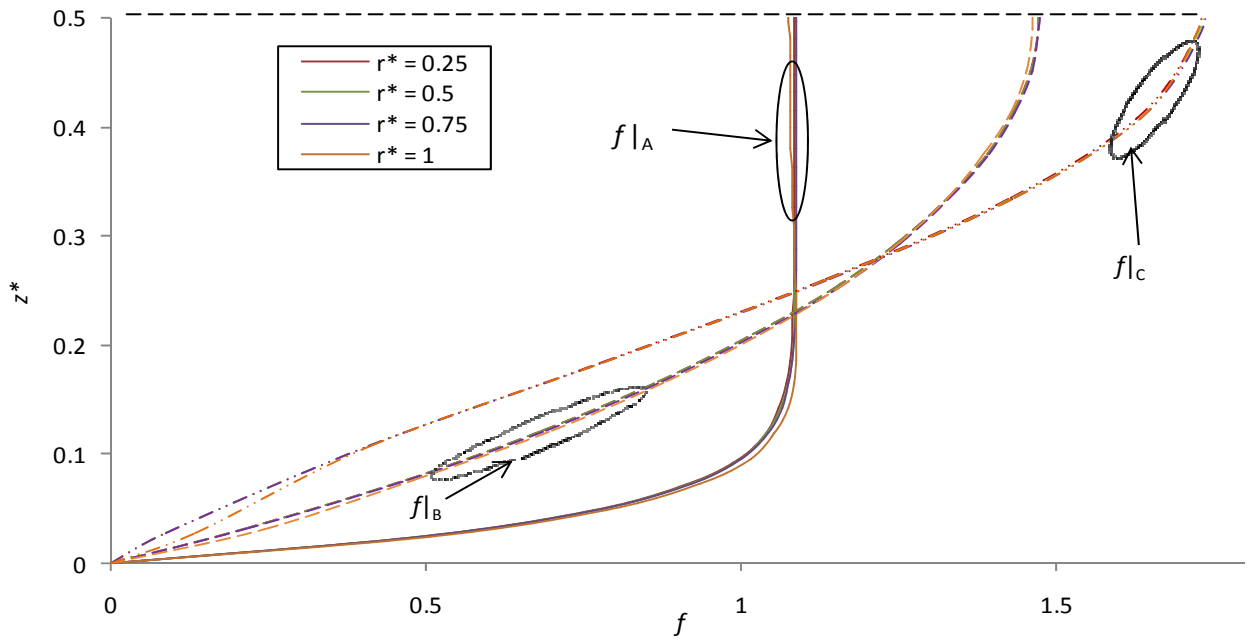


Figure 6-6: CFD dimensionless radial fluid velocities at time instants **A**, **B** and **C**

At each time instant, the shapes of $f$ are so similar they appear as a single curve in Figure 6-6. However, on closer inspection close to the wall interface, it can be seen that $f_{r^*=1}|_B$.and $f_{r^*=1}|_C$ stray noticeably off the other superimposed $f$ values. This is once again speculated to be due to the abovementioned edge effects.

The CFD dimensionless radial velocities are determined using the 'DRV 0.1ms', 'DRV 1ms', and 'DRV 1.5 ms', Excel spreadsheets in CD-Appendix B. Thereafter the 'CFD vs Analytical' Excel spreadsheet (CD-Appendix B) is used to develop Figures 6-5 and 6-6.

It is found that both the parallel flow assumption and the assumption of a negligible axial pressure gradient are adversely affected by an increase in disc separation. Nevertheless at a ratio of radius to disc separation of up to $1:6$, the axial pressure gradient may still be considered negligible and the parallel flow assumption may still be considered sufficiently accurate[a].

## 6.4 Comparison of CFD with Theoretical Models

At time instants **A**, **B** and **C** the CFD generated dimensionless radial velocities are compared against those of the following models:

a. QSL model (Section 5.6, p.26) - analytically determined.
b. QSCL model (Section 5.7, p. 32) - analytically determined.
c. QS model (Section 5.5, p. 24) - numerically determined.

This comparison *assumes* that the CFD results are dictated by the exact kinematic model (Section 5.4, p.23), i.e. the solution of equation (5-10). Furthermore the mesh motion is assumed to accurately[b] correspond to the numerically determined disc velocity, acceleration and resultant separation as calculated by Excel (spreadsheet 'CFD hypothetical experiment', CD-Appendix B), hence errors such as truncation and rounding are considered negligible.

[a] These conclusions are reached from an additional CFD simulation in which the initial disc separation of 4 mm is increased to 10 mm (all other parameters are identical); the resulting dimensionless axial velocities and pressure distributions contours at 0.1 ms are given in Appendix D.

[b] It is noted that equation (5-9), p. 21, will not be exactly satisfied because of the slight transverse pressure gradient and slight deviation or the parallel flow as shown in Figure 6-3 and Figure 6-6 respectively.

In order to ultimately establish the dimensionless radial velocities of the QSL and the QSCL models, the instantaneous shape parameter and corrected shape parameter values are respectively determined by equation (5-16) (Section 5.6, p. 26) and equation (5-29) (Section 5.7, p. 33). Truncated values of both the shape parameter and corrected shape parameter traces are plotted on the left-hand scale of Figure 6-7. Due to the large range and small variations between $\lambda$ and $\lambda_{cor}$ these two traces appear as a single line. Hence, in order to distinguish between these two traces and to determine small values of $\lambda$ and $\lambda_{cor}$ ($\lambda, \lambda_{cor} < \pm 50$), $\pm\lambda$ and $\pm\lambda_{cor}$ are plotted on a log scale on the right-hand scale of Figure 6-7.

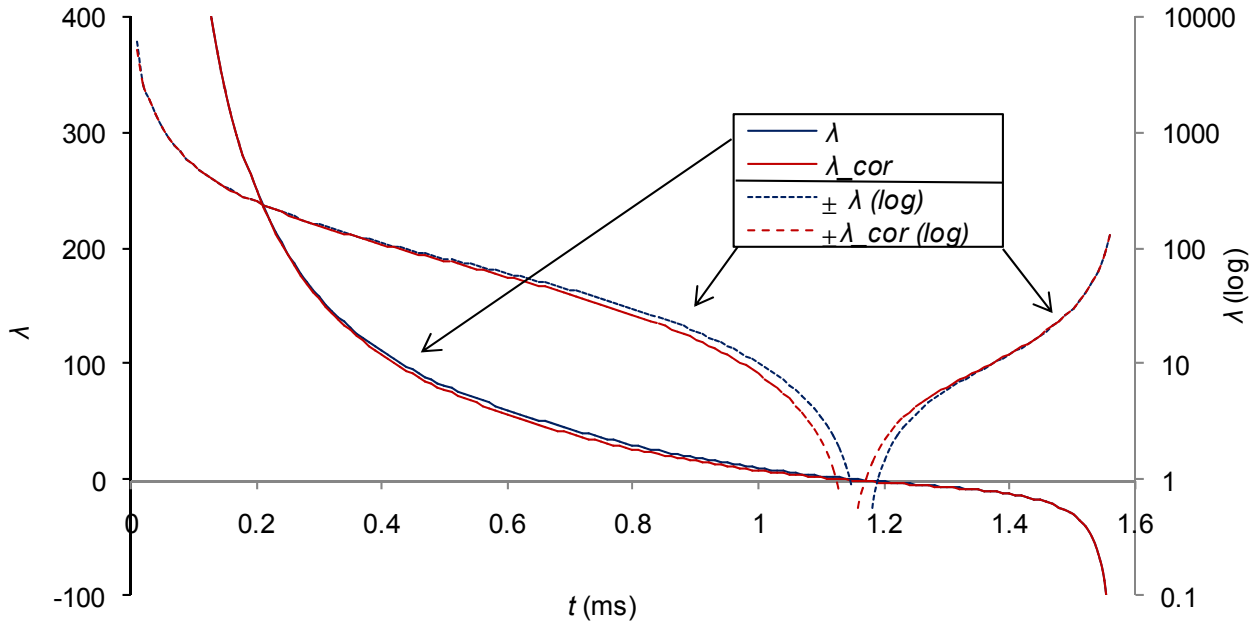


Figure 6-7: Shape parameter vs time

The shape parameter and corrected shape parameter at time instant **A**, **B** and **C** are given by:

i. **A**: $t = 0.1$ ms; $\lambda = 525.41 \approx \lambda_{cor} = 525.13$
ii. **B**: $t = 1.$ ms; $\lambda = 10.91$, $\lambda_{cor} = 8.18$
iii. **C**: $t = 1.5$ ms; $\lambda = -30.09 \approx \lambda_{cor} = -30.11$

The exact $\lambda$ and $\lambda_{cor}$ values (above) are taken from the Excel spreadsheet 'CFD hypothetical experiment' (CD-Appendix B).

Since the values of $\lambda$ and $\lambda_{cor}$ at **A**, **B** and **C** have been established, the corresponding dimensionless radial velocities of the QSL and QSCL models are calculated with the use of equations (5-19) and (5-24), pp. 27-28.

The dimensionless velocities of the QS model are determined numerically with the use of the MATLAB's Simulink toolbox ('QS model' program given in CD-Appendix A, block diagrams of which are shown in Appendix B). As discussed in Section 5.5, p. 24, two trial variables, representing $f''|_{z^*=0}$ and $f'|_{z^*=0}$, are needed to iteratively solve for these dimensionless velocities, and as further discussed in Section 5.6, p. 26, the starting values for these two trial variables may be obtained from the QSL model. However, it is found that more accurate starting values are obtained from the QSCL model. These starting values are varied through a double iterative process and are ultimately solved for by satisfying the boundary conditions (Section 5.3, p. 21), yielding the dimensionless velocities of the QS model.

The values of $f''|_{z^*=0}$ and $f'|_{z^*=0}$ for the QS, QSL and QSCL models are given in Appendix C. It is recalled that $p \propto f''|_{z^*=0}$ [equation (5-31), p. 34].

The dimensionless radial velocities of the QS, QSL and QSCL models are plotted against the CFD generated dimensionless radial velocities at the corresponding time instants. However, unlike Figure 6-6, only a single $f$ trace at an arbitrary radius is plotted for the CFD solution because approximate radial invariance has been established for $f$ (Figure 6-6, p. 52). Therefore, the dimensionless radial velocity at 50% disc radius is arbitrarily chosen for this comparison.

Figure 6-8 superimposes the dimensionless radial velocities of the CFD solution and the QS, QSL, and QSCL models at time instant **A** (0.1 ms). The difference between the dimensionless radial velocities of the QS and QSL/QSCL models are visually indistinguishable, hence it can be inferred that non-linear term $D_2$' [equation (5-10)] is negligible at this time instant. This finding is further supported in that both QSL and QSCL models have near identical $\lambda$ and $\lambda_{cor}$ values. Moreover, a discrepancy of about 0.4% at $z^* = 1/2$ is observed between the dimensionless radial velocities of the CFD solution and QS/QSL/QSCL models; this reveals that the shape evolution term $C_2$' may also considered to be negligible at this time instant.

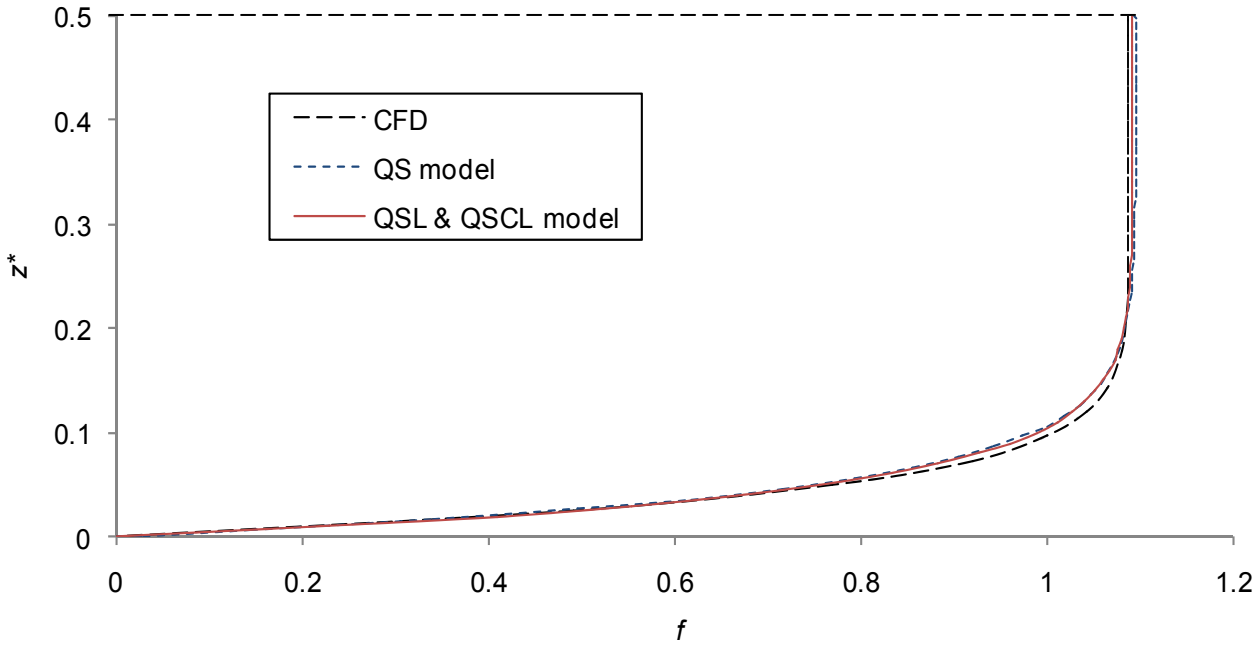


Figure 6-8: Dimensionless radial velocities at time A

Figure 6-9 superimposes the dimensionless radial velocities of the CFD solution and the QS, QSL, and QSCL models at time instant **B** (1 ms). The dimensionless radial velocities of the CFD solution and all theoretical models show a discrepancy of less than 0.5% at $z^* = 1/2$. This negligible discrepancy suggests that both the shape evolution term $C_2$' and the non-linear term $D_2$' [equation (5-10)] are negligible at this time instant.

Finally, Figure 6-10 superimposes the dimensionless radial velocities of the CFD solution and the QS, QSL, and QSCL models at time instant **C** (1.5 ms). The dimensionless radial velocities of the QS and QSL/QSCL models are negligibly different on a visual basis. Hence it can be inferred that non-linear term $D_2$' [equation (5-10)] is negligible at this time instant. This finding is supported by both the QSL and QSCL models having near identical $\lambda$ and $\lambda_{cor}$ values (similar to that at time instant **A)**. However, the CFD solution lags about 5% (at $z^* = 1/2$) behind the QS/QSL/QSCL models dimensionless radial velocities at time instant **C**; this error is associated with the omission of the shape evolution term $C_2$' [equation (5-10)]. Nevertheless term $C_2$' may still tentatively be inferred to be negligible.

It is however found that if the values of $\lambda \approx \lambda_{cor} = -24.8$, which corresponds to a time of $t = 1.485$ ms, is used as opposed to that at $t = 1.5$ ms for time instant **C** (Excel spreadsheet 'CFD hypothetical experiment', CD-Appendix B), the resultant QSL and QSCL models dimensionless radial velocity profile

corresponds almost identically to CFD trace (Figure 6-10). This suggests that $\lambda \approx \lambda_{cor}$ has effectively been lagged by approximately 15 μs at time instant **C**. This seemingly insignificant time lag (less than 1% of the stroke period) has a considerable effect on the resultant dimensionless radial velocity profiles due to the steep gradient of $\lambda$, $\lambda_{cor}$ with respect to time at time instant **C**, as shown in Figure 6-7.

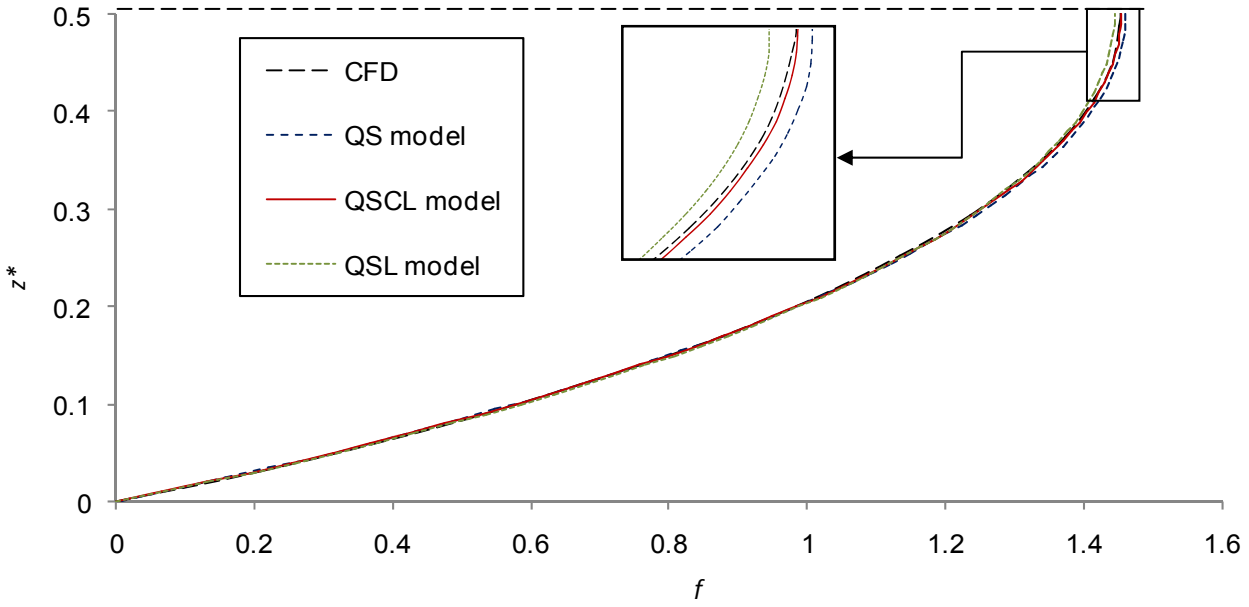


Figure 6-9: Dimensionless radial velocities at time B

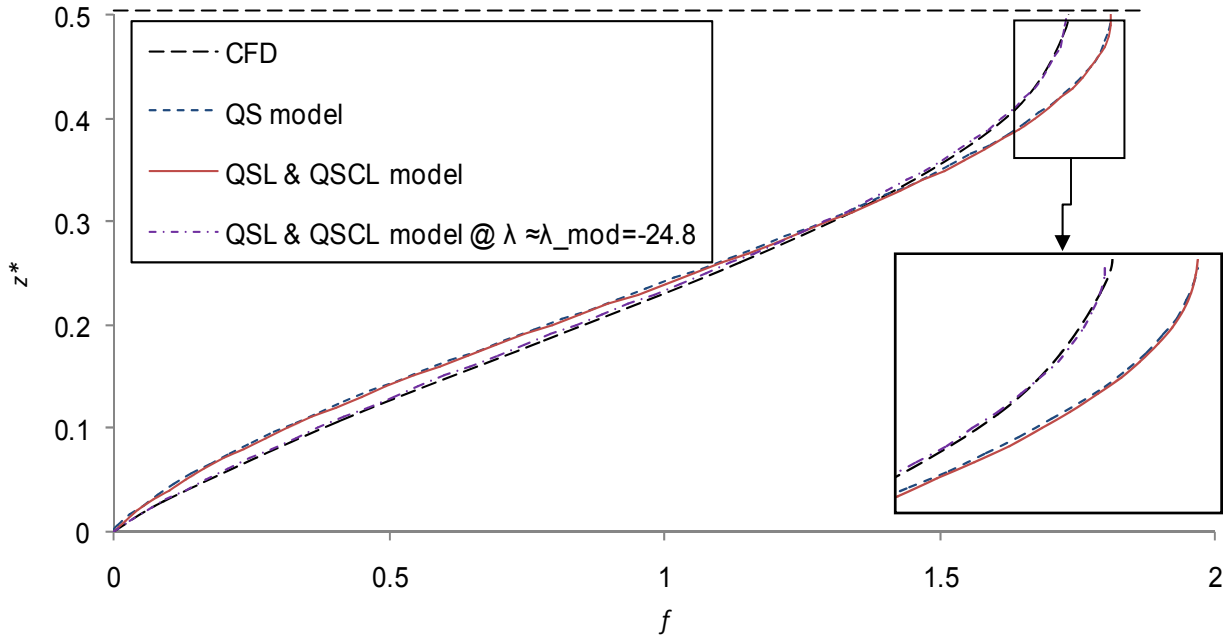


Figure 6-10: Dimensionless radial velocities at time C

Figure 6-11 shows the evolution ratio [Section 5.9, p. 36, equation (5-33)] applied to the hypothetical disc motion. It can be seen that $X$ remains well below 10% throughout the pressure *development* ($t \leq 1$ ms) of the experimental stroke and hence the quasi-steady approximation may be considered applicable throughout this phase. This is supported by the good agreement of the dimensionless radial velocity profiles of the CFD and the QS model at time instants **A** and **B** in Figures 6-8 and 6-9 respectively. However, $X$ forms a spike as $t \to 1.16$ ms (truncated in Figure 6-11), which occurs when the sum of terms ($C' + C'D'$) [equation (5-10), p. 23] intersects a zero value ($\lambda = 0$). This spike is speculated to be the major contributor for the effective 15 μs lag in CFD solution at time instant **C** (Figure 6-10), refer to Section 5.9 p. 36.

Hence the errors associated with the quasi-steady approximation are *convincingly* negligible when $\lambda > 0$ (Figures 6-8 and 6-9), whereas when $-4\pi^2 < \lambda < 0$, the errors associated with the quasi-steady approximation are at best only *tentatively* negligible (Figure 6-10) for this hypothetical experiment.

The 'CFD vs Analytical' Excel spreadsheet used to develop Figures 6-5, 6-9 and 6-10 are given in CD-Appendix B.

The resultant central pressure traces of the QS, QSL and QSCL models are obtained by substituting the resultant instantaneous values of $f''|_{z^*=0}$ into equation (5-31), p. 34, at $r^* = 0$. These resultant pressure traces are shown in relation to the CFD generated central pressure trace in Figure 6-12. The lubrication approximation and the inviscid/inertial model are also plotted in Figure 6-12, i.e. equations (2-8), p. 8 and equation (5-2), p. 20, respectively. These *simplistic* models serve as an illustration of the significant increase in analytical modeling accuracies of the QSL, QSCL and QS models.

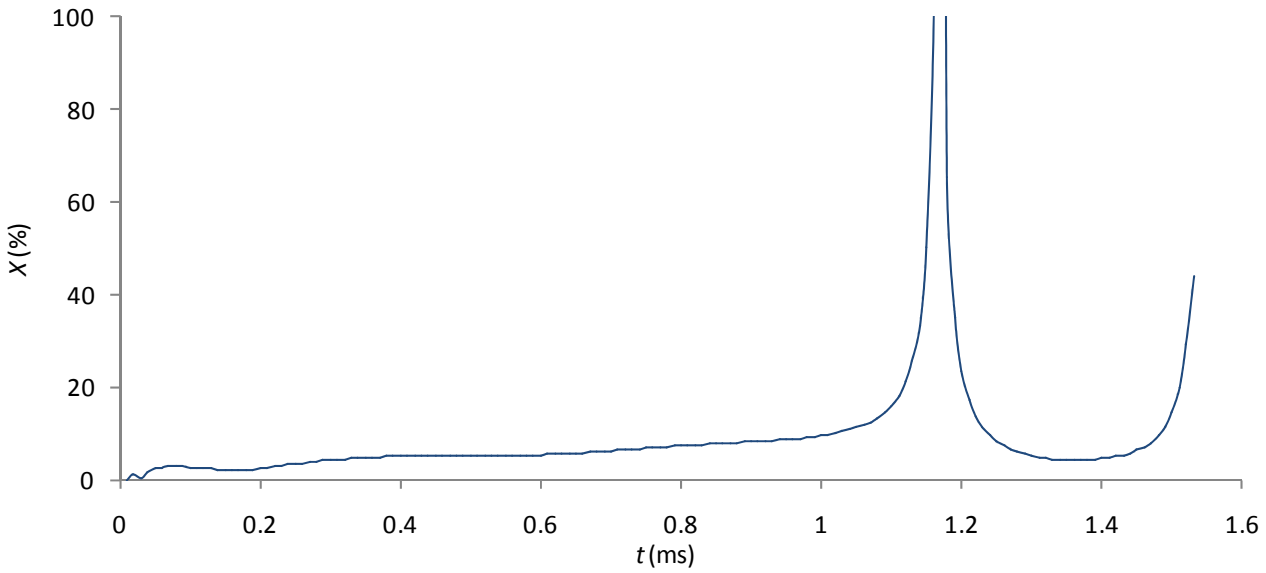


Figure 6-11: Evolution ratio vs time

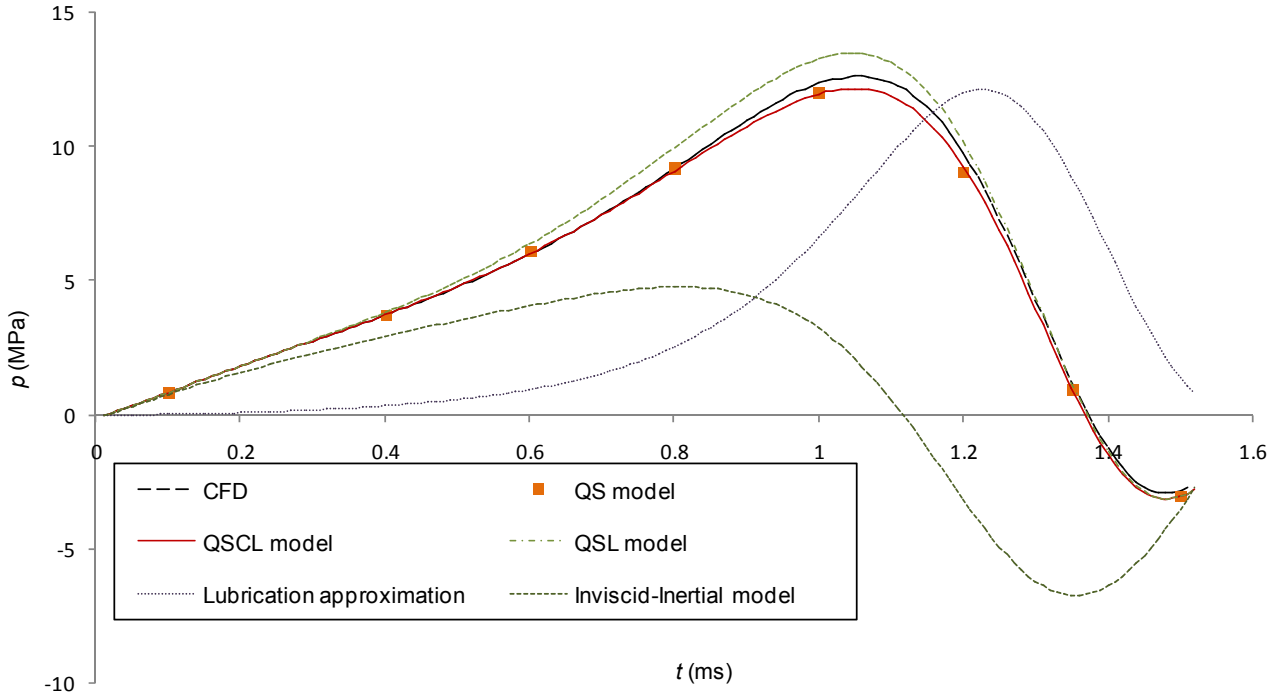


Figure 6-12: CFD and theoretical central pressure traces vs time

Overall, there is poor shape and magnitude correlation between the central pressure traces of the simplistic models (lubrication approximation and inviscid/inertial model) and that of the CFD generated

central pressure trace (Figure 6-12). However, in the early stroke stages ($t \leq 0.2$ ms), the trace of the inviscid/inertial model corresponds closely with the CFD generated pressure trace.

A fairly close correlation between the QSL model and the CFD generated pressure traces is observed with only 7% discrepancy between the two traces during the pressure peak (Figure 6-12). Furthermore, as expected, this correlation is significantly improved on by the QSCL model which has a mere -3% discrepancy between the two traces during the pressure peak. The QSCL model also corresponds accurately with the QS[a] model in that it intersects every QS model marker, i.e. less than 2% error (Appendix C, in which $f''|_{z^*=0} \propto p_{cent}$). Therefore, the QSCL model is assumed to accurately account for all spatial inertia.

The accurate correlation between the QS model markers and the CFD generated pressure trace [less than -3% during the major pressure development (Figure 6-12)] suggests that the quasi-steady approximation, (Section 5.5, p.24), is an appropriate assumption for this specific experiment.

It is noted that seemingly negligible deviations in theoretical dimensionless radial velocities (as compared against CFD) may result in comparatively large deviations in the resultant pressure differences (as compared against CFD) or vice-versa; see Figures 6-9, 6-10 and 6-12. The reason for this apparent incongruity is that the pressure development is proportional to $f''|_{z^*=0}$ and not $f$, i.e. $f''|_{z^*=0}$ is the uniquely fine curvature of $f$ at the disc/s interface which cannot be visually ascertained from plots of $f$.

[a] Only eight QS model markers because of the intensive manual iterative processes used to derive the $f''|_{z^*=0}$ and $f'|_{z^*=0}$ values, refer to Section 5.5, p. 23.

### 6.4.1 Kuzma's solution

Kuzma's successive approximation [Section 2.4, p. 13, equation (2-19)] is applied to the hypothetical disc kinematics (Figure 6-1). The resultant central pressure traces in addition to that of the QSCL model is compared against the CFD solution in Figure 6-13. The errors associated with these theoretical models (relative to the CFD trace) are also displayed in Figure 6-13 on the secondary right–hand scale. Positive/negative spikes (truncated in Figure 6-13) of these error traces occur at $t \to 1.38$ ms due to the zero intercept of the CFD trace not coinciding with the theoretical trace intercepts.

Kuzma's approximation is in good agreement with the CFD results with an associated error of about 15% at the stroke initiation (Figure 6-13). Yet as $t \to 0.8$ ms, i.e. as $\lambda, \lambda_{cor} \to 0$, the associated error decreases because the radial velocity profiles become more parabolic in shape which is Kuzma's first approximation (Section 2.4, p. 12). On the other hand the pressure trace of the QSCL model has an almost negligible associated error of ±1% during this development phase of the experimental stroke. However, for $t >$ 0.8 ms, both the theoretical models stray increasingly from the CFD solution with time, it is speculated that this is due to the quasi-steady approximation which both models make. This speculation is supported by the increase in the evolution ratio during this region as can be seen in Figure 6-11.

The dimensionless velocity profiles of Kuzma's approximation at time instants **A**, **B** and **C** are shown in Figure 6-14. It can be seen that at time instant **B** (1 ms) and **C** (1.5 ms) the dimensional velocities are similar to those shown in Figures 6-9 and 6-10 respectively. However, at time instant **A** (0.1 ms), the dimensional velocity diverges radically from what is predicted by CFD due to the actual dimensionless velocities (CFD) being almost square in shape as opposed to parabolic (Kuzma's first approximation).

Hence the application of Kuzma's approximation to highly transient squeeze flow systems results in relatively accurate pressure traces ($\pm$10% through the significant pressure proportion of the experimental stroke), which in turn produces accurate resultant radial velocity profile at relatively low Reynolds numbers or shape parameters of $\lambda < 50$. However, Kuzma's approximation fails to predict accurate radial velocity profiles at high Reynolds numbers or shape parameters of $\lambda \geq 50$. Therefore, in order to yield more accurate dimensionless radial velocities throughout a highly transient squeeze flow it is recommended that the QSCL, or the less complex QSL model, is used.

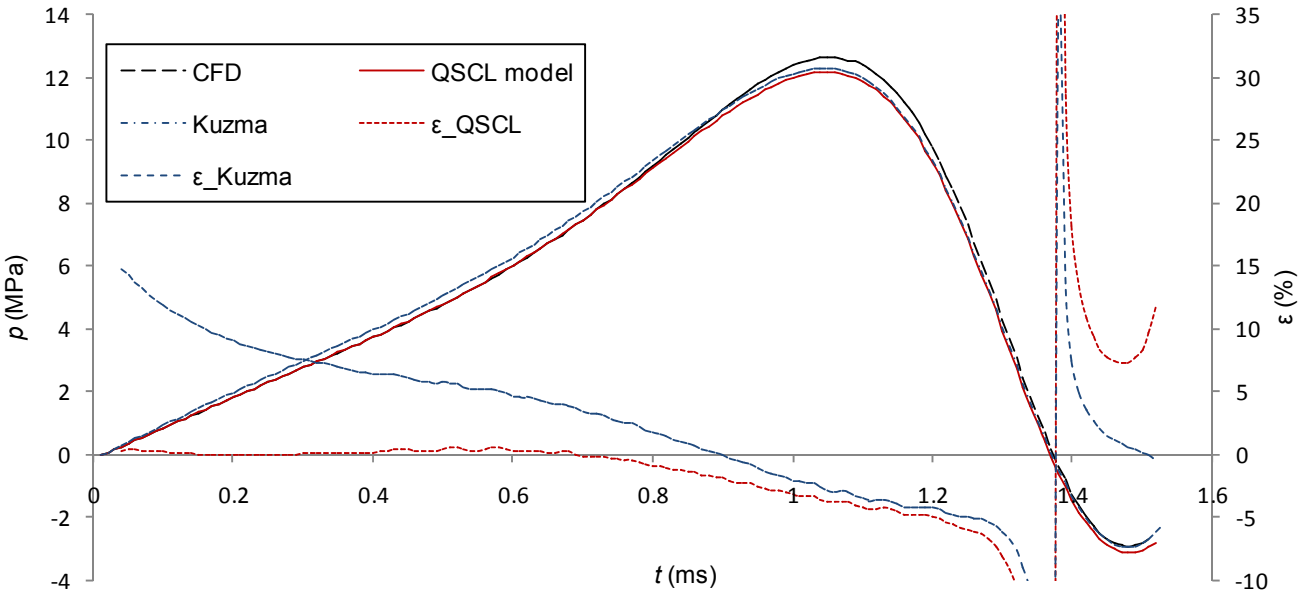


Figure 6-13: Central pressure traces of CFD, Kuzma's approximation and the QSCL model traces vs time

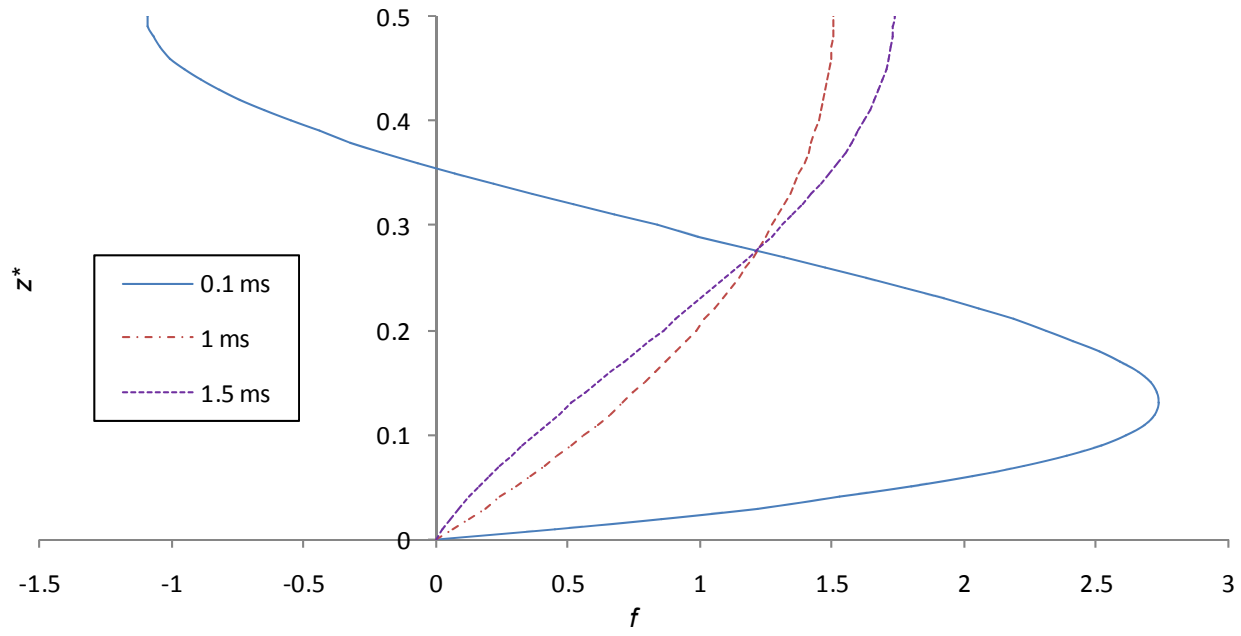


Figure 6-14: Dimensionless radial velocities of Kuzma's approximation at time instants **A**, **B** and **C**

## 6.5 Symmetrical versus Asymmetrical Squeezing Motions

Spatial inertia is the only pressure development parameter that is affected by symmetrical or asymmetrical squeezing motions (Section 2.1.2, p.3). This can be seen by in equation (5-10), p. 23, in which term $D_2^{'}$ is the only term that incorporates the dimensionless axial coordinate $z^*$.

The differences in central pressure traces resulting from symmetrical and asymmetrical squeezing motions for highly transient squeeze flows are currently not quantified. Therefore, an additional CFD simulation is set up which is identical to the hypothetical experiment (Section 6, p. 47) apart from incorporating an asymmetrical as opposed to a symmetrical squeezing motion.

Figure 6-15 shows the resultant central pressure traces of the top and bottom discs of the asymmetrical squeezing motion experiment, in addition to that of the symmetrical squeezing motion experiment

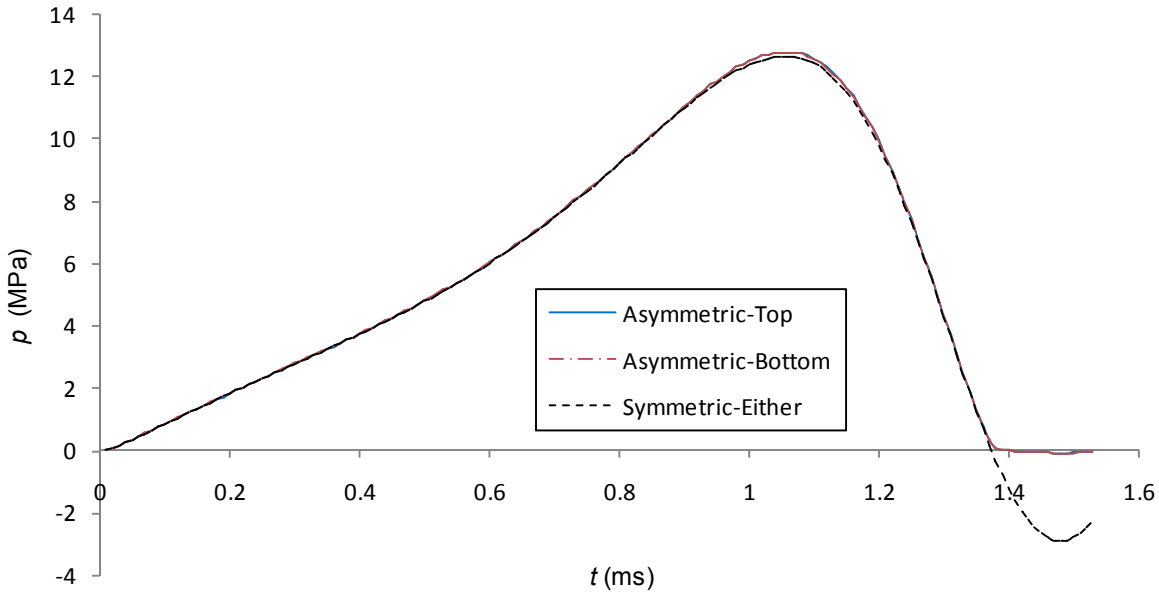


Figure 6-15: Resultant pressure traces of asymmetrical and symmetrical squeezing systems

Considering positive pressures, $t < 1.35$ ms, all three pressure traces in Figure 6-15 are visually so similar that they appear as a single curves. However, it can be shown numerically that the discrepancies between the top and bottom asymmetric pressure traces lie within $\pm 1\%$ of each other throughout significant positive pressure developments, $0.05 < t < 1.35$ ms, with only a 0.1% discrepancy during the major pressure spike: This value is in agreement with that predicted by Phan-Thien's transmission loss,

equations (2-30a, b), p. 17. On close examination of Figure 6-15 it can be seen that the symmetrical central pressure trace lies marginally below (less than 1.5%) both top and bottom asymmetric central pressure traces during the major pressure developments. Hence from this CFD comparison it can be inferred that symmetrical and asymmetrical squeezing motions experiments negligibly different pressures (pressure gradients) for positive pressures.

Now considering negative pressures, $t > 1.38$ ms (Figure 6-15), it can be seen that the symmetrical squeezing motion central pressure traces appears to continue along the trend established by positive pressure traces to reach a minimum pressure of about -3 MPa. However, both the asymmetric squeezing motion central pressure traces appear discontinuous and form a negligible pressure plateau; this result is clearly erroneous and is speculated to be a CFD error.

Therefore, the resultant pressure traces obtained from *asymmetrical* squeezing motion *experimentation* may be *approximated* as *symmetrical* squeezing motion *experimentation*. Hence, *asymmetrical* squeezing motion *experimental* results may be directly compared against *symmetrical* squeezing motion *theory*.

The ‘Asymmetric squeeze’ Excel spreadsheet used to develop Figure 6-15 is given in CD-Appendix B.

# 7 EXPERIMENTATION

The theoretical models derived for highly transient axi-symmetric squeeze flows (Section 0, p.19) are shown to be accurate when compared against hypothetical squeeze flows as modelled by CFD (Section 6, p. 47). It is ultimately intended to compare the theoretical models against experimental results; in order to achieve this aim, experimentation is planned and conducted as defined and elaborated upon within this chapter.

## 7.1 Experimental Planning

Recalling Section 1, p. 1, two test categories are proposed for experimentation:

i. Drop-hammer tests, where a drop-hammer is dropped from a predetermined height onto the upper disc that is initially separated from its stationary lower counterpart.
ii. Contact-hammer tests, where the drop-hammer is initially in contact with the upper disc that is initially separated from its stationary lower counterpart.

Drop-hammer tests are used to induce highly transient axi-symmetric squeeze flows and are classified as *constant energy squeeze flows* [Section 3, p. 18]. On the other hand, contact-hammer tests are expected to follow traditional 'creeping' axi-symmetric squeeze flow experimentation and thus yield viscous dominated results.

Test results are intended to show the following:

a. Experimental consistency of tests, and if adequately repeatable:
b. Trends of experimental variables with varying parameters.

Corresponding to point (a), each test is to be repeated a minimum of five times in order to establish test consistency. Henceforth sets of five or more identically repeated tests are called *test-sets*. Corresponding to point (b), assuming the test results are adequately repeatable, tests-sets are conducted at varied parameters which include:

i. Drop mass $M$ (kg).
ii. Initial disc separation $h_0$ (mm).
iii. Drop height $H$ (mm). Contact-hammer can be considered a special case of drop-hammer test where $H = 0$ m.

In order to establish trends of experimental variables with varying parameters, a minimum of say five test-sets per parameter is required. Hence a complete parametric space would require a minimum of 5 (tests/test-set) $\times 5^3 = 625$ tests; this parametric space is visually represented as the rows, columns and depth of a three dimensional matrix in Figure 7-1, in which each test-set is represented by a cube.

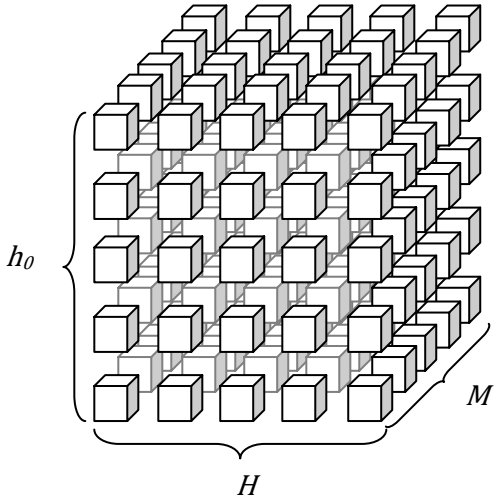


Figure 7-1: Complete experimental parametric space representation

This above complete parametric space (Figure 7-1) would not only be experimentally intensive to achieve, but would also yield protracted and tedious experimental results if represented in full.

Alternatively, if a single parameter is varied whilst the other two are kept constant, the resultant experimental variable trends are isolated for that particular varied parameter. These resulting trends may be represented by a single set of plots. Since this approach requires substantially less testing, the number of test-sets per varying parameter may be increased from five to, say ten; the result of which is a more accurate trend establishment.

Preceding these so-called *varying parameter* plots, a single test is proposed to be analysed in extensive detail. This so-called *reference test* is to be specifically selected from all conducted tests so to best illustrate the features of highly transient axi-symmetric squeeze flows.

The increments in drop-mass are limited to the masses of manufactured weight plates of approximately 5 kg each. On the other hand, both the parameters of initial disc separation and drop height may be varied

between the values of $0 < h_0 \leq 18$ mm (test cell limitation) and $0 < H \leq 3.5$ mm (ceiling height) respectively.

The planned parameter increments of all three parameters are given in Table 7-1 with the shaded blocks representing the values at which two of the parameters are fixed while the third is varied. Hence Table 7-1 gives the planned test-sets for drop-hammer tests and consists of a minimum of {5 (tests/test-set) × [10 ($M$ variation) + 10 ($H$ variation) + 8 ($h_0$ variation)]} = 140 tests. In addition a single contact-hammer test-set is performed (Section 7.3, p.80).

Table 7-1**:** Planned parameter variations.

| **Test number** | **Drop Mass (kg) $\pm 0.5$ kg** | **Drop Height (mm)** | **Initial Disc Separation (mm)** |
|---|---|---|---|
| 1 | 10 | 100 | - |
| 2 | 15 | 200 | - |
| 3 | 20 | 300 | 3 |
| 4 | 25 | 400 | 4 |
| 5 | 30 | 500 | 5 |
| 6 | 35 | 600 | 6 |
| 7 | 40 | 700 | 7 |
| 8 | 45 | 800 | 8 |
| 9 | 50 | 900 | 9 |
| 10 | 55 | 1000 | 10 |

## 7.2 Experimental Facilities

Experimental facilities consist of the drop-hammer test rig, the squeeze-flow test cell and various instruments. These facilities are discussed in the subsequent three sections.

### 7.2.1 Drop-hammer test rig

The test rig raises and drops the drop-hammer subassembly onto the squeeze flow test cell (Figure 7-2). This test rig effectively consists of the following components and subassemblies:

**Drop-hammer subassembly:** Comprises the hammer, nut and drop-weights. The drop-hammer is upwardly supported and axially guided by the *support frame*.

**Support frame:** Guides the drop-hammer along the *guide rails*.

**Guide rails:** Two solid Ø 50 mm steel bars (columns) secured to the floor and ceiling which guides both the *support frame* and *winch frame*.

**Winch frame:** Is winched up by the *motorised winch* and is latched to the support frame by the *latch release*.

**Motorised winch:** Elevates and lowers the *winch frame* (and *support frame* when latched onto the winch frame) with a 2:1 reduction pulley system.

**Pneumatic release latch subassembly:** Comprises the pneumatic cylinder and latch release. The latch releases the support frame (from the winch frame) when the pneumatic cylinder is activated, this is done when the operator throws the pneumatic release switch which is located 3 m away from the test rig (not shown in Figure 7-2).

**Shock absorbers:** Brings the *support frame* to a stop when impacted by the support frame's journal guides. This shock absorber system is constructed with re-enforced rubber tubing (Ø 50 mm I.D. and Ø 80 mm O.D.) which surround the *guide rails* and are externally supported by multiple (adjustable) pipe clamps.

**Safety arms:** Safety devices that pivot at the floor to make contact with the guide rails and hence prevent the support frame/drop-hammer from descending lower than a limiting safety height when the operator is working on the test cell.

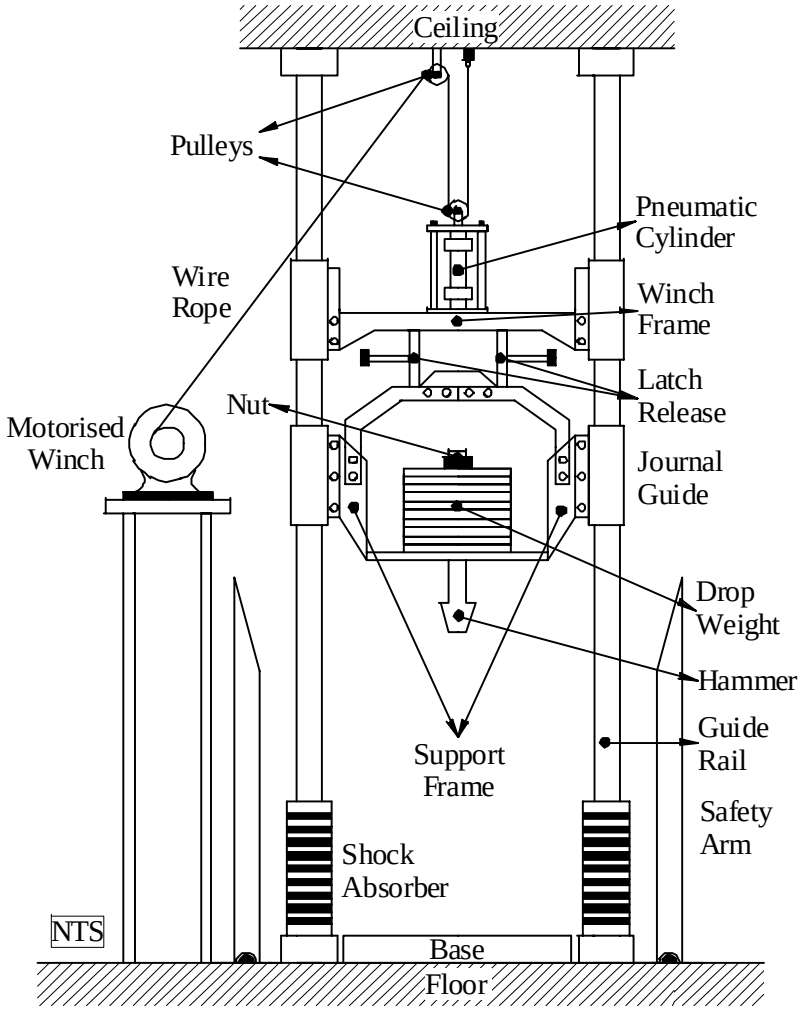


Figure 7-2: Test rig schematic (Courtesy of Mr. V Vythilingam)

The hammer protrudes through a hole in the cradle of the support frame, i.e. the drop-hammer subassembly is not fixed to the support frame (Figure 7-2). Instead, the lowest drop-weight contacts the cradle and thus axially supports the drop-hammer subassembly. Hence during a drop-hammer test, after the hammer makes contact with the test cell and begins to decelerate, the support frame continues falling until its journal guides contact the shock absorbers which stop its descent.

Although not shown in Figure 7-2, the entire test rig is housed within an expanded steel safety cage with an access door and hence is in compliance with health and safety regulations. This steel cage is used during drop-hammer tests.

## 7.2.2 Squeeze flow test cell

The test cell is the unit in which squeeze flows are induced and experimentally measured. Essentially this test cell assembly consists of four subassemblies as shown in Figure 7-3. In addition the front and right assembly diagrams and part lists are given on pages 70 and 71 respectively. The engineering drawing for the test cell components are available in CD-Appendix E.

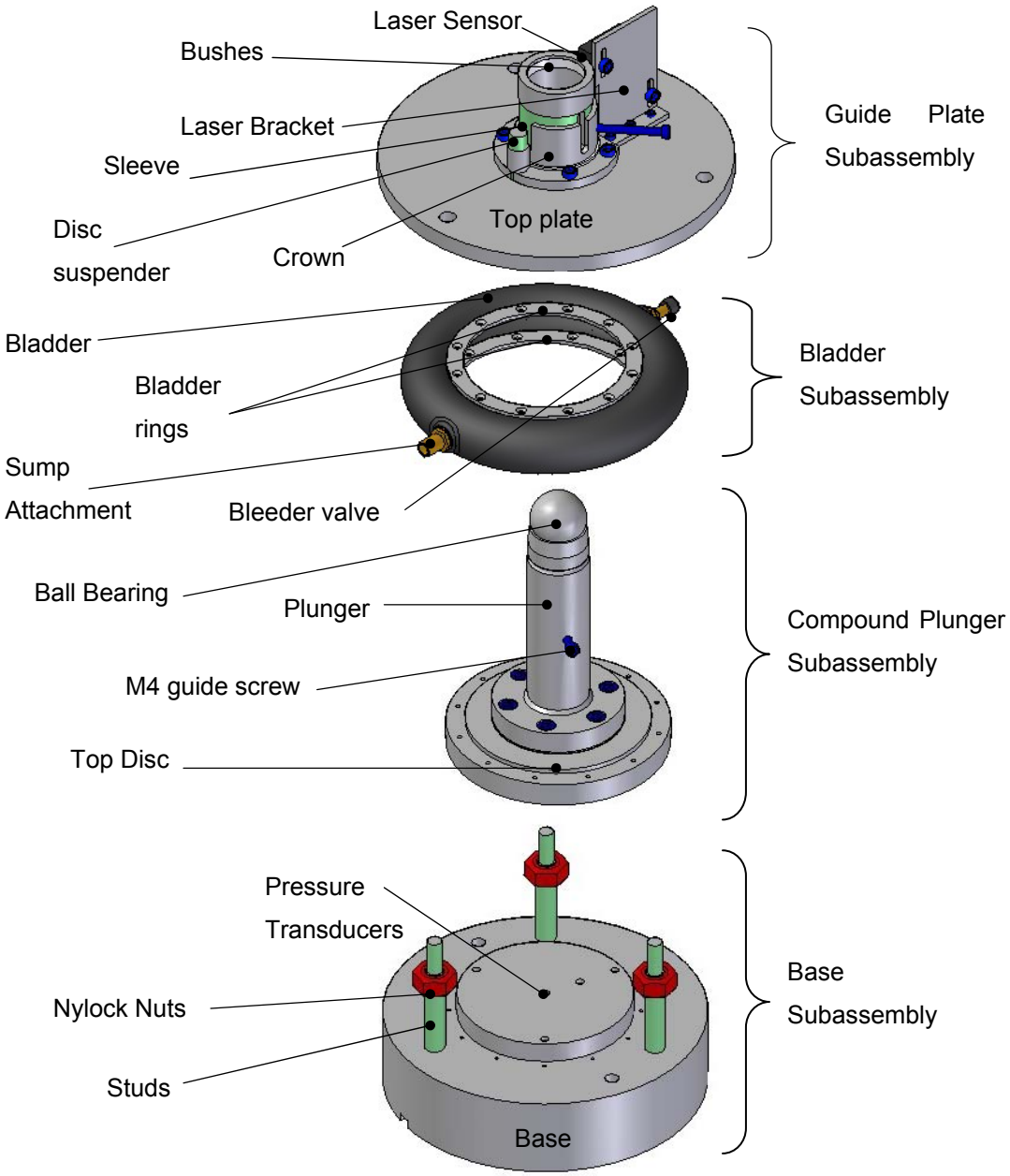


Figure 7-3: Four sub-assemblies of the test cell (CAD exploded views)

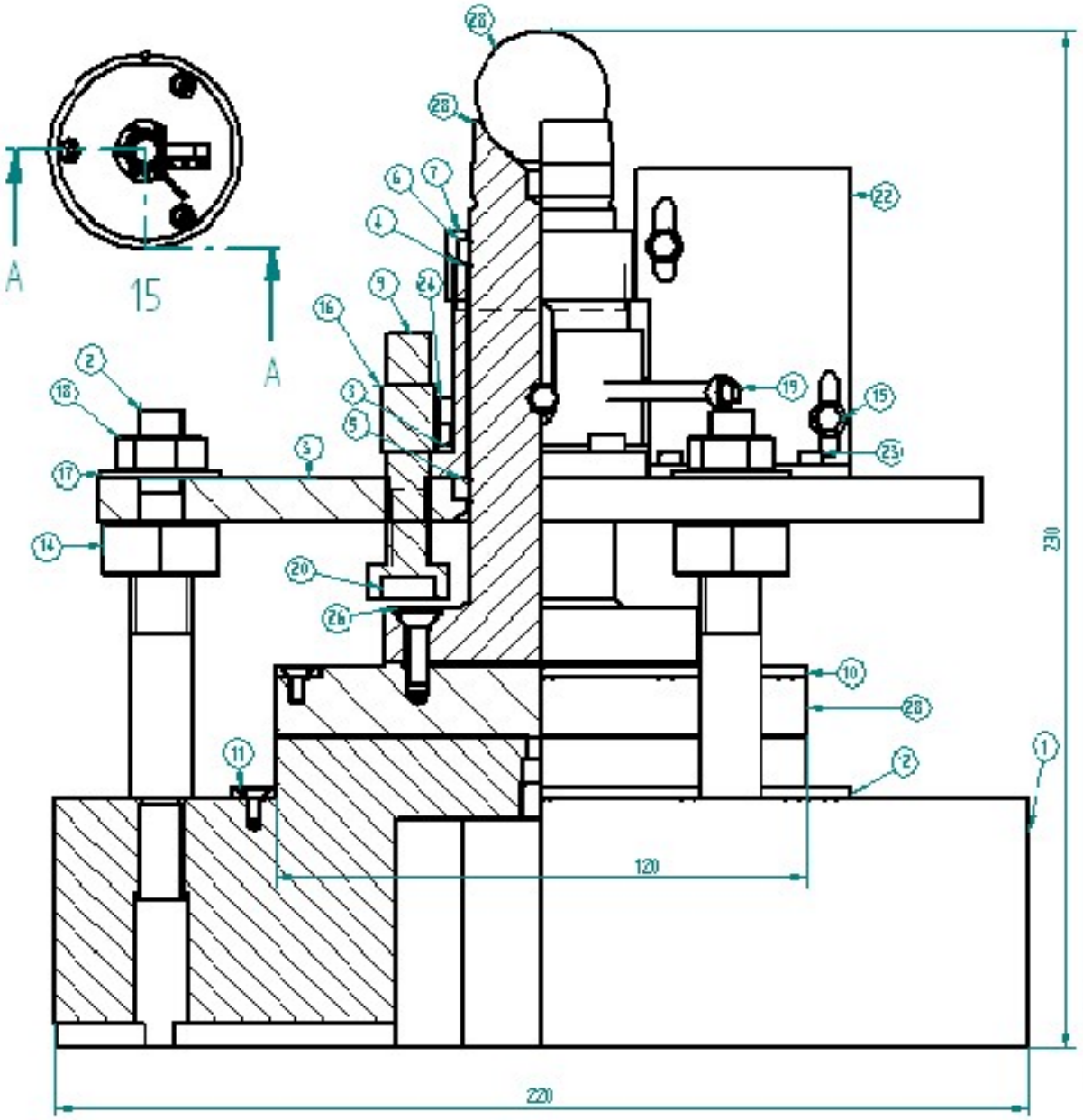


SECTION A-A

| Item Number | Title | Material | Quantity |
|---|---|---|---|
| 1 | Base plate | Mild steel | 1 |
| 2 | Stud | Mild steel | 3 |
| 3 | Top plate | Mild steel | 1 |
| 4 | Sleeve | Mild steel | 1 |
| 5 | Lower lash | Teflon | 1 |
| 6 | Upper lash | Teflon | 1 |
| 7 | Bush cap | Mild steel | 1 |
| 8 | Skin | Teflon | 1 |
| 9 | Disc separator | - | 1 |
| 10 | Top bladder retention ring | Mild steel | 1 |
| 11 | M3 countersunk screw | - | 24 |
| 12 | Bottom bladder retention ring | Mild steel | 1 |
| 14 | M14 air flight adjustment | - | 3 |
| 15 | M5 hex screw | - | 6 |
| 16 | Lock | Aluminium | 1 |
| 17 | M10 washer | - | 5 |
| 18 | M10 nut | - | 3 |
| 19 | M4 hex/Crowe lock & lever | - | 1 |
| 20 | Magnetic clip | - | 3 |
| 21* | Laser Position Sensor | - | 1 |
| 22 | Laser sensor bracket | Mild steel | 1 |
| 23 | M3 hex screw | - | 3 |
| 24 | Crowe | Mild steel | 1 |
| 26 | M5 hex screw | - | 6 |
| 27* | Rubber Bladder | | 1 |
| 28 | | | 1 |

| | NAME |
|---|---|
| DRAWN | ALEXIS BRASSINOS |
| SUPERVISOR | PROF. C.A. RIGS |
| APPROVED | PROF. C.A. RIGS |
| DATE | 22/07/2005 |

UNIVERSITY OF THE WITWATERSRAND

TITLE: ASSEMBLY-RIGHT

PROJECT: AIRBAG TRANSIENT SURFACE PRESSURE

SIZE: A3 MATERIAL: -

QUANTITY: 1

SCALE: 1:1 WEIGHT: DWG NO:

| Item Number | Title | Material | Quantity |
|---|---|---|---|
| 1 | Base plate | Mild steel | 1 |
| 2 | Stud | Mild steel | 1 |
| 3 | Top plate | Mild steel | 1 |
| 4 | Sleeve | Mild steel | 1 |
| 5 | Lower bush | Teflon | 1 |
| 6 | Upper bush | Teflon | 1 |
| 7 | Bush cap | Mild steel | 1 |
| 8 | Skin | Teflon | 1 |
| 9 | Disc separator | - | 1 |
| 10 | Top bladder retention ring | Mild steel | 1 |
| 11 | M3 countersunk screw | - | 1 |
| 12 | Bottom bladder retention ring | Mild steel | 1 |
| 13 | Fluid bladder | Rubber | 1 |
| 14 | Brass washer | Brass | 1 |
| 15 | M10 "S brass nut | Brass | 1 |
| 16 | Hose attachment | Brass | 1 |
| 17 | Air valve | Brass | 1 |
| 18 | Air valve cap | - | 1 |
| 19 | M14 nut (light adjustment) | - | 1 |
| 20 | M5 hex screw | - | 1 |
| 21 | Lock | Aluminium | 1 |
| 22 | M10 washer | - | 1 |
| 23 | M10 nut | - | 1 |
| 24 | M4 hex (Crow lock & lever) | - | 1 |
| 25 | Magnetic clip | - | 1 |
| 29 | Crow | Mild steel | 1 |
| 30 | Plunger base | Mild Steel | 1 |
| 31 | Plunger | EN-8 steel | 1 |
| 32 | M5 hex screw | - | 1 |
| 33 | Ball bearing | - | 1 |

| | NAME |
|---|---|
| DRAWN | [illegible] |
| SUPERVISOR | PROF. C.A. RUSS |
| APPROVED | PROF. C.A. RUSS |
| DATE | [illegible] |

UNIVERSITY OF THE WITWATERSRAND

TITLE: ASSEMBLY-FRONT

PROJECT: ANKLE TRANSKEFT SHOCK ABSORBERS

SIZE: A3 | MATERIAL: -

QUANTITY: 1

SCALE: 1:1 | WEIGHT: | DWG. NO.

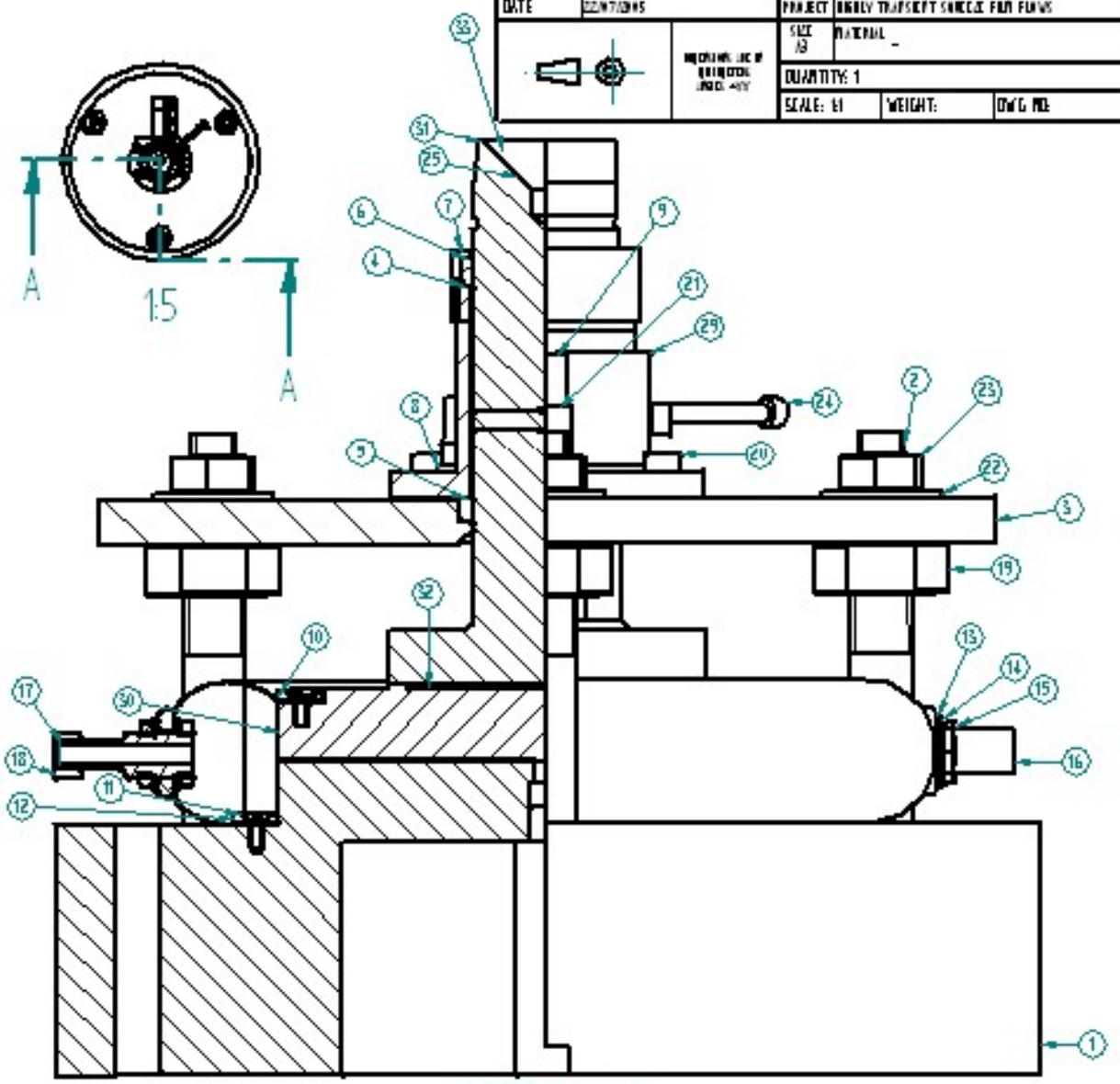


SECTION A-A

Although the assembly and operation of the test cell is relatively self explanatory, key design features of the above four sub-assemblies are given as follows:

## Base subassembly

- The base is bolted directly to the base of the test rig (Figure 7-2).
- The base (of which the bottom disc is a constituent) is manufactured from a single piece of steel to maximise rigidity.
- Pressure transducers are screwed directly into the base so that their diaphragms are flush (or slightly receded) from bottom disc face.
- Nylock nuts are used to adjust the alignment of the top plate which in turn aligns the top disc, in order that any manufacturing deviations can be corrected for.

## Compound plunger subassembly

- The components of the compound plunger subassembly and the bladder (including its top ring) are the only components that move axially during an experimental stroke.
- A compound, as opposed to a simple plunger, was designed as to maximise the specific rigidity of the top disc. Retrospective calculations (using the maximum experimental pressures) show a maximum axial flexure of 45 μm at 25 MPa is induced (liberal calculations); refer to Appendix E for calculations of flexure due to pressure and inertia.
- The ball bearing on top of the plunger is used to transmit the force applied by the drop-hammer directly (axially) downwards[a].
- The top of the plunger's shaft is uniquely shaped in a way to minimise (negate) the 'mushrooming' of the top of the shaft (like the anvil of a used chisel).
- The M4 guide screw (inserted through the axial slot in the sleeve and screwed radially into the plunger's shaft) is used tangentially restrain the plunger. It also allows the user to load the test-cell, i.e. separate the discs (subsequently discussed in Section 7.3, p. 80)

[a] Preliminary testing used a flat topped plunger, which resulted in highly eccentric pressure distributions. This in turn prompted the development of the eccentric paraboloid distribution theory and axi-symmetric corrective data processing; refer to Section 5.12, p. 42 and Section 7.5.2, p. 86 respectively.

### Bladder subassembly

- The bladder is made of flexible rubber and contains the working fluid between the top disc and the base. A rubber inner tube (Ø 200 mm O.D. and tube Ø 50 mm) is used to fabricate the bladder.
- Both of the bladder ring basses are bonded to the fluid bladder (contact adhesive). In this configuration when the bladder ring bases are fastened to the top disc and the test cell base (with twelve countersunk M3 screws for each seal) the bladder itself becomes a self sealing gasket.
- The sump attachment attaches the fluid bladder to an elevated fluid sump via flexible rubber or silicon tubing (see below).
- The bleed valve is used to fill/empty the fluid bladder (Section 7.2.4, p.77) and bleed out any air/air bubbles in the working fluid.

### Guide plate subassembly

- Although not visible in the above figures, the laser sensor measures the displacement of the top disc through a slot cut in the top plate.
- Also not discernable from the above figures, the crown is able to rotate around the sleeve if unimpeded by the guide screw, i.e. if the guide screw (and therefore the plunger subassembly) is sufficiently elevated.
- The M4 lever screw (screwed radially into the crown), is used as a lever to rotate the crown for contact-hammer tests and to lock the crown in position for drop-hammer tests (elaborated upon in Section 7.3.1, p.80).

It can be seen from the above figures that the test cell induces an asymmetric as opposed to a symmetric squeeze flow as elaborated upon in Section 6.5, p. 63.

### Sump subassembly

The fluid sump is an inverted 1.5 ℓ plastic bottle with a hole cut into its base as shown in Figure 7-4. The cap of the bottle is modified to be attached to flexible rubber or silicon tubing which in turn attaches to the sump attachment of the bladder subassembly (Figure 7-3). This sump is clamped onto a clamp stand,

this arrangement allows the sump to be raised or lowered and thus vary the ambient pressure within the bladder.

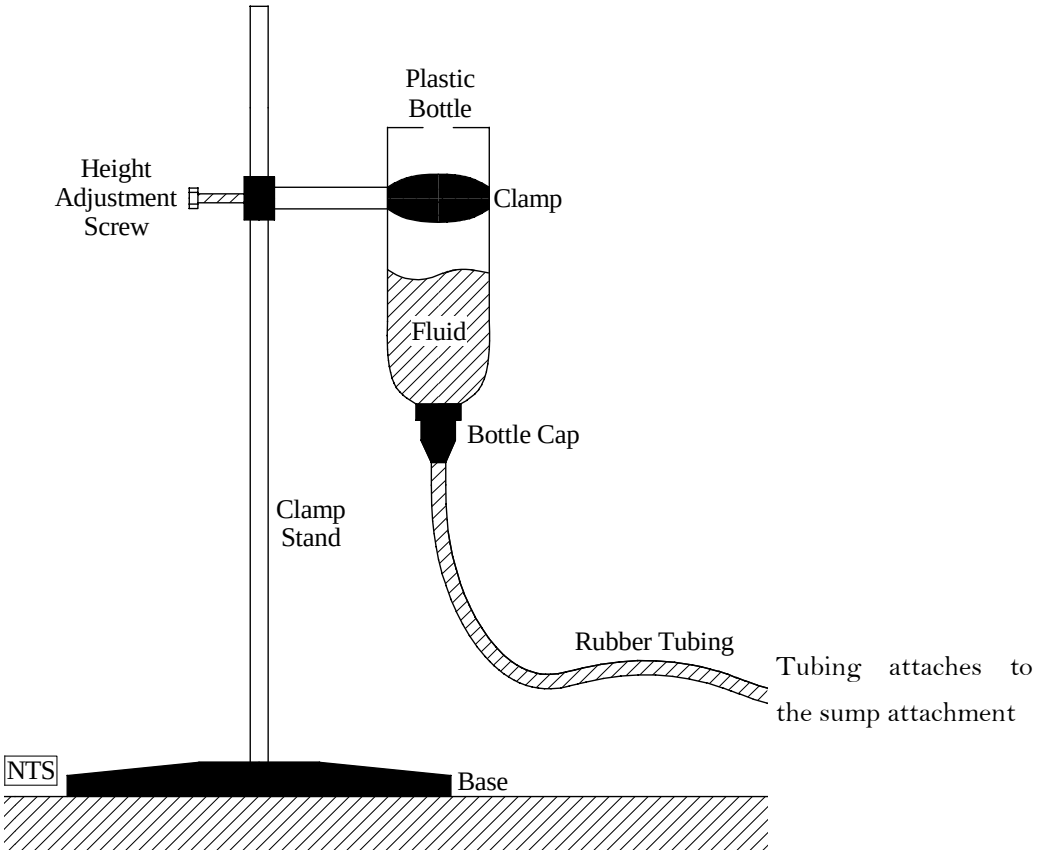


Figure 7-4: Sump subassembly schematic (courtesy of Mr. V Vythilingam)

## 7.2.3 Instrumentation

**Pressure Transducers:** Five pressure transducers are inserted into the test cell base. PCB PIEZOTRONICS pressure transducers are used; model 113A23 are used for the three outermost transducers and M109B12 models are used for the two inner transducers (Figure 7-7, p. 90). See Section 7.5.1, p. 84 for calibration coefficients and see Appendix G for pressure transducer specifications.

**Pressure transducer cables:** PCB PIEZOTRONICS coaxial cables are used to connect the pressure transducers to their respective signal conditioners.

**Signal conditioners:** PCB PIEZOTRONICS units amplify the voltage outputs of the pressure transducers. A dial indicator on the front panel of the signal conditioners indicates the incoming signal 'quality' from the transducers, i.e. whether the pressure transducers are operational or not.

**Laser displacement sensor:** This sensor measures the disc separation trace of the plunger ($h$ vs $t$). A KEYENCE LB12 sensor head with LB72 controller are used for this purpose (Appendix H). A laser sensor is used as opposed to a Linear Variable Differential Transformer (LVDT) due to its higher response frequency.

**DC power supply:** The laser sensor requires an external power supply of 12-24V DC. A LOADSTAR DC power supply, model PS-3030 is used for this purpose.

**PCP cables:** Coaxial PCP cables are used to connect the signal conditioners and the laser sensor controller to the multi-channel oscilloscope.

**Multi-channel digital oscilloscope:** A multi-channel digital oscilloscope is used to store the experimental output voltages from the pressure transducers and the laser sensor which are later transferred to computer for data processing. In addition this oscilloscope provides the user with experimental observation by displaying the output traces of the experimental stroke on its LCD screen. A Yokogawa DL708E 8CH DIGITAL SCOPE is used for this purpose.

**Tape measure:** A tape measure is required to measure the drop height. This measurement is taken between the height of the drop-hammer base and the top of the ball bearing at *zero disc separation*. The housing of the tape measure is fastened to a shock absorber of the test rig (using cable ties) and the end of the tape is secured to the journal guide of the winch frame (using tape) (Figure 7-2).

**Thermometer:** A thermometer is required for fluid temperature measurements at the time of experimentation (in order to calculate the viscosity). The thermometer is placed in the fluid sump: It is assumed that the difference in temperature between the fluid in the sump and the fluid bladder is negligible.

**Clamp stand:** A clamp stand is used to grip and adjust the elevation the fluid sump (Figure 7-4).

**Verniers:** Verniers are used to set the initial disc separation to a predetermined level.

## 7.2.4 Experimental setup

The test cell is set up by performing the sequential operations discussed in the following subsections.

### Pressure transducer insertion

Pressure transducers are inserted into the base of the test cell and sufficiently tightened (with a socket spanner) so not to loosen due to vibrations during experimentation. The pressure transducer diaphragms must not protrude from the bottom disc face, nor must they recede more than 0.05 mm from the disc surface.

To check for diaphragm protrusion, a razor blade is glided along the disc surface (as if shaving the disc). On the other hand, the base of the verniers is used to measure the recession of the pressure transducer's diaphragm. If a diaphragm protrudes from the disc surface a PCB PIEZOTRONICS brass washer is inserted between the seat of the pressure transducer and that of the test-cell base. The thickness of this washer may be reduced by rubbing it against glass paper with a finger (whilst regularly checking its thickness with verniers). Hence the correct seating tolerance of the pressure transducer may be achieved using the above techniques in an iterative fashion.

Pressure transducer cables are now attached to the pressure transducers in the base of the test cell and to the respective signal conditioners. Proper connection is checked by the output given on the signal conditioner dials and the live feed output on the oscilloscope when pressure is applied to the pressure transducer diaphragms with a finger.

### Test cell assembly

The test cell now is assembled as shown in the above assembly diagrams on pp. 70-71 with the exception that the fluid bladder subassembly is not attached. All dynamic test cell components are well lubricated with grease before assembly. Furthermore, the sump is assembled as shown in Figure 7-4 but is not yet attached nor filled.

## Disc alignment

To accurately align the discs, the following procedure is carried out:

i. The discs are separated.
ii. Three small pieces of tissue paper (~1 $cm^2$) are placed across the bottom disc circumference at equal radial spacing (~120˚).
iii. The discs are mated under no additionally applied load.
iv. The pieces of tissue paper are radially pulled and so that they are either torn or slip out from between the discs. In this way the level of the top disc can be inferred.
v. The top disc level is adjusted according using the nylock nuts (Figure 7-3).
vi. Steps 1-5 are repeated until all three tissue papers tear when pulled.

This procedure should result in an alignment tolerance of less than 25 μm at the disc circumference (measured by pulling a piece of tissue paper gripped with the verniers).

## Zero disc separation measurements

Before the fluid bladder is filled, the output voltage of the laser displacement sensor at zero disc separation is measured: This ensures that a fluid film is not responsible for an erroneous zero disc separation measurement (it is assumed that an air film is of negligible thickness).

This zero disc separation measurement is made by mating the aligned discs under an applied load (~20 kg applied to the plunger) and recording the output voltage measured by the laser sensor and displayed on the oscilloscope. This so-called 'grounded voltage' is determined at $V_{h_0} = 6.08$ V for the presented work, however this value will vary with experimental setups (positioning of components). Furthermore, in this zero disc separation configuration, the disc suspender is screwed down to its lowest position to make contact with the plunger. The verniers are then used to measure the protrusion height of the disc suspender from the top plate; this measurement is recorded and is used later in determining the initial disc separations for drop-hammer testing as later discussed in Section 7.3.2, p. 81.

## Bladder installation

The guide plate subassembly is then removed from the test rig assembly and the bladder subassembly is attached to the base attached with twelve M3 countersunk screws. Similarly the bladder is then attached to the top disc of the plunger subassembly. The guide plate subassembly is then replaced.

## Fluid bladder filling

The test cell is then attached to the sump subassembly as indicated in Figure 7-4. In order to fill the fluid bladder the procedure below is followed:

i. The test cell is placed on its side on the ground so that the bleed valve points upwards.
ii. The discs are separated (disc suspender is unscrewed) and the bleed valve cap is removed.
iii. The empty sump is lowered to its lowest position on the clamp stand.
iv. Approximately 1.5 $\ell$ of working fluid is gently poured into the top hole of the sump as to minimise the amount of air bubbles incurred by the pouring process. In this configuration the equilibrium level of fluid in the sump should be lower than the top of the bleed valve.
v. The sump is then raised to a position in which the fluid in the sump is at the same level, or marginally below the bleed valve level.
vi. This configuration is left until all the air bubbles in the bladder have diffused out of the fluid. If a viscous working fluid is being used (glycerine, say), this process may take several hours.
vii. The bladder is gently squeezed (i.e. fluid is slowly squeezed out of the bleed valve) at the same time the bleed valve cap is screwed onto the bleed valve to ensure no air bubbles are trapped in the bladder.

## Test cell installation

The pressure transducer wires are taped together and then taped within the radial slot in the base of the test cell (Figure 7-3): This ensures that the wires are not crimped between the base of the test rig and that of the test cell when placed in position.

The test cell is then secured to the centre of the test rig base with two M10 bolts and the thermometer is places in the fluid sump.

Finally the laser sensor and the pressure transducer wires are connected to the other instrumentation as previously elaborated upon in Section 7.2.3, p.75.

**Precautions:** During the test cell installation, when the operator must physically position him/herself (limbs) under the drop-hammer to position and secure the test cell, the safety arms are employed. This involves the following operations:

i. Elevating the drop-hammer (via winch) to about 5 cm above the safety arm level.
ii. Lowering the safety arms into position (contacting against the guide rails), i.e. the safe position.

Photographs of the above test cell setup procedures were taken and are shown in CD-Appendix F.

## 7.3 Procedure and Precautions

Many of the following operations refer to specific test rig and test cell components; hence it is assumed that the reader is familiar with Figures 7-2, 7-3 and the assembly diagrams on pp. 70-71. The methodology adopted for conducting experiments is elaborated upon in the following subchapters.

### 7.3.1 Contact-hammer testing procedure

For contact-hammer tests, the disc separator is removed from the test cell. Thereafter the procedure is as follows:

1. The oscilloscope is setup to record pressure transducer output voltages of about 0.01 V and a disc separation voltage difference of about 7 V (offset depends on setup), with an associated stroke period of ~100 ms. Setting up the oscilloscope is an iterative procedure and may require several preliminary tests before the captured data is satisfactory.
2. The fluid temperature is recorded.
3. The drop-hammer is loaded up to its full load of approximately 55 kg by loading the drop-hammer assembly with all ten plates. The nut must be securely tightened with a spanner so that the drop-hammer subassembly can be considered a homogenous mass.
4. The drop-hammer is winched up approximately 50 mm above the ball bearing (plunger subassembly).

5. The test cell is ‘loaded’ This procedure entails the following operations:
    a. Levering the M4 guide screw (and therefore the plunger subassembly) upwards against the top disc (a M10 Allen-key works well for this operation); this operation overcomes the negative force generated by the reverse squeeze flow. The guide screw is further elevated to above the top ridge of the crown.
    b. Rotating the crown (with the lever screw) and then releasing or lowering the guide screw: This positions the guide screw on ridge (top) of the crown and hence axially restrains the plunger into position. Only the maximum disc separation of 18 mm is used for contact-hammer tests, for reasons elaborated upon in Section 8.2, p.116.
6. The drop-hammer is lowered (winched) onto of the ball bearing (plunger subassembly). The drop-hammer is now radially but not axially supported by the support frame.
7. The stroke is initiated by rotating the crown (with the lever screw) so that the guide screw falls into its slot.
8. The resultant output voltages of the pressure transducers and the laser sensor are checked for consistency on the oscilloscope. If an experiment was found to be inconsistent, the experimental trace is saved but an additional set is added to the test-set.
9. Steps 1-9 are repeated until the contact-hammer test-set is completed.

### 7.3.2 Drop-hammer testing procedure

For drop-hammer tests, the disc separator is replaced (after completion of the contact-hammer test-set) and the crown’s lever screw is tightened. It acts like a grub screw and thus secures the crown into position during testing, i.e. makes the crown superfluous during drop-hammer tests.

1. The oscilloscope is setup to record pressure transducer output voltages ranging between 0.04 V and 0.4 V (dependant on parameters) and a disc separation voltage difference of about 4 V (offset depends on setup), with an associated stroke period of about 10 ms. Setting up the oscilloscope is an iterative procedure and may require several preliminary tests before the captured data is satisfactory.
2. The fluid temperature is recorded.
3. If necessary, the drop-hammer is reloaded to its designated mass by adding or removing plates to the drop-hammer assembly. The nut must be securely tightened with a spanner so that the drop-hammer subassembly can be considered a homogenous mass.

4. The drop-hammer is winched to approximately 50 mm above the ball bearing (plunger subassembly).
5. If necessary, the initial disc separation is adjusted, this procedure entails the following operations:
    a. Un-tightening the disc suspender lock so that the disc separator may be adjusted.
    b. Adjusting (screwing/unscrewing) the disc separator to increase or decrease the initial disc separation.
    c. Measuring the protrusion height of the disc separator with the verniers and subtracted from the zero disc separation measurement (Section 7.2.4, p.77) to obtain the initial disc separation value. Hence through an iterative process of Steps 5b and c, the initial disc separation can be set.
    d. Re-tightening the lock: This ensures that the disc separator does not move due to test cell vibrations.
6. The test cell is 'loaded', this procedure entails the following operations:

    Levering the M4 guide screw (attached to the plunger subassembly) upwards against the top disc (an M10 Allen-key works well for this operation); this operation overcomes the negative force generated by the reverse squeeze flow. The guide screw is further elevated until the plunger makes contact with the magnetic clip and is hence 'latched' into position.
7. The drop-hammer is then further winched to its designated drop height.
8. The experimental stroke is initiated by throwing the pneumatic release switch.
9. The resultant output voltages of the pressure transducers and the laser sensor are checked for consistency on the oscilloscope. If an experiment was found to be inconsistent, the experimental trace was still saved but an additional set was added to the test-set.
10. Steps 1-9 are repeated until all test sets as outlined in Table 7-1 and the associated text are completed.

## Precautions

Although omitted from the above drop-hammer test procedure, the safety cage (Section 7.2.1, p. 68) is used during drop-hammer tests for specific health and safety requirements. A safety cage or similar device is recommended if these drop-hammer tests are to be replicated. Moreover, it is recommended that hearing protection be used during experimentation.

## 7.4 Observations

Due to the brief experimental stoke periods of $T < 10$ ms for drop-hammer tests and $T < 10$ ms for contact-hammer tests, direct physical experimental observations are unattainable. However, it was noted that directly after drop-hammer experimental strokes, the drop-hammer would bounce back off the top of the plunger (like a bouncing ball) before proceeding to impact the plunger again. This post-experimental bouncing was not quantified but visually ascertained and heard by a secondary metallic thud after the initial impact. Furthermore, it was noted that the impact region of the drop-hammer plastically deformed (dented) after drop-tests.

During experimentation, the temperature was noted to fluctuate between the narrow range of 18±1˚C[a]

Figure 7-5 show the voltage traces for a typical drop-hammer test (the reference-test) as viewed on the oscilloscope during testing.

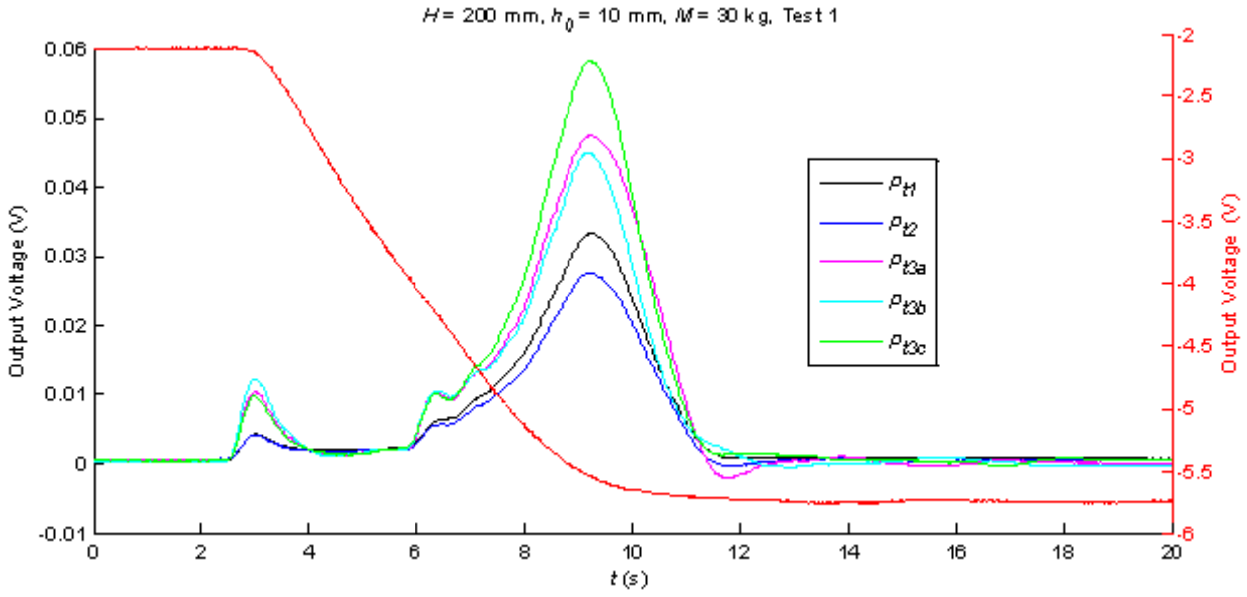


Figure 7-5: Output voltage traces (reference experiment)

The output voltages from the pressure transducers are given on the left-hand scale of Figure 7-5 while the output voltage from the laser sensor is given on the secondary right-hand axis in red (due to the

[a] For the purposes of error analysis, the viscosity change due to temperature fluctuation is investigated.

differences in voltage magnitudes). The oscilloscope used during experimentation allowed the user to scale (magnify) the output voltages and hence view all six of the above traces on the same set of axes. Furthermore, this function allowed the output voltages of the pressure transducers to be scaled (roughly calibrated) to yield the approximate pressure scaling relative to each other, i.e. roughly normalise pressures. During experimentation, these experimental observations were important to allow the operator to visually compare traces of repeated tests within test-sets and in so doing, identify and make note of the outlying test/s and repeat more tests if necessary.

## 7.5 Data Processing

Experimental data was saved on the oscilloscope and transferred to computer. These data are given in CD-Appendix B in a MATLAB format; the tests are appropriately named with a nomenclature, an example of which is given as follows:

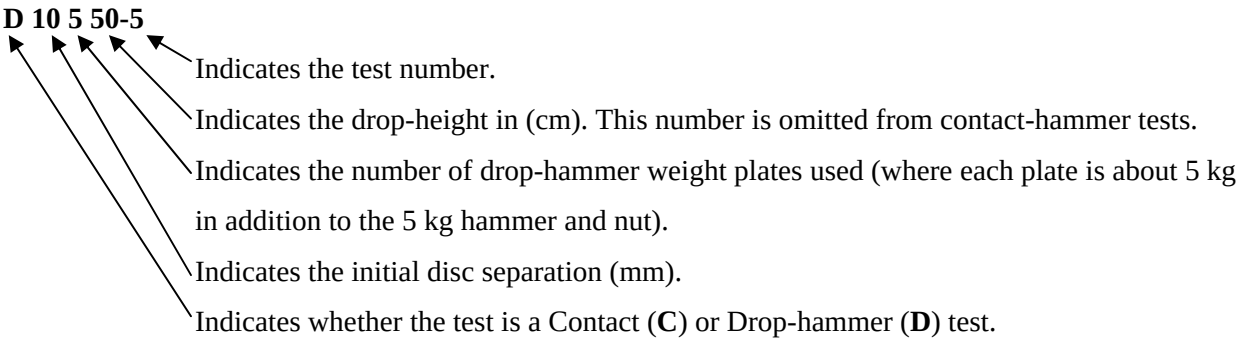


### 7.5.1 Elementary operations

Although elementary, the following data processing operations discussed in within this section are relatively abstract when viewed in isolation from the results (processed data). Therefore, it is recommended that the reader proceeds to Section 7.5.2, p. 90, and refers to this section when additional information of the stated data processing operation is required.

The following elementary data processing operations are carried out within the MATLAB ‘Process’ program (CD-Appendix B):

## Calibration

The pressure transducers are inter-calibrated against a new, factory calibrated pressure transducer. Inter-calibration involves the comparison of output voltages between the existing and new pressure transducers which all measure an impulsive pressure spike applied to the same body of fluid (this procedure is elaborated upon in Appendix F). The inter-calibration constants are given in Table 7-2.

Table 7-2: Pressure transducer information and calibration constants

| **Pressure transducer** | **Radial position (mm) and radial percentage (%)** | **Model** | **Serial number** | **Calibration constants (linear fit)** | | **Uncertainty bound coefficients [$\sigma$]** |
|---|---|---|---|---|---|---|
| | | | | **Gradient [$m$]** | **Intercept [$c$]** | |
| $p_{t1}$ | 0 (0%) | M109B12 | 3870 | 0.061 | 0.132 | 2000 |
| $p_{t2}$ | 27 (45%) | M109B12 | 3869 | 0.064 | 0.131 | 2000 |
| $p_{t3a}$ | 54 (90%) | 113A23 | 6707 | 0.063 | 0.993 | 200 |
| $p_{t3b}$ | 54 (90%) | 113A23 | 7933 | 0.067 | 0.981 | 200 |
| $p_{t3c}$ | 54 (90%) | 113A23 | 6706 | 0.055 | 1.065 | 200 |

The calibration coefficient of a given pressure transducer is given by

$$cal = (mV + c) \times 0.07282 \text{ V/MPa} \tag{7-1}$$

where $V$ is the pressure transducer's output voltage.

The calibration constant of the laser sensor set to 0.4 V/mm (Appendix H). This calibration was tested with verniers across its full range and shown to be accurate.

## Uncertainty bound calculations

It is empirically found that conservative uncertainty bounds coefficients, defined as ε, follow the relationship:

$$\varepsilon = cal \pm \frac{2V|_{\max}}{\sigma V} \tag{7-2}$$

where $cal$ is obtained equation (7-1) and $\sigma$ is obtained from Table 7-2 (refer to Appendix F for derivations).

## Smoothing

Second order low-pass digital Butterworth filters are used to smooth the raw data output voltages. A normalised cutoff frequency of 0.02 is used to smooth pressure traces and a normalised cutoff frequency of 0.005 is used to smooth disc separation, velocity and acceleration traces. These above filtering values are empirically selected and tested by superimposing the unsmoothed against the smoothed traces, where it is visually observed that the noise associated with the unsmoothed traces is eliminated by the filter but the dominant features remain visually unaltered (Appendix I).

## Stroke initiation/termination

The experimental stroke initiation and termination values are respectively taken when the pressure transducer measurement of $p_{t1}$ exceeds and fall below 2% of the maximum pressure.

## Pressure trace truncations

The pressure traces are truncated at 10% of the stroke length preceding the stroke initiation and at 1% of the stroke length after the stroke termination, see above. This relatively small value of 1% is used to eliminate the erroneous pressure traces associated with termination of the experimental stroke, see Figure 7-5.

## Normalised pressure distribution truncations

The normalised pressure distribution truncations are taken at the experimental stroke initiation and termination values (see above).

## Zeroing time

The time scale is shifted in such a way that zero-time corresponds to the experimental stroke initiation, (see above).

## Zeroing pressure

It can be seen in Figure 7-5 that the output voltages of the pressure transducers are not zero before the stroke initiation; hence the respective pressure transducer output voltages are offset to 0 V before the stroke initiation.

## Differentiation

The disc separation trace is differentiated with respect to time to yield the disc velocity. In turn, the disc velocity (after being smoothed, see above) is differentiated with respect to time to yield the disc acceleration. The MATLAB 'gradient' function is used to differentiate the above traces.

## Normalised parabolic pressure distribution constants

Theoretically a radial parabolic pressure distribution is invariably established [equation (5-9), p. 23]. The normalised parabolic pressure distribution constants are calculated as

$$p_{tn}/p_{t1} = \left(1 - r^{*2}\right), \tag{7-3}$$

so that $p_{t2}$ and $p_{t3}$ (see Table 7-2) are respectively calculated as follows:

i. $p_{t2}/p_{t1} = 0.798 \approx 80\%$
ii. $p_{t3}/p_{t1} = 0.19 \approx 20\%$.

## Normalised pressure distribution uncertainty bound calculations

The uncertainty bounds of the normalised pressure distribution values are calculated in a similar way in which the unprocessed normalised pressure distribution values are calculated. For example, the upper normalised pressure distribution uncertainty bound for $p_{t2}$ is calculated by dividing the upper uncertainty bound of $p_{t2}$ by the lower uncertainty bound of $p_{t1}$ and vice-versa.

## Inferred circumferential pressure offset

Assuming a parabolic radial pressure distribution is invariably established, the instantaneous resultant circumferential pressure $p_R$ may be inferred by fitting a second order, least-square polynomial fit to the instantaneous values of $p_{t2cor}$ (axi-symmetric corrected), and $p_{t3ave}$ (averaged) (later discussed in Section 7.5.2, p. 90) while fixing its value at $p_{t1}$ as shown in Figure 7-6. Thereafter, the instantaneous values of $p_R$ may be inferred.

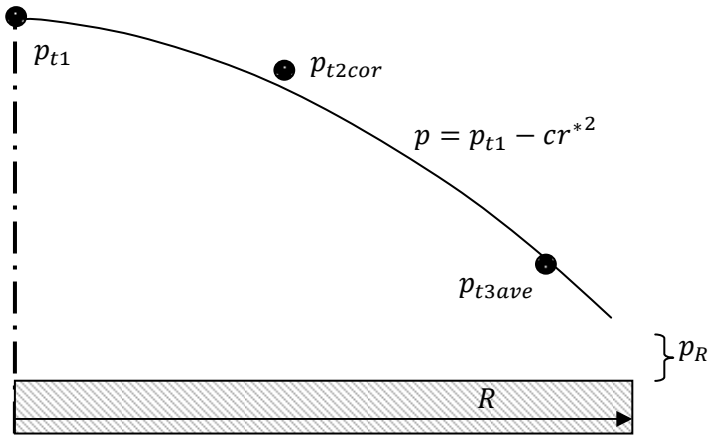


Figure 7-6: Second order, least-square polynomial pressure distribution fitting

## Approximate analytical circumferential pressure offset

A theoretical model of the fluid bladder being modelled as a sources flow is introduced in Section 5.11 (Circumferential Pressure Approximation), p. 41. This data processing operation continues from this theoretical model, more specifically, recalling equation (5-46), the equation constants are set to the experimental values as follows:

- $\varphi = 2\pi/3$ is approximated.
- $b_i$ may be approximated as half of the disc separation as shown in Figure 5-10.
- $b_o$ is approximated to have an average radius 15 mm; this is a mean value between a flaccid bladder (pre-experimental stroke) and fully inflated bladder (post-experimental stroke).

Hence equation (5-46) becomes

$$p_{cir} = -\frac{3\rho R}{4\pi}\ddot{h}\ \ln\frac{30}{h}. \tag{7-4}$$

## Parabolic carpet plots

Sixty second-order, least square polynomials are fitted to three pressure transducer measurements at regular disc separation intervals (Figure 7-6) which then merged together to yield a carpet plot. As with Figure 7-6 the circumferential gauge pressure has not been set to zero and therefore is a floating parameter.

## Spline carpet plot

Same as above except using a spline fit as opposed to a polynomial fit.

## Axi-symmetric pressure distribution shapes

As above, a spline fit is fitted to three pressure transducer measurements which in turn are rotated through $2\pi$ to give a (dimensionless) axi-symmetric pressure distribution shape.

## 7.5.2 Eccentricity corrections

This data processing operation follows on from the analysis in Section 5.12 (Eccentric Pressure Distributions), p. 43, which assumes a sinusoidally eccentric paraboloid pressure distribution with a zero offset pressure may be established due to experimental errors. At any time instant during an experimental stoke, both the orientation and magnitude of eccentricity of the skewed paraboloid are unknown. However, both these quantities may be inferred from the interrelationship the instantaneous pressure transducer measurements. Hence corrections may then be made to these measurements in order to correct for associated eccentricity errors.

The test rig measures the central pressure and so by equation (5-51) the maximum pressure may be determined. Assuming that $\sigma \leq 0.3$ through significant pressure developments of the experimental stroke, by equation (5-51) $p_{max} = 1.025\, p_{cent}$, hence it may be approximated that $p_{max} \approx p_{cent}$.

The symmetry angle $\phi$ is defined as the angle made between the plane of symmetry of the eccentric paraboloid with a line passing through $p_{t1}$, $p_{t2}$ and $p_{t3a}$ as shown in Figure 7-7.

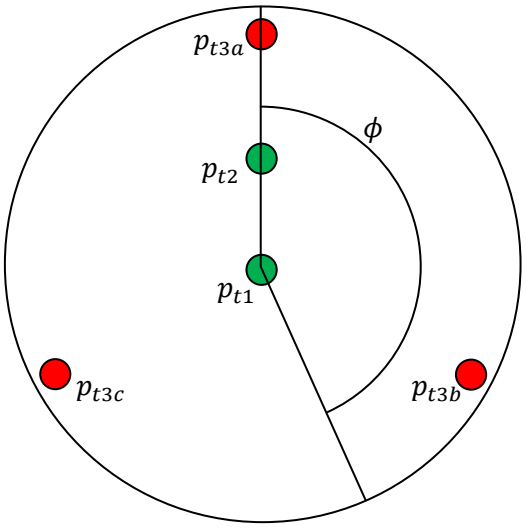


Figure 7-7: Pressure transducer placement and symmetry angle

Equation (5-47) may be written as

$$p^* = \left(1 - r^{*2}\right) + \left(r^* - r^{*3}\right)\sigma\psi \qquad (7\text{-}5)$$

where $\psi$ is introduced as the *sinusoidal displacement* and is assigned for the three axi-symmetric (outermost) pressure transducers which are angularly spaced $2\pi/3$ apart at equal radii (as shown in Figure 7-7). Hence $\psi_a, \psi_b$ and $\psi_c$ are respectively giving as

$$\psi_a = \cos\theta \qquad \psi_b = \cos\left(\theta + \frac{2\pi}{3}\right) \qquad \psi_c = \cos\left(\theta + \frac{4\pi}{3}\right). \tag{7-6a, b, c}$$

Plotting $\psi_a, \psi_b$ and $\psi_c$ with respect to $\theta$ in Figure 7-8 gives three sinusoidal curves with the properties that their sum is zero and the sum of their squares is a constant[a].

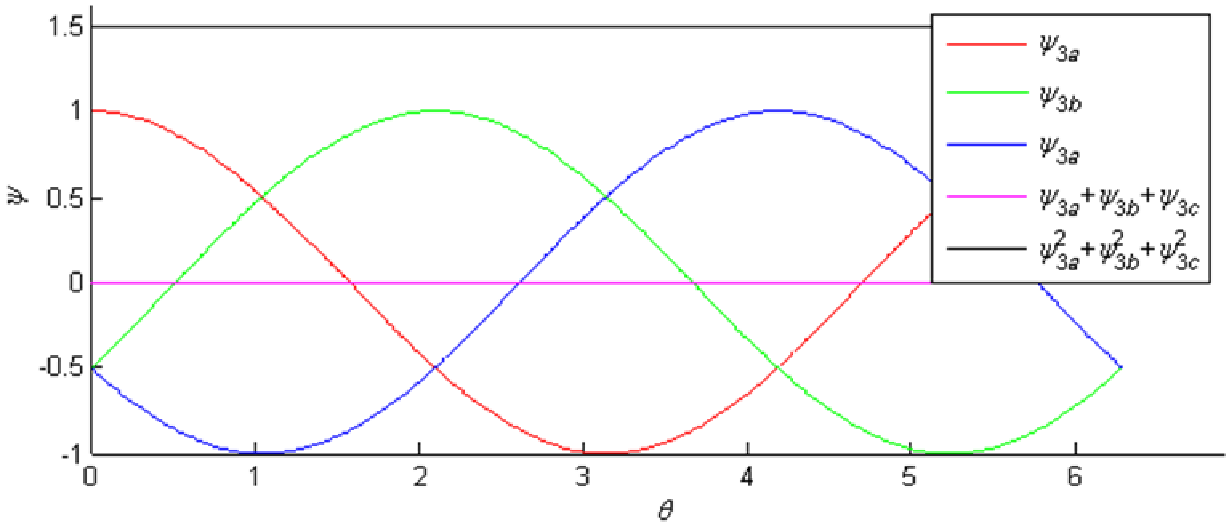


Figure 7-8: Sinusoidal angular displacement vs skewness angle

These two properties are expressed as

$$\psi_a + \psi_b + \psi_c = 0 \tag{7-7}$$

and

[a] Only the applications (and not proofs) of these relationships are relevant in the context of this thesis.

$$\psi_a{}^2 + \psi_b{}^2 + \psi_c{}^2 = \frac{3}{2} \tag{7-8}$$

respectively.

Similar to equations (7-7) and (7-8), it can be shown from equations (7-5), (7-6a, b, c), (7-7) and (7-8) that

$$p_{t3ave} = \frac{(p_{t3a} + p_{t3b} + p_{t3c})}{3} \tag{7-9}$$

where $p_{t3ave}$ is the average pressure from all $p_{t3}$ transducers, and

$$\chi|_{r_3^*} = \frac{2}{3}\sqrt{(p_{t3a} - p_{t3ave})^2 + (p_{t3a} - p_{t3ave})^2 + (p_{t3a} - p_{t3ave})^2}. \tag{7-10}$$

where $\chi$ is the eccentricity magnitude recalled from equation (5-48) in which $\chi \equiv \chi^* R$. Using the above approximation that $p_{max} \approx p_{cent}$ and equations (5-48), (5-50) and (5-51), it can be shown that

$$\sigma \approx 2\xi^* \approx \frac{\chi|_{r_3^*}}{p_{t1}\left(r_3^* - r_3^{*3}\right)}. \tag{7-11}$$

where $r_3^*$ is the dimensionless radius at which all $p_{t3}$ transducers are situated. For practical data processing operations, it is unnecessary to solve for $\sigma$ as $p_{t1}$, $p_{t2}$ and $p_{t3a}$ lie on the same radial line (angular displacement) as shown in Figure 7-7. Instead from equation (7-5) where $r_2^* = 0.45$ and $r_3^* = 0.9$, it can be shown that

$$\frac{p_{t2} - p_{t2cor}}{p_{t1}} = 0.359\sigma\psi_a \qquad \text{and} \qquad \frac{p_{t3a} - p_{t3ave}}{p_{t1}} = 0.171\sigma\psi_a \tag{7-12a, b}$$

where $p_{t2cor}$ is the eccentricity corrected $p_{t2}$ value. Hence from equations (7-12a, b), $p_{t2cor}$ is solved as

$$p_{t2cor} = p_{t2} + 2.1\frac{p_{t3ave} - p_{t3a}}{p_{t1}}. \tag{7-13}$$

It can be seen from equation (7-13) that if $p_{t2cor}$ is calculated for a skewed parabolic pressure distribution with an associated circumferential pressure offset, then the resultant $p_{t2cor}$ value will not yield an absolutely accurate correction under the above analysis. However, the correction associated with a positive pressure offset will always be under-corrected and hence it will always be *advantageous* to *correct* results for a *skewed parabolic pressure distribution* with an associated *positive pressure offset* (more accurate than uncorrected results). On the other hand it can be shown that the correction associated with a negative pressure offset will always be over-corrected; this over-correction value reaches twice the optimum correction value (calculated at zero offset pressure) at a negative pressure offset of $p_{cir} \approx -0.4p_{t1}$. Hence it is *advantageous* to *correct* for a *skewed parabolic pressure distribution* with an associated *negative pressure offset* not below -40% of $p_{t1}$.

Furthermore, it is noted that skewed non-parabolic pressure distributions (a measure of which has not been established) will not yield absolutely accurate corrections under the above analysis. It is however *assumed* that pressure distributions that *deviate marginally* from *eccentric paraboloid* distributions (i.e. distributions that tend towards eccentric conical or cylindrical volumes) will be *advantageously* corrected for.

As a matter of academic interest, if a skewed parabolic distribution with no circumferential pressure offset is assumed, the symmetry angle $\phi$ is given by

$$\phi = \cos^{-1}\psi_a$$

in which $\psi_a$, in addition to $\psi_b$ and $\psi_c$, is calculated by

$$\psi_a = \frac{p_{t3a} - p_{t3ave}}{\chi|_{r_3^*}}, \qquad \psi_b = \frac{p_{t3b} - p_{t3ave}}{\chi|_{r_3^*}}, \qquad \psi_c = \frac{p_{t3c} - p_{t3ave}}{\chi|_{r_3^*}}. \qquad \text{(7-14a, b c)}$$

However, as can be seen from Figure 7-8, the values of $\psi_a$ are symmetrical about $\pi$. Therefore, in order to determine whether $\phi$ lies within the first/second or third/forth quadrant it is noted that $\psi_b - \psi_c$ is positive for $0 \leq \phi \leq \pi$ and negative for $\pi \leq \phi \leq 2\pi$. Hence $\phi$ is determinable for $0 \leq \phi \leq 2\pi$ by

$$\phi = \cos^{-1}\psi_a\,;\ \psi_b - \psi_c \geq 0 \qquad \phi = 2\pi - \cos^{-1}\psi_a\,;\ \psi_b - \psi_c < 0. \qquad \text{(7-15a ,b)}$$

### 7.5.3 Test selection

It is subsequently shown in Section 8.3, p.121, that experiments are highly repeatable by superimposing various experimental variables on the same set of axes. This is done by the MATLAB 'Selection' program (CD-Appendix B). However, outlying traces do occur during certain tests which may be identified using this selection program. Hence these tests are excluded from the *Averaging* process (Section 7.5.4) as not to adversely influence the subsequently composed *varying parameter plots* (Section 7.5.5) in which these averaged results are utilized. The eliminated tests are given in the 'Exclusion table' Excel spreadsheet given in CD-Appendix C.

### 7.5.4 Test averaging

The selected tests (Section 7.5.3) are aggregated to render an averaged test which is in turn used to determine varying parameter plots (Section 7.5.5). This is done by the 'Averaging' programs (CD-Appendix B, found in the respective Varying Parameter folder). These programs render averaged results which are saved in a MATLAB format with the same naming nomenclature defined in Section 7.5, p. 84, with the exception that the test number is omitted. These averaged results are given in CD-Appendix B in an 'Averaged' folder within the appropriate Varied Parameter folders.

### 7.5.5 Varying parameter plots

Finally the averaged tests (Section 7.5.4) are used to render varying parameter plots. This is done by MATLAB 'VP' (Varying Parameter) programs where:

- VP-H: processes carpet plots for drop-Height variations.
- VP-M: processes carpet plots for drop-Mass variations.
- VP-h0: processes carpet plots for initial disc separation variations.

These 'VP' programs are given in CD-Appendix B within the appropriate 'Averaged' folder.

# 8 RESULTS AND DISCUSSION

Experimental data obtained from the testing procedure (Section 7.3, p. 80) are development by various data processing operations (defined in Section 7.5, p. 84) by the MATLAB 'Process' program (CD-Appendix B) to yield experimental results presented within the subsequent two sections (Sections 8.1 and 8.2). In order to optimise the following discussion, experimental results are sequentially presented and concisely discussed within these sections with data processing operations only being specified but not elaborated upon. Hence if the reader requires information on specific data processing operations, Section 7.5, p. 84 (Data Processing) may be referred to.

Within Sections 8.1 and 8.2 various experimental variables are determined with the intension of ultimately comparing experimental results against theory [Section 0 (Theoretical Analysis), p. 19]. For example the comparison of instantaneous experimentally determined radial pressure distributions against the theoretically determined parabolic distribution and the comparison of the experimental central pressure trace with those theoretically determined.

## 8.1 Reference Test Results

The first test (test 1) conducted with the initial conditions of $H$ = 500 mm, $h_0$ = 10 mm and $M$ = 30 kg was selected as the *reference test* (Section 7.1, p. 65). Only this test is analysed in extensive detail within this section.

Before proceeding with the experimental results of the reference test, it must pre-emptively be noted that tests comprising test-sets (identical initial conditions) are highly repeatable, as is later shown in Section 8.3, p. 121. This is important to justify the methodology of analysing only one test in extensive detail. In turn, varying parameter carpet plots, subsequently presented in Section 8.4, p. 125, show the change of experimental variables (features) with a varying experimental parameter.

Within all figures (or all figures on the same page), the parameters of drop-height $H$, initial disc separation $h_0$, drop-mass $M$ and test-set number are specified within the graph title.

### 8.1.1 Pressure and disc separation traces

The resultant pressure traces for the reference experiment, measured by pressure transducers 1, 2, 3a, 3b and 3c (the radial and angular positions of which are specified in Table 7-2, p. 85, and shown in Figure 7-7, p. 90) are displayed on the left-hand scale of Figure 8-1 with respect to time. In addition to these pressure traces, the disc separation trace is displayed on a secondary right-hand scale as a red trace.

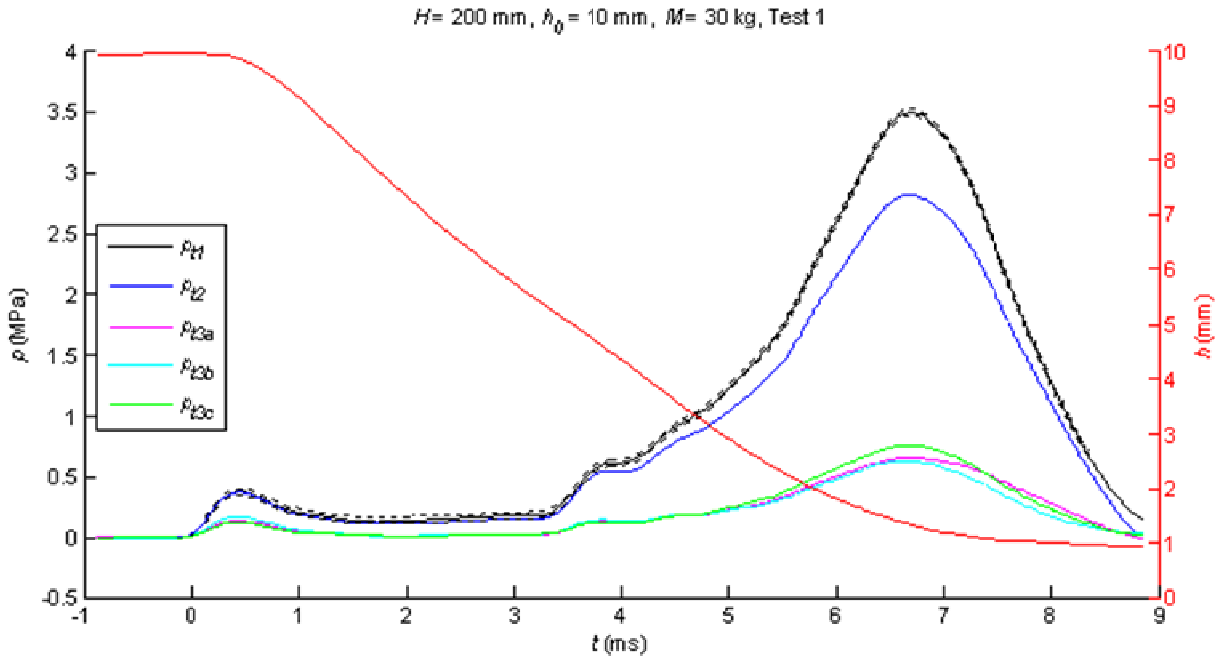


Figure 8-1: Pressures and disc separation vs time

The data processing operations required to yield Figure 8-1 include *calibration*, *uncertainty calculations*, *smoothing*, *zeroing time* and *pressure trace truncating* (Section 7.5.1, p. 84).

For the sake of neatness, only upper and lower uncertainty bounds for $p_{t1}$ (central pressure measurement) are included as the dotted black lines in Figure 8-1. The uncertainty bounds for the other pressure transducers become pertinent when establishing the radial pressure distributions as subsequently shown in Figure 8-3 and discussed in the associated text. The laser displacement sensor has a measurement tolerance of $\pm 50$ µm (Appendix H); hence for the sake of neatness the disc separation uncertainty bounds are omitted from Figure 8-1 as their inclusion results in a marginally thicker $h$ trace.

Since the instantaneous disc separation measurements are known (Figure 8-1), various experimental variables may be plotted with respect to disc separation as opposed to time (as is subsequently done in Figures 8-19 and 8-20, p. 120). Both these domains are useful for different evaluations; plotting curves on the disc separation domain is particularly useful for varying parameter carpet plots where in general, the stroke period varies but the stroke displacement remains relatively constant (Section 8.4, p. 125).

## Feature classification

The following features are visually ascertained from Figure 8-1 and classified as follows:

- The preliminary pressure spike:

  This small pressure spike develops at the stroke initiation, peaks with a maximum central pressure of 0.4 MPa at $t$ = 0.45 ms and lasts for approximately 1 ms.

- The major pressure spike:

  This pressure spike peaks at $t$ = 6.8 ms and reaches a maximum central pressure of about 3.5 MPa at 1.5 mm disc separation.

- The bridging region:

  This is the lower pressure region that bridges the preliminary and major pressure spikes and has a time interval of $1 \leq t \leq 3.5$ ms.

- The residual fluid film:

  It is seen by the disc separation trace that the plunger does not come to rest at zero disc separation. Instead, a residual fluid film is responsible for a 0.9 mm post experimental stroke disc separation. This residual fluid film continues to diminish with respect to time after the termination of the experimental stroke, following an asymptotic relationship. Hence it is assumed that the discs never make contact when encompassing a fluid film. For this reason, the grounded disc separation value of $h \approx 0$ must be measured when the discs are dry (Section 7.2.4, p. 77).

## 8.1.2 Disc velocity and acceleration

In addition to the pressure and the disc separation traces shown in Figure 8-1, the first and second disc separation time derivatives (disc velocity and disc acceleration respectively) are crucial experimental quantities in determining theoretically modelled pressure traces. These derivatives are shown on the right-hand scale of Figure 8-2 with the central pressure trace plotted on the left-hand scale for purpose of correlating events.

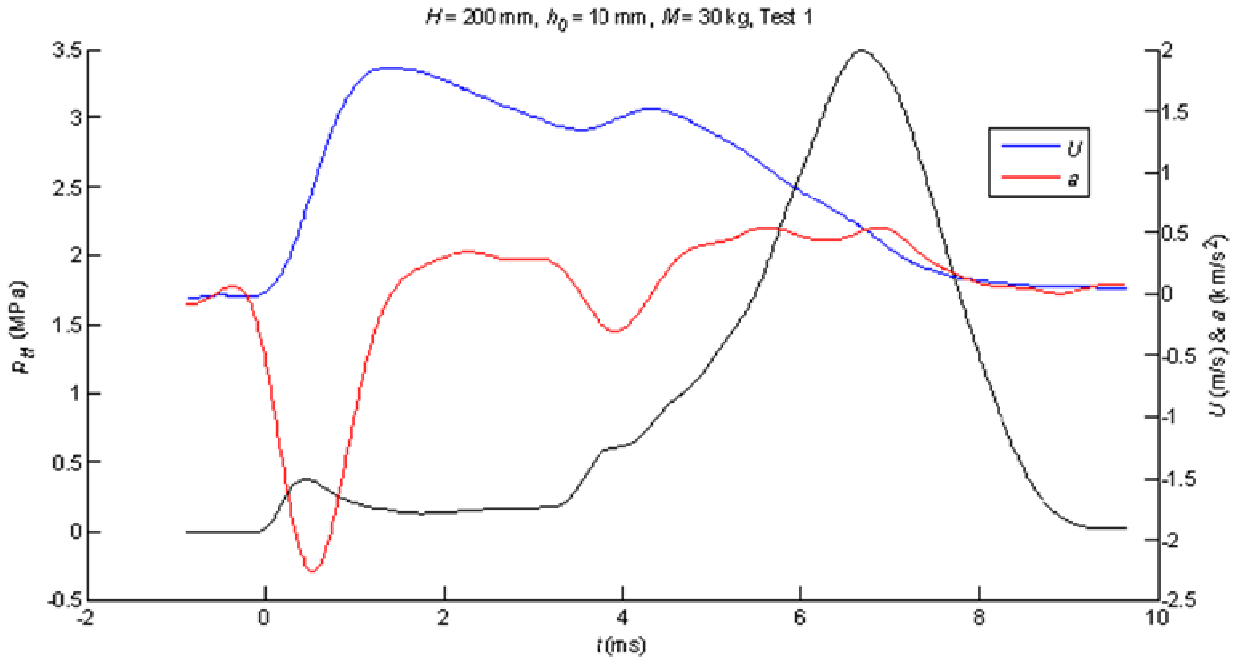


Figure 8-2: Central pressure, velocity and acceleration vs time

The disc velocity trace is obtained by *differentiating* and then *smoothing* (Section 7.5.1, p. 84) the disc separation trace. The disc acceleration trace is in turn obtained by differentiating and then smoothing the disc velocity trace. The uncertainty bounds of both the disc velocity and acceleration traces cannot be accurately determined due to the utilisation of the smoothing algorithms.

From Figure 8-2, the velocity is seen to increases through the preliminary pressure spike and reaches a maximum value of 1.85 m/s at 1.4 ms through the bridging region. The maximum measured negative acceleration is -2250 m/s$^2$ which occurs at 0.5 ms and its peak corresponds relatively accurately with the

peak of the preliminary pressure spike; this strongly suggests that the preliminary pressure spike is an acceleration dominant pressure development.

If the drop-hammer were in direct contact with the plunger subassembly during the major pressure spike, then a direct correlation between the acceleration trace and the pressure spike would be observed according to Newton's second law ($p \propto m\ddot{h}$); this is not observed in Figure 8-2. It is later shown in Figure 8-10 and the associated text that the reason for this poor acceleration/pressure correlation is due to bouncing of the plunger relative to the drop-hammer. Furthermore, if the maximum disc velocity of 1.85 m/s through the bridging region is compared against an unimpeded drop-hammer impact velocity of $V = \sqrt{2gH} = 1.98$ m/s (elementary kinematic equations), then a velocity discrepancy of only 7% is observed. This relatively minor velocity discrepancy cannot account for the energy dissipation associated with the pressure development and other energy losses. Instead, this higher than expected experimental disc velocity supports the above inference that the plunger bounces relative to the drop-hammer during the bridging region as shown Figure 8-10.

### 8.1.3 Radial pressure distribution

The *normalised pressure distribution* values are calculated by dividing the instantaneous pressures measurements of transducer 1 to 3c by transducer 1 and plotting the resultant dimensionless traces with respect to time as represented by the solid lines on the left-hand scale of Figure 8-3. The associated *normalised pressure distribution uncertainty bounds* (Section 7.5.1, p. 84) are also been included in Figure 8-3 as dotted lines with colours corresponding to their respective normalised pressure distribution trace. Moreover, the theoretical *normalised parabolic pressure distribution constants* (Section 7.5.1, p. 84) are also plotted as horizontal dashed lines with the blue and magenta lines corresponding to the theoretical (parabolic) values of normalised pressure distribution 2 and 3 respectively. *Pressure distribution truncations* (Section 7.5.1, p. 84) are used to exclude the error dominated pressure distributions associated with small pressures. Finally the central pressure trace has been included on the right-hand scale of Figure 8-3 for the purpose of correlation events.

It is recalled from equation (5-9), p. 23, and associated text that an axi-symmetric parabolic radial pressure distribution is invariably theoretically established for a squeeze flow system under the parallel flow assumption. In conjunction with this parabolic radial pressure distribution, a zero circumferential pressure boundary condition is generally assumed. However, from Figure 8-3 it is apparent that the

pressure distribution is both eccentric and offset by a circumferential pressure during preliminary pressure spike and bridging regions of the experimental stroke: If an axi-symmetric parabolic pressure distribution with zero circumferential pressure were invariably established, the normalised pressure distribution uncertainty bounds in Figure 8-3 would enclose their respective theoretical parabolic normalised pressure distribution constants throughout the experimental stroke.

Hence applying the *eccentricity correction* procedure (Section 7.5.2, p. 90) to the unprocessed normalised pressure distribution values (Figure 8-3) gives Figure 8-4. By comparing in Figure 8-3 with Figure 8-4 it can be seen that the normalised pressure distribution values have only been marginally altered. The normalised pressure distribution uncertainty bounds have been omitted from Figure 8-4 due to associated data processing (mathematical) complexities; however as a heuristic, the uncertainty bounds can be thought of as (instantaneously) similar those given in Figure 8-3. In this light it is clear that the reference test is offset by a circumferential pressure during the preliminary pressure spike and the bridging regions.

The eccentricity correction procedure results in negligibly altered normalised pressure distribution traces for this specific test, i.e. the pressure distribution of the reference test is relatively concentric throughout the stroke (a contributing factor in the selection of the reference test). However, the effectiveness of this corrective procedure is best illustrated when comparing the superimposed unprocessed and eccentricity corrected normalised pressure distribution traces of a whole test-set (repeated tests) against each other. This is subsequently done in Section 8.3, p. 121, in which Figures 8-22a and 8-22b show that this procedure greatly reduces the spread of the normalised pressure distribution traces by about 60% during the major pressure spike.

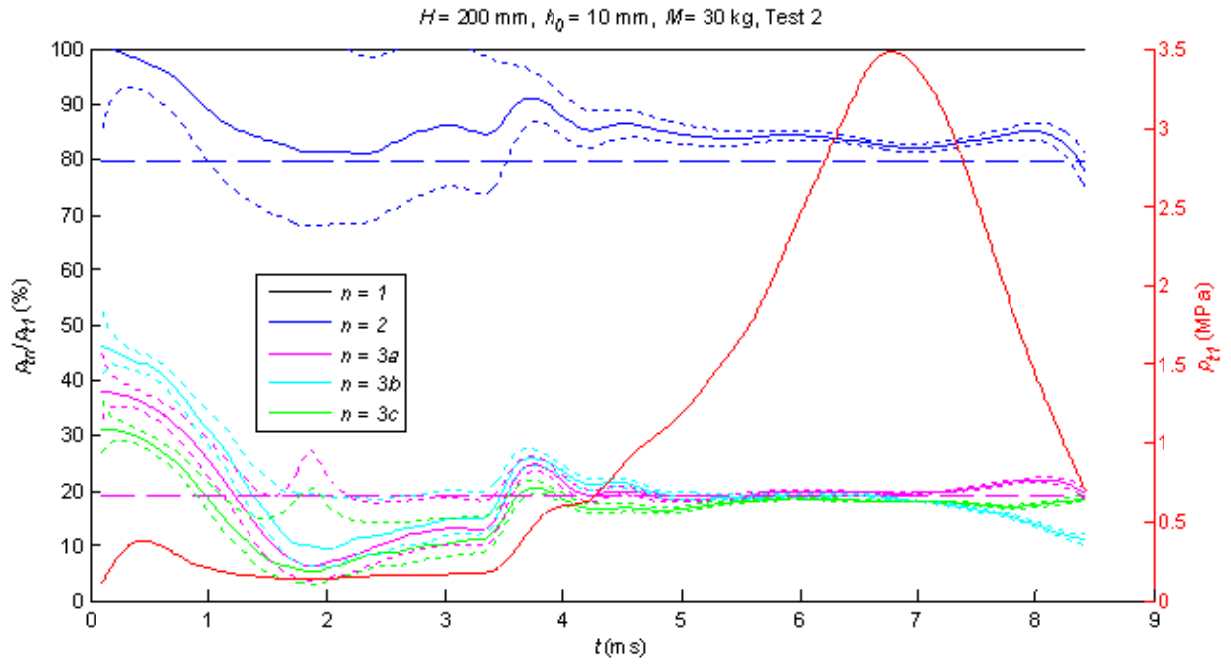


Figure 8-3: Normalised pressure distribution values and central pressure vs time

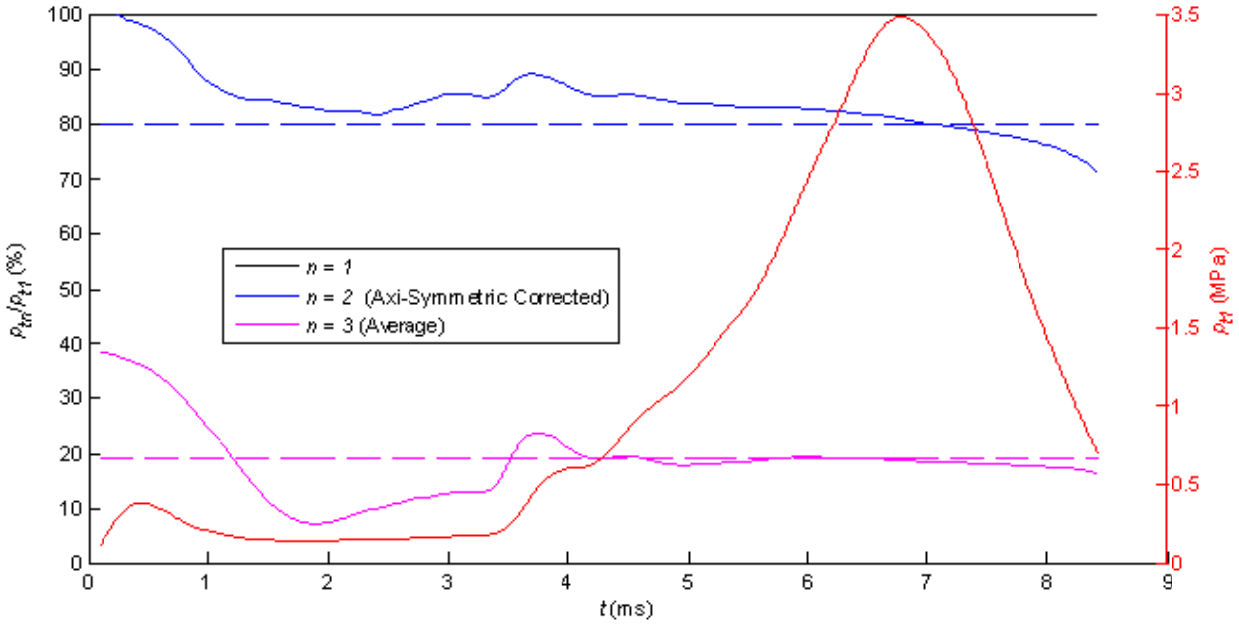


Figure 8-4: Eccentricity corrected normalised pressure distribution values and central pressure vs time

Applying the *inferred circumferential pressure offset* (Section 7.5.1, Figure 7-6, p. 88) to the eccentricity corrected normalised pressure distribution traces (Figure 8-4) yields Figure 8-5. In addition to the

eccentricity and offset corrected normalised pressure distribution values, the inferred instantaneous resultant circumferential pressure offset $p_R$ is also given as a percentage of $p_{t1}$ in Figure 8-5. By comparing Figure 8-5 with Figure 8-4, it can be seen that this technique significantly corrects the normalised pressure distribution traces towards that of a parabolic distribution during the preliminary pressure spike and the bridging region.

Additionally, the *approximate analytical* technique is used to solve for the *circumferential pressure offset* $p_{cir}$ [the empirical model of which derived in Section 5.11, p. 41 into which constants for the experimental system are substituted in Section 7.5.1, p. 84, equation (7-4)]. Hence, using the approximate theoretical values of the circumferential pressure $p_{cir}$ as opposed to the experimentally inferred $p_R$ values, the corrected normalised pressure distribution traces are given by Figure 8-6.

Comparing Figure 8-6 with Figure 8-5 it can be seen that the analytical normalised circumferential pressure $p_{cir}/p_{t1}$ follows the trend of the inferred normalised circumferential pressure $p_R/p_{t1}$ almost identically but at a lesser magnitude. This comparison strongly supports the analysis of the bladder being approximated to a source flow in which temporal inertial forces (a strong function of disc acceleration) are dominant [equation (7-4), p. 89].

Despite the pressure distribution being corrected for instantaneous eccentricity and circumferential pressure offsets, it is still apparent from both Figures 8-6 and 8-5 that normalised pressure distribution 2 is still largely exceeding (~20%) its parabolic normalised pressure distribution constant during the preliminary pressure spike [with uncertainly bounds being inferred as comparable to those given in Figure 8-3]. The interpretation of this is that the pressure distribution is not parabolic during this region, and tends towards the shape of a truncated cone.

Notwithstanding the good correlation of the analytical and experimentally inferred circumferential pressures offsets observed in Figures 8-6 and 8-5, various experimental assumptions made in applying the theoretical model ($p_{cir}$) are purely speculative and are therefore questionable. Furthermore, the experimentally inferred pressure offset ($p_R$) assumes that the radial pressure distribution is parabolic; this assumption is clearly false as shown by Figures 8-6 and 8-5 (as discussed above). Therefore, this offset correction model is only applied to the reference experiment results.

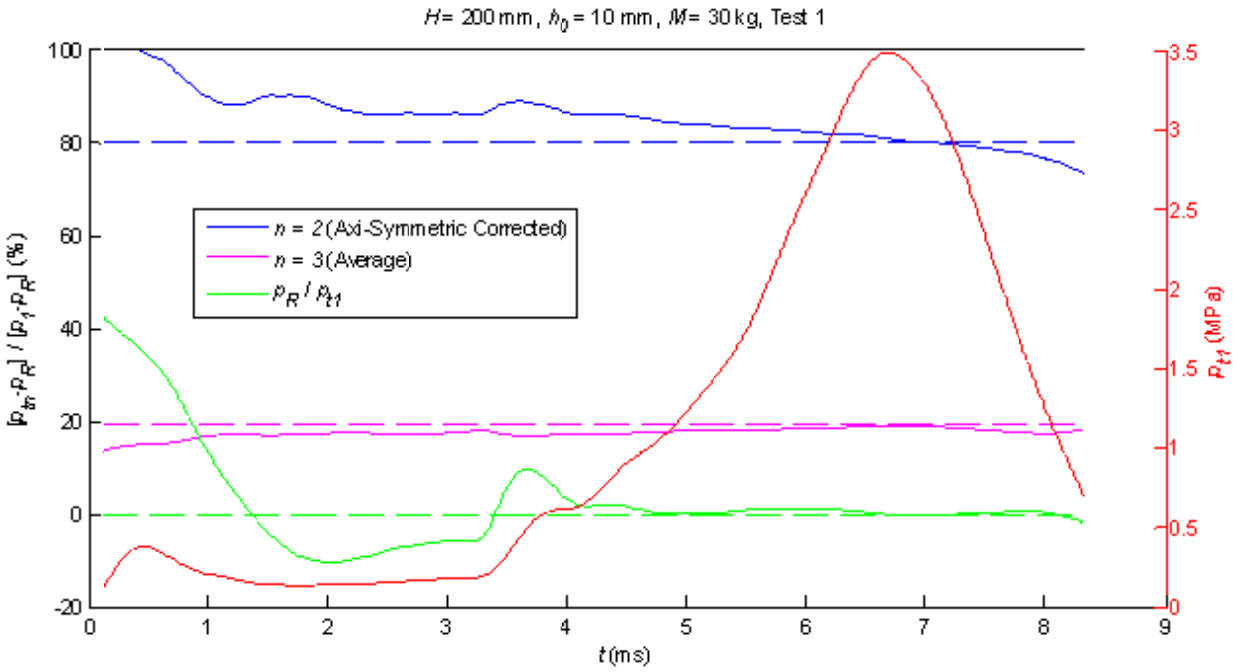


Figure 8-5: Eccentricity and offset corrected (inferred) normalised pressure distribution values and central pressure vs time

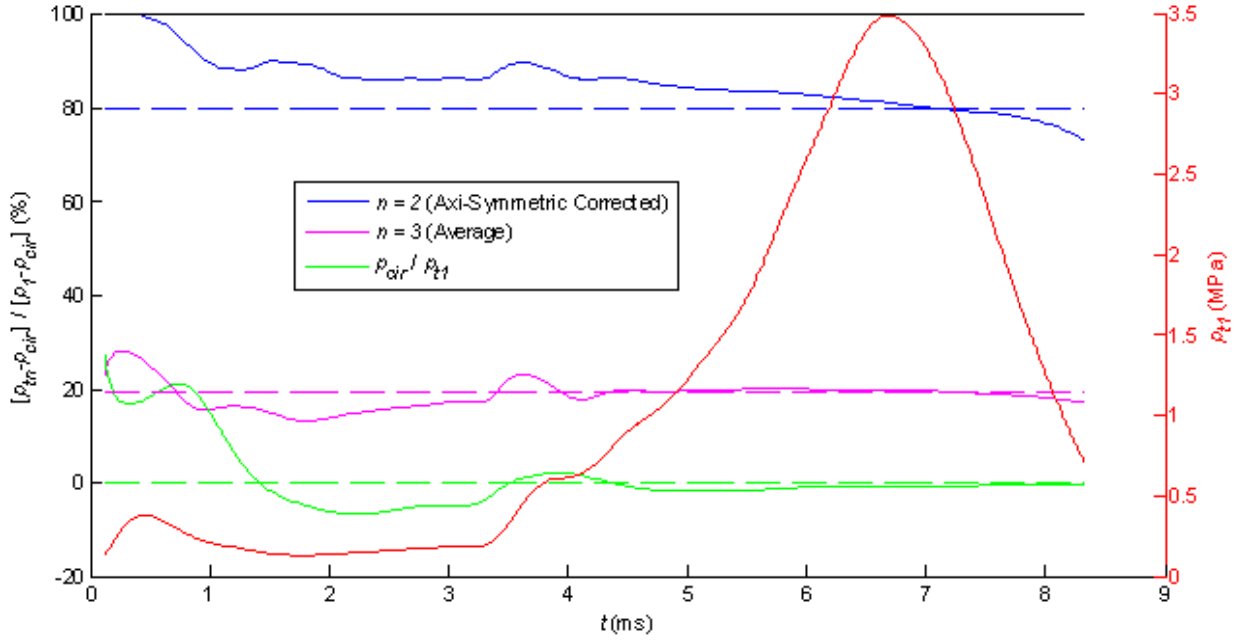


Figure 8-6: Eccentricity and offset corrected (analytical) normalised pressure distributions and central pressure vs time

In isolation, the reference experiment, with its relatively loose uncertainty bounds, is not a compelling argument for the establishment of a non-parabolic pressure distribution (Figures 8-5 and 8-3). However, it is subsequently shown in Figure 8-40, p. 141, that all ten of the averaged test traces (each of which is averaged from a minimum of four tests) have an eccentricity corrected normalised pressure distribution values of $90 \leq p_{t2}/p_{t1} \leq 100\%$ throughout the preliminary pressure spike. Hence these averaged normalised pressure distribution traces are similar to Figure 8-3 and thus would yield similar eccentricity and offset corrected pressure distributions to those given in Figures 8-5 and 8-6.

On the other hand, throughout the major pressure spike, the eccentricity and offset corrected normalised pressure distribution traces (Figures 8-5 and 8-6) appear to be in good agreement with parabolic pressure distribution constants, with negligible inferred circumferential pressures.

Hence, in conclusion, it may tentatively be stated that a concentric parabolic pressure distribution is established during the major pressure spike with a negligible associated offset pressure, while during the preliminary pressure spike a non-parabolic pressure distribution with a relatively significant circumferential pressure offset is established. However, the *ratio* of *parabolic* pressure distribution *deviation* to circumferential *pressure offset* is *undeterminable* with the current test cell. During the bridging region the uncertainty bounds are too large to reach a conclusion (Figure 8-3); henceforth only the pressure distributions associated with the preliminary and the major pressure spikes are investigated.

The *axi-symmetric pressure distribution shapes* (Section 7.5.1, p. 84) at the preliminary pressure spike peak and the major pressure spike peak are respectively presented in Figures 8-7a and b; their shapes give a more intuitive representation of these pressure distribution variations.

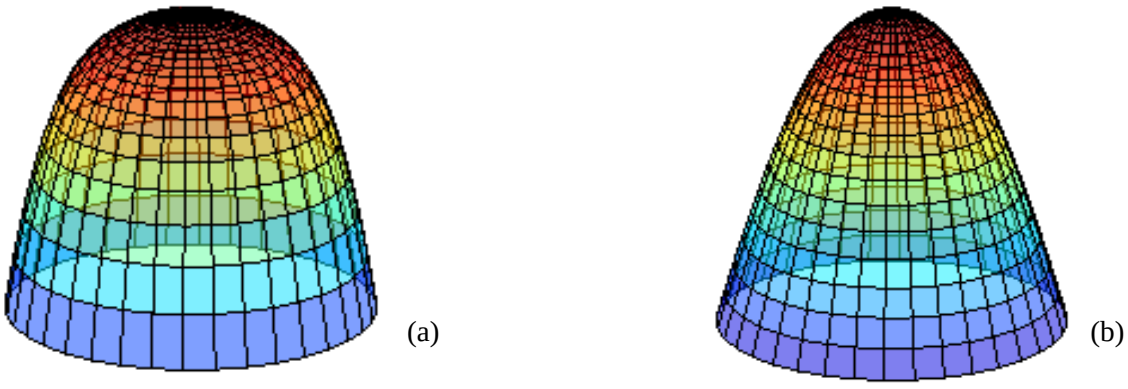

(a) (b)

Figure 8-7: Axi-symmetric pressure distribution shapes at:
(a) the preliminary pressure spike peak (b) the major pressure spike peak.

### 8.1.4 Three-dimensional plots

A more informative way to view Figure 8-1, so that both central pressure and associated pressure distributions may simultaneously be viewed, is to plot the pressure with respect to disc separation and disc radius. Hence each pressure trace may be plotted along its appropriate disc radius as shown by the dashed lines below in Figure 8-8 where $p_{t2cor}$ (eccentricity corrected) and $p_{t3ave}$(averaged value) are shown by the blue and red dashed lines respectively while the black dashed line shows the pressure measured by $p_{t1}$. The circumferential gauge pressure has not been set to zero in Figure 8-8 and so it is a floating parameter. The data processing operation used to yield this *parabolic carpet plot* is discussed in Section 7.5.1, p. 84.

The above process is repeated for the preliminary pressure spike to yield Figure 8-9. However, unlike Figure 8-8, a *spline carpet plot* (Section 7.5.1, p. 84) now replaces the second order polynomial fitted carpet plot. Similarly, the circumferential gauge pressure has not been set to zero in Figure 8-9 and so it is a floating parameter.

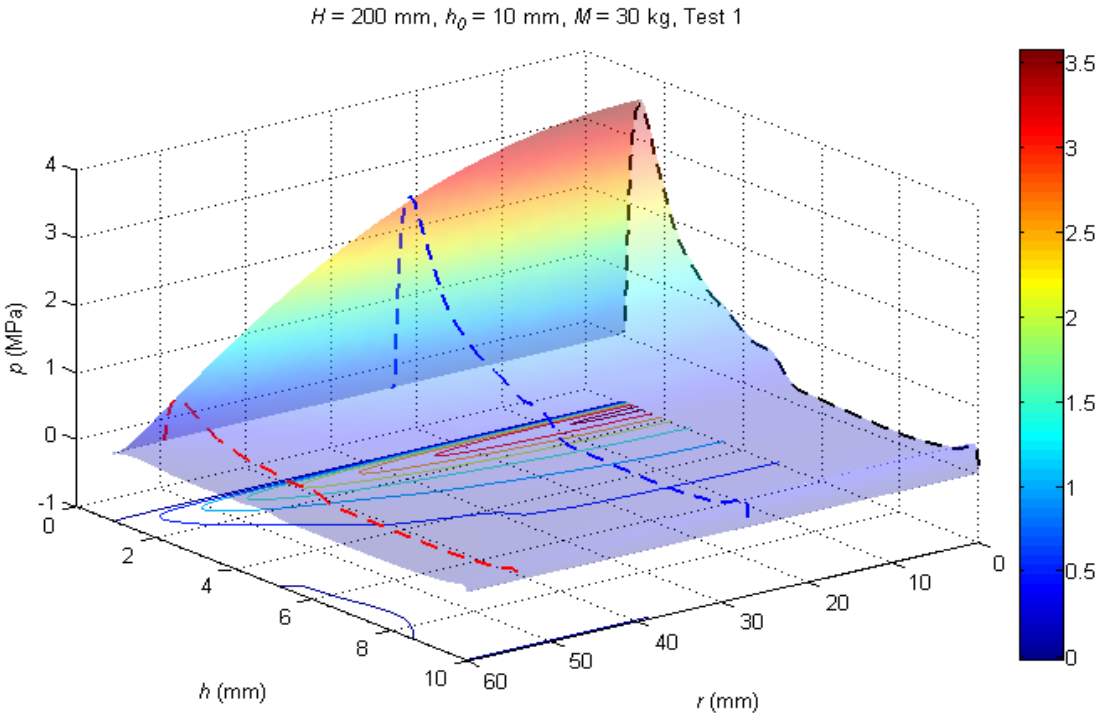


Figure 8-8: Pressure vs radius vs height

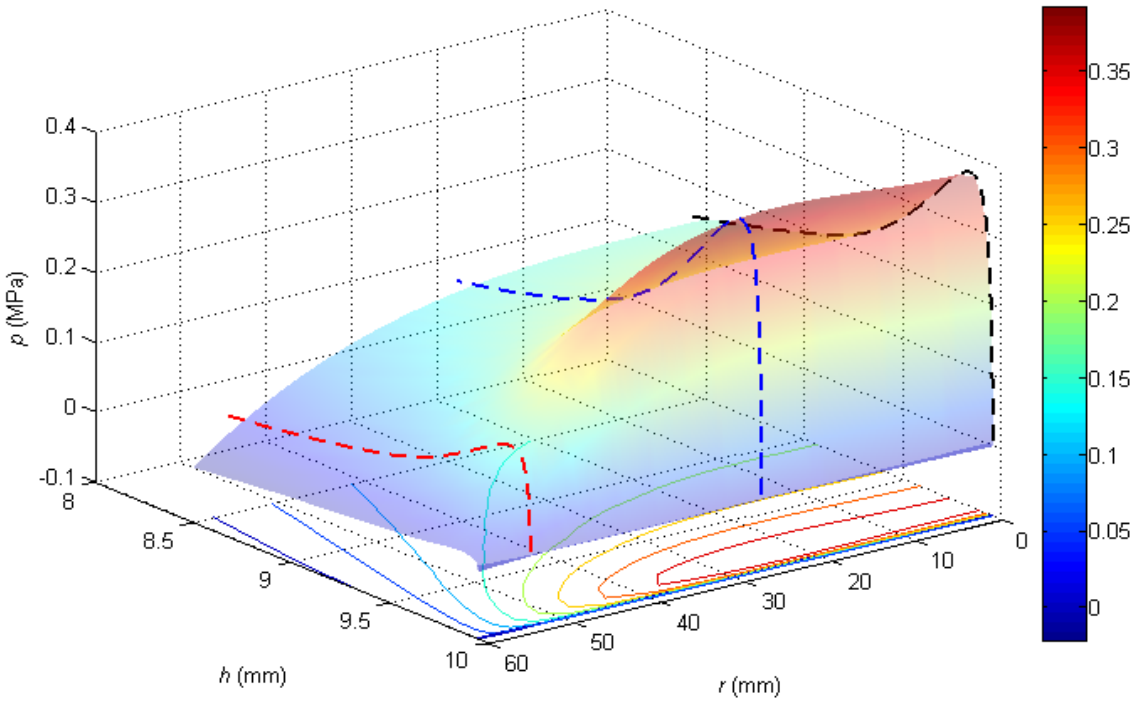


Figure 8-9: Pressure vs radius vs height (preliminary pressure spike)

### 8.1.5 Force and energy calculations

Numerically integrating instantaneous spline fitted pressure plots over the disc area yields an approximate instantaneous force exerted by the pressure $F_{pre}$. Furthermore, since the instantaneous acceleration (Figure 8-2) and mass of the plunger (2.1 kg) are known, the resultant force $F_{res}$ exerted on the plunger may be calculated by Newton's second law. Thereafter, since both the force due to pressure and resultant force exerted on the plunger are known, the force exerted by the drop-hammer on the plunger $F_{mass}$ may be inferred as the difference of these forces. These three forces are plotted in Figure 8-10 below.

Figure 8-10 reveals that the plunger bounces relative to the drop-hammer throughout the bridging region of the experimental stroke ($1.5 < t < 3.2$ ms) consistent with $F_{mass} \approx 0$. Initially it was assumed that the masses of both the drop-hammer and the plunger would combine as a homogenous mass soon after impact. This assumption is false and holds implications for theoretical modelling of the system in that a homogeneous mass may not be assumed in order to couple the disc acceleration with the pressure development between the discs, according to Newton's second law.

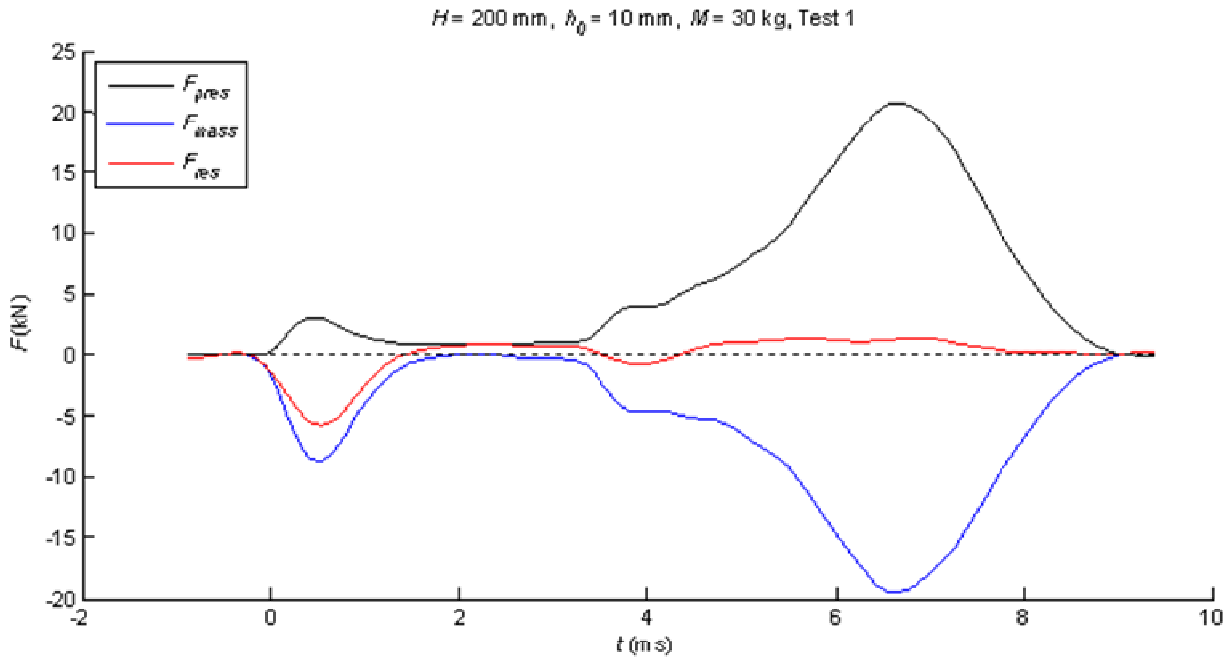


Figure 8-10: Force due to pressure, applied force and resultant force vs disc separation

The work done by the pressure is given by $W_{pre} = \int F_{pre}\, dh$; for the above experiment this value is calculated as $W_{pre} = 41.62$ J. The gravitational potential energy of the drop-hammer is calculated as

$$E_G \approx MgH, \tag{8-1}$$

where the initial disc separation $h_0$ is not included in equation (8-1) because $H \gg h_0$ [with the exception of very low drop heights ($H < 200$ mm)]. The gravitational potential energy of the above test is calculated at $E_G = 58.8$ J. So by the first law of thermodynamics the energy of the drop-hammer and the work due to pressure development may be equated to reveals a discrepancy of 29%.

Non-conservative energy losses such as friction of the drop-hammer cradle along the drop-hammer columns (Figure 7-2, p. 69) and thermal energy transfer to the working fluid are speculated to account for the above energy losses. It is also recalled that plastic deformation of the drop-hammer, which was noted on the impact area of the drop-hammer after testing (Section 7.4, p. 83), will contribute to energy losses. On the other hand, it is also recalled that the drop-hammer bounced off the plunger after the experimental stroke (Section 7.4, p. 83); therefore the impact dynamics of the systems are a combination of restitution and dissipation dynamics. Since the above energy transfers cannot individually be quantified, $\eta$ is introduced as the energy transfer coefficient where

$$W_{pres} = \eta E_G. \tag{8-2}$$

Hence for the reference test (above) $\eta = 71\%$.

### 8.1.6 Application of theoretical models

In order to apply the various theoretical models to the experimental stroke, it is first necessary to obtain the fluid kinematic viscosity. During experimentation, the temperature was noted to fluctuate between 18±1˚C[a] which yields a viscosity range of $\mu = 1.63^{+0.18}_{-0.16}$ Pa.s (refer to the Excel 'Viscosity' Spreadsheet Appendix C, composed from data obtained from Dorsey (1995). Furthermore, due this small temperature fluctuation, a density of $\rho = 1262$ kg/m$^3$ is relatively constant(Dorsey, 1995). The kinematic viscosity

[a] For the purposes of error analysis, the viscosity change due to temperature fluctuation is investigated.

may therefore be obtained by $\nu \equiv \mu/\rho$ [equation (2-6)] yielding $\nu = 1.292^{+0.143}_{-0.127} \times 10^{-3}$ m$^2$/s [not the same as used for the CFD modelling (Section 6, p. 47)].

Before theoretically modelling the central pressure traces, it is of interest determine the instantaneous pressure generation mechanisms, i.e. the terms of the exact kinematic model [equation (5-10), p. 23] that are predominantly responsible for the pressure developments at any time instant.

For the sake of convenient referencing, the inertial composition [equation (5-5)], traditional Reynolds number [equation (2-5)] and the dynamic Reynolds numbers [equations (5-40) and (5-41)] are respectively recalled as follows

$$\Re = \left|\frac{\ddot{h}h}{\dot{h}^2} - 1\right|, \qquad Re_{trad} \equiv -\frac{h\dot{h}}{\nu},$$

$$Re_{dyn} = \frac{1}{2}\sqrt{\lambda}\coth\frac{\sqrt{\lambda}}{2} - 1 \quad \text{for } (\lambda > 0) \quad \text{and} \quad Re_{dyn} = \frac{1}{2}\sqrt{|\lambda|}\cot\frac{\sqrt{|\lambda|}}{2} - 1 \quad \text{for } (\lambda < 0).$$

The inertial composition indicates the ratio of temporal to spatial inertia (Section 5.2, p. 21) and the dynamic Reynolds numbers[a] indicates the ratio of inertial to viscous forces (Section 5.10, pp 38). The above parameters are shown on the right-hand scale of Figure 8-11 with the central pressure trace plotted on the left-hand scale for purposes of correlating events.

As shown before for the CFD model (Figure 6-2, pp 49), the traditional Reynolds number has poor correlation with the dynamic Reynolds number, once again indicating that the traditional Reynolds number is a poor representation of the ratio of inertial to viscous forces for highly transient squeeze flows.

Figure 8-11 shows that $Re_{dyn} > 5$ during the preliminary pressure spike indicating inertial force dominance. Furthermore, within this region the inertial composition is approximately of order two ($\Re$ truncated in Figure 8-11); hence during the preliminary pressure spike it is inferred that temporal inertia [term *$C_1$'* of equation (5-10), p. 23] is dominant. On the other hand, during the major pressure spike $Re_{dyn} \approx 0$, indicating that viscous forces [term *$B_1$'* of equation (5-10), p. 23.] are dominant.

[a] The shape parameter values used in determining the dynamic Reynolds number are pre-emptively obtained from Figure 8-13.

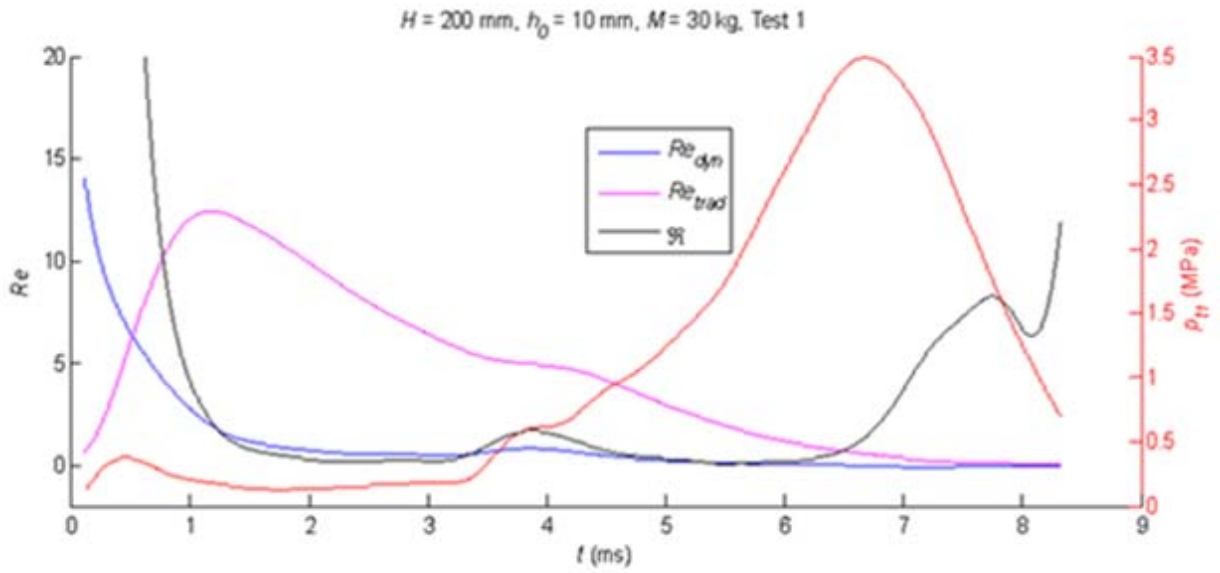


Figure 8-11: Traditional and dynamic Reynolds numbers and inertial composition vs time

Before the various quasi-steady models are applied to the reference test, it is important to determine whether or not a quasi-steady approximation is applicable for the theoretical modelling of the above experimental results. Hence the evolution ratio $X$ (Section 5.9, p. 36) is recalled as the magnitude of the partial time-derivative term divided by the inertial terms used in determining the QSL model (Sections 5.6, p. 26). Thus $X$ is desired to be as low as possible to validate the quasi-steady approximations made by both the QSL model and the QSCL model (Sections 5.7, p. 32). The evolution ratio is recalled from equation (5-33) as

$$X \equiv \left| \frac{2}{3\left[\frac{\ddot{h}}{\dot{h}} - \frac{2\dot{h}}{h}\right]} \dot{f}\Big|_{z^*=1/2} \right|$$

where $\dot{f}\big|_{z^*=1/2}$ is calculated by equation (5-35)[a], which makes use of the values in Table 5-1, as elaborated upon in Section 5.9, p. 36. The evolution ratio is plotted with respect to time in Figure 8-12.

[a] The shape parameter values used in determining the evolution ratio number are pre-emptively obtained from Figure 8-13.

Figure 8-12 truncates the sharp $X$ spike occurring at $t = 6.6$ ms which corresponds to $\lambda = 0$. Notwithstanding this spike, $X$ predominantly lies below 10% throughout the experimental stroke, with a subsidiary spike peaking at $X{\sim}30\%$ at $t = 1.1$ ms, the beginning of the bridging region. In general, the averaged magnitude of $X$ is similar to that obtained for the CFD experiment shown in Figure 6-11, p. 59; thus $X$ may tentatively be considered as sufficiently small throughout the experimental stroke for a quasi-steady approximation to be considered accurate. This therefore permits the applications of both QSCL and QSL models.

Theoretical pressure traces are obtained by inserting instantaneous experimental values of $h, \dot{h}$ and $\ddot{h}$ and fluid constants $\nu$, $\mu$ and $\rho$ into the following models:

- *Lubrication Approximation* [equation (2-8)] defined in Sections 2.4, p. 8.
- *Inviscid/Inertial Model* [equation (5-2)] defined in Sections 5.1, p. 20.
- *QSL Model* [equations (5-16) and (5-31)] defined in Sections 5.6, p.26.
- *QSCL Model* [equations (5-29) and (5-31)] defined in Sections 5.7, p.32.

*The above theoretical pressure traces are then compared against experimentally measured pressures in order to test the respective models validity*. It is emphasized that, in principle, the above comparative technique is no different (for example) to substituting specified values of $\dot{h}$ into the well documented lubrication approximation to obtain a theoretical disc separation trace.

All of the above modes predict invariably parabolic radial pressure distributions, hence only the central theoretical pressure traces ($r^* = 0$) of these models are compared against the central pressure transducer trace. However, it must be recalled that the experimentally measured central pressure traces have un-quantified associated non-parabolic pressure distributions and circumferential offset pressure, especially during the preliminary pressure spike (refer to Figure 8-6 and associated text). Hence direct comparisons between experimentally measured and theoretical central pressure traces must be made tentatively.

In order to generate central pressure traces for the QSL and QSCL models, the instantaneous values of the shape parameter and corrected shape parameter are required. The shape parameter [equation (5-16), p. 26] and corrected shape parameter [equation (5-29), p. 33] are respectively recalled as follows

$$\lambda \equiv \frac{1}{\nu}\left(\frac{\ddot{h}h^2 - 2\dot{h}^2 h}{\dot{h}}\right) \qquad \text{and} \qquad \lambda_{cor} \equiv \frac{1}{\nu}\left[\frac{\ddot{h}h^2 + (\kappa - 2)\dot{h}^2 h}{\dot{h}}\right]$$

in which the linearization variable $\kappa$ is given by the polynomial as a function of $\lambda$ in Figure 5-5, p. 32. Both the shape parameter and corrected shape parameter are plotted on a log scale against time in Figure 8-13, in which $\lambda$ and $\lambda_{cor}$ are plotted as solid lines whereas $-\lambda$ and $-\lambda_{cor}$ are plotted as dashed lines. Uncertainty bounds for $\lambda$ are calculated by inserting the upper and lower fluid viscosity limits (arising from temperature change) and the upper and lower disc separation uncertainty limits (laser sensor measurement tolerance) into equation (5-16), p. 26, while disc velocity and acceleration are assumed to be absolutely accurate (uncertainties unavailable due to the use of smoothing algorithms). Subsequently the upper and lower limits (traces) of $\lambda$ are used to obtain the upper and lower limits of $\kappa$, which in turn are used to calculate the uncertainty of $\lambda_{cor}$ (explained above). Hence the upper and lower uncertainty bounds of $\lambda_{cor}$ are included in Figure 8-13, however for the sake of clarity the uncertainties of $\lambda$ are omitted.

In addition to ultimately calculating the theoretical central pressures, the shape parameter and corrected shape parameter traces can be used to calculate the instantaneous dimensionless radial fluid velocity profiles by equations (5-19) and (5-24). Alternatively, using Figure 5-3, p. 30, the approximate dimensionless radial fluid velocity profiles may be inferred. However, it must be recalled that an asymmetrical squeezing motion is experimentally induced (Section 2.1.2, p. 3), whereas the theory assumes a symmetrical squeezing motion, so the experimental dimensionless radial fluid velocities would differ slightly (become skewed as a function of disc velocity) from those theoretically predicted.

At the peak of the preliminary pressure spike, $\lambda \approx \lambda_{cor} \approx 5000$ (Figure 8-13), hence a radial flow with a well defined boundary layer and associated high sheer stresses at the disc interfaces is established. During the major pressure spike, $\lambda \approx \lambda_{cor} \approx 0$, hence the radial flow tends to a parabolic velocity profile (lubrication approximation). The minimum measured value for the shape parameter at the termination of the experimental stroke is $\lambda \approx \lambda_{cor} \approx -0.4$; therefore the resultant minimum dimensionless radial fluid velocity would never appear visually different from a parabolic velocity profile (Figure 5-3, p. 30).

The instantaneous values of $\lambda$ and $\lambda_{cor}$ are used to derive corresponding $f''|_{z^*=0}$ values calculated by the polynomial curve fits given in Figures 5-6 and 5-7, p. 35. In turn, these $f''|_{z^*=0}$ values are substituted into equation (5-31) (Section 5.8, p. 34) recalled as

$$p = \frac{R^2\mu}{4}\frac{\dot{h}}{h^3} f''|_{z^*=0}\left(1 - r^{*2}\right)$$

to yield the respective central pressure traces of the QSL and the QSCL models (the circumferential pressure offset is assumed to be zero).

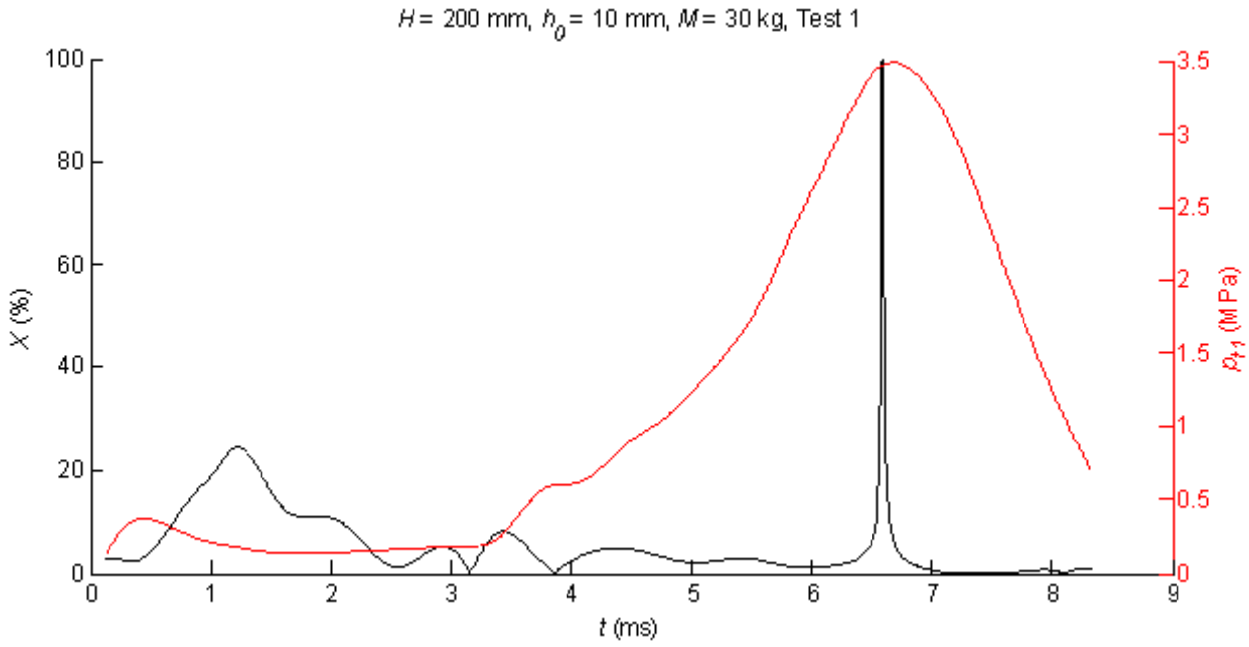


Figure 8-12: Evolution ratio and central pressure vs time

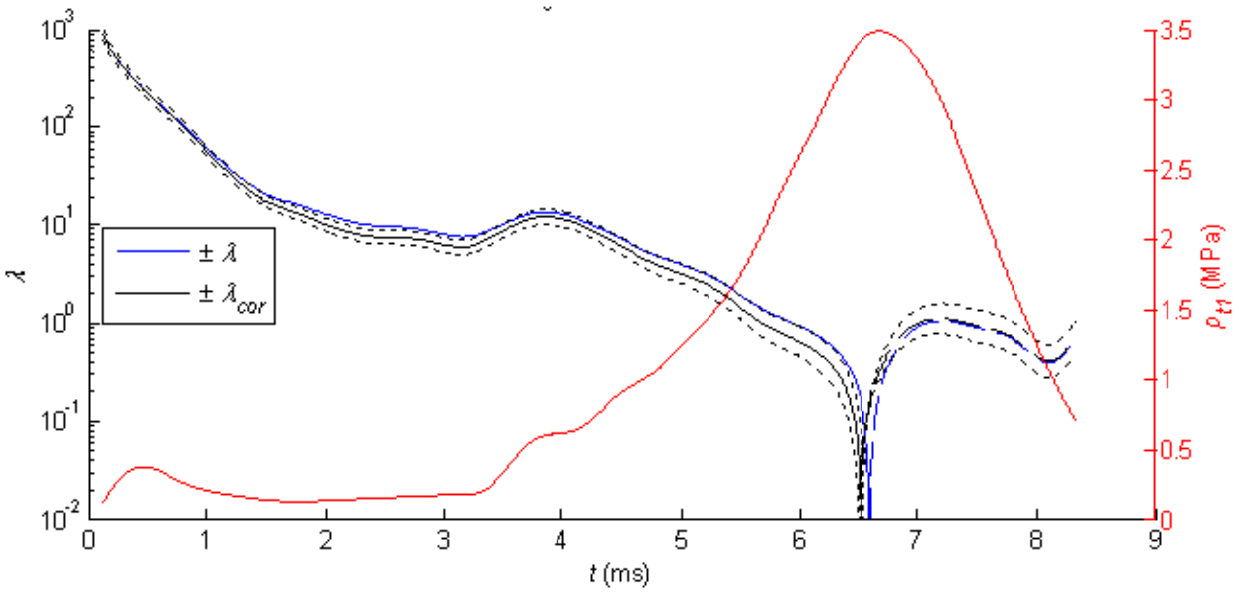


Figure 8-13: Shape parameter, corrected shape parameter and central pressure vs time.

The central pressure traces of the QSL and QSCL models are plotted alongside the experimental pressure traces in Figure 8-14. Also included are the upper and lower uncertainty bounds of the QSCL model given by red dotted lines. The uncertainty bounds of the QSL model are omitted for the sake of neatness (they are similar to those of the QSCL model). These uncertainty bounds are calculated in a similar way in which $\lambda$ and $\lambda_{cor}$ are calculated, in that viscosity and disc separation measurement uncertainties are included in equation (5-31) in addition to the uncertainties of $\lambda_{cor}$.

The QSL and QSCL pressure traces are very similar, but the QSCL model produces marginally more accurate (closer to experimental) results during the bridging region during which disc velocities are highest (magnified insert in Figure 8-14). The uncertainty bounds of the QSCL trace overlap those of the experimental pressure trace for the entire experiment with the exception of the tail end of the experimental stroke and the initial development of preliminary pressure spike (Figure 8-14 insert). Corresponding to this initial inaccuracy, it can be seen that the theoretical preliminary pressure spike lags behind the experimental pressure trace by approximately 200 μs. It is speculated that this theoretical lag is due to second order effects such as rig flexure, laser sensor frequency response lag and smoothing errors.

Superimposing the central pressure traces of the *simplistic models*, namely the *lubrication approximation* and *inviscid/inertial model*, alongside the experimentally measured central pressure trace yields Figure 8-15. Figure 8-15 is plotted directly below Figure 8-14 to promote visual comparison between all theoretically modelled pressure traces. Uncertainty bounds of these simplistic models are also included in Figure 8-15 which are calculated in a similar way to those of the QSCL model. Due to the assumed disc acceleration accuracy, the inviscid/inertial model has a negligible associated uncertainty, whereas the uncertainty bound of the lubrication approximation is comparable to that of the QSCL model.

Both the QSL and QSCL models (Figure 8-14) show a marked increase in accuracy over the lubrication approximation and inviscid/inertial model (Figure 8-15). Nevertheless, it can be seen that the pressure trace of the inviscid/inertial model corresponds relatively accurately with the experimentally measured preliminary pressure spike, whereas the pressure trace of the lubrication approximation corresponds relatively accurately with the experimentally measured major pressure spike Therefore, for the sake of a *simplistic approximation* the *preliminary pressure spike* may be approximated to be *inertial dominant* (and is approximately modelled by the inviscid/inertial model) whereas the *major pressure spike* may be assumed to be *viscous dominant* (and is approximately modelled by the lubrication approximation).

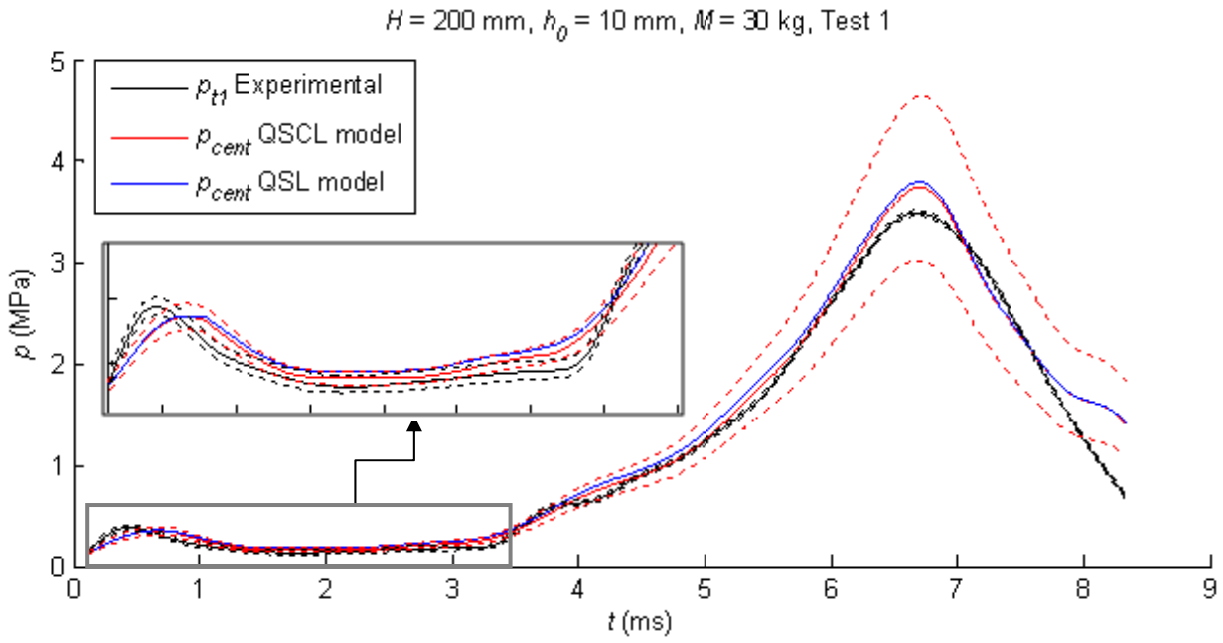


Figure 8-14: Experimental and the QSCL and QSL models central pressures vs time

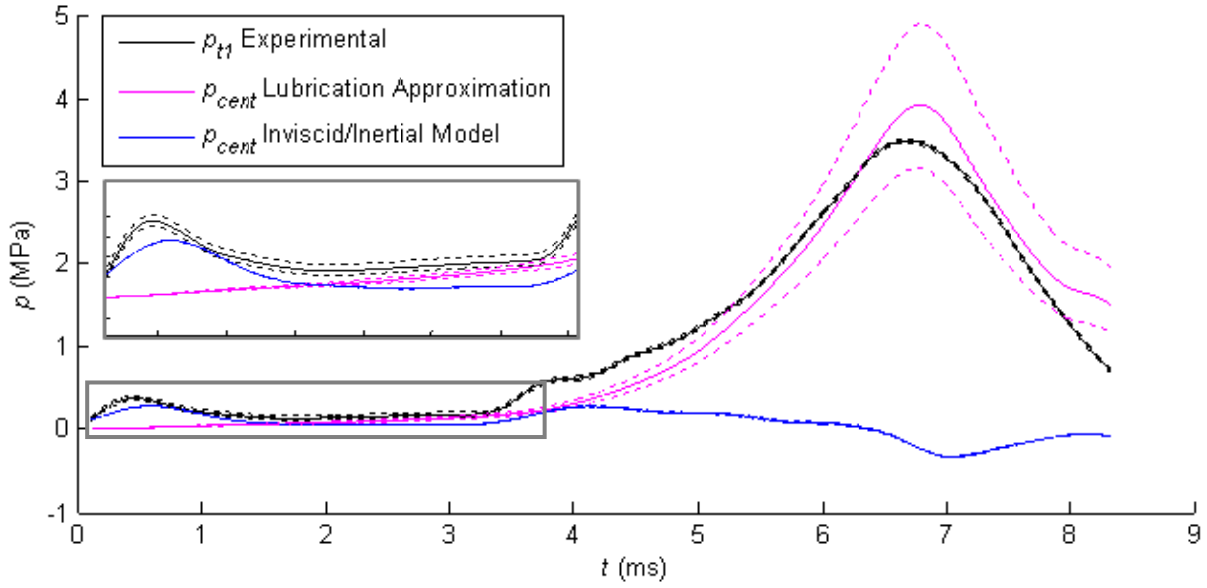


Figure 8-15: Experimental and simplistic theoretical central pressures vs time

## 8.2 Contact-Hammer Test Results

Contact-hammer tests are a special set of drop-hammer tests where the drop height is set to zero before the experimental stroke initiation, i.e. the drop-hammer makes contact with the plunger before the initiation of the experimental stroke. As a consequence of the low energies involved in contact-hammer tests the resultant pressures are relatively low ( $p_{max} < 0.6$ MPa). Hence in order to maximise the pressures measured during the contact-hammer tests, both the initial disc separation and the drop-hammer mass are set to their maximum values of 18 mm and 55 kg respectively. Therefore, only a single contact-hammer test-set is performed so that the resultant maximum resultant pressure is approximately two orders of magnitude greater than the ambient noise of the pressure transducers.

Contact-hammer tests have a resultant central pressure trace as shown on the left-hand scale of Figure 8-16. In addition the velocity and acceleration traces have been plotted on the right-hand scale.

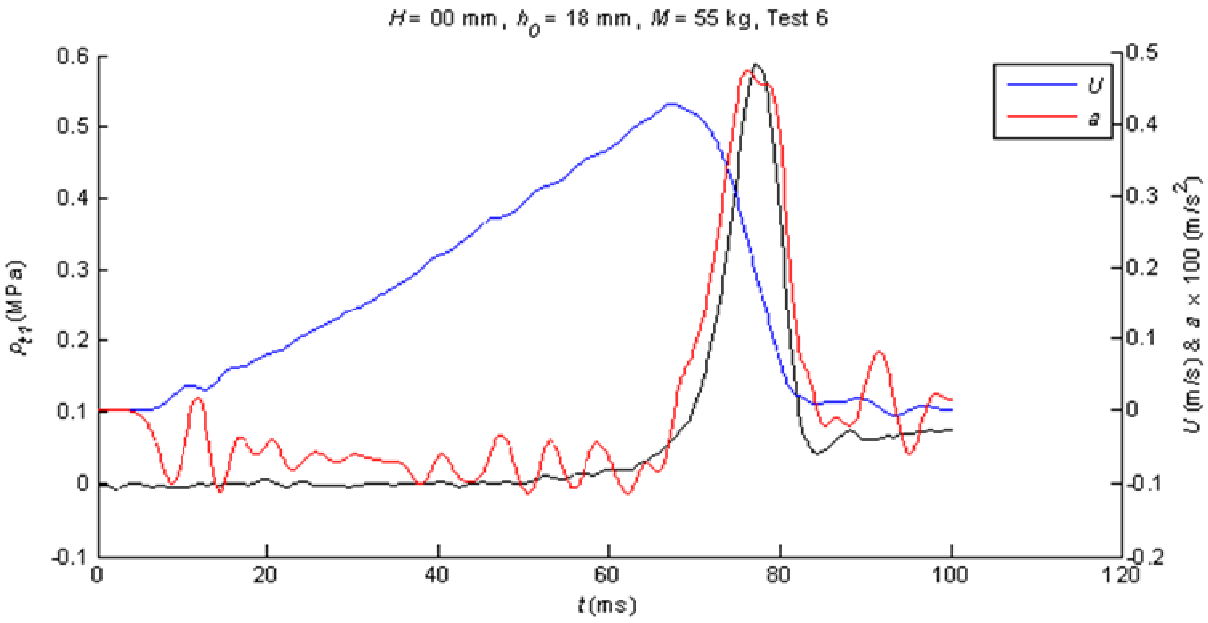


Figure 8-16: Central pressure, velocity and acceleration vs time (contact-hammer test)

Comparing this contact-hammer test against a drop-hammer test (reference test), i.e. Figure 8-16 versus Figure 8-2, p. 98, the following differences are noted:

i. The contact-hammer test has no large negative acceleration during the stroke initiation (associated with the drop-hammer impact) and therefore no preliminary pressure spike, only pressure transducer noise until $t > 60$ ms.
ii. The contact-hammer test has a maximum velocity of approximately one order of magnitude smaller than drop-hammer tests.
iii. The experimental stroke period of the contact-hammer test is approximately one order of magnitude larger than drop-hammer tests.

It is also noted that the contact-hammer test (Figure 8-16) has good correlation between the major pressure spike trace and the positive acceleration trace [unlike the above drop-hammer tests (Figure 8-2, p. 98)]. It may therefore be inferred that no significant bouncing occurs between the plunger and the drop-hammer. This inference is further supported by an average acceleration of approximately -8 $ms^{-2}$ during $0 < t < 60$ ms, which correlates to a slightly retarded gravitational free-fall.

Viewing the pressure distributions based on an inferred least-square second order polynomial fit (as previously performed in Figure 8-5, p. 103, and described in the associated text) yields Figure 8-17. Alternatively viewing the pressure measurements and associated pressure distribution variation as a 3-dimensional plot (as previously composed in Figure 8-9 and described in associated text) yields Figure 8-18.

Both Figures 8-17 and 8-18 show that the pressure distribution is close to parabolic. However, from Figure 8-17 it can be seen that this parabolic pressure distribution is associated with a back pressure of up to 25 kPa during the major pressure spike. It is speculated that this back pressure arises from the elastic strain of the rapidly inflated fluid bladder (Section 7.2.2, p. 70). This circumferential offset pressure generation mechanism is negligible in the context of drop-hammer tests due to the substantially higher pressures generated.

Plotting the shape parameter during the major pressure spike yields Figure 8-19, it can be seen that the shape parameter has a comparatively narrow range of $-0.9 < \lambda < 3.5$, i.e. visually indistinguishable from a parabolic radial velocity (Figure 5-3, p. 30). This indicates that during contact-hammer tests, the pressure development of the major pressure spike is viscous dominant. This conclusion is supported by the similarity (less than 2% difference) of the central pressure traces of the QSCL model and lubrication

approximation in Figure 8-20, both of which correspond well (entirely within uncertainty bounds) to the experimentally measured central pressure trace.

Although not included within any of the figures, the evolution ratio $X$ lies within the narrow range of $X < 1.5\%$, with the exception of the sharp $X$ spike corresponding to $\lambda = 0$. This small value suggests that term $C_1$' of equation (5-10) is negligible throughout the contact-hammer experiment and hence a quasi-steady approximation is applicable.

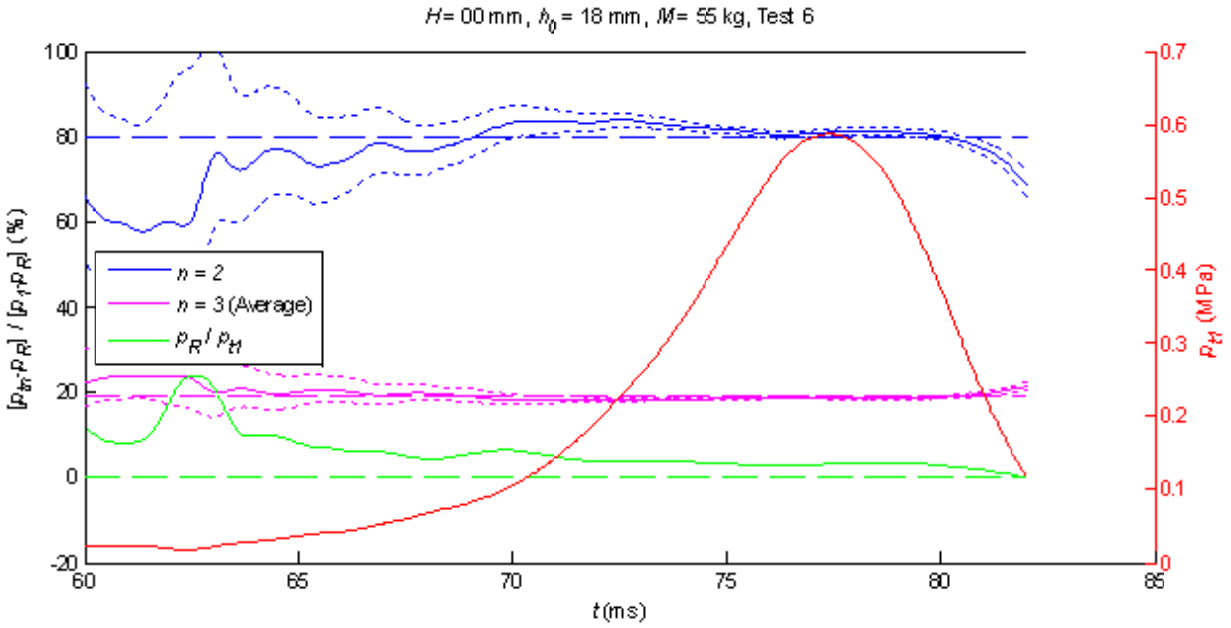


Figure 8-17: Normalised pressure distributions (poly-fit cor) and central pressure vs time (contact-hammer test)

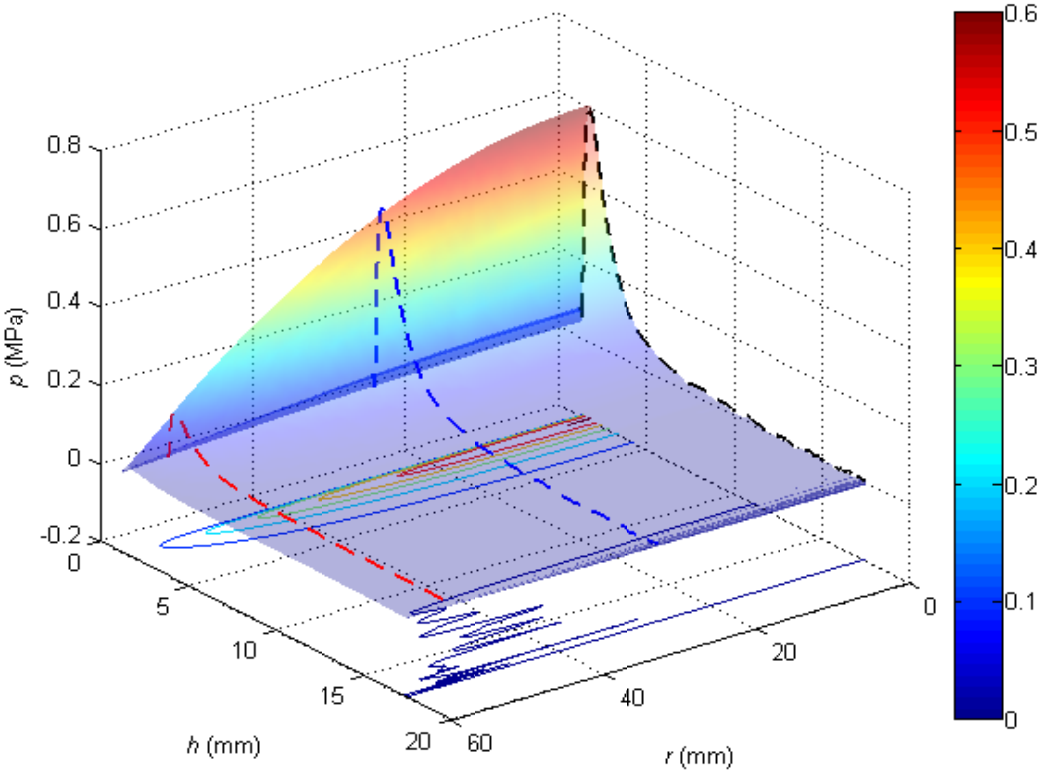


Figure 8-18: Pressure vs disc separation vs radius (contact-hammer test)

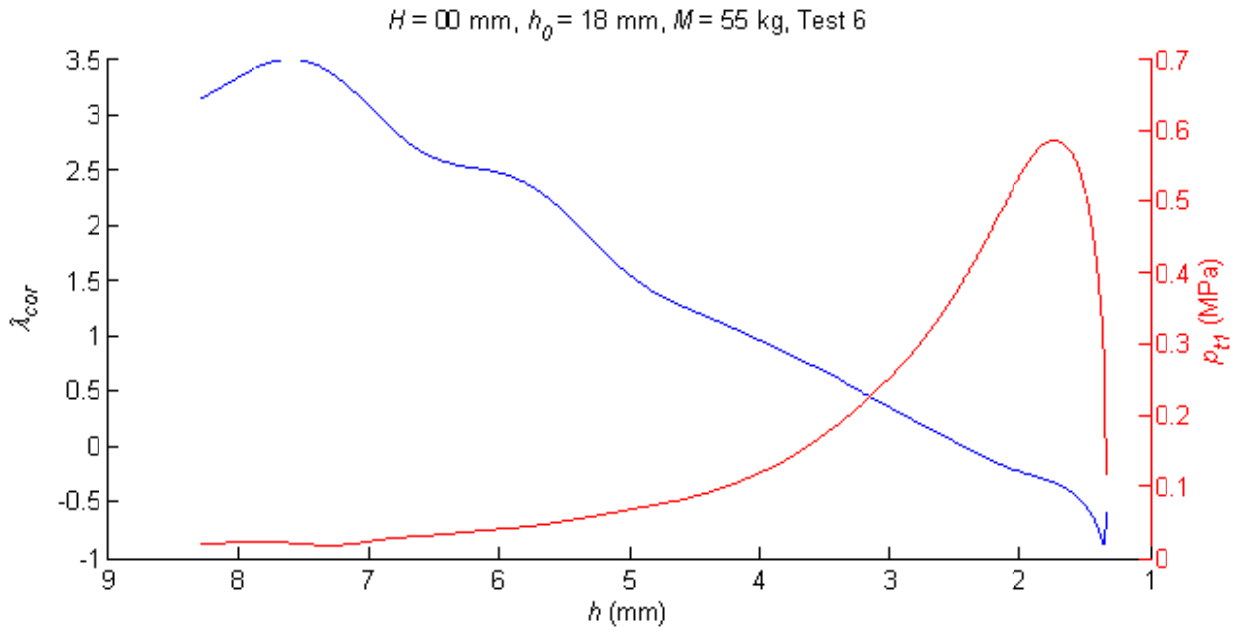


Figure 8-19: Shape parameter variation and central pressure vs disc separation (contact-hammer test)

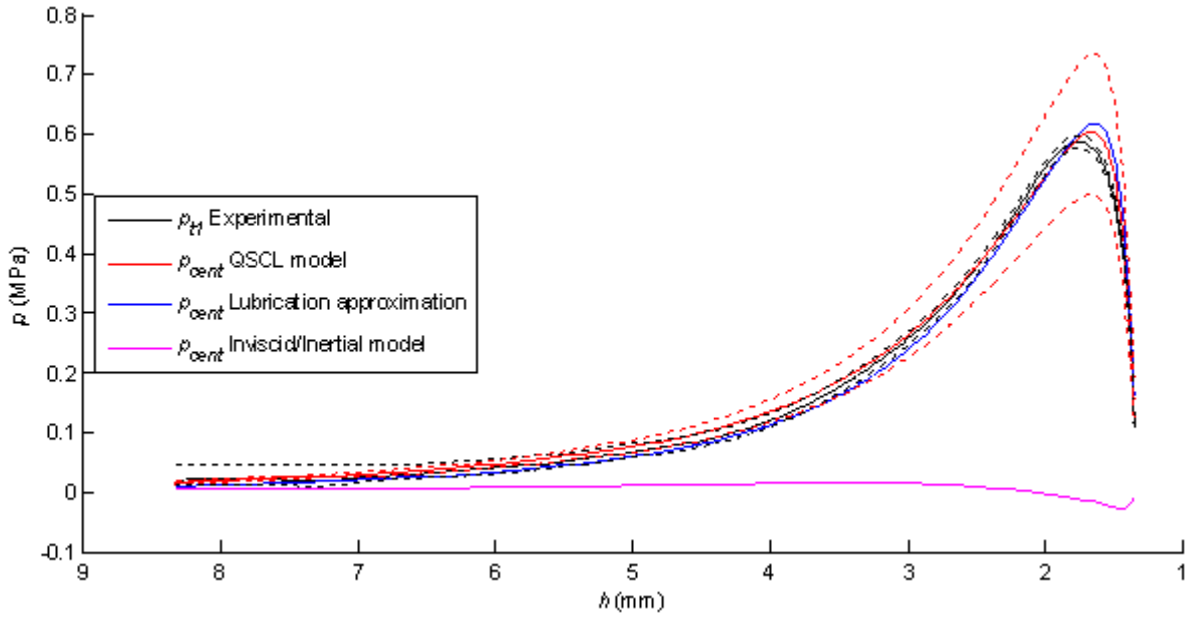


Figure 8-20: Experimental and theoretical central pressures vs disc separation (contact-hammer test)

## 8.3 Repeatability of Results

As stated in Section 7.1, p. 65, every test-set consists of a minimum of five repeated tests. Tests are repeated in order to determine the experimental repeatability or consistency. Superimposing various variables on the same axes allows visual assessment of experimental repeatability. Hence through this process outlying tests may be identified and eliminated before the respective test-set is averaged. These averaged tests are in turn used to yield varying parameter carpet plots as defined in Section 8.4, p. 125.

A test-set with an initial dropped height of 500 mm, as opposed to the 200 mm of the reference test is analysed for experimental consistency within this section. The superimposed pressure traces for $p_{t1}$, $p_{t2}$ and $p_{t3a}$ are shown in Figure 8-21.

Figure 8-21 shows that the five superimposed pressure traces for $p_{t1}$ are acceptably repeatable, with a spread of only about 3% during the major pressure spike peak. The repeatability of pressure traces of pressure transducers 2 and 3a have discrepancies of up to 6% during the major pressure spike. This latter trend is also true for the pressure traces of pressure transducers 3b and c, however, for the sake of brevity these plots are omitted.

It can be seen in Figure 8-21 that there are discrepancies in the initial disc separation of up to 0.3 mm. Such experimental errors can be attributed to grit being caught in between the magnetic clip and the plunger (see assembly diagram on p. 70).

Figure 8-22 shows five superimposed uncorrected (a) and eccentricity corrected (b) normalised pressure distribution 2 traces [Section 7.5.2, p. 90, equation (7-13)], which are placed directly on top of each other to aid visual comparison. The eccentricity correction of normalised pressure distribution 2 is most accurate where the circumferential pressure is relatively small; i.e. the major pressure spike (see Figure 8-5 and the associated text), which is expected because temporal inertia affects are small. Hence during the major pressure spike ($4 > h > 0.8$ mm) the spread is reduced by up to 65%. This illustrates the effectiveness of the eccentricity correcting model in correcting axi-asymmetric parabolic pressure distributions.

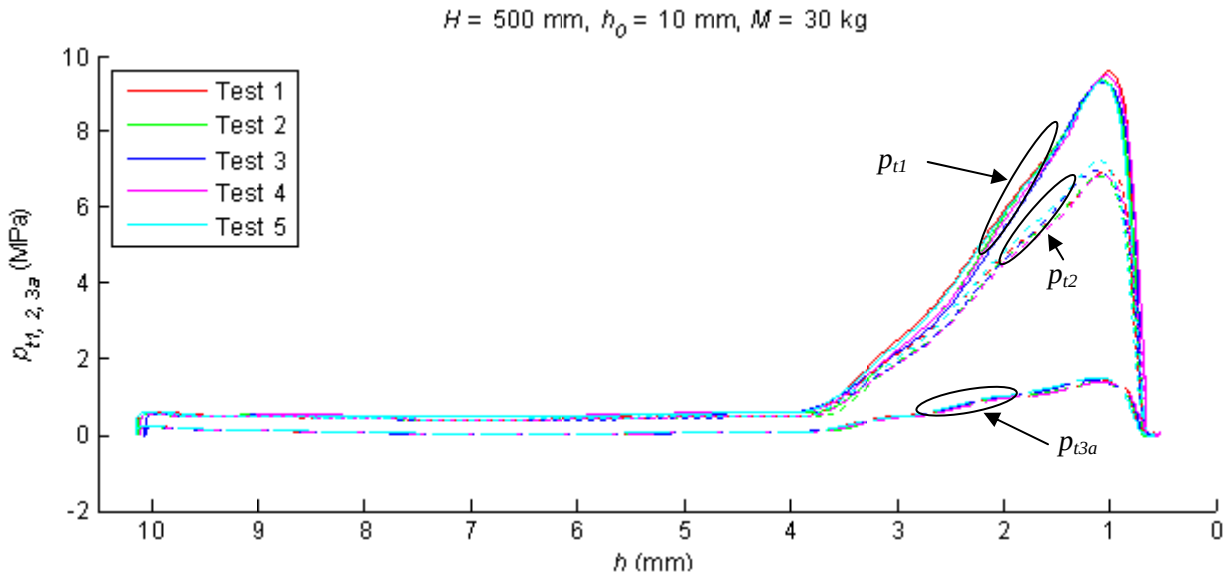


Figure 8-21: Pressure transducers 1, 2 and 3a vs disc separation (superimposed test-set results)

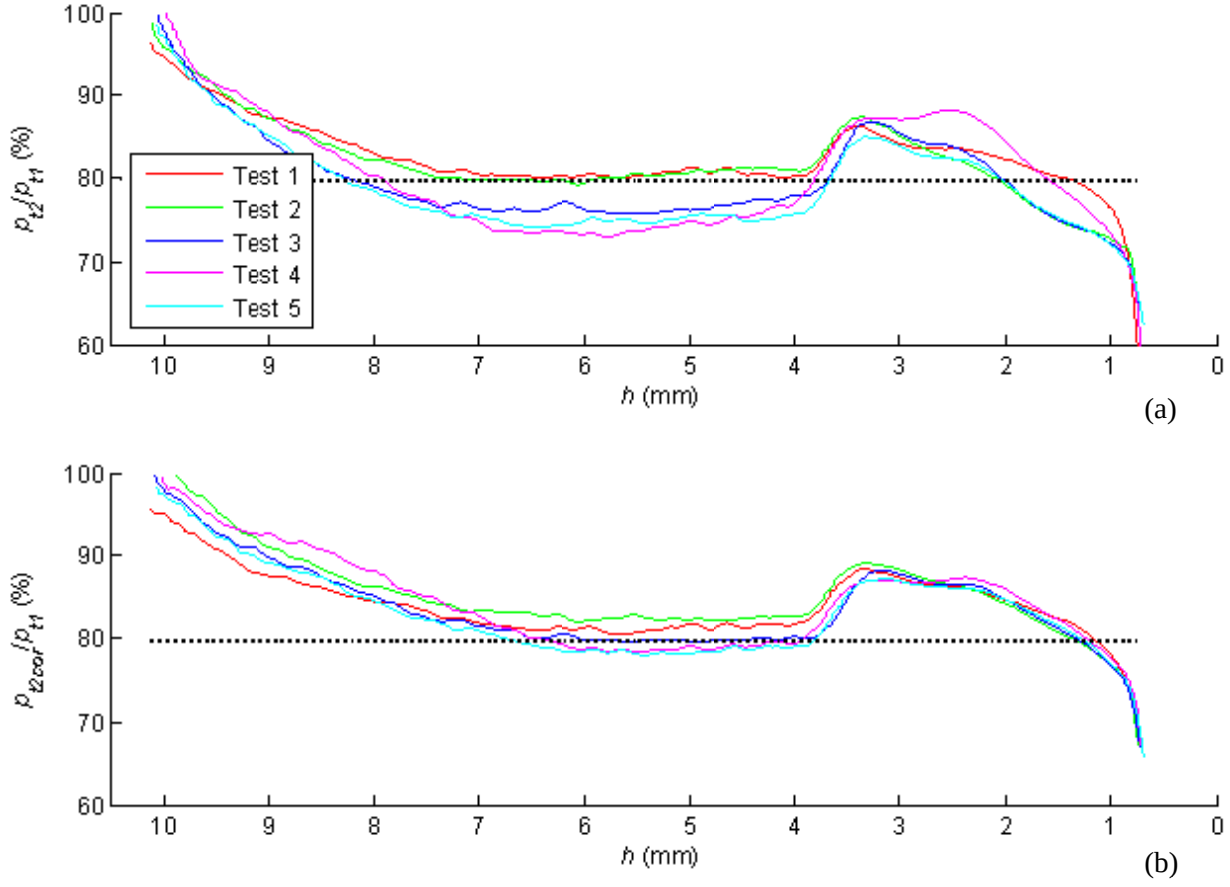


Figure 8-22: Uncorrected (a) and eccentricity corrected (b) normalised pressure distribution 2 vs disc separation (superimposed test-set results)

Normalised pressure distribution 3a, 3b, 3c and 3ave [the average value (Section 7.5.2, p. 90)] are grouped together in Figure 8-23 (a) to (d) to aid visual comparison. It can be seen in Figure 8-23 that normalised pressure distribution 3ave has approximately one third the spread of 3a, 3b or 3c, hence yielding more accurate results.

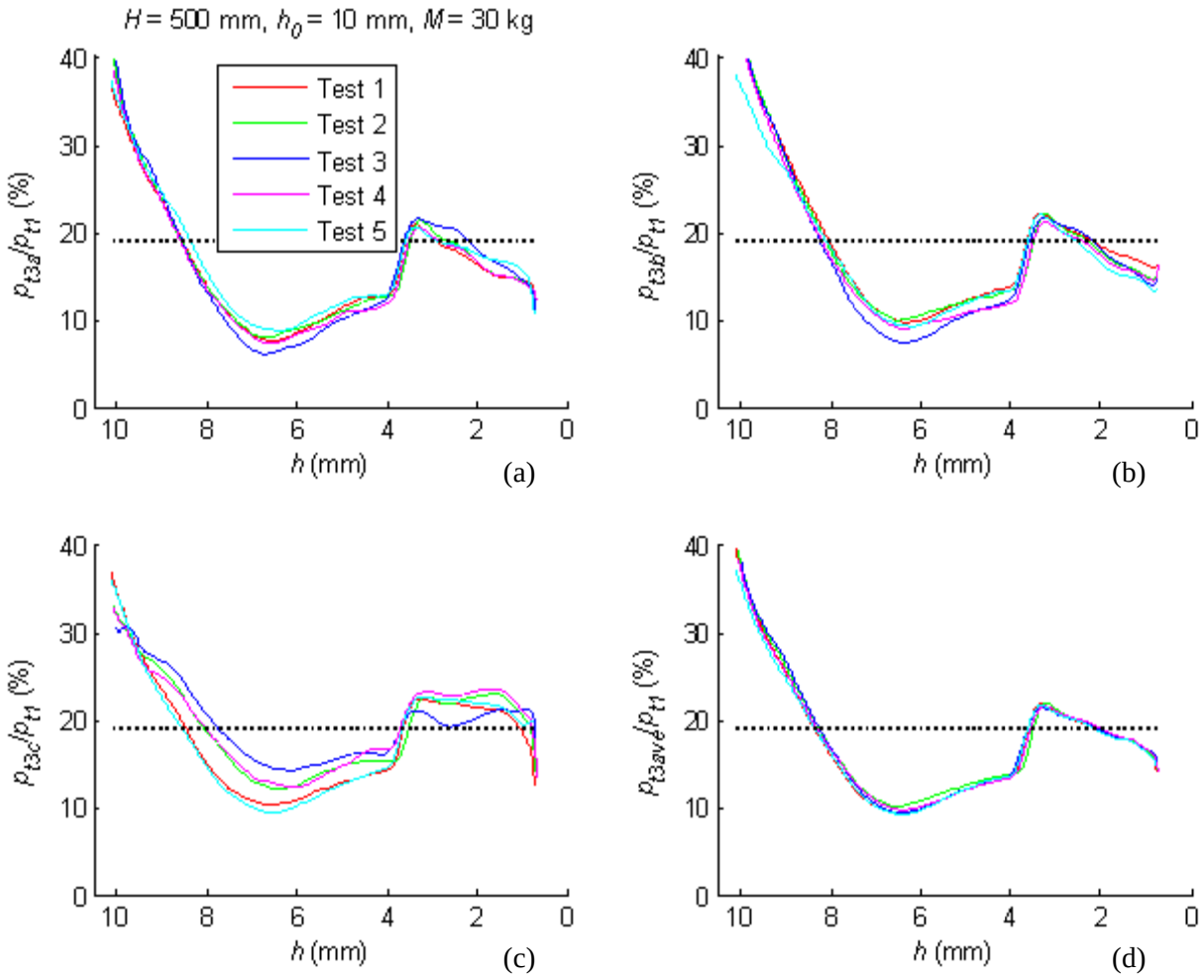


Figure 8-23: Normalised pressure distribution 3a (a), 3b (b), 3c (c) and 3ave (d) vs disc separation (superimposed test-set results)

When disc separation vs time traces are superimposed on the same axis, the result appears as a thick curve from which no visually ascertainable differences between the individual traces can be made, so this plot is omitted. However, this spread becomes more pronounced with increasing time derivatives; hence the superimposed plots of disc velocity vs separation and disc acceleration vs separation are given in Figures 8-24 and 8-25 respectively.

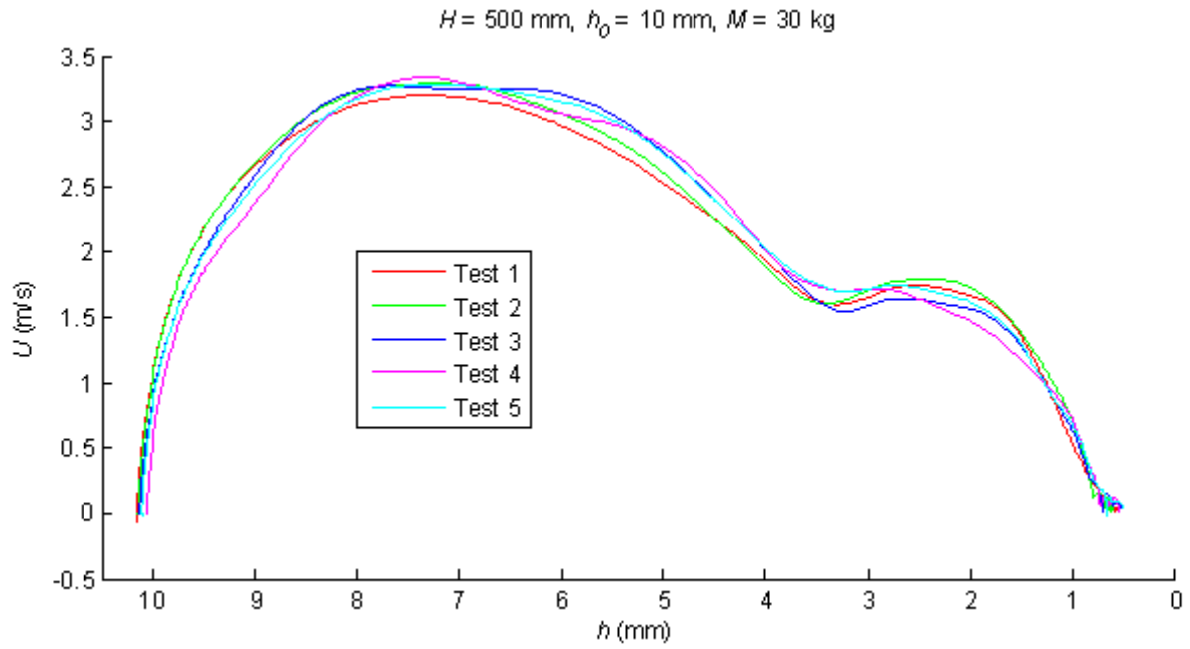


Figure 8-24: Velocity vs disc separation (superimposed test-set results)

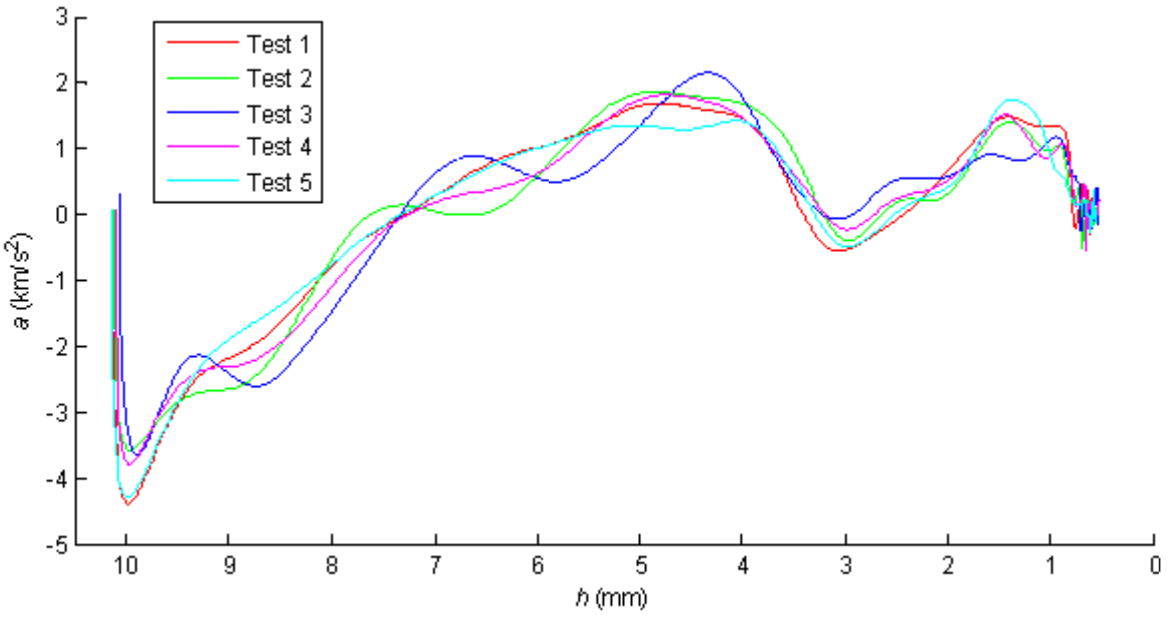


Figure 8-25: Acceleration vs disc separation (superimposed test-set results)

Figure 8-24 shows an appreciable spread of velocity traces throughout the experimental stroke. However, the general shapes of the velocity traces are very similar and therefore no outlying tests were identified.

On the other hand, Figure 8-25 shows that test 3 strays most significantly from the mean spread of the acceleration traces, particularly during the major pressure spike ($4 > h > 0.5$ mm). Therefore, test 3 is omitted from the test-set before the experimental variables are aggregated to produce the averaged test with parameters given by $H$ = 500 mm, $h_0$ = 10 mm and $M$ = 30 kg (Section 7.5.4, p. 94). The outlying tests for every test-set are listed in the Excel 'Exclusion table' in CD-Appendix C

## 8.4 Final Results

Various aggregated experimental variables [obtained from averaged tests (Section 7.5.4, p. 94)] including central pressure, normalized pressure distribution values, disc velocity and acceleration may in principle be obtained as a function of drop height ($H$), drop mass ($M$) and initial disc separation ($h_0$) as independent parameters. Hence varying parameter carpet plots have been constructed by (i.) varying $H$ while keeping $M$ and $h_0$ constant, (ii.) varying $M$ while keeping $H$ and $h_0$ constant, and (iii.) varying $h_0$ while keeping $H$ and $M$ constant. These are reflected in Sections 8.4.1 to 8.4.3 respectively.

### 8.4.1 Drop height variation

Figure 8-26 shows the variation of central pressure traces with disc separation for $h_0 \approx 10$ mm corresponding to ten drop heights (ten 3-dimensional line plots). In addition, a carpet plot is fitted (interpolated) to these ten 3-dimensional line plots so that pressure at any given disc separation and drop height can be visually interpolated by means of the corresponding colour-bar (right of the figure). Finally a contour plot is displayed on the floor of Figure 8-26, where the contour lines correspond to the marked increments of the colour-bar. Hence it can be seen that the shapes (scale) of the major pressure spikes appear virtually proportional to drop height.

Similarly Figure 8-27 shows the preliminary pressure spikes as a function of drop height (identical to Figure 8-26 with magnified z-axis and truncated y-axis). It can be seen that the preliminary pressure spikes also appear to be scaled with drop height. The jagged edge at the stroke initiation in Figure 8-35 is due to the truncation operations used to yield the carpet plots.

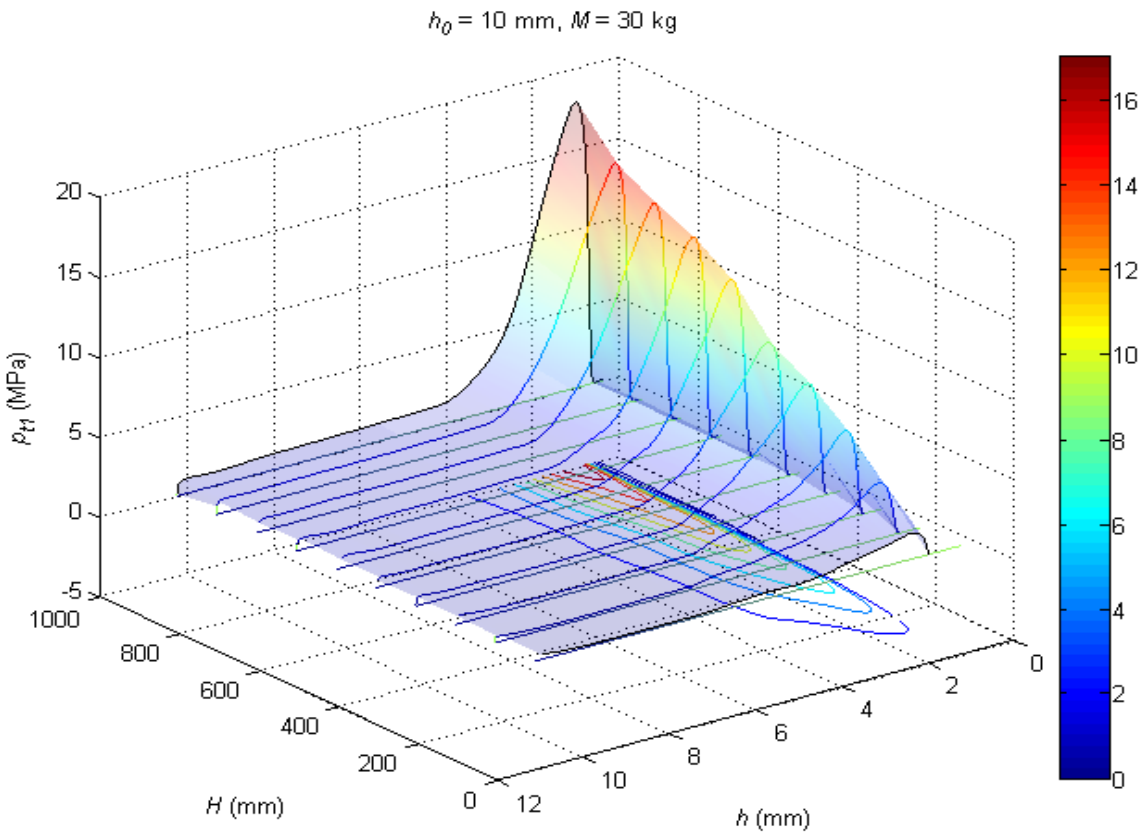


Figure 8-26: Central pressure vs drop height vs disc separation

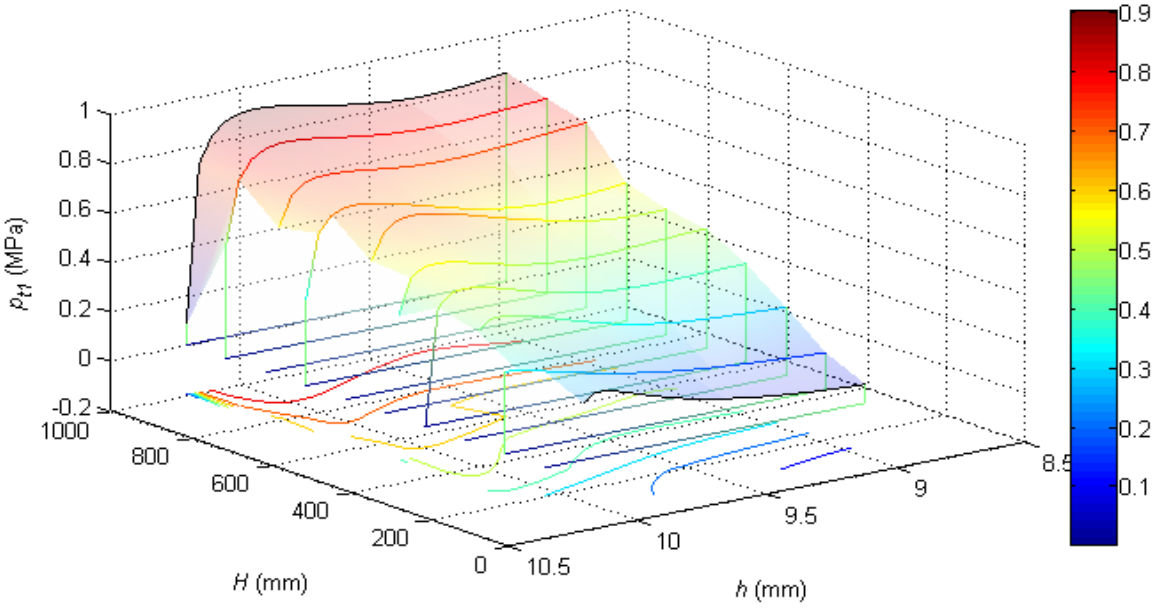


Figure 8-27: Central pressure vs drop height vs preliminary disc separation

Likewise, Figures 8-28 and 8-29 respectively show the variation of disc velocity and acceleration with disc separation for $h_0 \approx 10$ mm corresponding to ten drop heights (ten 3-dimensional line plots). These 3-dimensional plots are augmented with auxiliary contour plots to their right.

Included within the auxiliary contour plots are black dotted lines, which represent the separations at which the maximum pressures (of the major pressure spikes) occur. They are called the *peak pressure lines* and are from now on included in all auxiliary contour plots.

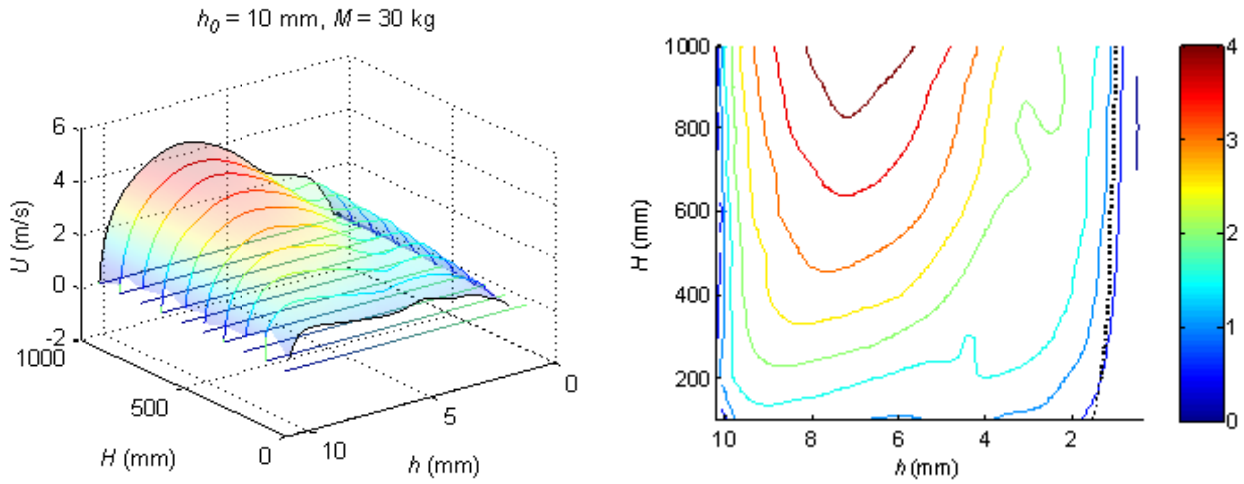


Figure 8-28: Disc velocity vs drop height vs disc separation

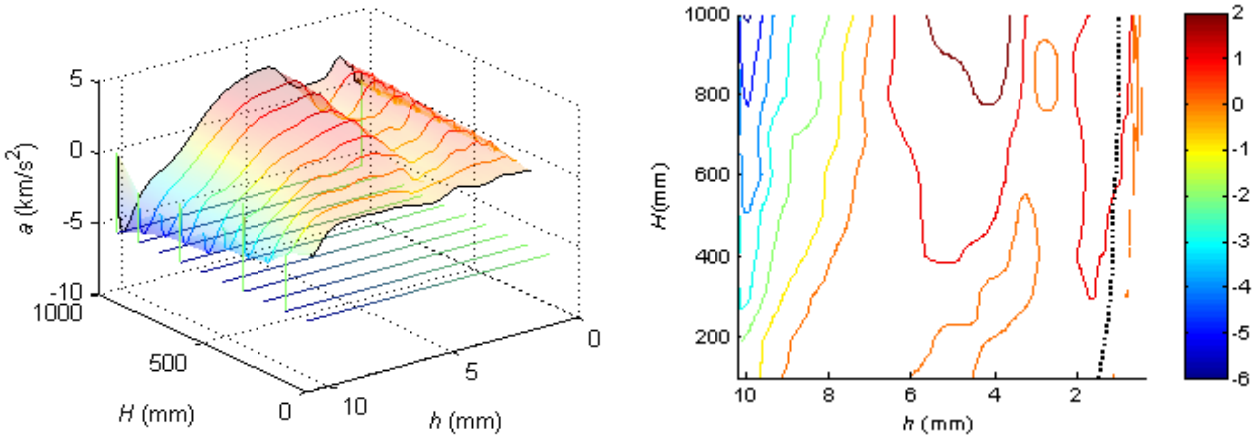


Figure 8-29: Disc acceleration vs drop height vs disc separation

Figure 8-29 shows that during the preliminary pressure spike peaks ($h_0 \approx 10$ mm), the disc acceleration increases approximately linearly with increasing drop height.

When following the peak pressure lines in the contour plots of Figure 8-28, it can be seen that for $H > 300$ mm, all major pressure spikes occur at $U \sim 0.75$ m/s. The lubrication approximation [equation (2-8), p. 8] shows that $p \propto U/h^3$, or $h \propto \sqrt[3]{1/p}$ when applied to this above observation. This asymptotic relationship is experimentally observed (but not quantified) by the peak pressure lines ($1 \leq h \leq 1.5$ mm) in the auxiliary contour plots (most apparent in subsequent Figure 8-30 due to the magnified disc separation axis). Hence this simplistic analysis and supports the claim that the major pressure spike is a viscous dominant feature.

A further simplistic analysis has been conducted in which the preliminary pressure spike is approximated as being inertial dominant. When conducting an order of magnitude analysis to the inviscid/inertial model [equation (5-2), p.20] during the preliminary region ($h > 9$ mm), it can be shown that $p \propto a/h$ (using instantaneous values of $h, \dot{h}$ and $\ddot{h}$ ascertained from Figures 8-28 and 8-29). Figure 8-27 shows that the preliminary pressure spike occurs at an approximately constant disc separation and Figure 8-29 shows that the disc acceleration is proportional to the drop height, $a \propto H$. Applying these observations to the above inviscid/inertial approximation results in $p \propto H$, which is experimentally observed in Figure 8-27, thus supporting this simplistic analysis.

Figure 8-30 shows the experimental central pressure variations with drop height (a) measured experimentally, (b) modelled by the QSCL model and (c) modelled by the lubrication approximation. Both theoretical models of the central pressure variation with increasing drop height appear to correlate satisfactorily with that experimentally measured during the major pressure spike. However, the peak pressure lines in the auxiliary contour plots indicate that the disc separation at which the peak pressures occur are more accurately modelled by the QSCL model than by the lubrication approximation. Moreover, it can also be seen from the auxiliary contour plots that the magnitudes of the developing major pressure spikes are more accurately modelled by the QSCL model than by the lubrication approximation. The above correlations have previously been observed in isolation for the reference test as shown in Figures 8-15 and 8-14.

On the other hand for larger drop heights of $H > 500$ mm, it can be seen in from Figure 8-30 that the central pressure variation of the QSCL model becomes increasingly erratic with drop height relative to the lubrication approximation (view the jagged edge of the major pressure spike in Figure 8-30b).

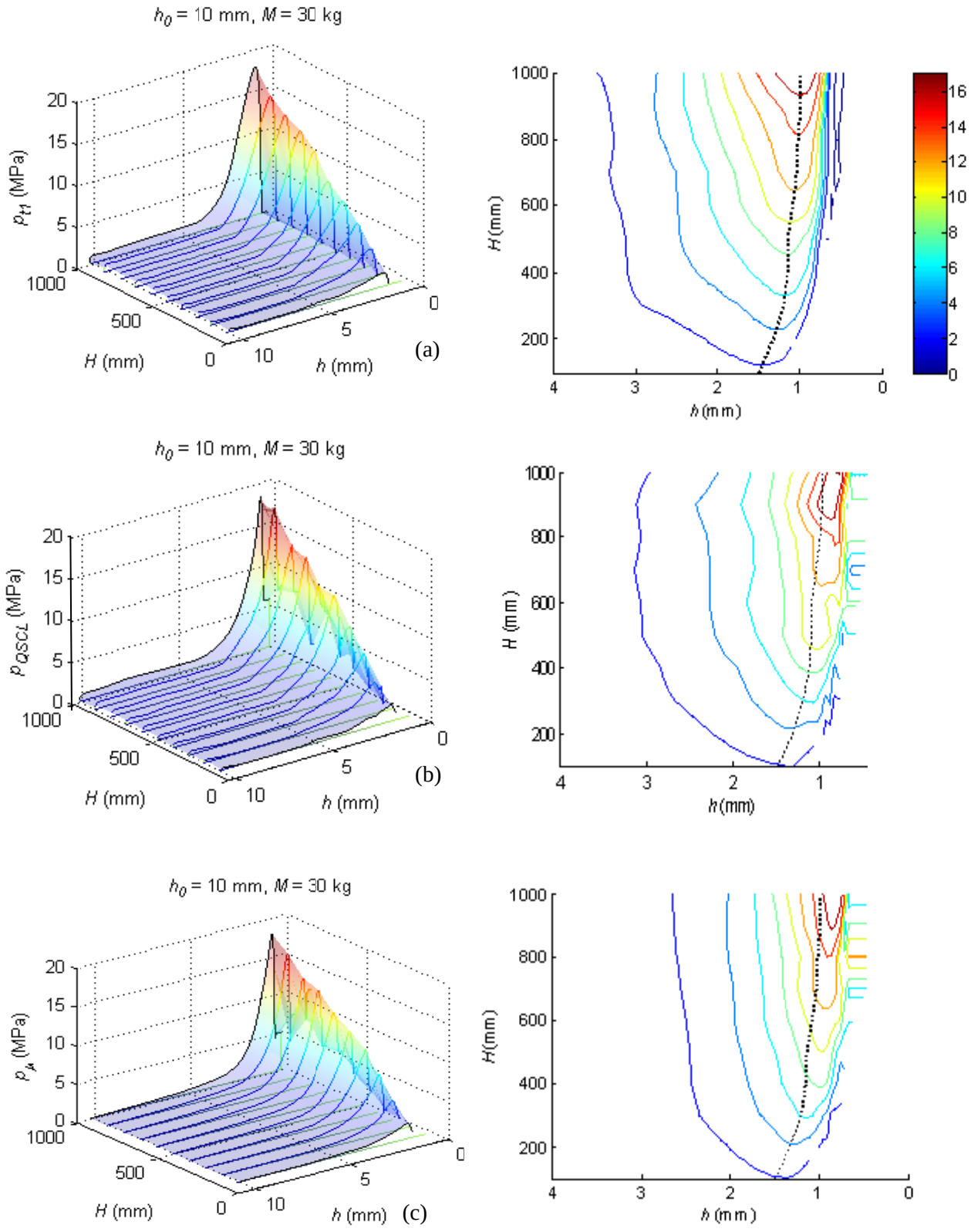


Figure 8-30: Central pressure vs drop height vs disc separation: (a) Experimental (b) QSCL model (c) Lubrication approximation

Figure 8-31 shows the variations of the preliminary pressure spike with drop height (a) measured experimentally, (b) modelled by the QSCL model, (c) modelled by the lubrication approximation and (d) modelled by the inviscid/inertial model (identical to Figure 8-30 with magnified z-axis and truncated y-axis).

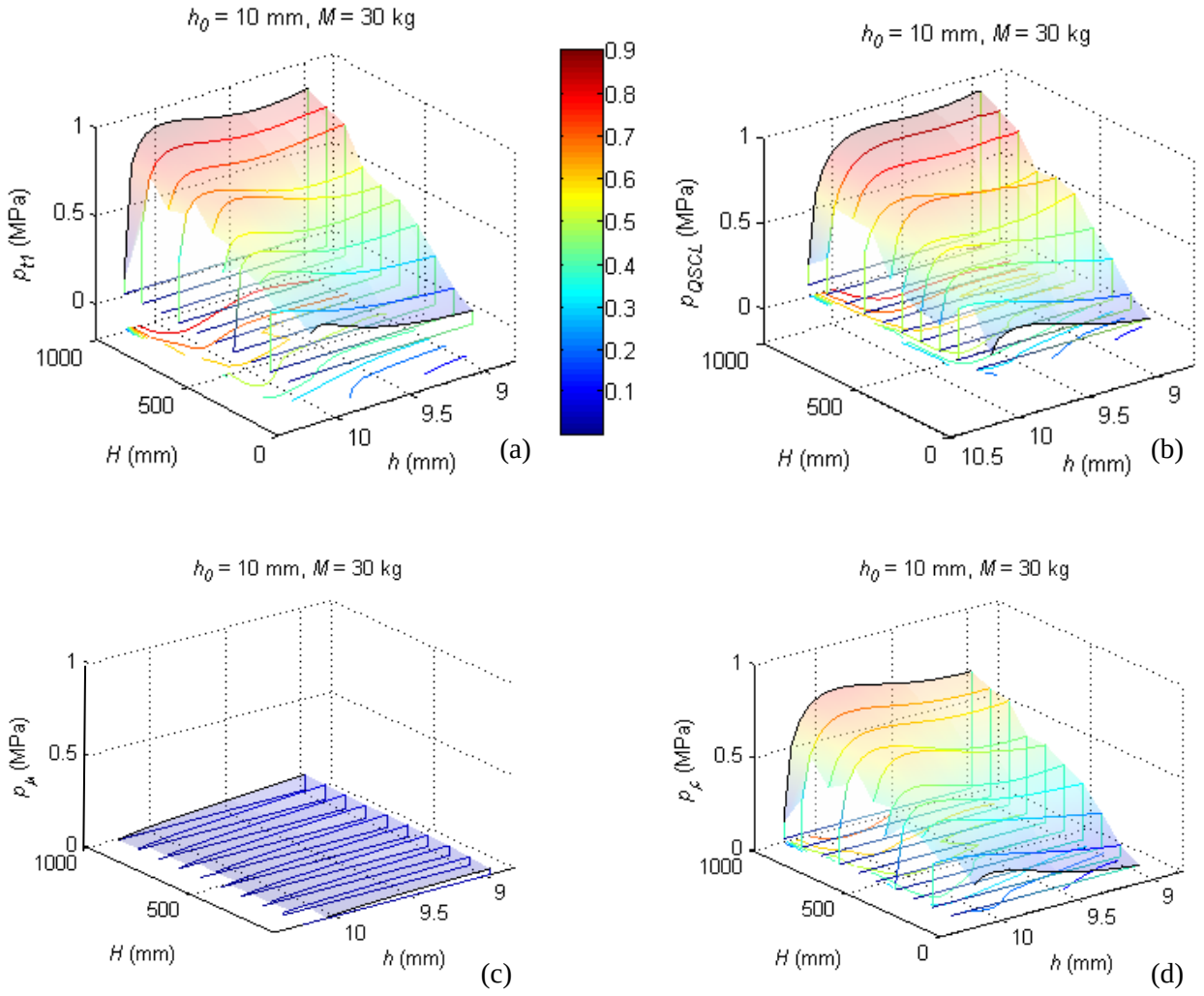


Figure 8-31: Central pressure vs drop height vs preliminary disc separation: (a) Experimental (b) QSCL model (c) Lubrication approximation (d) Inviscid/Inertial model

Figure 8-31 shows that the preliminary pressure spikes developed by the QSCL model correspond satisfactorily on a visual basis with the experimental results. Likewise the inviscid/inertial model shows similar trends albeit at an approximately 20% lower magnitude. It is also noted that the preliminary

pressure spikes of the theoretical models are more rounded towards the peak magnitudes than those of the experimental results. It is speculated that this deviation is due to second order effects such as rounding errors. As expected, the lubrication approximation does not develop a preliminary pressure spike. The above correlations have previously been observed in isolation for the reference test as shown in Figures 8-15 and 8-14 (similar to the major pressure spike correlations).

Figure 8-32 shows the eccentricity corrected normalised pressure distribution 2 traces (Section 7.5.2, p. 90) and the averaged normalised pressure distribution 3 traces (Section 7.5.2, p. 90) versus disc separation corresponding to ten drop heights. It can be seen that the normalised pressure distribution values are relatively stable between $4 > h > 1$ mm (between the initial development and peak of the major pressure spike) where $p_{t2cor}/p_{t1} \approx 80\%$ and $p_{t3ave}/p_{t1} \approx 20\%$ indicating that the radial pressure distribution is approximately parabolic and is not offset by a significant circumferential pressure. However, during the decline of the major pressure spike ($h < 1$ mm), these distribution values become unstable.

On the other hand, during the preliminary pressure spike and the bridging region ($10 > h > 4$ mm), the normalised pressure distribution values in Figure 8-32 follow a trend virtually independent of drop height, which is identical to the trend established by the reference test (Section 8.1.3, p. 99). Hence during the preliminary pressure spike it is strongly suggested that a non-parabolic radial pressure distribution is established with an associated offset pressure (Section 8.1.3, p.99).

Figure 8-33 shows the gravitational potential energy $E_G$ and the work due to pressure $W_{pre}$ (Section 8.1.5, p. 107.) plotted against drop height (for all drop height test-sets). The $W_{pre}$ values used to compose the $W_{pre}$ curve are taken as the average value for each test-set, whereas the upper and lower $W_{pre}$ uncertainty bounds (included as dotted lines) correspond to the upper and lower values of tests within the test-sets. It can be seen that $E_G \propto H$ since $M$ and $g$ are constants. Furthermore, it can be seen that $W_{pre}$ also increases approximately linearly with respect to drop height; therefore after introducing a mean energy transfer coefficient of $\bar{\eta} = 65\%$ [equation (8-2)] it can be seen that the $W_{pre}$ trace corresponds satisfactorily to $\bar{\eta}E_G$ (largely within error bounds). This relationship is expected because the major pressure spike (the dominant energy dissipation mechanism) is also linearly scaled with increasing drop height (Figure 8-26) and the associated pressure distributions are relatively independent of drop height (Figure 8-32).

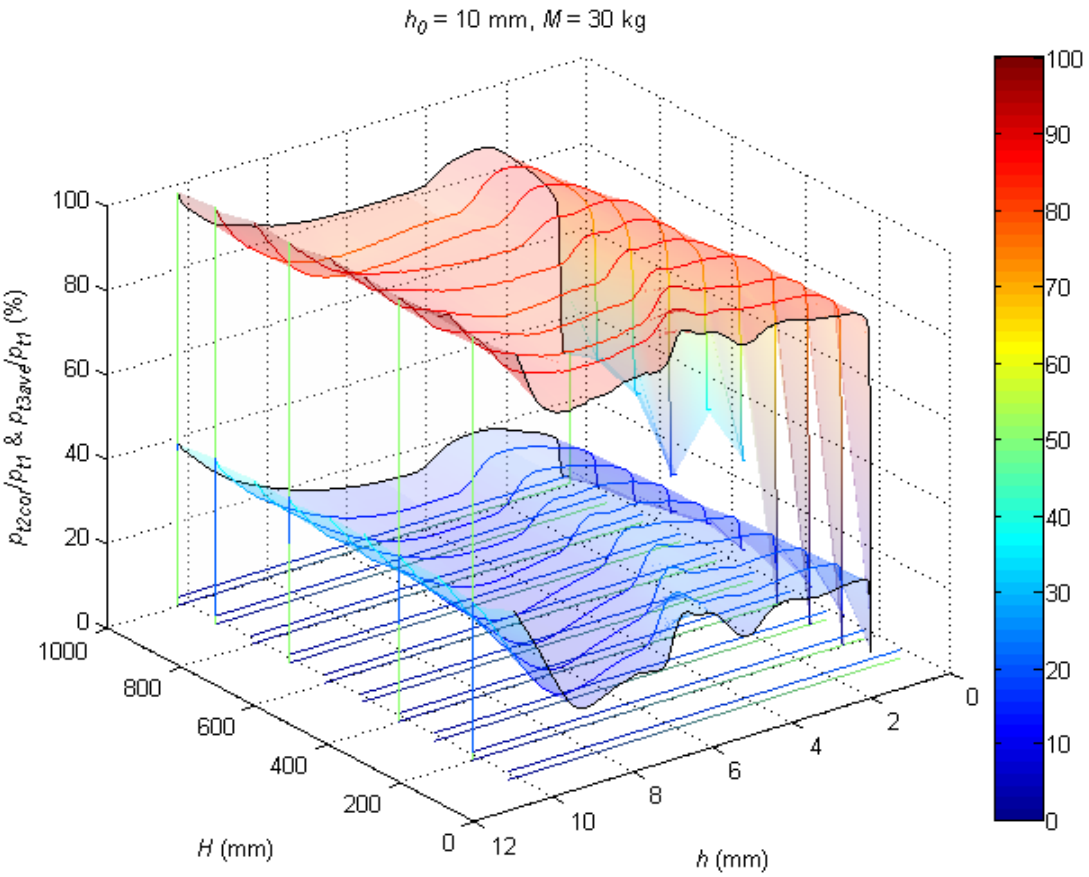


Figure 8-32: Normalised pressure distribution 2(cor) and 3(ave) vs drop height vs disc separation

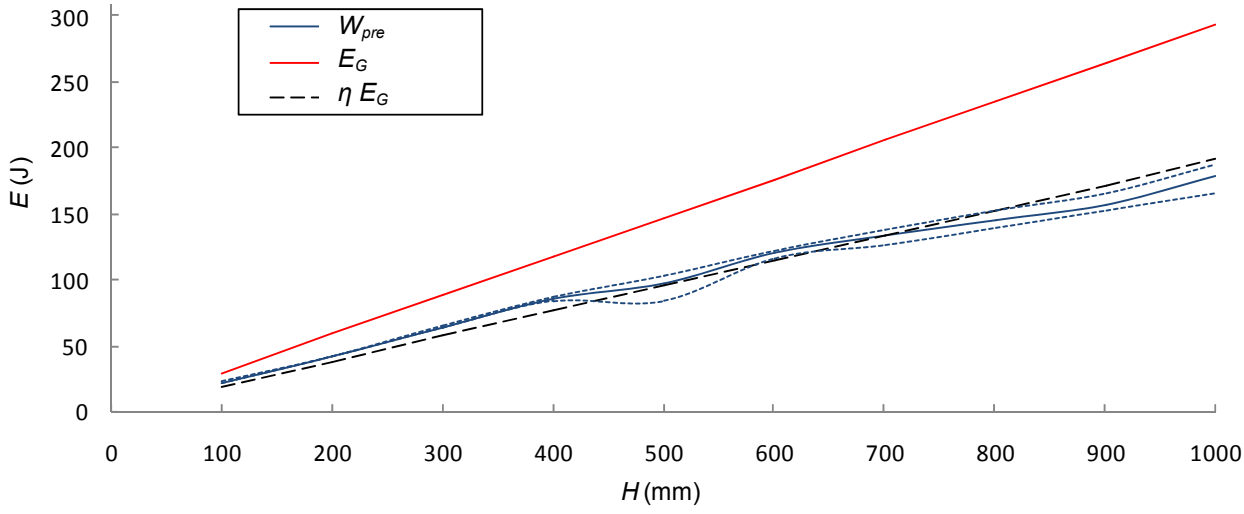


Figure 8-33: Energy vs drop height

### 8.4.2 Drop mass variation

The plots presented within this section are developed the identical way in which the drop height variation plots are developed, therefore descriptions of the construction of the plots presented within this section are omitted but can be referenced by the paragraphs following the corresponding plots of drop height variation in Section 8.4.1, p. 125. Furthermore, many of the trends observed for drop mass variations are identical to those for drop height variations, therefore similar trend descriptions and evaluations are referred to in Section 8.4.1, p. 125.

Figure 8-34 shows the variation of central pressure traces with disc separation for $h_0 \approx 10\,\text{mm}$ corresponding to ten drop masses (ten 3-dimensional line plots). It can be seen that the scaling of major pressure spikes appear to be proportional to drop mass, similar to that of the drop height variation (Figure 8-26). However, unlike the drop height variations, when the preliminary pressure spikes are viewed in Figure 8-35, it can be seen that the preliminary pressure spikes are also virtually independent of drop mass.

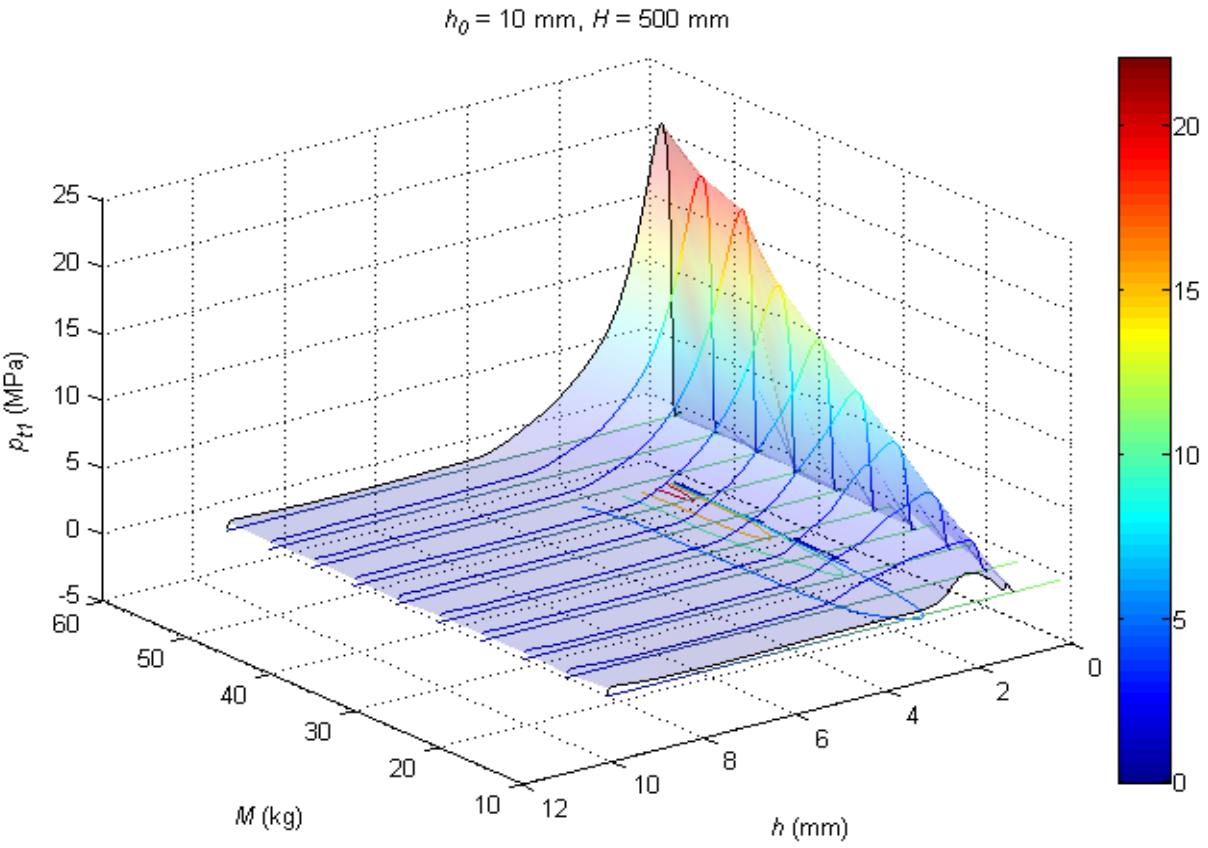


Figure 8-34: Central pressure vs drop mass vs disc separation

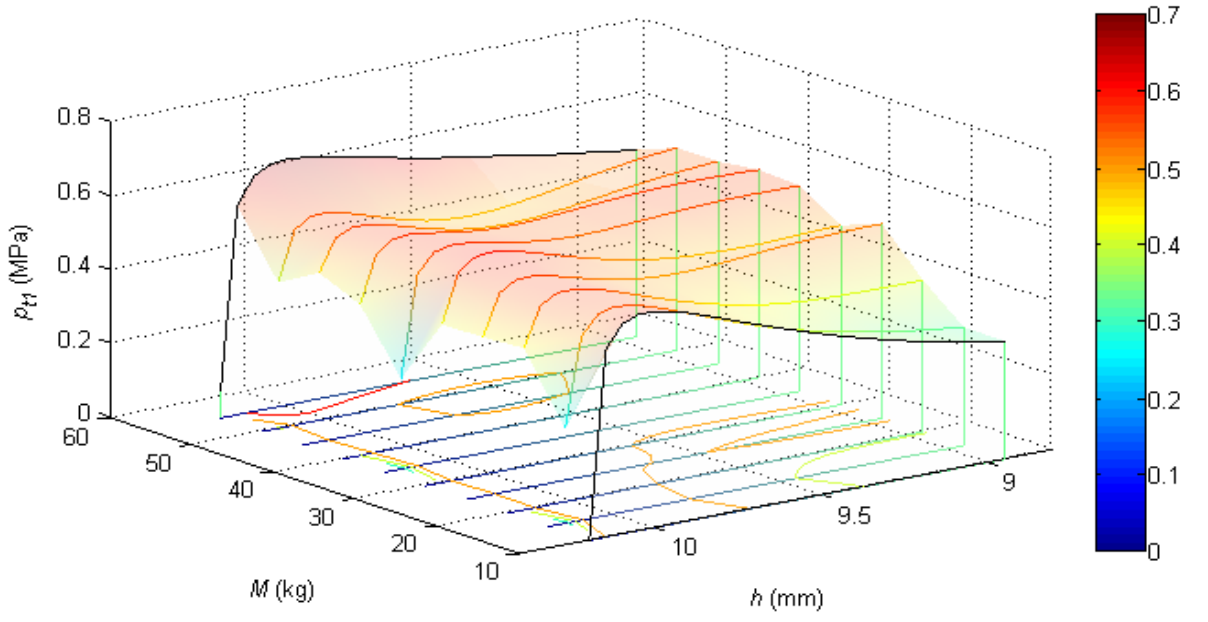


Figure 8-35: Central pressure vs drop mass vs preliminary disc separation

Similarly, Figures 8-36 and 8-37 respectively show the variation of disc velocity and acceleration with disc separation for $h_0 \approx 10$ mm corresponding to ten drop masses (ten 3-dimensional line plots). It can be seen that during the preliminary disc separation ($h > 9$ mm), the disc velocity and acceleration are approximately independent of the drop mass; this is due to the drop-hammer impacting the plunger at similar velocities for every test-set (regardless of drop-mass) and therefore inducing near identical preliminary disc velocities and accelerations throughout the preliminary stages of the disc separation. As expected the result of this relatively consistent disc separation, velocity and acceleration give relatively invariant preliminary pressure spikes, as previously shown in Figure 8-35.

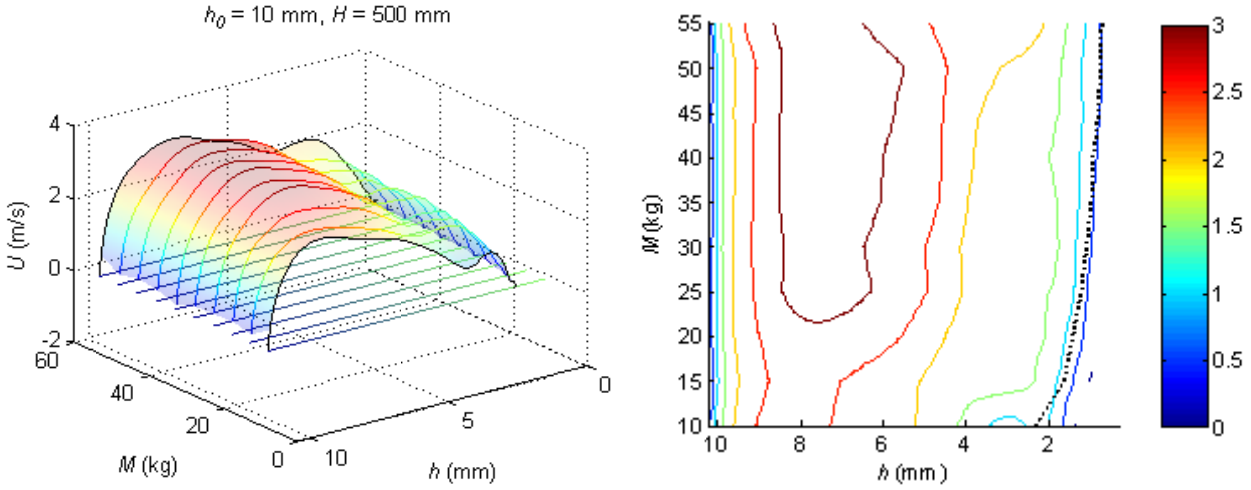


Figure 8-36: Disc velocity vs drop mass vs disc separation

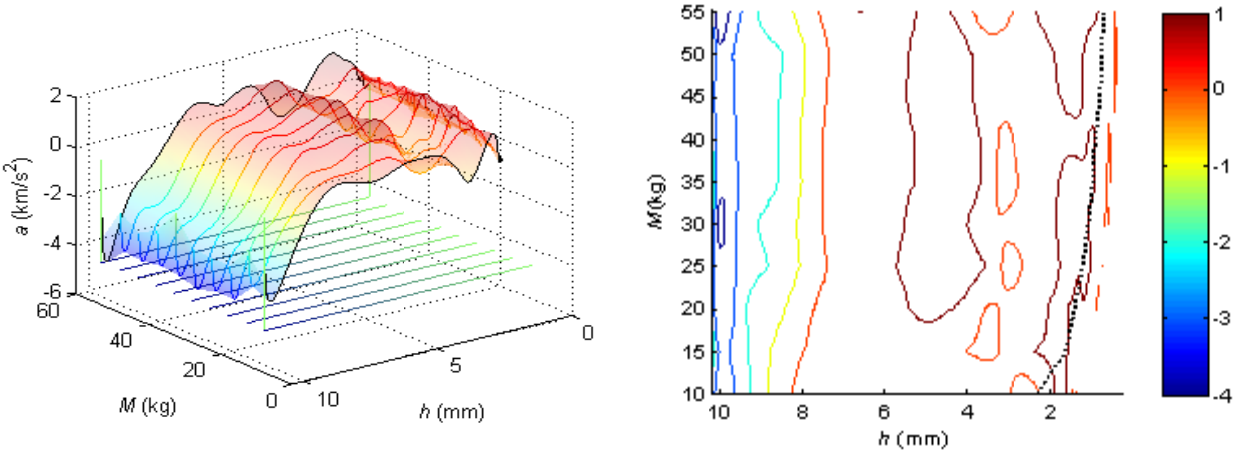


Figure 8-37: Disc acceleration vs drop mass vs disc separation

By following the peak pressure lines in the auxiliary contour plots of Figures 8-36 and 8-37 for $M >$ 15 kg, it can be seen that all major pressure spikes occur at relatively stable disc accelerations $a \sim 1$ km/s$^2$ and velocities $U \sim 0.5$ m/s, irrespective of drop mass. On close investigation of the disc velocities at the peak pressure line (Figure 8-36), it is counterintuitive to note that the velocities actually decrease slightly with increasing major pressure spike magnitudes, albeit through a limited disc velocity range of $0.75 \leq U \leq 0.5$ m/s. Furthermore, similarly to drop height variation, the peak pressure line tends asymptotically towards zero disc separation as drop mass increases, within limits of $0.7 \leq h \leq 2.3$ mm (intercepting $h = 1$ mm at $M \approx 30$ kg). Therefore, similar to the drop height variations, the above observations are supportive of the major pressure spike being approximated as a lubrication approximation (Section 8.4.1, p. 125).

Figure 8-38 show the experimental central pressure variations with drop mass (a) measured experimentally, (b) modelled by the QSCL model and (c) modelled by the lubrication approximation. For lower drop masses of $M \leq 35$, both theoretical models show the central pressure variation with increasing drop mass correlates satisfactorily with that experimentally measured during the major pressure spike.

However, for higher drop masses of $M > 40$, there is poor correlation: the lubrication approximation exceeds the measured major pressure spike by up to 50% and the QSCL model appears radically erratic and exceeds the measured pressure by up to 100% (truncated in Figure 8-38b). A similar, but less extreme trend of theoretical models producing increasing erratic pressure variations at diminishing disc separations has previously been observed for drop height variations (Figure 8-30).

The above erratic theoretical pressure modelling trends may result from one or more of the following factors:

i. Measurement tolerances of the laser sensor.
ii. Rig flexure which may lead to further inaccurate disc separation measurements. Both (i) and (ii) will adversely affect the subsequent disc velocity and acceleration derivations.
iii. Fluid compressibility affects.
iv. Disc flexure [even though retrospective calculations have shown that this flexure is small with deflection of less than 45 μm (Appendix E)].
v. Smoothing algorithms used in determining disc acceleration and velocity.

Corresponding to point (i.), considering the laser sensor has a measurement tolerance of $\pm 50$ μm (Appendix H) at a disc separation of 0.7 mm the disc separation uncertainty is $\pm 7\%$, applying the inverse

cubic relationship of the lubrication approximation $p \propto 1/h^3$ [equation (2-8), p. 8] results in a pressure uncertainty of $\pm 23\%$. Furthermore, the above analysis neglects the disc velocity error (also proportionate to disc separation measurements) [corresponding to point (ii.)].

Referring to Figures 8-14 and 8-15, p. 115, it can be seen that both the QSCL model and the lubrication approximation have similar uncertainty bounds. However, both these uncertainty bounds assume that disc velocity and acceleration are absolutely accurate (uncertainties are unavailable due to the use of smoothing algorithms). This assumption is clearly false, as can be seen by comparing Figure 8-44 with Figure 8-45, p. 144, which reveals that the higher the time derivative, the greater the associated spread of superimposed traces, i.e. uncertainty bounds. Hence the uncertainty bounds of the lubrication approximation should be larger those presented in Figure 8-14, and the uncertainty bounds of the QSCL model should be even larger than those of the lubrication approximation. Correspondingly the QSCL model results in a more erratic modelling trend than the lubrication approximation (Figure 8-39b, c).

As a heuristic, a limiting disc separation value may be approximated, below which the application of the theoretical models becomes too erratic (error dominated). From Figures 8-30 and 8-38 the *minimum disc separation modelling value* is estimated at 1 mm.

Despite the more erratic peak pressure values of the QSCL model relative to the lubrication approximation, the magnitude of the development of the major pressure spikes is more accurately modelled by this model as seen on the auxiliary contour plots in Figure 8-38.

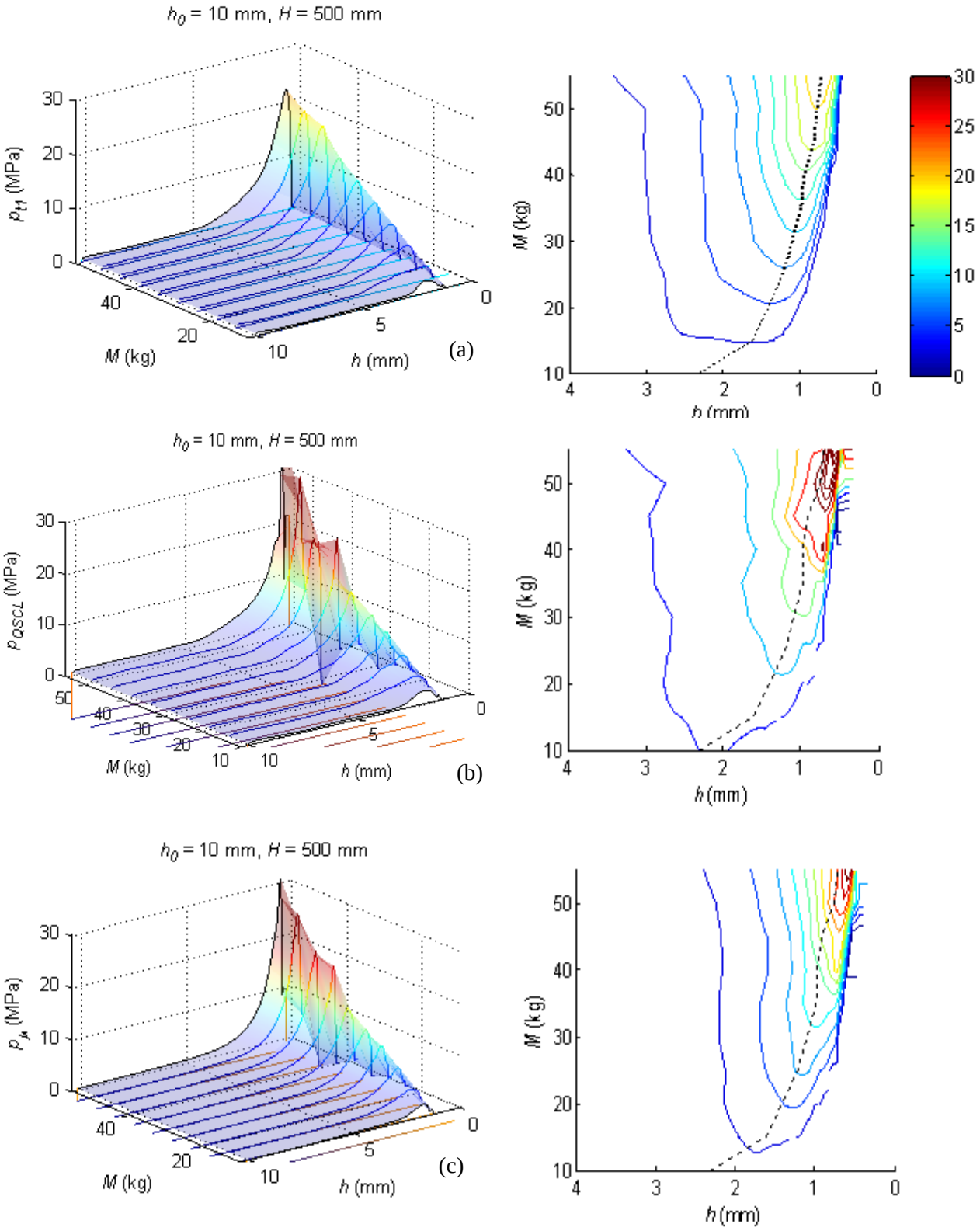


Figure 8-38: Central pressure vs drop mass vs disc separation: (a) Experimental, (b) QSCL model (c) Lubrication approximation

Figure 8-39 shows the variations of the preliminary pressure spike with drop mass (a) measured experimentally, (b) modelled by the QSCL model, (c) modelled by the lubrication approximation and (d) modelled by the inviscid/inertial model (identical to Figure 8-38 with magnified z-axis and truncated y-axis).

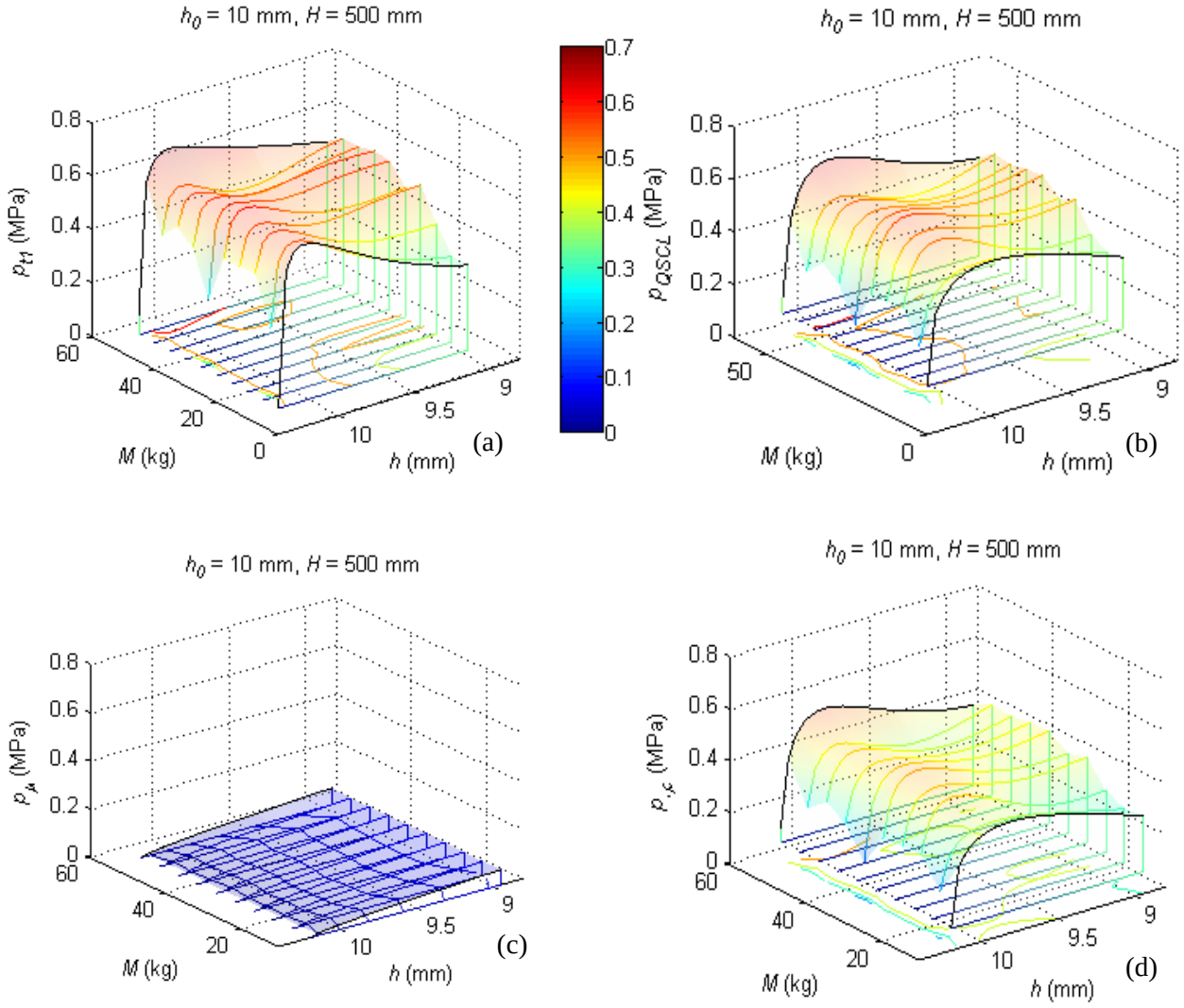


Figure 8-39: Central pressure vs drop mass vs preliminary disc separation: (a) Experimental, (b) QSCL model (c) Lubrication approximation

Notwithstanding the approximate invariance of the preliminary pressure spike with drop mass (discussed in the text associated with Figure 8-35), the correlations between the experimental and theoretical models

observed in Figure 8-39 are identical to those observed for drop height variations (Figure 8-31 and associated text, p. 130).

Figure 8-40 shows the eccentricity corrected normalised pressure distribution 2 traces (Section 7.5.2, p. 90) and the averaged normalised pressure distribution 3 traces (Section 7.5.2, p. 90) versus disc separation corresponding to ten drop masses. The variations observed in Figure 8-40 is almost identical to those observed for the drop height variations (Figure 8-32). Hence for descriptions of the observed trends in Figure 8-40 refer to the text associated with Figure 8-32.

Figure 8-41 shows the gravitational potential energy $E_G$ and the work due to pressure $W_{pre}$ (Section 8.1.5, p. 107.) plotted against varying drop mass for all test-sets. The correlation between $E_G$ and the work due to pressure $W_{pre}$ in Figure 8-41 is virtually identical to those observed for drop height variations as shown in Figure 8-33. Hence for descriptions of the observed trends in Figure 8-41 refer to the text associated with Figure 8-33.

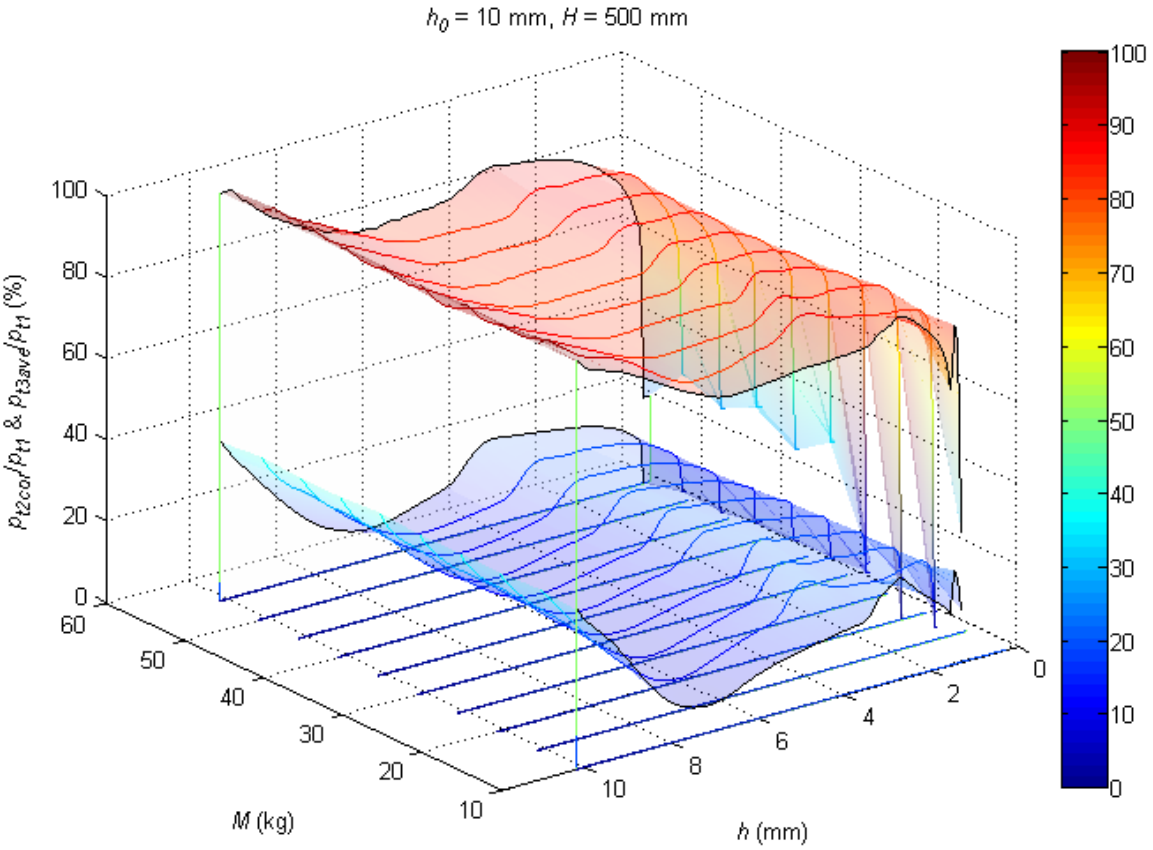


Figure 8-40: (a) Normalised pressure distribution 2 (cor) and 3(ave) vs drop mass vs disc separation

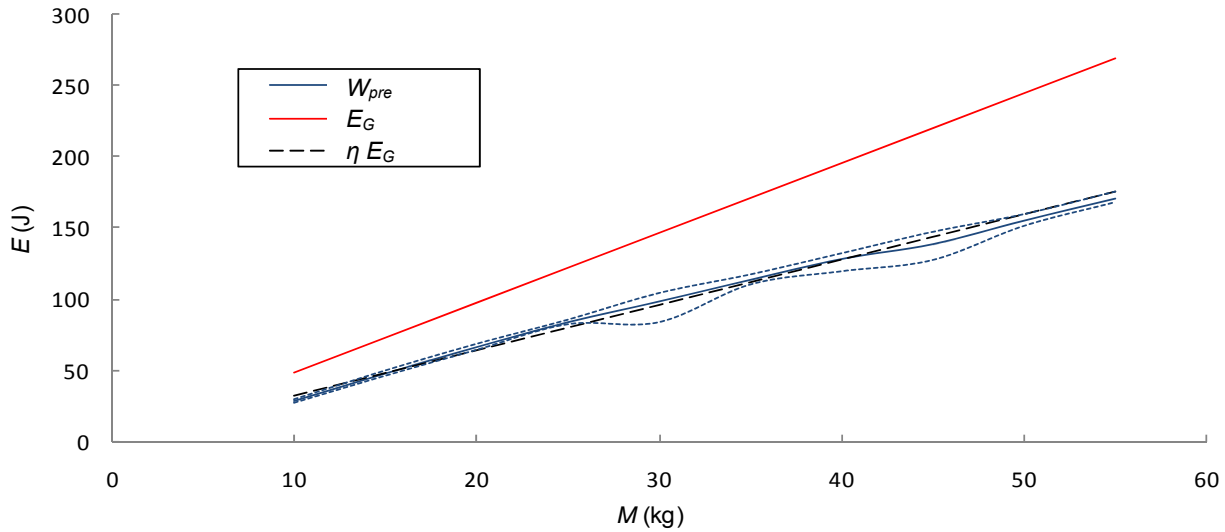


Figure 8-41: Energy vs drop mass

### 8.4.3 Initial disc separation variations

The plots presented within this section are constructed the identical way in which the drop height variation plots are constructed. Therefore, descriptions of the developments of the plots presented within this section are omitted, but can be referenced within the text associated with the corresponding plots of drop height variation (Section 8.4.1, p. 125).

Figure 8-42 shows the variation of central pressure traces with disc separation corresponding to eight initial disc separations (eight 3-dimensional line plots). It can be seen that the scaling of major pressure spikes are relatively independent of initial disc separation.

Unlike the plots of varying drop mass (Figure 8-35) and drop height (Figure 8-26) it is not possible to directly view (magnify) the preliminary pressure spikes in Figure 8-42 due to their staggered positioning. Instead the preliminary pressure spikes are viewed from an oblique angle as indicated by the arrow in Figure 8-42 to give Figure 8-43(a). Figure 8-43(a) shows that the preliminary pressure spike peaks increase with decreasing initial disc separations, however, the relationship between these two variables is unclear; therefore the preliminary pressure spike *peak values* of the experimental preliminary pressure spikes are plotted with respect to initial disc separation in
Figure 8-43(b). An empirical hyperbolic curve is also fitted to the experimental preliminary pressure spike peak values in Figure 8-43(b), in conjunction with the theoretical model values for the preliminary pressure spike peaks. The preliminary pressure spike peak at $h_0 = 3$ mm has been omitted from Figure 8-43(b) because, as can be seen from Figure 8-43 (a), the preliminary pressure spike has completely merged with the major pressure spike. This is also true for the preliminary pressure spike of the QSCL model.

From Figure 8-43(b) it can be seen that the peaks of the preliminary pressure spikes follows a hyperbolic relationship $p = k/h_0$, where $k$ is empirically determined as $k = 6000$. The QSCL model is in good agreement with the experimentally measured preliminary pressure spikes. The inviscid/inertial model's preliminary pressure spike values are on average 80% that of the experimentally measured pressure spikes; this ratio has previously been observed in both the drop mass variations (Figure 8-39) and the drop height variations (Figure 8-31). For low initial disc separations of $h_0 < 5$ mm, it can be seen that preliminary pressure spike of the inviscid/inertial model no longer accurately correlates with the

experimental results; this indicates that the pressure generation mechanism is not inertial dominant and therefore the inviscid/inertial model may no longer be considered an accurate approximation.

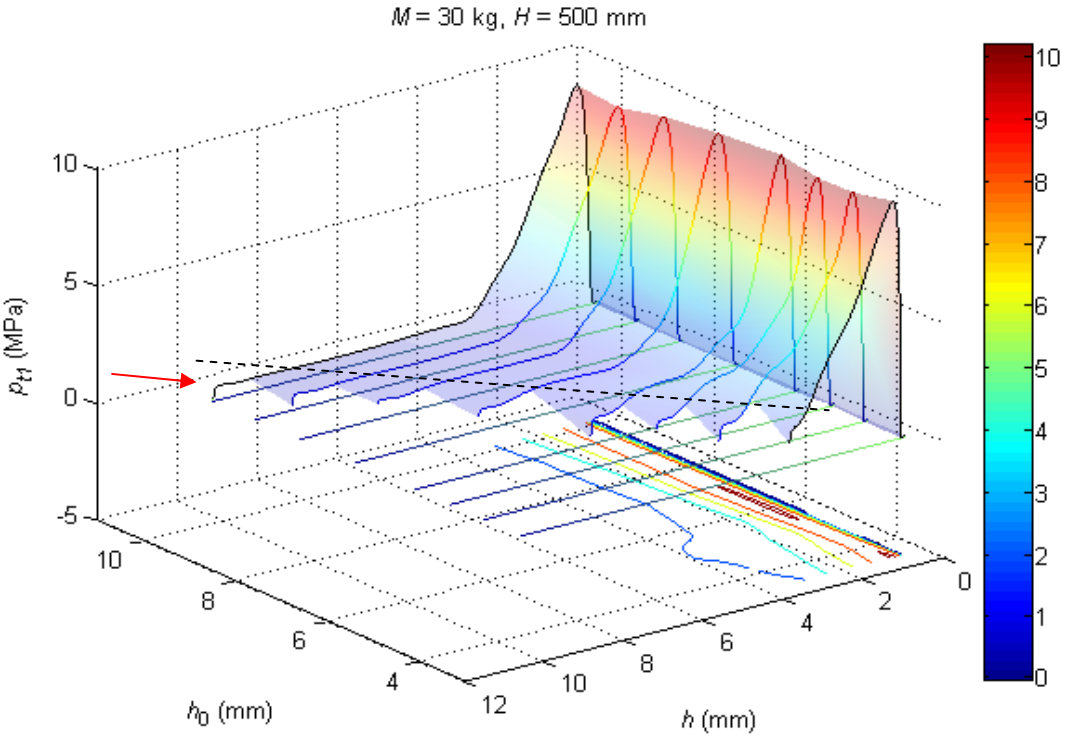


Figure 8-42: Experimentally measured central pressure vs initial disc separation vs disc separation

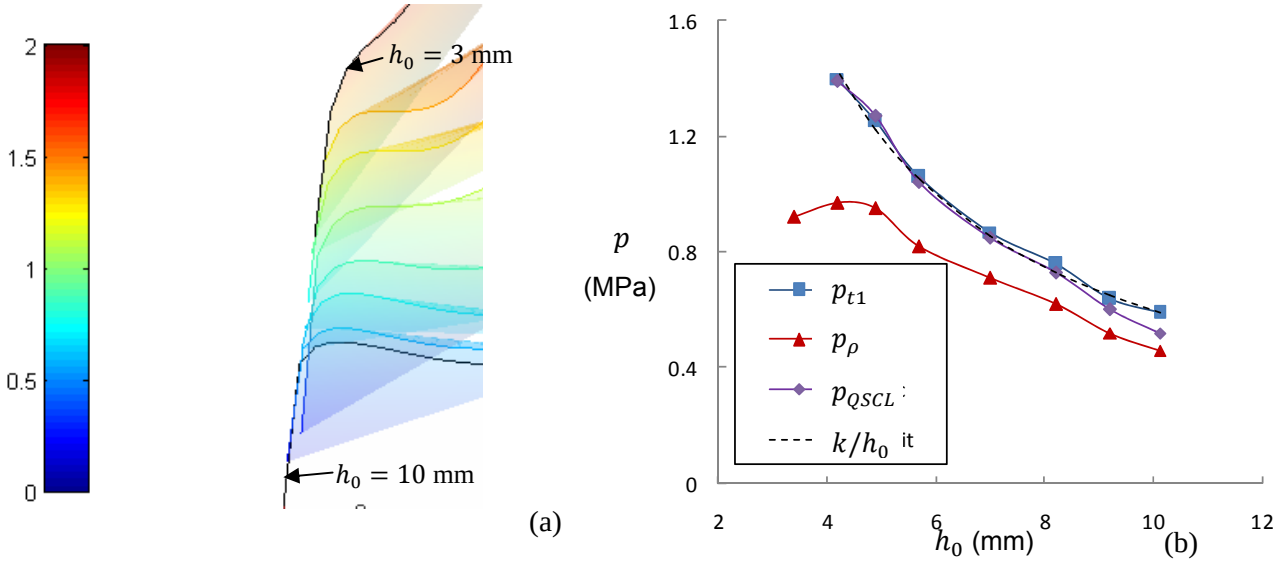


Figure 8-43: (a) Oblique view of Figure 8-42 (b) Experimental and theoretical central pressures of preliminary pressure spike vs initial disc separation.

Figures 8-44 and 8-45 respectively show the variation of disc velocity and acceleration with disc separation corresponding to eight initial disc separations (eight 3-dimensional line plots).

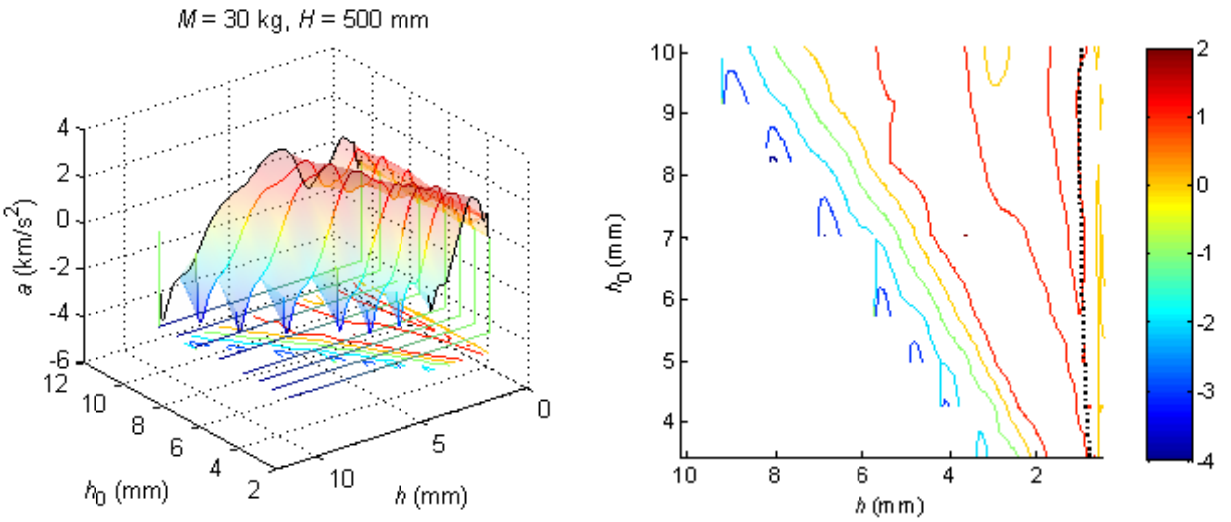


Figure 8-44: Disc velocity vs initial disc separation vs disc separation

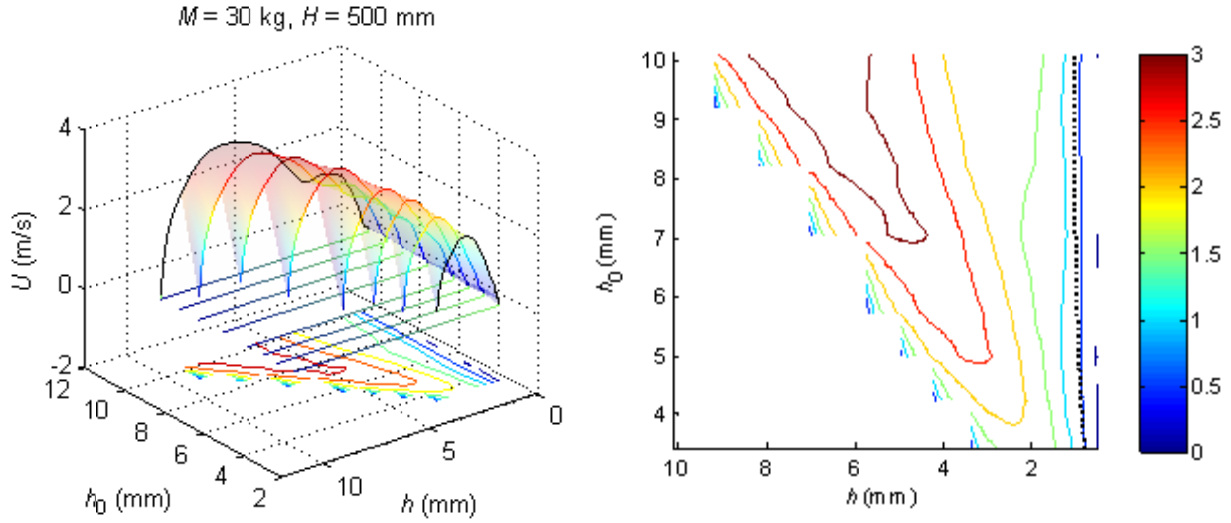


Figure 8-45: Disc acceleration vs initial disc separation vs disc separation

From the auxiliary contour plots in Figures 8-44 and 8-45, it can be seen that all major pressure spikes occur within relatively stable values of disc velocities ($U$ ~ 0.5 m/s) and accelerations ($a$ ~ 1 km/s2), irrespective of initial disc separations. This trend of major pressure spike occurring through relatively

stable disc velocities and accelerations has previously been observed for both the drop mass variations (Figures 8-36 and 8-37) and drop height variations (Figures 8-33 and 8-28). However, unlike drop mass and height variations, the major pressure spike peaks for varying initial disc separations occur at a relitively constant disc separation values of $h \approx 0.8$ mm (seen by the near vertical the peak pressure line in the contour plots of Figures 8-44 and 8-45).

The application of theoretical models to the major pressure spikes, for varying initial disc separations, yields highly erratic results and are thus omitted. This modelling trend of erratic results at low disc separations of $h < 1$ mm has previously been estimated in Figure 8-38, p. 138, and is discussed in the associated text.

For $h_0 > 4$, it can be seen from Figures 8-44 and 8-45 that the preliminary pressures spikes occurs within a relatively stable range of velocities ($U \sim 1$ m/s) and accelerations ($a \sim -3$ km/s$^2$). Hence, approximating the preliminary pressure spike as inertial dominant and after performing an order of magnitude analysis on equation (5-2), as elaborated on in the text associated with Figures 8-28 and 8-29, it can be shown that $p \propto \ddot{h}/h$ or $p \propto 1/h$ since disc acceleration is relatively invariant; this hyperbolic relationship can be seen in Figure 8-43.

Figure 8-46 shows the eccentricity corrected normalised pressure distribution 2 traces (Section 7.5.2, p. 90) and the averaged normalised pressure distribution 3 traces (Section 7.5.2, p. 90) versus disc separation corresponding to eight initial disc separations. For large initial disc separations, the pressure distribution observed in Figure 8-46 is almost identical to that observed for drop height and drop mass variations (Figure 8-32 and associated text). However, as the initial disc separation decreases, the lower normalised pressure distribution values, associated with the bridging region, also decreases until they disappears at $h_0 \sim 6$ mm. This observation is supported by the disappearance of the bridging region in Figure 8-42 also at $h_0 \sim 6$ mm. As further expected by this trend, the assumedly offset and non-parabolic pressure distribution associated with preliminary pressure spike (Figure 8-5 and associated text) directly merges with the parabolic pressure distribution of the major pressure spike at $h_0 \sim 3$ mm (Figure 8-46).

Figure 8-47 shows the gravitational potential energy $E_G$ and the work due to pressure $W_{pre}$ (Section 8.1.5, p. 107.) plotted against initial disc separations for all test-sets. It can be seen that $E_G$ is constant since both $H$ and $M$ are constants. The ratio between $E_G$ and the work due to pressure $W_{pre}$ in Figure 8-47 is approximately constant at $\bar{\eta} = 65\%$ [equation (8-2)], as previously calculated for both the drop height

(Figure 8-33) and drop mass (Figure 8-41) variations. The observation of a relatively constant $W_{pres}$ value in Figure 8-47 is in keeping with the relative invariance of the major pressure spikes with varying initial disc separations (Figure 8-46) and with a relatively constant associated pressure distribution (Figure 8-46).

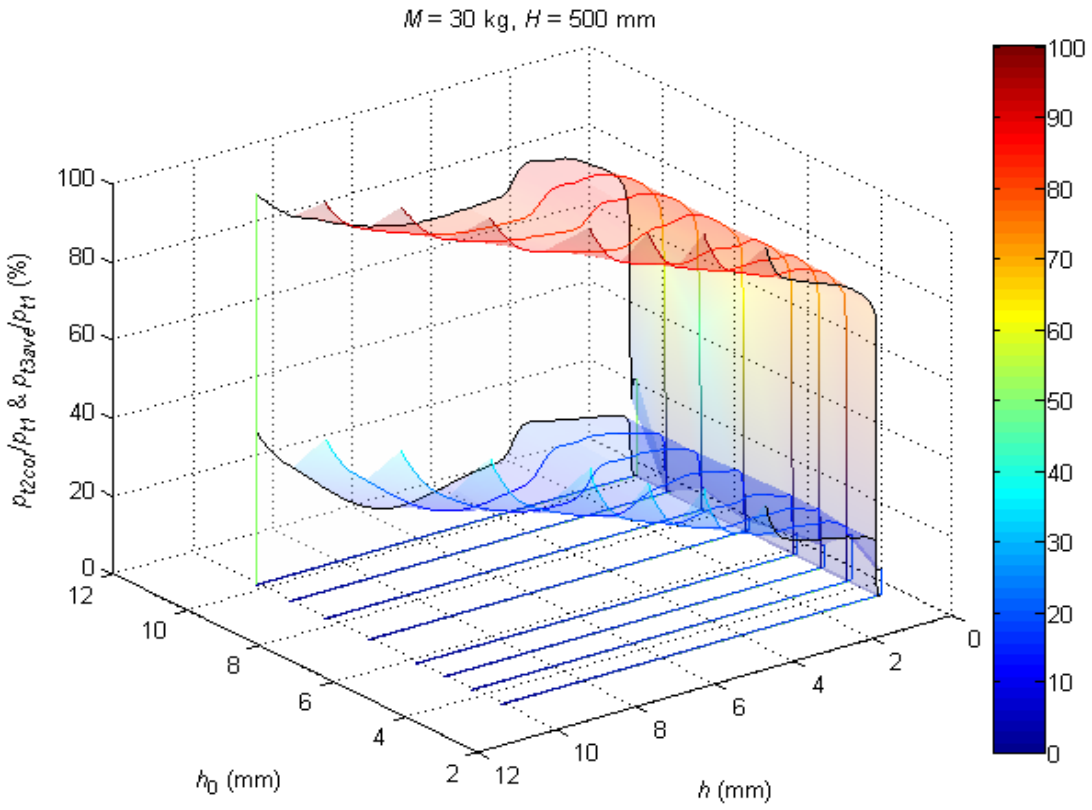


Figure 8-46: Normalised pressure distribution 2(cor) and 3(ave) vs initial disc separation vs disc separation

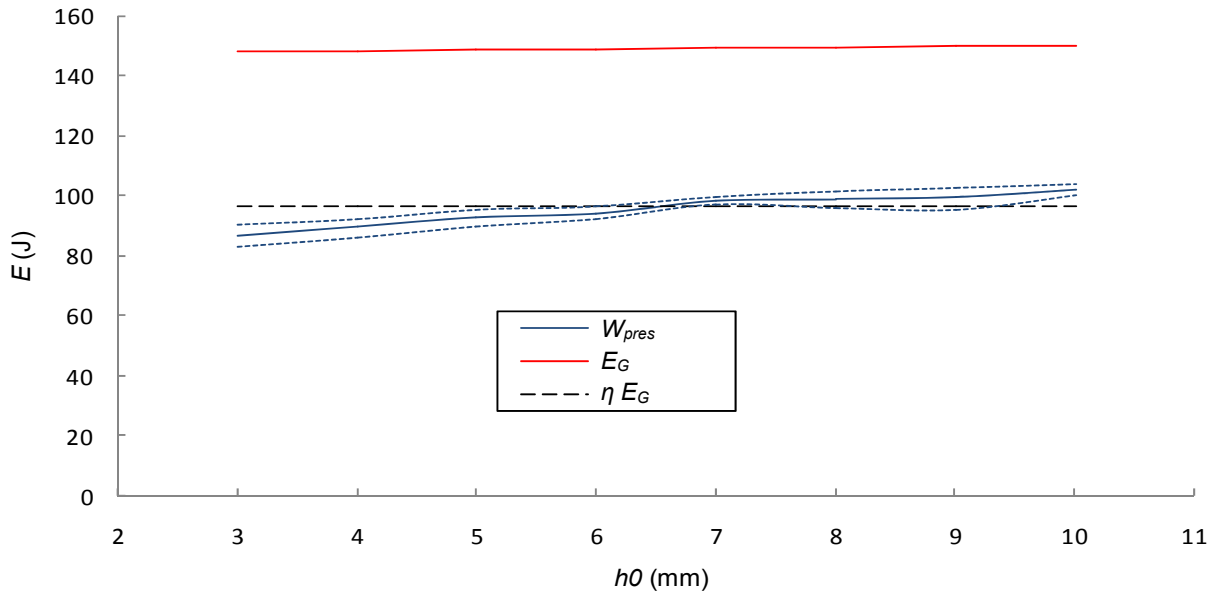


Figure 8-47: Energy vs initial disc separation

# 9 CONCLUSIONS

Through theoretical analysis, CFD modelling and physical experimentation, the following conclusions regarding highly transient squeeze flows have been established:

1. CFD shows that the parallel flow assumption appears to be valid over a range of disc separation to disc radius ratios as large as 1:6, far exceeding those encountered in typical lubrication situations. Consequently, the exact kinematic squeeze flow equation (5-10), p. 23, is valid, consistent with an invariably parabolic radial pressure distribution.
2. The exact kinematic squeeze flow equation was reduced to a Quasi-Steady (QS) model in the form of a semi-linear differential equation which is numerically (computationally) determinable. This model neglects the rate of change of the dimensionless radial velocity profile.
3. Neglect of the non-linear term (which according to an approximate analysis accounts for less than 20% of total spatial inertia) in the QS model further reduced it to an analytically determinable linear differential equation - the Quasi-Steady Linear (QSL) model.
4. Subsequently, the QSL model was amended to account for the neglected non-linear term by means of a linear approximation, thus yielding the analytically determinable Quasi-Steady Corrected linear (QSCL) model.
5. The resultant pressure traces and dimensionless radial fluid velocities of the above theoretical models were compared against a hypothetical CFD highly transient squeeze flow system (which is assumed to be exactly dictated by the exact kinematic model [equation (5-10), p. 23] and hence the following correlations were shown:
    a. The QS model had excellent correlation with the CFD results (discrepancies of $< \sim 5\%$), hence validating the quasi-steady approximation as being sufficiently accurate for the specific hypothetical squeeze flow.
    b. The QSL model is shown to have relatively good correlation with the CFD results, (discrepancies of $< \sim 10\%$), hence revealing the neglected non-linear term may be considered as marginally significant.
    c. The QSCL model is shown to agree almost exactly with the QS model (discrepancies of $< \sim 2\%$), hence validating the linear approximation made by the QSCL model to account for spatial inertia.
6. A so-called *evolution ratio*, derived for evaluating the applicability of the quasi-steady assumption, suggested that a quasi-steady approximation for the above hypothetical model was accurate, thus reinforcing the applicability of the QS and therefore the QSCL models. This

analysis may be applied to any transient squeeze flow system if the disc dynamics (instantaneous separation, velocity and acceleration) are known.

7. When applied to highly transient squeeze flows, the QS and QSCL models both produced radial fluid velocities and resultant central pressure traces that are more accurate than the other reviewed models, although the current system – in contrast with most previous ones - embraced situations in which the disc acceleration was very large.
8. CFD showed that the resultant pressure distributions arising from asymmetrical (one disc moving) and symmetrical (both discs moving) squeezing motions are virtually identical, resulting in less than $\pm 1\%$ difference for positive pressures. Hence, experimental asymmetrical squeeze flow pressure measurements were compared directly against symmetrical squeeze flow theoretical predictions.
9. Experimental results for impact-induced, *constant energy* squeeze flows, generally showed that two pressure spikes were induced; firstly the *preliminary pressure spike* which occurs at the *stroke initiation* associated with large disc accelerations and secondly the *major pressure spike* which *precedes* the *stroke termination*, associated with diminishing disc separations.
10. The effects of eccentricity were successfully corrected for during the measured major pressure spike, for which the radial pressure distribution was observed to be closely parabolic in shape and the circumferential pressure offset was small. However, the effects of eccentricity, circumferential pressure offset and non-parabolic radial pressure distributions during the preliminary pressure spike were non-negligible, and could not be individually isolated and quantified using the current test-cell.
11. Despite the uncertainties mentioned in item 10, non-parabolic radial pressure distributions were observed during the preliminary spike that could be attributed to compressibility effects and/or violation of the parallel flow assumption (item 1).
12. The evolution ratio (item 6) suggested that the experimental data could be regarded as quasi-steady in nature, hence supporting their comparison with the QSL and QSCL models.
13. The measured disc separations, derived velocities and accelerations, when substituted into the above theoretical models yield theoretical (central) pressure traces. The following inferences could be made by comparing these theoretical pressure traces with the corresponding experimental central pressure trace:
    a. The simple inviscid/inertial model, p. 20 encapsulates the essential physics of the system, during the preliminary pressure spike, where disc acceleration and therefore fluid temporal inertia effects are dominant.

b. As expected, the lubrication approximation correlated satisfactorily with experimental results towards the termination of the experimental stoke (major pressure spike) where the disc separation was small and therefore viscous effects were dominant.
c. The QSL model held good correlation with experimental results throughout the experimental stroke, encompassing successively a dominance of temporal inertia, spatial inertia and viscous effects. By taking cognisance of the non-linear effects, the QSCL model yielded marginally better results.

14. The lubrication approximation, and to a greater extent the QSCL model, resulted in theoretical pressures of the major pressure spike that held good agreement with experimental pressure measurements for the major pressure spikes at relatively large disc separations of $h > 1.2$ mm and poor agreement with experimental pressure measurements at relatively small disc separations of $h < 1$ mm. It is speculated that this trend is predominantly due to the measurement tolerance of the laser sensor and rig flexure which at large disc separations results in relatively small measurement errors and vice-versa.
15. It was found the overall energy dissipation coefficient of the above experimentation is relatively constant at $\bar{\eta} = 65\%$.

# 10 FUTURE WORK

To order to further the investigation of highly transient squeeze flows, the following recommendations are put forward:

1. Program a CFD model to more accurately replicate an experimental test (for example the reference test). This would entail: (i) accurately replicating the experimental disc velocity versus time, this could be done by using multiple piecewise continuous polynomial curve fits, (ii) modelling the fluid bladder, (iii) modelling a compressible fluid.

   The resultant CFD pressures may thereafter be compared directly against the experimentally measured pressures.
2. Using the CFD bladder model (item 1), evaluate the analytically derived bladder flow dynamics (Section 5.11, p. 41).
3. Improve the accuracy of the instantaneous disc separation measurements: This can be done by using a more accurate displacement sensor (with smaller measurement tolerances), for example a Halls effect sensor, this in turn should yield more accurate theoretical results.
4. Alternatively or additionally, if the overall experimental disc separations are larger (in particular the final disc separation), the relative disc separation errors are reduced thus increasing the accuracy of theoretical pressure results. This can be achieved by: (i) using a larger disc diameter, (ii) using a higher viscosity fluid, (iii) externally limiting the disc separation, i.e. not allowing the discs to come to rest under the force of the generated pressure.
5. Attempt to solve the QSL model with the inclusion of the shape evolution term [equation (5-10), p. 23] i.e. all terms of equation (5-10) excluding $D_2'$. The resultant partial differential equation could *potentially* be analytically solved with the use of the *diffusion* or *heat equation*.
6. If (5) is possible, attempt to reconcile the result of the partial differential equation to include the non-linear term $D_2'$of equation (5-10). p. 23, in a similar fashion to which the QSL model is corrected to include this term by the derivation of the QSCL model (Section 5.7, p. 32). The result should be a more accurate analytically determinable approximate solution of exact kinematic model (Section 5.4, p. 23).
7. Design a hypothetical disc motion and select an appropriate kinematic viscosity for which the QSCL model predicts a shape parameter variation of $\lambda < -4\pi^2$ (as for the hypothetical case); this would assumedly initiate the onset of turbulence. Hence, attempt to experimentally reproduce this hypothetical disc motion (presumably not using a drop-hammer system) and therefore experimentally induce a turbulent squeeze flow: It is speculated that the resulting turbulent flow

should result in a pressure (squeeze force) change and therefore should be experimentally measurable.

8. Investigate highly transient squeeze flows for non-Newtonian fluids.

# 11 REFERENCES


**Batra R L and A Kanasamy** Inertia effects in rhodynamic lubrication of a squeeze film bearing [Book]. - 1989. - Vol. 131.

**Bird P J and Leider R B** Univ. of Wisconsin Rheology Research Center Rep. No. 22 [Journal] // Ind. Eng. Chem. Fund., 13. - 1973. - pp. 336-342.

**Brindley G, Davies J M and Walters K** Elastico-viscous squeeze films. Part 11 [Journal] // J. non-Newtonian Fluid Mech. 1. - 1976. - pp. 19–37.

**Dorsey N E** INTERNET.http://www.dow.com/glycerin/recourses/table18.htm [Book]. - New York : [s.n.], 1995.

**Dorsey N E** INTERNET.http://www.dow.com/glycerin/recourses/table4_91100.htm [Book]. - New York : [s.n.], 1995.

**Engmann J, Servais C and Burbidge A S** Squeeze flow theory and applications to rheometry: A review [Journal] // J. non-Newtonian Fluid Mech. Vol. 132. - 2005. - pp. 1–27.

**Grimm R J** Squeezing flows of Newtonian liquid films, an analysis including fluid inertia [Journal] // Appl. Sci. Res. - 1976. - Vol. 32. pp. 149-166.

**Gupta P S and Gupta A S** Squeezing flow between parallel plates [Journal]. - [s.l.] : Wear, 1977. - 2 : Vol. 45.

**Hamza E A and MacDonald D A** A fluid film squeezed between two plane surfaces [Journal] // J. Fluid Mech. 109. - 1981. - pp. 147–160.

**Ishizawa S** The unsteady larninar flow between two parallel discs with arbitrarily varying gap width [Journal] // Bull. of JSME . – 1966-. Vol. 35. pp. 533-550.

**Jackson J D** A story of squeezing flow [Journal] // Appl. Sci. Res. A 11. - 1962. - pp. 148-152.

**Jones A F and R Wilson S D** On the failure of lubrication theory in squeezing flows [Journal] // J. Lubric. Tech. 97. - 1975. - p. 101.

**Kramer J M** [Journal] // Appl. Sci. Res. 30. - [s.l.] : Univ. of Wisconsin Rheology Research Center Rep. No. 15, 1974.

**Kuzma D C** Fluid inertia effects in squeeze films [Journal] // Appl. Sci. Res. 18. - 1967. - pp. 15-20.

**Kuzma D C, Maki E R and JR Donnelly** [Journal] // J. Fluid Mech. 19. - 1964.

**Lawrence C J, Kuang Y and Weinbaum S** The inertial draining of a thin fluid layer between parallel plates with a constant normal force. Part 2. Boundary layer and exact numerical solutions [Journal]. - New York : J. Fluid Mech., 1985. - Vol. 156.

**Leider P J** Squeezing flow between parallel disks II [Journal] // I&EC Fund. 13. - 1974. - p. 342.

**Lin J R and R Hung C** Combined effects of non-Newtonian rheology and fluid inertia forces on the non-linear transient behaviour in circular squeeze films [Journal] // Proc. IMechE Vol. 221 Part 1: J. Engineering Tribology. - 2007. - pp. 535-541.

**McClelland M C and Fmlayson B A** Squeezing flow of elastic liquids [Journal]. - [s.l.] : J non-Newtonian Fluid Mech, 1983. - 2 : Vol. 13. - 181-203.

**Phan-Thien N and Tanner I R** Viscoelastic squeeze-film flows-Maxwell fluids [Journal] // J. Fluid Mech. 129. - [s.l.] : J Fluid Mech, 1983. - Vol. 129. - pp. 265–281.

**Phan-Thien N** The transmission loss of squeeze-film flow of Newtonian and some viscoelastlc fluids. [Journal]. - [s.l.] : ASME Jur Lub Tech, 1986. - 1 : Vol. 24.

**Phan-Thien N, Dudek J and Boger D V** Squeeze film flow of ideal elastic liquids [Journal] // J. non-Newtonian Fluid Mech.- 1985. - Vol. 18. - pp. 227–254.

**Phan-Thien N, Sugeng F and Tanner I R** The squeeze-film flow of a viscoelastic fluid [Journal] // J. non-Newtonian Fluid Mech., 1987. - 1 : Vol. 24. - pp. 97–119.

**Rashidi M M, Shahmohamadi H and Dinarvand S** Analytic approximate solutions for unsteady two-dimensional and axisymmetric squeezing flows between parallel plates [Journal] // Mathematical Problems in Engineering, - 1998. - Article ID 935095.

**Reynolds 0** On the theory of lubrication and its application to Mr. Beauchamp Tower's experiments including an experimental determination of the viscosity of olive oil [Journal] // Phil. Trans. Roy. Soc. Al77. - [s.l]., 1886. - Vol. 40. - pp. 157-234.

**Roark R** Roark's Formulas for Stress and Strain [Book]. - [s.l.] : MaGraw Hill, 1975.

**Rukmani R and Usha R** Arbitary squeeze flow between two disks [Journal] // Internat. J. Math. & Math. Sci.. - [s.l.] :, 1994: Vol. 17. - pp. 779-782.

**Schlichting H** Boundary Layer Theory [Book]. - [s.l.] : McGraw-Hill, 1960.

**Scott J R** Theory and application of the parallel-plate plastometer [Journal] // : Trans Inst Rubber Ind, 1931. - Vol. 7. p. 169.

**Stefan J** Versuche uber die schienbare Adhesion Sitzungsber [Journal] // Sitz. Kais. Akad. Wiss.. - 1874. - pp. 713-735.

**Tichy J A** An approximate analysis of fluid inertia effects in axisymmetric laminar squeeze film flow at arbitrary Reynolds number [Journal] //: Appl Sci Res, 1981: Vol. 37. - pp. 301-312.

**Tichy J A and Modest M F** A simple low deborah number model for unsteady hydrodynamic lubrication including fluid inertia [Journal] // Journal of Rheology in press.., 1980. - Vol. 24.

**Van Dyke M** Perturbation Methods in Fluid Mechanics [Book]. - [s.l.] : Parabolic Press, 1964. - p. 35.

**Wang C Y** The squeezing of a fluid between two plates [Journal] // ASME J. of Appl. Mech. 43 (4).. - 1976. - pp. 579-584.

**Weinbaum S, Lawrence C J and Kuang Y** The inertial draining of a thin fluid layer between parallel plates with a constant normal force. Part 1. Analytic solutions; inviscid and small-but finite-Reynolds-number limits [Journal]. J. Fluid Mech., 1985. - Vol. 156.

# 12 BIBLIOGRAPHY

**Salvadori M and Schwartz R** Differential Equations in Engineering Problems [Book]. - Columbia, USA: University of Columbia : Pretice-Hall inc., 1954.

**Schlichting H** Boundary Layer Theory [Book]. - [s.l.] : McGraw-Hill, 1960.

**Smith M** Style guide for writing theses and dissertations [Book]. - Johannesburg, South Africa: University of the Witwatersrand : [s.n.], 1995.

**White F** Viscous Fluid Flow [Book]. - Rhode Island, USA: University of Rhode Island : McGraw-Hill, 1991.

# 13 APPENDICES

## Appendix A: Analysis Calculations

The complete set of Navier Stokes Equations in cylindrical coordinates ($z$, $r$ and $\theta$) is given as

$$\rho\left(\frac{\partial v_r}{\partial t}+v_r\frac{\partial v_r}{\partial r}+\frac{v_\theta}{r}\frac{\partial v_r}{\partial \theta}-\frac{{v_\theta}^2}{r}+v_z\frac{\partial v_r}{\partial z}\right) = \rho g_r-\frac{\partial p}{\partial r}+\mu\left(\frac{\partial^2 v_r}{\partial r^2}+\frac{1}{r}\frac{\partial v_r}{\partial r}+\frac{v_r}{r^2}+\frac{1}{r^2}\frac{\partial^2 v_r}{\partial \theta^2}-\frac{2}{r^2}\frac{\partial v_\theta}{\partial \theta}+\frac{\partial^2 v_r}{\partial z^2}\right) \quad (13\text{-}1)$$

$$\rho\left(\frac{\partial v_\theta}{\partial t}+v_r\frac{\partial v_\theta}{\partial r}+\frac{v_\theta}{r}\frac{\partial v_\theta}{\partial \theta}+\frac{v_r v_\theta}{r}+v_z\frac{\partial v_\theta}{\partial z}\right) = -\frac{1}{r}\frac{\partial p}{\partial \theta}+\mu\left(\frac{\partial^2 v_\theta}{\partial r^2}+\frac{1}{r}\frac{\partial v_\theta}{\partial r}-\frac{v_\theta}{r^2}+\frac{1}{r^2}\frac{\partial^2 v_\theta}{\partial \theta^2}-\frac{2}{r^2}\frac{\partial v_r}{\partial \theta}+\frac{\partial^2 v_\theta}{\partial z^2}\right) \quad (13\text{-}2)$$

$$\rho\left(\frac{\partial v_z}{\partial t}+v_r\frac{\partial v_z}{\partial r}+\frac{v_\theta}{r}\frac{\partial v_z}{\partial \theta}+v_z\frac{\partial v_z}{\partial z}\right) = \rho g_z-\frac{\partial p}{\partial z}+\mu\left(\frac{\partial^2 v_z}{\partial r^2}+\frac{1}{r}\frac{\partial v_z}{\partial r}+\frac{1}{r^2}\frac{\partial^2 v_z}{\partial \theta^2}+\frac{\partial^2 v_z}{\partial z^2}\right) \quad (13\text{-}3)$$

where $\rho, t, \mu,\ g$ and $p$ which respectively denote density, time, dynamic viscosity, gravitational acceleration and pressure.

The following squeeze flow assumptions are made:

i. The flow is incompressible and isothermal.
ii. Gravitational body forces are negligible.
iii. The disc separation $h$, is small in comparison to the disc radius $R$.
($\Rightarrow \partial(\text{all velocities})/\partial z \gg \partial(\text{all velocities})/\partial r$ ).
iv. Axial flows are negligible, i.e. the flow is two-dimensional ($\Rightarrow v_z \approx 0$).
v. The flows are axi-symmetric ($\Rightarrow \partial/\partial\theta's = 0;\ v_\theta = 0$).

These assumptions are now applied to the Navier-Stokes equations (13-1), (13-2) and (13-3), as follows

$$\rho\left(\frac{\partial v_r}{\partial t}+v_r\frac{\partial v_r}{\partial r}+\frac{v_\theta}{r}\frac{\partial v_r}{\partial \theta}-\frac{v_\theta^2}{r}+v_z\frac{\partial v_r}{\partial z}\right)$$

(A) (B1) (v) (v) (B2)

$$=\rho g_r-\frac{\partial p}{\partial r}+\mu\left(\frac{\partial^2 v_r}{\partial r^2}+\frac{1}{r}\frac{\partial v_r}{\partial r}+\frac{v_r}{r^2}+\frac{1}{r^2}\frac{\partial^2 v_r}{\partial \theta^2}-\frac{2}{r^2}\frac{\partial v_\theta}{\partial \theta}+\frac{\partial^2 v_r}{\partial z^2}\right)$$

(ii) (C) (iii) (iii) (iii) (v) (v) (D)

$$\rho\left(\frac{\partial v_\theta}{\partial t}+v_r\frac{\partial v_\theta}{\partial r}+\frac{v_\theta}{r}\frac{\partial v_\theta}{\partial \theta}+\frac{v_r v_\theta}{r}+v_z\frac{\partial v_\theta}{\partial z}\right)$$

(v)

$$=-\frac{1}{r}\frac{\partial p}{\partial \theta}+\mu\left(\frac{\partial^2 v_\theta}{\partial r^2}+\frac{1}{r}\frac{\partial v_\theta}{\partial r}-\frac{v_\theta}{r^2}+\frac{1}{r^2}\frac{\partial^2 v_\theta}{\partial \theta^2}-\frac{2}{r^2}\frac{\partial v_r}{\partial \theta}+\frac{\partial^2 v_\theta}{\partial z^2}\right)$$

(v) (v)

$$\rho\left(\frac{\partial v_z}{\partial t}+v_r\frac{\partial v_z}{\partial r}+\frac{v_\theta}{r}\frac{\partial v_z}{\partial \theta}+v_z\frac{\partial v_z}{\partial z}\right)$$

(iv)

$$=\rho g_z-\frac{\partial p}{\partial z}+\mu\left(\frac{\partial^2 v_z}{\partial r^2}+\frac{1}{r}\frac{\partial v_z}{\partial r}+\frac{1}{r^2}\frac{\partial^2 v_z}{\partial \theta^2}+\frac{\partial^2 v_z}{\partial z^2}\right).$$

(ii) (iv)

Hence equation (13-1) is reduced to

$$\frac{dp}{dr}=\mu\frac{\partial^2 v_r}{\partial z^2}-\rho\left(\frac{\partial v_r}{\partial t}+v_r\frac{\partial v_r}{\partial r}+v_z\frac{\partial v_r}{\partial z}\right) \qquad (13\text{-}4)$$

(A) (B) (C) (D1) (D2)

and equation (13-3) is reduced to

$$\frac{\partial p}{\partial z}\approx 0. \qquad (13\text{-}5)$$

Furthermore, the continuity of the flow system can be given as

$$\frac{\partial v_r}{\partial r} + \frac{v_r}{r} + \frac{\partial v_z}{\partial z} = 0. \tag{13-6}$$

From the condition of continuity, the mean velocity through any radial strip is given as

$$\overline{v_r} = -\frac{r}{2}\frac{\dot{h}}{h}. \tag{13-7}$$

The parallel flow assumption is given by

$$v_r = -\frac{r}{2}\frac{\dot{h}}{h}g' = -\frac{r}{2}\frac{\dot{h}}{h}f(z^*, t) \quad \text{and} \quad v_z = \dot{h}g(z^*, t), \tag{13-8a, b}$$

where $t$ is time, $g$ is the dimensionless axial velocity and the prime denotes a derivative with respect to the dimensionless axial derivative $z^*$ which is defined as

$$z^* \equiv \frac{z}{h}. \tag{13-9}$$

The dimensionless radial velocity $f$ is introduced as $g' = f$. The dimensionless axial and radial fluid velocity profiles for a symmetrical squeezing motion have the following boundary conditions:

i. Symmetry of the dimensionless radial velocity dictates that

$$f'\left(\frac{1}{2}\right) = g''\left(\frac{1}{2}\right) = 0. \tag{13-10}$$

ii. Flow conservation is embodied in

$$\int_0^{\frac{1}{2}} f\, dz^* = \int_{\frac{1}{2}}^1 f\, dz^* = -g(0) = g(1) = \frac{1}{2}. \tag{13-11}$$

iii. The no-slip condition on the discs is given by

$$f(0) = g'(0) = 0. \tag{13-12}$$

Substituting equations (13-8a, b) into term *C* of equation (13-7) by the chain rule results in

$$\frac{\partial v_r}{\partial t} = \frac{\partial \overline{v_r}}{\partial t} g' + \overline{v_r} \dot{g}' \tag{13-13}$$

where the dot accent ( $\dot{}$ ) denote the partial time derivative. Values of $\overline{v_r}$ [equation (13-7)] are substituted into equation (13-13) yielding

$$\frac{\partial v_r}{\partial t} = -\frac{r}{2}\left[\frac{\ddot{h}h - \dot{h}^2}{h^2}\right] g' - \frac{r}{2}\frac{\dot{h}}{h}\dot{g}'. \tag{13-14}$$

Substituting equations (13-8a, b) into term $D_1$ of equation (13-7) gives

$$v_r \frac{\partial v_r}{\partial r} = \frac{r}{4}\left(\frac{\dot{h}}{h}\right)^2 g'^2. \tag{13-15}$$

The axial velocity, equation (13-8b), is substituted into the $D_2$ term of eqaution (13-7) to give

$$v_z \frac{\partial v_r}{\partial z} = -\frac{r}{2}\left(\frac{\dot{h}}{h}\right)^2 g g''. \tag{13-16}$$

Substituting equation (13-8a) into term *B* of equation (13-7) gives

$$\frac{\partial^2 v_r}{\partial z^2} = -\frac{r}{2}\frac{\dot{h}}{h^3} g''' \tag{13-17}$$

Finally recalling the definition of kinematic viscosity given as

$$\nu \equiv \frac{\mu}{\rho} \tag{13-18}$$

when equations (13-14), (13-15), (13-17) and (2-6) are substituted into equation (13-7) and rearranged as to make $dp/dr$ the subject of the formula

$$\frac{dp}{dr} = -r\frac{\rho}{2}\left\{\nu\frac{\dot{h}}{h^3}g''' - \left(\frac{\dot{h}}{h}\right)^2(g-z^*)g'' - \left(\frac{\dot{h}}{h}\right)\dot{g}' + \frac{1}{2}\left(\frac{\dot{h}}{h}\right)^2 g'^2 - \left[\frac{\ddot{h}}{h} - \left(\frac{\dot{h}}{h}\right)^2\right]g'\right\}. \qquad (13\text{-}19)$$

In order to eliminate the radial pressure distribution term from the dimensionless velocity terms in equation (13-19) with the intension of ultimately solving for the dimensionless velocities, the expression is differentiated with respect to $z^*$, since $dp/dz \approx 0$ [equation (2-2)] to give

$$\underset{(B_1')}{\nu\left(\frac{\dot{h}}{h^4}\right)g'^v} - \underset{(D_2')}{\left(\frac{\dot{h}^2}{h^3}\right)(g-z^*)g'''} - \underset{(C_2')}{\left(\frac{\dot{h}}{h^2}\right)\dot{g}''} - \underset{(C_1')\ (C'D')}{\left[\frac{\ddot{h}}{h^2} - 2\left(\frac{\dot{h}^2}{h^3}\right)\right]g''} = 0. \qquad (13\text{-}20)$$

As elaborated upon within the thesis (Section 5.5, p. 24, and Section 5.6, p. 26), if only terms *$B_1$'*, *$C_1$'* and *C' D'* are considered, equation (13-20) becomes

$$\gamma g'^v - [\alpha - 2\beta]g'' = 0 \qquad (13\text{-}21)$$

where

$$\alpha = \frac{\ddot{h}}{h^2} \qquad \beta = \frac{\dot{h}^2}{h^3} \qquad \gamma = \nu\frac{\dot{h}}{h^4}. \qquad (13\text{-}22a, b, c)$$

which is an analytically determinable linear ordinary differential equation and can be given in the form

$$(D^2 - \lambda)k = 0 \qquad (13\text{-}23)$$

where $D = d/dz^*$, $\lambda$ is the dimensionless shape parameter defined as

$$\lambda \equiv \frac{\alpha - 2\beta}{\gamma} \equiv \frac{1}{\nu}\left(\frac{\ddot{h}h^2 - 2\dot{h}^2h}{\dot{h}}\right) \qquad (13\text{-}24)$$

and

$$k(z^*) = \frac{df}{dz^*} = \frac{d^2g}{dz^{*2}}. \tag{13-25}$$

Equation (13-23) has three potential solution categories defined as follows:

- $\lambda > 0$ results in an exponential solution.
- $\lambda < 0$ results in oscillatory solution.
- $\lambda = 0$ results in a border-case solution.

The solution for equation (13-23) is in the form of a linear differential equation where

$$k(z^*) = Ae^{\sqrt{\lambda}z^*} + Be^{-\sqrt{\lambda}z^*} \tag{13-26}$$

or alternatively given by

$$k(z^*) = g''(z^*) = a\lambda \cosh\sqrt{\lambda}z^* + b\lambda \sinh\sqrt{\lambda}z^*. \tag{13-27}$$

The integral of equation (13-27) is given by

$$f(z^*) = g'(z^*) = a\sqrt{\lambda} \sinh\sqrt{\lambda}z^* + b\sqrt{\lambda} \cosh\sqrt{\lambda}z^* + c \tag{13-28}$$

and the integral of equation (13-28) is given by

$$g(z^*) = a \cosh\sqrt{\lambda}z^* + b \sinh\sqrt{\lambda}z^* + cz^* + e. \tag{13-29}$$

Boundary conditions (i) [equation (13-10)] and (iii) [equation (13-12)] are substituted into equations (13-27) and (13-28) respectively to yield

$$a + e = -\frac{1}{2} \qquad \text{and} \qquad b\sqrt{\lambda} + c = 0$$

so that when substituting these values into equation (13-29) and (13-28), the result is

$$g(z^*) = a\left(\cosh\sqrt{\lambda}z^* - 1\right) - \frac{1}{2} + b\left(\sinh\sqrt{\lambda}z^* - \sqrt{\lambda}z^*\right) \tag{13-30}$$

and

$$f(z^*) = g'(z^*) = a\sqrt{\lambda}\sinh\sqrt{\lambda}z^* + b\sqrt{\lambda}\left(\cosh\sqrt{\lambda}z^* - 1\right) \tag{13-31}$$

respectively.

When boundary condition (ii) [equation (13-11)] is substituted into equation (13-30) the result is

$$g\left(\frac{1}{2}\right) = 0 = a\left(\cosh\frac{\sqrt{\lambda}}{2} - 1\right) - \frac{1}{2} + b\left(\sinh\frac{\sqrt{\lambda}}{2} - \frac{\sqrt{\lambda}}{2}\right) \tag{13-32}$$

and when boundary condition (i) [equation (13-10)] is substituted into equation (13-27), it follows that

$$g''\left(\frac{1}{2}\right) = 0 = \lambda a\cosh\frac{\sqrt{\lambda}}{2} + \lambda b\sinh\frac{\sqrt{\lambda}}{2}$$

$$\therefore b = -a\coth\frac{\sqrt{\lambda}}{2} \tag{13-33}$$

So now $a$ and $b$ may be obtained by simultaneously solving equations (13-33) and (13-32) ultimately resulting in

$$a = \frac{1}{\sqrt{\lambda}\coth\frac{\sqrt{\lambda}}{2} - 2} \tag{13-34}$$

and

$$b = \frac{-\coth\frac{\sqrt{\lambda}}{2}}{\sqrt{\lambda}\coth\frac{\sqrt{\lambda}}{2} - 2}. \tag{13-35}$$

Hence for exponential solutions ($\lambda > 0$) equations (13-34) and (13-35) are substituted into equation $f(z^*)$ as follows

$$g(\lambda, z^*) = \frac{\left(\cosh\sqrt{\lambda}z^* - 1\right) - \left(\sinh\sqrt{\lambda}z^* - \sqrt{\lambda}z^*\right)\coth\frac{\sqrt{\lambda}}{2}}{\sqrt{\lambda}\coth\frac{\sqrt{\lambda}}{2} - 2} \tag{13-36}$$

$$f(\lambda, z^*) = \frac{\sinh\sqrt{\lambda}z^* - \left(\cosh\sqrt{\lambda}z^* - 1\right)\coth\frac{\sqrt{\lambda}}{2}}{\coth\frac{\sqrt{\lambda}}{2} - \frac{2}{\sqrt{\lambda}}} \tag{13-37}$$

Futhermore the first and second dimensionless axial derivatives are respectively given by

$$f'(\lambda, z^*) = \frac{\sqrt{\lambda}\left(\cosh\sqrt{\lambda}z^* - \sinh\sqrt{\lambda}z^*\coth\frac{\sqrt{\lambda}}{2}\right)}{\coth\frac{\sqrt{\lambda}}{2} - \frac{2}{\sqrt{\lambda}}} \tag{13-38}$$

$$f''(\lambda, z^*) = \frac{\lambda\left(\sinh\sqrt{\lambda}z^* - \cosh\sqrt{\lambda}z^*\coth\frac{\sqrt{\lambda}}{2}\right)}{\coth\frac{\sqrt{\lambda}}{2} - \frac{2}{\sqrt{\lambda}}} \tag{13-39}$$

For the case of oscillatory solutions, a complex value of $\lambda$ is substituted into the above exponential solutions, in which

$$-\lambda = \left(i\sqrt{|\lambda|}\right)^2 \tag{13-40}$$

where $i = \sqrt{-1}$ .

Hence for oscillatory solutions ($\lambda < 0$), dimensionless axial velocity $g(z^*)$, the dimensionless radial velocity $f(z^*)$ and its first and second dimensionless axial derivatives are respectively given by

$$g(\lambda, z^*) = \frac{\left(\cos\sqrt{|\lambda|}z^* - 1\right) - \left(\sin\sqrt{|\lambda|}z^* - \sqrt{|\lambda|}z^*\right)\cot\frac{\sqrt{|\lambda|}}{2}}{\sqrt{|\lambda|}\cot\frac{\sqrt{|\lambda|}}{2} - 2}. \tag{13-41}$$

$$f(\lambda, z^*) = -\frac{\sin\sqrt{|\lambda|}z^* + \left(\cos\sqrt{|\lambda|}z^* - 1\right)\cot\frac{\sqrt{|\lambda|}}{2}}{\cot\frac{\sqrt{|\lambda|}}{2} - \frac{2}{\sqrt{|\lambda|}}} \tag{13-42}$$

$$f'(\lambda, z^*) = -\frac{\sqrt{|\lambda|}\left(\cos\sqrt{|\lambda|}z^* - \sin\sqrt{|\lambda|}z^*\cot\frac{\sqrt{|\lambda|}}{2}\right)}{\cot\frac{\sqrt{|\lambda|}}{2} - \frac{2}{\sqrt{|\lambda|}}} \tag{13-43}$$

$$f''(\lambda, z^*) = \frac{|\lambda|\left(\sin\sqrt{|\lambda|}z^* + \cos\sqrt{|\lambda|}z^*\cot\frac{\sqrt{|\lambda|}}{2}\right)}{\cot\frac{\sqrt{|\lambda|}}{2} - \frac{2}{\sqrt{|\lambda|}}}. \tag{13-44}$$

# Appendix B: QSL and QS Model Block Diagrams

QSL model

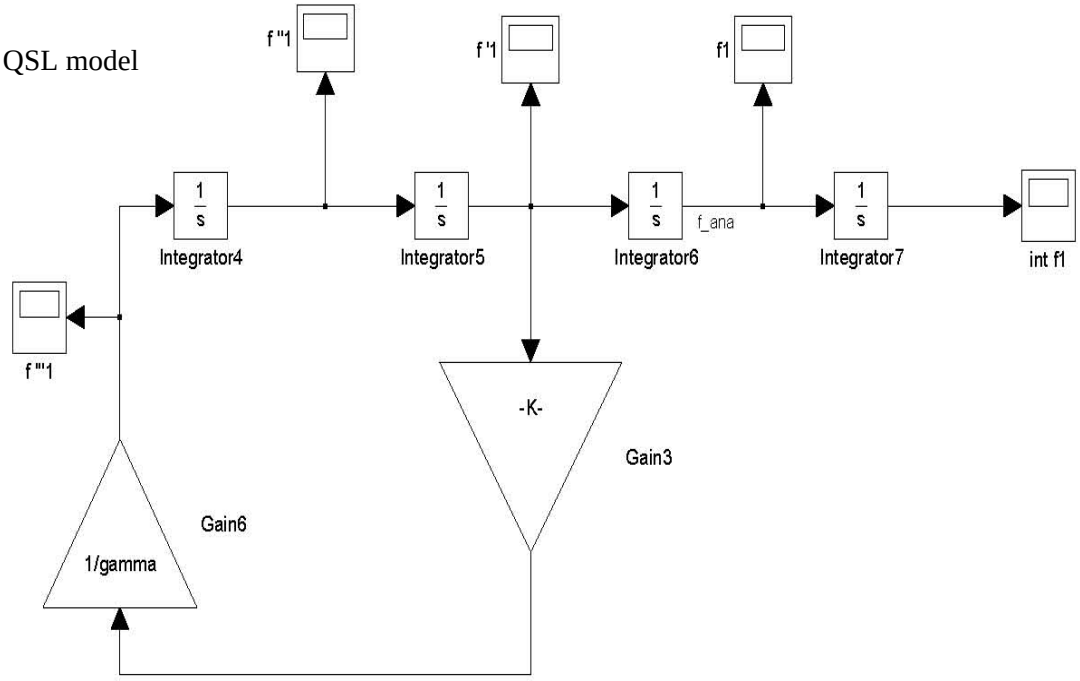


QS model

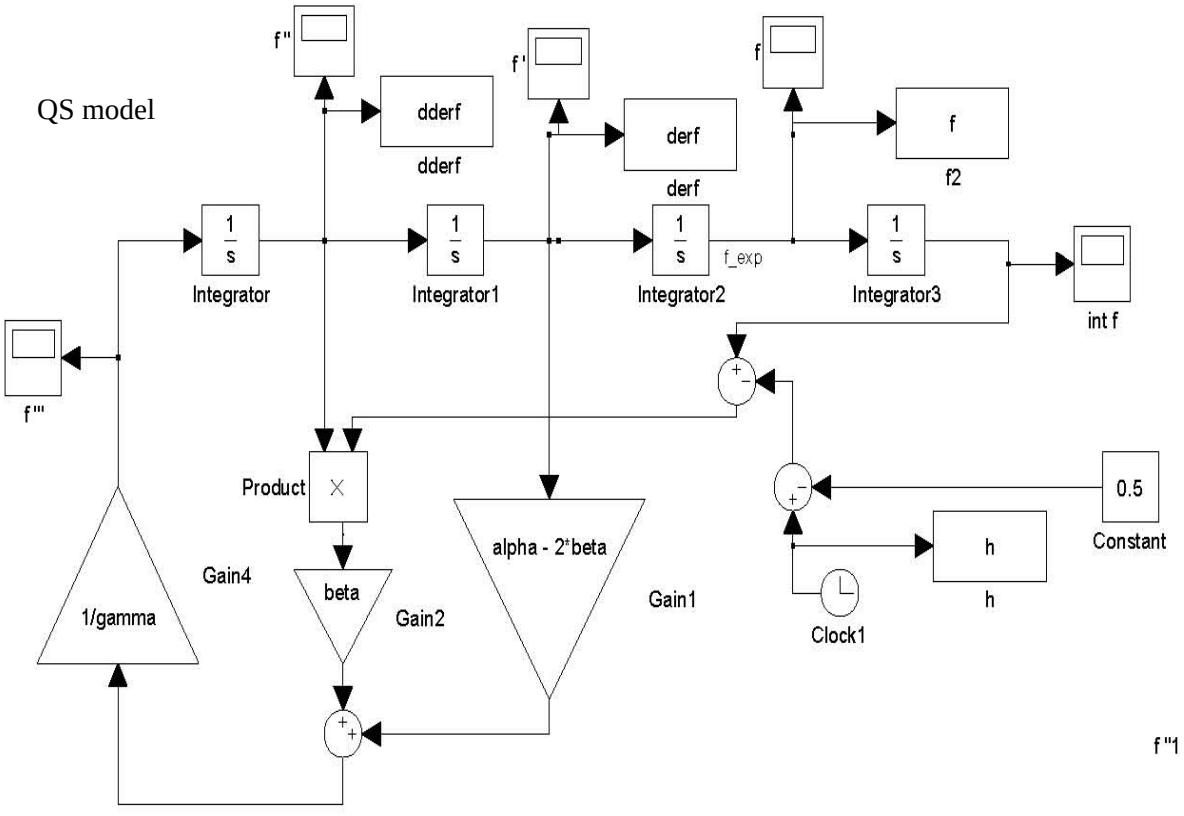

# Appendix C: Theoretical Model Comparison

| t | 0.1 | Model | f'\|z*=0 | f''\|z*=0 |
|---|---|---|---|---|
| α | -1.67E+08 | QSAL | 25.113016 | -575.63626 |
| β | 2.58E+05 | QSML | 25.107043 | -575.347971 |
| γ | -3.19E+05 | QS | 25.107043 | -575.35894 |

| t | 0.4 | Model | f'\|z*=0 | f''\|z*=0 |
|---|---|---|---|---|
| α | -5.81E+08 | QSAL | 12.99737 | -136.859936 |
| β | 7.66E+07 | QSML | 12.867151 | -133.716617 |
| γ | -6.62E+06 | QS | 12.867151 | -133.42 |

| t | 0.6 | Model | f'\|z*=0 | f''\|z*=0 |
|---|---|---|---|---|
| α | -5.77E+08 | QSAL | 10.453323 | -81.3139162 |
| β | 3.72E+08 | QSML | 10.216583 | -76.7634469 |
| γ | -2.19E+07 | QS | 10.1 | -75.55 |

| t | 0.8 | Model | f'\|z*=0 | f''\|z*=0 |
|---|---|---|---|---|
| α | -2.23E+06 | QSAL | 8.5282327 | -47.2423547 |
| β | 1.17E+09 | QSML | 8.2720285 | -43.1991181 |
| γ | -7.76E+07 | QS | 8.2 | -42.7 |

| t | 1 | Model | f'\|z*=0 | f''\|z*=0 |
|---|---|---|---|---|
| α | 2.13E+09 | QSAL | 6.9525283 | -24.097492 |
| β | 2.58E+09 | QSML | 6.7747769 | -21.736414 |
| γ | -2.96E+08 | QS | 6.75 | -21.825 |

| t | 1.2 | Model | f'\|z*=0 | f''\|z*=0 |
|---|---|---|---|---|
| α | 6.48E+09 | QSAL | 5.8486015 | -10.1995118 |
| β | 2.65E+09 | QSML | 5.7702115 | -9.27997713 |
| γ | -7.93E+08 | QS | 5.73 | -9.3 |

| t | 1.35 | Model | f'\|z*=0 | f''\|z*=0 |
|---|---|---|---|---|
| α | 7.69E+09 | QSAL | 5.0891816 | -1.64523872 |
| β | 8.16E+08 | QSML | 5.059322 | -1.32462249 |
| γ | -7.11E+08 | QS | 5.059322 | -1.326 |

| t | 1.5 | Model | f'\|z*=0 | f''\|z*=0 |
|---|---|---|---|---|
| α | 3.63E+09 | QSAL | 2.0045183 | 26.07806066 |
| β | 1.68E+07 | QSML | 1.9987512 | 26.12101786 |
| γ | -1.20E+08 | QS | 1.9987512 | 26.12101786 |

# Appendix D: CFD Results of Large Initial Disc Separations

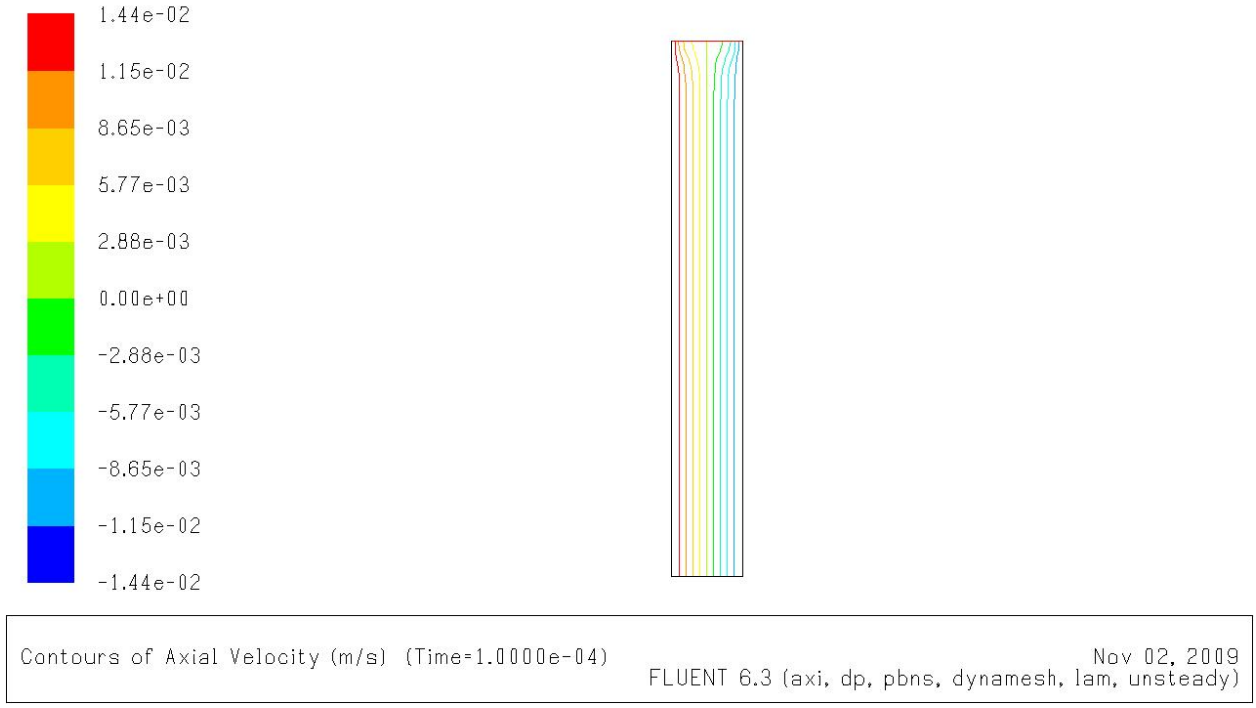


Figure 13-1: CFD axial velocity contours ($h_0 = 10$ mm)

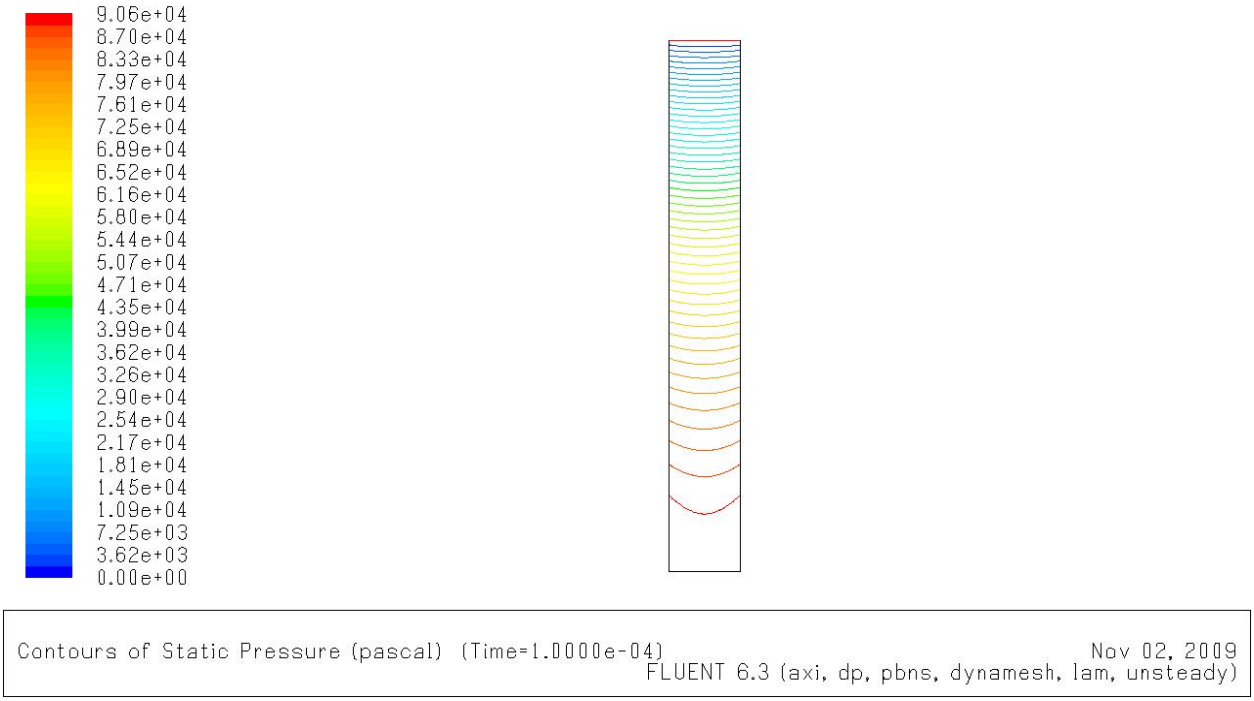


Figure 13-2: CFD pressure distribution contours ($h_0 = 10$ mm)

# Appendix E: Disc Flexure

A compound plunger (Figure 13-3) was selected as opposed to a simple plunger due to its higher specific rigidity for a given pressure distribution. This compound plunger was designed to sustain minimal disc flexure under a parabolic pressure distribution (Figure 13-4).

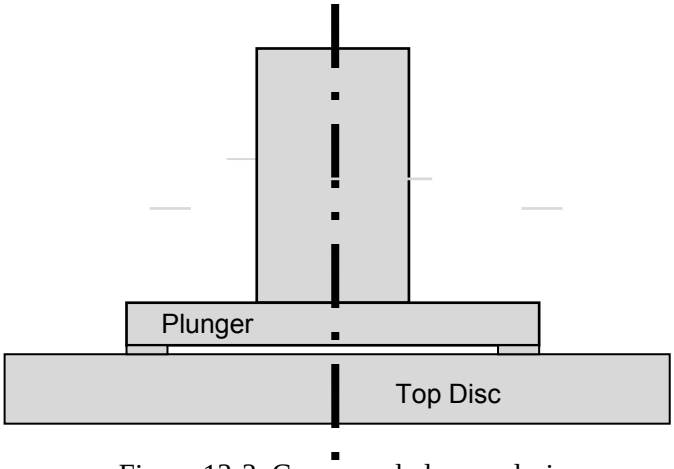


Figure 13-3: Compound plunger design

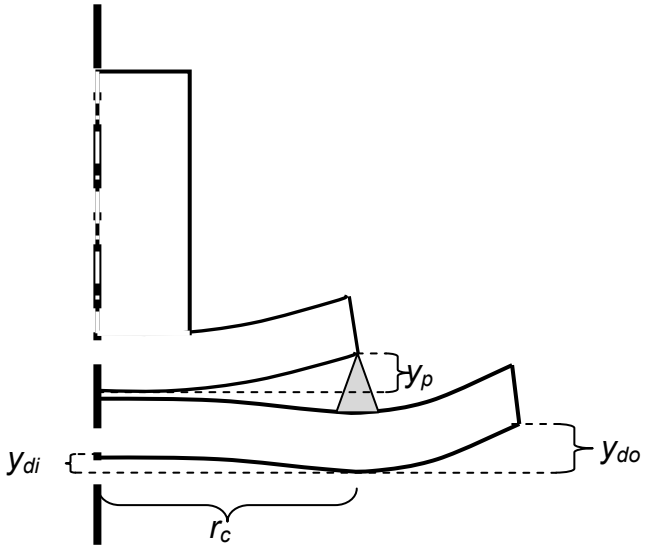


Figure 13-4: Magnified flexure of compound plunger under parabolic pressure distribution.

The equations used in determining the flexure and stress of the compound plunger are obtained from equations for thin plate flexure (Roark, 1975). The equations used assume that the thickness of the discs do not exceed more than a quarter of the maximum transverse distance, this assumption has been violated

for the compound plunger under investigation, however it is speculated that this violation yields more conservative results for both the stress and flexure.

Only solutions for radially increasing parabolic pressure distributions are presented. Hence, the principal of superposition is used in which these 'inverse' parabolic pressure profile is subtracted from a uniform pressure distribution (of the same maximum pressures) yielding radially decreasing parabolic pressure profile (corresponding to the measured system). The flexure of the circumference of the top disc (Figure 13-3) is calculated separately from the flexure at the centre of the top disc, however both these flexures are coupled by the stress occurring at $r_c$.

The dimensions of the top disc are taken as $a = 60$ mm, $b = 0$ mm, $t = 12$ mm (see the engineering drawings in CD-Appendix E) whereas Young's modulus and Poisson's ratio for steel is given as $E = 200$ GPa and $\nu = 0.3$ respectively. It is found through a manual iterative process that if $r_c$ is set to $r_c = 31$ mm a similar deflection is obtained at both the circumference and centre of the top disc (Figure 13-4: Magnified flexure of compound plunger under parabolic pressure distribution.). These deflection values and resultant stress at $r_c$ are respectively given as

$$y_{di} \approx y_{do} \approx 1.8 \times 10^{-12} p_{cent} \text{ m} \quad \text{and} \quad \sigma_r \approx 2.25 p_{cent} \text{ Pa} \tag{13-45}$$

where $p_{cent}$ is recalled as the central pressure. Calculations for the above equations are carried out in MATLAB, the 'disc flexure' code given in CD-Appendix A. At the maximum experimentally measured pressure of about 25 MPa (Figure 8-34, p. 134), the maximum deflections are stress is approximately 45 μm and 56 MPa respectively. It is calculated that this compound plunger has a deflection of less than 1/10 that of a simple plunger (with the same top disc dimensions). The maximum deflection and stress of the plunger (top component) is respectively given as

$$y_p \approx 2.5 \times 10^{-12} p_{cent} \text{ m} \quad \text{and} \quad \sigma_p \approx 14.5 p_{cent} \text{ Pa} \tag{13-46}$$

In addition to the deflection calculations due to the pressure, the deflection of the top disc due to inertia may be equated to an uniform pressure acting upon the disc which may be calculated by $p_{eqv} = F/A$ or $p_{eqv} = \rho t \ddot{h}$. This equivalent pressure has been calculated at a maximum acceleration of about 6 km/s$^2$ (Figure 8-29, p. 127), and a conservatively high steel density of 8000 kg/m$^3$, at which the equivalent

pressure is $p_{eqv} = 77$ kPa. At this relatively negligible equivalent pressure, the stress and deflection of the plunger's disc due to inertial affects are negligible.

After all the experimentation was conducted the plunger's disc was checked for permanent yield. There was no visually detectable permanent yield.

# Appendix F: Inter-Calibration

Since the pressure transducers used for experimentation are high frequency response transducers, they cannot be calibrated with a traditional *Budenberg* type pressure transducer calibrator because the pressure is generated slowly and therefore the charge decay rate is too fast to yield accurate results. Furthermore, no local (South African) facility to re-calibrate these pressure transducers is available. Hence all the pressure transducers used in the test rig are inter-calibrated against a brand new, factory calibrated PCB 113A23 pressure transducer (see attached page- pressure transducer serial # 19131).

Inter-calibration involves the comparison of output voltages between the test-rig's existing pressure transducers and that of a newly calibrated pressure transducer which all measure an impulsive pressure spike applied to the same body of fluid, thus the calibration coefficients of constants of the test-rig's existing pressure transducers may be inferred.

The inter-calibration ring (engineering drawings in CD-Appendix E) is used to convert the existing test-rig into a cylinder/piston assembly as shown in Figure 13-5.

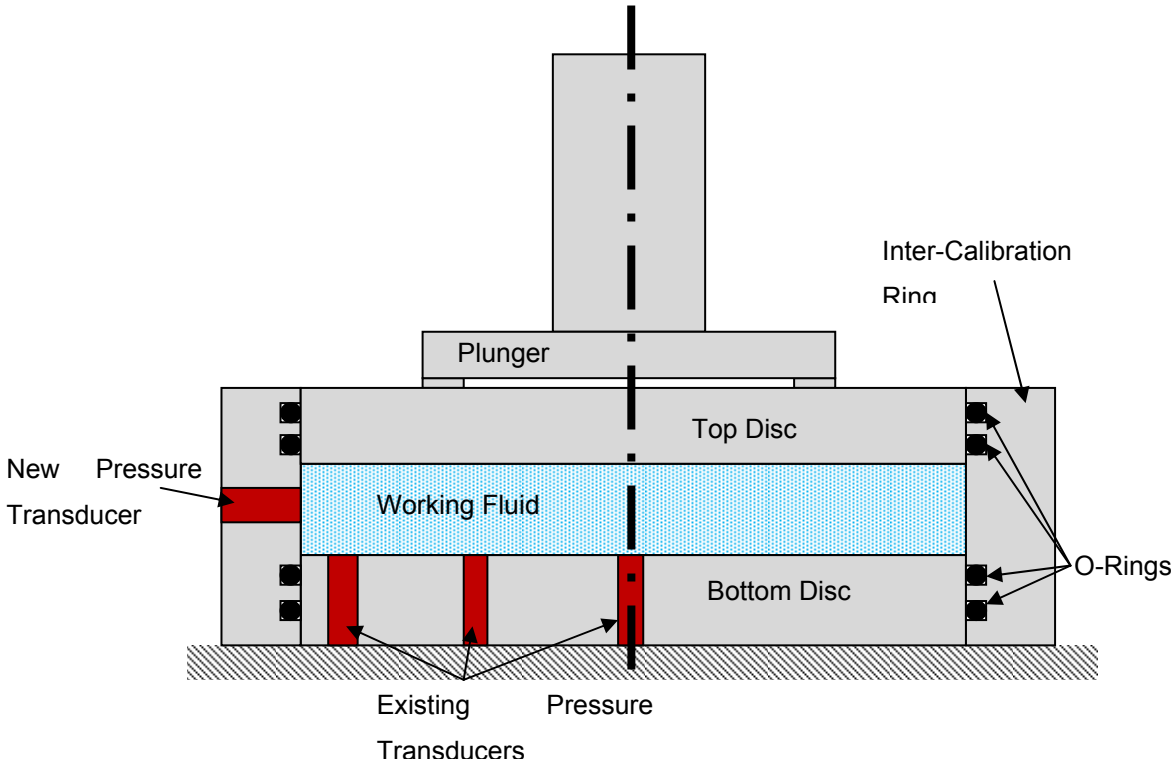


Figure 13-5: Inter-calibration test-rig

## Procedure

The inter-calibration procedure closely follows that of the experimental procedure for drop-hammer tests as elaborated upon in Section 7.3, p. 80. The number of inter-calibration tests is limited to ten in which the maximum pressure measured by the reference pressure transducer is 25 MPa.

## Results

The calibration coefficient of the new pressure transducer (Serial #: 19131) is given as 0.5021 mV/PSI (see attached page), or $cal_n = 0.07282$ V/MPa. In turn, the test-rig's pressure transducers output voltages are calculated as a straight line curve fit with respect to the new pressure transducer's output voltage in order to account for non-linearity that may have occurred during previous usage. Table 13-1 gives the inter-calibration results for the test-rigs pressure transducers.

Table 13-1: Pressure transducer information and calibration constants

| **Pressure transducer** | **Radial position (mm) and radial percentage (%)** | **Model** | **Serial number** | **Calibration constants (linear fit)** | | **Uncertainty bound coefficients [$\sigma$]** |
|---|---|---|---|---|---|---|
| | | | | **Gradient [$m$]** | **Intercept [$c$]** | |
| $p_{t1}$ | 0 (0%) | M109B12 | 3870 | 0.061 | 0.132 | 2000 |
| $p_{t2}$ | 27 (45%) | M109B12 | 3869 | 0.064 | 0.131 | 2000 |
| $p_{t3a}$ | 54 (90%) | 113A23 | 6707 | 0.063 | 0.993 | 200 |
| $p_{t3b}$ | 54 (90%) | 113A23 | 7933 | 0.067 | 0.981 | 200 |
| $p_{t3c}$ | 54 (90%) | 113A23 | 6706 | 0.055 | 1.065 | 200 |

Hence the calibration coefficient of an above given pressure transducer is given as

$$cal = (mV + c) \times 0.07282 \text{ V/MPa} \tag{13-47}$$

where $V$ is the pressure transducer's output voltage.

## Uncertainty Bounds

It is empirically found that conservative uncertainty bound coefficients, defined as ε, follow the formula

$$\varepsilon = cal \pm \frac{2V|_{\max}}{\sigma V} \tag{13-48}$$

where $V$ is the output voltage of the pressure transducer and $\sigma$ is defined as the uncertainty bound coefficient where, for the 113A23 pressure transducers, $\sigma = 200$ and for the M109B12 pressure transducers $\sigma = 2000$. This difference in uncertainty bound coefficient is due to differences in the calibration coefficients range between the different pressure transducer models.

# Appendix G: Pressure Transducer Specifications

# Appendix H: Laser Displacement Sensor Specifications

# LB SERIES
LASER DISPLACEMENT SENSORS

## SPECIFICATIONS

| Model | | Controller | LB-70 | LB-72 |
|---|---|---|---|---|
| | | Sensor head | LB-11 | LB-12 |
| Reference distance[1] | | | 100 mm | 40 mm |
| Measuring range | | | ±40 mm | ±10 mm |
| Light source | | | Invisible semiconductor laser<br>Wave length: 780 nm, Max. output: 3 mW | |
| | Pulse duration | | 70 µs | 15 µs |
| | Class | FDA | Class IIIb | |
| | | IEC 825-1 11.1993 | Class 3B | |
| | | DIN EN 60825-1 07.1994 | Klasse 3B | |
| Spot diameter[2] | | | 1.0 x 2.0 mm | 1.0 mm |
| Linearity[5] | | | 1.6% of F.S. (within 80 to 120 mm) | 1% of F.S. |
| Resolution[3] | | | 10 µm (at 500 ms)/40 µm (at 20 ms)/180 µm (at 0.7 ms) | 2 µm (at 60 ms)/15 µm (at 2 ms)/50 µm (at 0.15 ms) |
| STABILITY indicator | | | LED (RED, GREEN, YELLOW) | |
| Output | Analog | Voltage[4] | ±4 V (0.1 V/mm) | ± 4 V (0.4 V/mm) |
| | | Impedance | 100 Ω | |
| | Alarm | | NPN open collector: 50 mA (40 V) max. Residual voltage: 1 V max (N.C.) | |
| Zero point adjustment range | | | 60 mm to 140 mm | 30 mm to 50 mm |
| Span adjustment range | | | 0.1 V/mm±30% | 0.4 V/mm±30% |
| Response frequency | | | DC to 700 Hz (at 0.7 ms) (-3 dB)/DC to 18 Hz (at 20 ms) (-3 dB)/DC to 0.6 Hz (at 500 ms) (-3 dB) | DC to 3 KHz (at 0.15 ms) (-3 dB)/DC to 200 Hz (at 2 ms) (-3 dB)/DC to 6 Hz (at 60 ms) (-3 dB) |
| Sensitivity | | | WHITE, BLACK, and AUTO (switch-selectable) | |
| Temperature fluctuation[5] | | Sensor head | 0.02% of F.S./°C | 0.04% of F.S./°C |
| | | Controller | 0.04% of F.S./°C | 0.03% of F.S./°C |
| Laser control input | | | NPN open collector or non-voltage contact | |
| Ambient light[6] | | | 4,000 lux max. | |
| Ambient temperature | | | 0 to +50 °C | |
| Relative humidity | | | 35 to 85% | |
| Power supply | | | 12 to 24 VDC ±10% Ripple (P-P): 10% max. | |
| Power consumption | | | 120 mA max. | |
| Housing | | Sensor head | Die-cast zinc-based alloy | |
| | | Controller | Polycarbonate | |
| Weight (including cable) | | Sensor head | Approx. 180 g | Approx. 250 g |
| | | Controller | Approx. 185 g | Approx. 185 g |

1. Distance from the surface of the laser-emitting portion of the sensor head.
2. The beam spot is visible when the object (white paper) is placed at a distance of 100 mm (40 mm: LB-72) from the laser-emitting portion of the sensor head.
3. The value when the object (white papaer ) is measured at a distance of 100 mm (40 mm: LB-72) from the laser-emittintg portion of the sensor head.
4. The range can be expanded to -5 V to +5 V by using the 0-ADJ and SPAN adjuster trimmers.
5. F.S. stands for a measurement range of 80 mm (20 mm: LB-72).
6. Incandescent lamp or fluorescent lamp.

## DIMENSIONS

(Unit: mm)

### Sensor head
LB-11
LB-12

Items marked with * are different from those of LB-11.

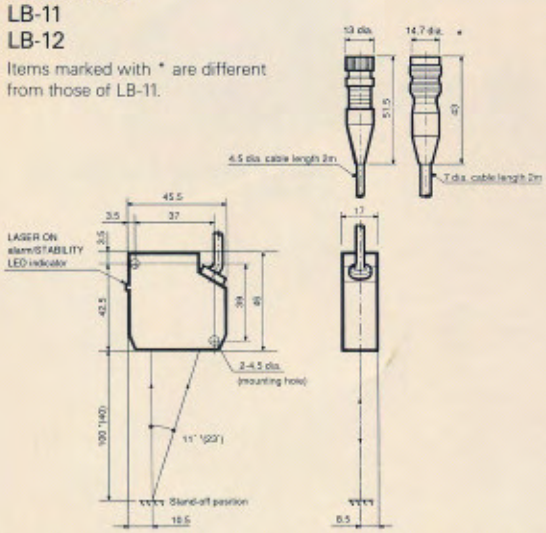


### Controller
LB-70
LB-72

Items marked * are different from those of LB-70

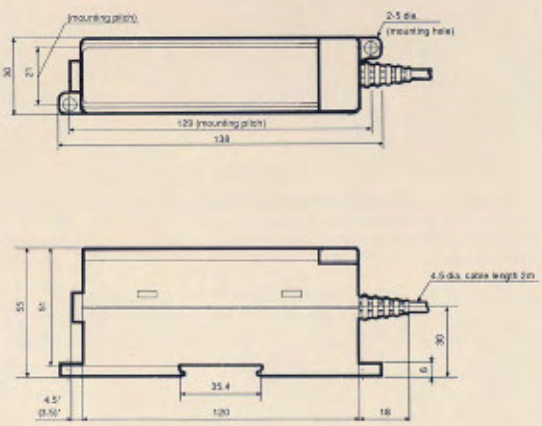


### SAFETY

The laser displacement sensor LB series is classified as a FDA Class IIIb (IEC Class 3B) laser product, and is identified as such by the warning label shown in the figure below, which also shows other warning labels affixed to the covers. If the operator stares directly into the beam, damage can be caused to the operator's eyes.

### Drawings

LB-70/LB-11



Specifications are subject to be changed without notice

KEYENCE
KEYENCE CORPORATION


**Headquarters**
1-3-14, Higashinakajima, Higashiyodogawa-ku,
Osaka, 533, Japan
PHONE: 81-6-379-2211 FAX: 81-6-379-2131

**KEYENCE CORPORATION OF AMERICA**
**New Jersey office:**
50 Tice Blvd. Woodcliff Lake, NJ 07675
PHONE: 201-930-1400 FAX: 201-930-0088
**Ohio office:**
PHONE: 614-799-3400 FAX: 614-799-3401
**Chicago office:**
PHONE: 708-775-1110 FAX: 708-775-1169
**Atlanta office:**
PHONE: 404-499-5390 FAX: 404-499-5391
**Los Angeles office:**
PHONE: 310-540-2254 FAX: 310-316-1032

**KEYENCE DEUTSCHLAND GmbH**
Friedrich-List-Straße 44
70771 Leinfelden-Echterdingen, F.R.G.
PHONE: 0711-796061 FAX: 0711-7977799

**KEYENCE UK LIMITED**
379 South Row, Witan Gate East
Central Milton Keynes MK9 2PN, UK
PHONE: 01908-696900 FAX: 01908-696777




LB-C-5-1194 Printed in Japan

# Appendix H: Smoothing Evaluation

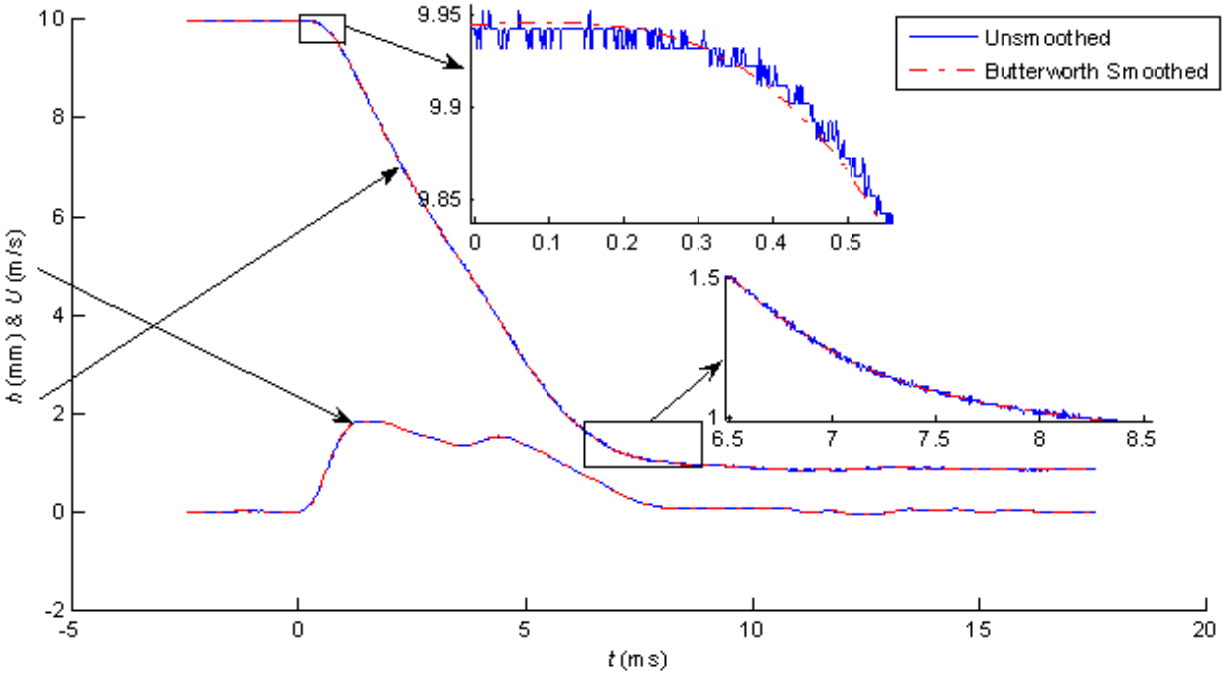


Figure 13-6: Smoothing evaluation of disc separation and velocity traces

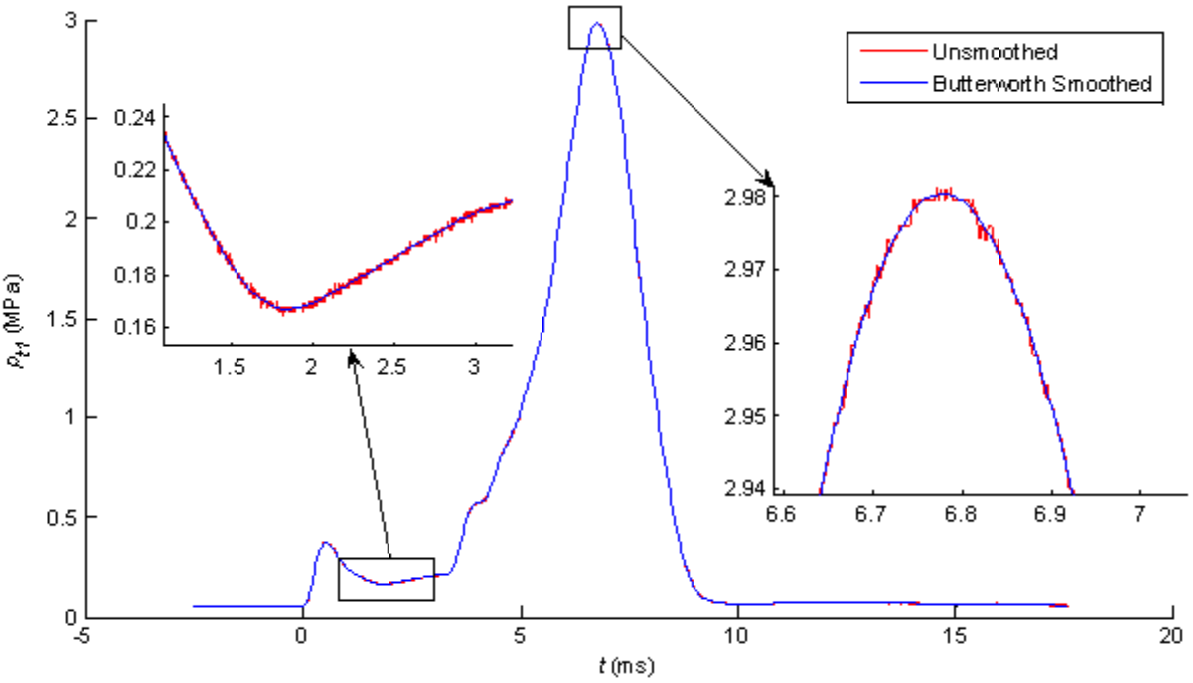


Figure 13-7: Smoothing evaluation of pressure traces